THE TEMPORAL VARIABILITY OF ANTHROPOGENIC CARBON STORAGE IN THE LABRADOR SEA

by

Lorenza Raimondi

Submitted in partial fulfillment of the requirements
for the degree of Doctor of Philosophy

at

Dalhousie University
Halifax, Nova Scotia
August 2021

To my Mamma and Papi for their endless support and love.

TABLE OF CONTENTS

LIST OF TABLES

LIST OF FIGURES

ABSTRACT

The Labrador Sea is a key region for the transport of anthropogenic carbon (C_{ant}) into the ocean interior. The formation of Labrador Sea Water (LSW) provides a direct path for atmospheric gases to be exchanged with the deep ocean. However, model projections suggest there is potential for significant future reduction of convection depth and LSW formation in response to increased freshwater input from Greenland. In order to predict how physical changes will affect the fate of C_{ant} in the Labrador Sea, it is crucial to understand how the storage of C_{ant} has been evolving in the region.

In this PhD thesis I present the first multi-decadal (1993-2016) estimate of C_{ant} in the Central Labrador Sea based on two indirect methods (Transit Time Distribution; TTD further extended to 1986, and extended Multiple Linear Regression; eMLR), and I compare these estimates to Dissolved Inorganic Carbon (DIC) observations.

I first focus on the quality of the carbonate chemistry data by assessing the internal consistency of the carbonate system. I recommend best practices to perform calculations of the carbonate system parameters and I highlight the importance of conversion to *in situ* conditions of temperature and pressure for comparisons with measurements performed with autonomous sensors.

For the application of the TTD method I calculate the saturations of CFC-12 and SF_6 from observations and show their strong temporal variability in this region. Therefore I provide reconstructed saturations of these tracers to accurately estimate C_{ant} with the TTD method here.

By using the eMLR method with different time intervals and starting years, I show that the choice of starting year can greatly affect the estimates of C_{ant} storage rate and therefore mislead the interpretation of the role of the Labrador Sea in sequestering C_{ant}. Both methods to estimate C_{ant} highlighted the importance of assumptions implied in a proxy method, they revealed that the storage of C_{ant} is non-steady over time and that the temporal variability of the C_{ant} storage in the region appears to be associated to the strength of convection.

Overall this thesis highlights the importance of a multi-disciplinary long-term monitoring program and represents a solid base for validation of biogeochemical models.

LIST OF ABBREVIATIONS AND SYMBOLS USED

Abbreviations	Description	Units
AABW	Antarctic Bottom Water	
AMOC	Atlantic Meridional Overturning Circulation	
ANOVA	Analysis of Variance	
AO	Atlantic Ocean	
ArO	Arctic Ocean	
AR7W	Atlantic Repeat Hydrography Line 7 West	
ASW	Artificial Seawater	
AZOMP	Atlantic Zone Off-Shore Monitoring Program	
BIO	Bedford Institute of Oceanography	
C_{ant}	Anthropogenic Carbon	$\mu mol\ kg^{-1}$
CFCs	Chlorofluorocarbons	
CFC-12	Dichlorodifluoromethane	$pmol\ kg^{-1}$
CLIVAR	Climate and Ocean: Variability, Predictability and Change	
CRM	Certified Reference Material	
CS	Constant Saturation	$\%$
CTD	Conductivity, Temperature and Depth	
DFO	Department of Fisheries and Ocean (Canada)	
DIC	Dissolved Inorganic Carbon	$\mu mol\ kg^{-1}$
DIW	Deep Intermediate Water	
dLSW	deep Labrador Sea Water	
DSOW	Denmark Strait Overflow Water	
EEP	Eastern Equatorial Pacific	
eMLR	Extended Multiple Linear Regression	
fCO_2	Fugacity of CO_2	
GLODAPv2	Global Ocean Data Analysis Project (version 2)	

Abbreviations	Description	Units
GOM	Gulf of Mexico	
GO-SHIP	Global Ocean Ship-based Hydrographic Investigations Program	
GP	Goyet & Poisson	
H	Hansson	
HM	Hansson and Mehrbach	
$I_{C_{ant}}$	Column Inventory of C_{ant}	$mol\ m^{-2}$
IO	Indian Ocean	
L	Lueker	
LSW	Labrador Sea Water	
M06	Millero (2006)	
M73	Mehrbach (1973)	
MC	Monte Carlo Simulation	
MLD	Mixed Layer Depth	m
MLR	Multiple Linear Regression	
MPM	Mojica-Prieto & Millero	
MSE	Mean Squared Error	
NADW	North Atlantic Deep Water	
NAO	North Atlantic Oscillation	
NEADW	North East Atlantic Deep Water	
NWESSU	North Western European Shelf Seas	
NS	North Sea	
OCIM	Ocean Circulation Inverse Model	
OGCM	Ocean General Circulation Model	
P	Pressure	$dbar$
pCO_2	Partial Pressure of CO_2	μatm
PO	Pacific Ocean	
P_T	soluble reactive phosphorus	$\mu mol\ kg^{-1}$
R	Roy (1993)	
RMSE	Root Mean Square Error	

Abbreviations	Description	Units
S	Storage (Chapter 1)	
S	Salinity (all other Chapters)	
SF_6	Sulfur Hexafluoride	$fmol\ kg^{-1}$
Si_T	Silicate	$\mu mol\ kg^{-1}$
SPNA	Subpolar North Atlantic	
SR	Storage Rate	$mol\ m^{-2}\ y^{-1}$
SSE	Sum of Square of Errors	
SSR	Sum of Square of Regression	
SST	Total Sum of Square	
SW	Seawater	
T	Temperature	$^{\circ}C$
TA	Total Alkalinity	$\mu mol\ kg^{-1}$
T_{in}	Lateral Transport into idealized box	
T_{out}	Lateral Transport out of idealized box	
TTD	Transit Time Distribution	
uLSW	upper Labradro Sea Water	
U	Uptake	
U-pCO_2	Underway pCO_2	μatm
U-pH	Underway pH	
VS	Variable Saturation	$\%$
WUS	Western US Coast	

Greek symbol	Description	Units
α	significance level	
$\alpha*$	adjusted significance level	
Γ	Mean Age of Transit Time Distribution	
Δ	Width of Transit Time Distribution	
ΔDIC_{obs}	Temporal Change of the Observed DIC	$\mu mol\ kg^{-1}$
		$mol\ m^{-2}\ y^{-1}$
ΔDIC_{eMLR}	Temporal Change of C_{ant} estimated with eMLR	$\mu mol\ kg^{-1}$
		$mol\ m^{-2}\ y^{-1}$

Greek symbol	Description	Units
ΔDIC_{TTD}	Temporal Change of C_{ant} estimated with TTD	$\mu mol\ kg^{-1}$
		$mol\ m^{-2}\ y^{-1}$
ΔDIC	DIC Residuals (measured-calculated)	$\mu mol\ kg^{-1}$
ΔpH	pH Residuals (measured-calculated)	
$\Delta p\mathrm{CO}_2$	$p\mathrm{CO}_2$ Residuals (measured-calculated)	μatm
ΔTA	TA Residuals (measured-calculated)	$\mu mol\ kg^{-1}$
$\epsilon\ \varepsilon$	errors of linear regressions	
θ	potential temperature of water	$^{\circ}C$
ν	Degrees of Freedom	
ρ	*in situ* density anomaly	$kg\ m^{-3}$
σ_θ	sigma-theta of water	$kg\ m^{-3}$
σ_2	potential density anomaly	
	with reference pressure of 2000 dbar	$kg\ m^{-3}$
Ω_{Ar}	Aragonite Saturation State	
Ω_{Ca}	Calcite Saturation State	

ACKNOWLEDGEMENTS

How do you properly thank all the people that supported you for such a long time? It seems like an impossible task to me but I will try my best.

First of all I would like to thank my Committee Members Toste Tanhua, Katja Fennel and Eric Oliver for their invaluable feedbacks and suggestions provided throughout my PhD. In particular I would like to thank Toste Tanhua for his patience, for sharing his expertise with me but most of all for showing me that (even in academia) it is possible to maintain a good work/life balance. I would like to thank my co-supervisor Kumiko Azetsu-Scott, particularly for replying that first (probably not so well written) email I sent her back in 2013. Kumiko, with just one email you have opened a world of new exciting opportunities for me and I cannot thank you enough for that.

My most heartfelt thanks go to my supervisor Doug Wallace. I am not going to lie, it was a bumpy road, and it took us a bit to oil this machine but I honestly couldn't be happier and prouder to call you my supervisor. Thank you Doug for all the laughs, family chats and the "good old days" stories you have shared with me over the years. Thank you for always pushing me to be a better scientist but (almost) always in a fatherly way. I will forever cherish the (impromptu) chemistry, ethics and grammar lessons during our meetings and I am forever thankful to have been able to be part of your team. Over the years I have developed a huge appreciation for your great (sometimes impossible) ideas, your enthusiasm and excitement about science but most of all I have learnt that you are a great person, a supportive supervisor and a true feminist (not just in words but in actions). Finishing my PhD while also starting my family has only been possible thanks to your support, so thank you.

I would like to thank all my collaborators and co-authors, in particular Robin Matthews, Claire Boteler and Igor Yashayaev for their huge support throughout the preparation of our papers.

During these years I have had the luck to not just sit at my desk but also spend a considerable amount of hours at sea and in a laboratory, hours that I share with some truly amazing people. First of all the fellows and friends a the Bedford Institute of Oceanography, in particular Steve Duerkens, Darlene Child, Yuri Geshelin, Richard

Nelson, Mark Ringuette, Andrew Cogswell, Peter Thamer, and Tim Perry. Most of all I would like to thank Steve Punshon. Steve, you are one of the persons I feel lucky to have encountered in my life, I will forever cherish your English humour, your lessons about gas chemistry and all the laughs we have shared over the years. A big thanks goes also to my lab group, in particular to my office mate Lin for all the laughs and frustration shared over the years, Ricardo, Aly, Sebastian and Qiang for the coffee breaks and chats in the office. Most of all I would like to thank Dasha, for being a great friend, supporter and collaborator throughout the years, I have learnt so much from you Dasha and I will forever remember all the times we have chatted about science and not-so-science stuff over sushi.

To my fellow DOSA members and everyone in the Oceanography Department...what can I say, you have been able to maintain my mental sanity and make me feel at home since the first day I stepped foot in this department. A special thank goes to my gold team: Lori, Jackie and Markus, you made administration fun and something I would look forward to just because I could talk to you. You have been a huge support throughout these years and I will miss you so much. Thanks to Nadine, Christoph, Colleen, Jacoba and Laura for sharing laughs, great nights out, get-aways at cottages, hikes and of course many MATLAB crises. You are my Hali-family and I will forever remember the time we have spent together.

To my MVP: Krysten Rutherford. I don't think I need to say any of this because I am sure you already know it all but sometimes its' better to write it down than saying it in person. I couldn't do this PhD without you. You have been an amazing support, the best cheerleader a girl can have on her side and a fantastic friend. Thank you for sharing your knowledge, your friendship and most of all many (many) tears and laughs with me over the years. I am so lucky to call you my friend.

To my family: Piera and Ranieri you have managed to make me feel your love and support even with an ocean standing between us! I have missed you every single day of my PhD but I always knew I could count on you no matter the distance and no matter how many days we didn't talk on the phone. I couldn't do life without you. Mamma e Papà non potrò mai ringraziarvi abbastanza per tutto il supporto e gli sproni che mi avete dato durante tutti i miei anni di Università. Grazie per avermi sempre ricordato che, con impegno, avrei potuto fare qualsiasi cosa desiderassi nella vita. Non tutti i genitori la pensano così per questo voglio ringrazirvi per avermi fatto scegliere gli studi a cui ero appassionata. Se sono arrivata fino a qui è solo grazie alla vostra lungimiranza riguardo

la mia educazione, ai vostri tantissimi sacrifici e il vostro amore. Vi amo con tutto il mio cuore e spero di portarvi un pò di felicità con questo mio traguardo.

Last but absolutely not least I need to thank my new little family. First my partner Francesco. You have been the best academic supporter I could have ever asked for. Thanks for all your pep talks, the hours spent going through equations I didn't understand on my own and for celebrating every little one of my achievements like it was your own. Thank you for all the laughs and happy moments you have brought into my life, even in the darkest time. Thank you for being the best friend, life partner and father but most of all for not being afraid of any challenges and for always trying to be the best version of yourself for our son and myself. Finally the biggest thank goes to my son. Totò, if for whatever reasons you will read this one day I want you to know that you have been the strongest driver of this endeavour. Even though you are only (almost) three years old at the time I am writing this, you have been able in such short time to change my life in the best way possible. You push me to be a better researcher, mom and overall better person. You put everything in perspective and in the toughest time you are able to erase all of my fears and doubts with just one smile. I hope that with this thesis I am able to teach you the same lesson my parents thought me when I was a very young girl and that is: any goal can be achieved when you put effort in. I love you.

CHAPTER 1

INTRODUCTION

1.1 The Oceanic Carbon Sink

Atmospheric levels of carbon dioxide (CO_2) have been dramatically increasing since the industrial revolution as the result of fossil fuel burning and land use change (*Keeling et al.*, 2005). The change in carbon dioxide concentrations relative to pre-industrial values due to anthropogenic activities, like fossil fuel combustion and cement manufacture, is defined as "excess" or "anthropogenic" carbon dioxide (Excess CO_2 or C_{ant}; *Wallace*, 2001).

Only a fraction of the carbon emitted stays in the atmosphere (the "airborne fraction") since other sinks, namely the ocean and land, also remove and store anthropogenic CO_2 as part of the global carbon cycle. The ocean represents one of the strongest sinks of C_{ant} with a cumulative net sink representing approximately 40-45% of the CO_2 emitted by fossil fuel burning over the past 200 years (*DeVries*, 2014; *Gruber et al.*, 2019b; *Khatiwala et al.*, 2013; *Sabine et al.*, 2004).

Because the Excess CO_2 in the ocean represents only a fraction of the total dissolved CO_2, it is difficult to distinguish the anthropogenic signal from the natural one. Additional complications are due to the lack of analytical procedure to measure C_{ant} concentrations. In fact direct observation of the increase in C_{ant} concentrations in the ocean is only possible if changes in the isotopic signature of CO_2 are taken into account (Seuss Effect; *Keeling*, 1979).

For these reasons, several indirect methods have been developed to obtain an estimate of C_{ant} concentrations in the ocean (see *Sabine and Tanhua*, 2010, for a detailed summary of the methodologies available). These methods have been developed based on both carbonate chemistry and transient tracers data, as well as employing ocean modelling. A common

assumption of these methods is that they imply a steady-state ocean circulation between the pre-industrial's and today's conditions. Nevertheless, it is very likely that this assumption of steady-state ocean circulation is not representative of the real ocean, particularly for highly dynamic regions like the Labrador Sea. In order to obtain a better understanding of if a steady-state ocean assumption is reasonable, there is a need for long time series of ocean observations which are currently a rarity.

The above-mentioned methods to estimate C_{ant} have been applied to assess the column inventories of C_{ant} (*Gruber et al.*, 2019b; *Khatiwala et al.*, 2009; *Sabine et al.*, 2004; *Waugh et al.*, 2006), and to quantify the air-sea fluxes and transport of this gas in the ocean interior (*DeVries*, 2014; *Gruber et al.*, 2009; *Gerber et al.*, 2009; *Khatiwala et al.*, 2013; *Mikaloff Fletcher et al.*, 2006). While the values of global net oceanic sink of C_{ant} obtained by these different methods agree within their uncertainties, significant differences in the C_{ant} distribution are observed regionally and along the water column.

Nevertheless, all the approaches show that the highest vertically integrated concentrations of C_{ant} are found in the North Atlantic[1], making this region the most intense open ocean accumulation area of anthropogenic carbon in the global ocean (*DeVries*, 2014; *Gruber et al.*, 2019b; *Khatiwala et al.*, 2013, 2009; *Sabine et al.*, 2004; *Waugh et al.*, 2006).

1.2 C_{ant} in the North Atlantic: Storage, Uptake and Transport

The excess or anthropogenic CO_2 can be exchanged from one reservoir to another, in fact C_{ant} makes its way into the ocean through the air-sea interface. This flux or net transport of C_{ant} from the atmosphere to the ocean is defined as "Uptake" (U). On the other hand, a change in the inventory over time within a reservoir is defined as "Storage" (S).

While storage and uptake of a reservoir must be equal on a global scale, in the ocean they could be geographically decoupled. Indeed uptake of C_{ant} occurs in certain regions on a larger scale than in others, and the storage of this C_{ant} can also regionally vary due to lateral transport (T_{in} and T_{out}) with either convergence or divergence of ocean currents (*Wallace*, 2001). The storage (i.e., rate of accumulation) in a conceptual box can therefore

[1] With different methods showing C_{ant} column inventories estimates ranging between 90 and 120 mol m^{-2} in 1994 in the Labrador Sea.

be summarized as by the following equation:

$$S = \frac{T_{IN} - T_{OUT}}{Surface\ Area} + U \tag{1.1}$$

where S refers to storage (in mol m^{-2} y^{-1}), T_{IN} and T_{OUT} represents the net transport into and out of the box (in mol y^{-1}), z is the bottom depth, the surface area is the area between the two transects used to calculate the transport (in m^{-2}) and U refers to the perturbation of the natural flux of CO_2 across the air-sea surface, or uptake due to higher atmospheric CO_2 (in mol m^{-2} y^{-1}).

One of the first global studies by *Sabine et al.* (2004) estimated the oceanic storage and studied the distribution of C_{ant} through the water column in the main ocean basins (Atlantic, Pacific and Indian). They observed that while most of C_{ant} was confined to the near-surface waters due to gas exchange across the air-sea interface (about 50% of C_{ant} was found at depths above 400 m), entrainment of C_{ant} in the ocean interior occurs in convergence zones, particularly in the North Atlantic, with vertical penetration reaching 3000 meters (m) depth. On the other hand, a much shallower entrainment is observed in equatorial regions. The reason for this irregular distribution of C_{ant} is to be found in the presence of either deep water formation or upwelling areas. Waters that have been recently in contact with the atmosphere, and have therefore high concentration of anthropogenic carbon, are transported in the ocean interior in deep convection zones like the Labrador and Irminger Seas in the North Atlantic. In contrast, when upwelling occurs old waters, with very low concentrations or no C_{ant}, are moved toward the surface where they get exposed to high concentrations of this gas. The dynamics described by *Sabine et al.* (2004) highlighted the central role that the Northwest Atlantic plays in the global sequestration of excess CO_2, and conveyed interest of the carbon community in this region. The authors estimated that, despite representing only 15% of the global ocean area, the North Atlantic accounts for about 23% of the anthropogenic CO_2 of the global ocean. Another study by *Tanhua et al.* (2007), showed that an even more broad distribution of C_{ant} is found in the North Atlantic water column. The entrainment observed in this study implies that more C_{ant}, than what previously estimated by *Sabine et al.* (2004), is reaching deeper parts of the ocean therefore potentially affecting the calcite and aragonite saturation horizons (limits between waters that are saturated and unsaturated with respect to calcite and aragonite).

Estimates of C_{ant} from different methods agree within their uncertainties on a global scale but the vertical and regional distribution, uptake and transport of C_{ant} are still under debate. In particular the highest storage of C_{ant} in the North Atlantic has been identified in different areas due to different locations of transport convergence. While studies involving Ocean General Circulation Models (OGCM) identified the subtropical North Atlantic as the major area of C_{ant} storage (*Mikaloff Fletcher et al.*, 2006; *Gerber et al.*, 2009; *Gruber et al.*, 2009), a study with an Ocean Circulation Inverse Model (OCIM) assessed that this higher storage occurs further north at mid-latitudes (*DeVries*, 2014). Nevertheless, a slightly northward sink is to be trusted as the southward shift of the maximum sink strength in the former models is due to an erroneous production of North Atlantic Deep Water (NADW) occurring too far south in the model.

Using five different estimates of C_{ant} (four carbon-based and 1 tracer-based) in the whole Atlantic Ocean, *Vázquez-Rodríguez et al.* (2009) found that while these methods are highly correlated and have similar variances in the large scale, significant regional variability is found among them particularly in the Antarctic Bottom Water (AABW) and the Nordic Seas. Furthermore the differences between methods of C_{ant} estimation are small in the Subtropics but larger for polar regions. Also in this study, as for OGCM approaches, the authors found that despite the method used, the maximum C_{ant} values are found in the subtropical gyre of the North Atlantic (between 20° and 50° N). Although different authors do not fully agree on the location of the highest storage in the North Atlantic, there is consensus on the fact that the water column inventory of C_{ant} in this region is the highest in the global ocean.

Despite this higher storage in the North Atlantic, there have been suggestions that the present-day flux of CO_2 across the air-sea interface, or Uptake, particularly in the sub-polar region, is not necessarily due to local perturbation by anthropogenic carbon (*Pérez et al.*, 2013). In fact, carbon based C_{ant} calculations coupled with water mass transport estimates made along several zonal transects of the North Atlantic (from 25° N to the Bering Strait) showed that the air-sea flux of C_{ant} is confined to the subtropical region of the basin, while the subpolar area is characterized by exchange of natural CO_2 across the interface. *Pérez et al.* (2013) identified that the main source of anthropogenic carbon into the subpolar region is the northward transport of tropical waters with high concentration of C_{ant}. A possible explanation for this differential uptake of anthropogenic and natural carbon by

$$S = T_{IN} - T_{OUT} + U$$

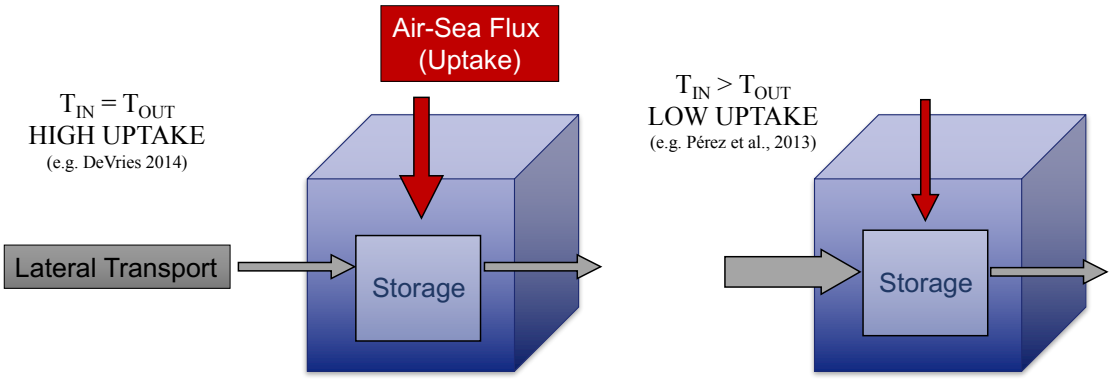

Figure 1.1: Conceptual box representing the high storage of C_{ant} in the North Atlantic due to potentially different processes according to different authors. Note that all processes shown in this schematic refer to C_{ant}.

the subtropical and subpolar regions of the North Atlantic is that waters coming from the South Atlantic reach saturation with respect to C_{ant} while moving northward into the subpolar gyre. This uptake decreases the capacity of this tropical water for further uptake with respect to C_{ant}. Therefore, contrarily to ocean inversions models that indicate a strong air-sea uptake of C_{ant} (*DeVries*, 2014; *Mikaloff Fletcher et al.*, 2006), the study by *Pérez et al.* (2013) showed evidences that it is the advection of southern C_{ant}-rich waters, the main driver of the high storage of anthropogenic carbon in this region. In Figure 1.1 a conceptual box of the North Atlantic illustrates the relative importance of different processes in determining a high storage of C_{ant} in the North Atlantic. The left box shows a high storage in the North Atlantic as a consequence of strong air-sea uptake of C_{ant} as suggested by *DeVries* (2014) and *Mikaloff Fletcher et al.* (2006), while the right box represents a high storage due to strong lateral transport of C_{ant} as suggested by *Pérez et al.* (2013).

By using DIC observations from different sections in the South Atlantic a previous study by *Holfort et al.* (1998) also studied the meridional transport of DIC, and similarly to *Pérez et al.* (2013) showed how the anthropogenic CO_2 is moved from the tropics into the North Atlantic. Although higher concentrations of natural CO_2 are found in cold waters due to higher solubility at low temperatures, counterintuitively higher concentrations of C_{ant} are found in warm waters (*Wallace*, 2001). This is due to the Uptake Factor (or Revelle factor) that increases with increasing temperatures, and may therefore contribute to the northward transport of C_{ant} described by *Pérez et al.* (2013).

On the other hand, a more recent study by *Ridge and McKinley* (2020) further validates the model-based theory that the air-sea uptake of C_{ant} occurs in the subpolar North Atlantic. Based on a combination of models and observations, the authors found that the subpolar air-sea flux of C_{ant} could be sustained by C_{ant}-depleted waters which are advected through a subsurface pathway known as the nutrient stream. It is important to highlight that all the studies mentioned include different definitions of subpolar and subtropical regions, with their boundaries set at different latitudes of the North Atlantic, which complicates the reconciliation of their results.

Further complications in understanding the North Atlantic uptake and storage of Excess CO_2 arises from the temporal variability of the convection and deep-water formation. Indeed deeper convection in certain years could result in a stronger uptake of C_{ant} compared to years with shallow water formation and therefore impact the storage rate among years.

1.3 Study Site: The Labrador Sea

Until recently, the Labrador Sea (see Figure 1.2) was thought to play a central role in influencing the Atlantic Meridional Overturning Circulation (AMOC) variability (*Yashayaev*, 2007) through temporal changes of the local formation of the Labrador Sea Water (LSW). More recent findings have highlighted the possibility that the transformation of shallow Atlantic waters into cold and deep waters occurring in the Irminger and Iceland basin could have a more central role in the variability of the overturning circulation than previously expected (*Lozier et al.*, 2019).

Nevertheless, this basin has a crucial role in the transport of gases into the ocean interior. The Labrador Sea represents a strong sink for CO_2 primarily as a result of biological carbon drawdown in spring and summer (*Körtzinger et al.*, 2008) and the formation and transport of recently-ventilated water masses (i.e., LSW) which causes the storage of anthropogenic CO_2 to be the most intense in the world ocean (*DeVries*, 2014; *Gruber et al.*, 2019b; *Sabine et al.*, 2004). The magnitude of the regional carbon sink and carbon storage, the variability of LSW formation on inter-annual and longer timescales (*Yashayaev and Loder*, 2016) and the potential for future reductions of LSW formation due to increased freshwater input from Greenland (*Böning et al.*, 2016), requires a need for long-term monitoring of ocean carbon in this region.

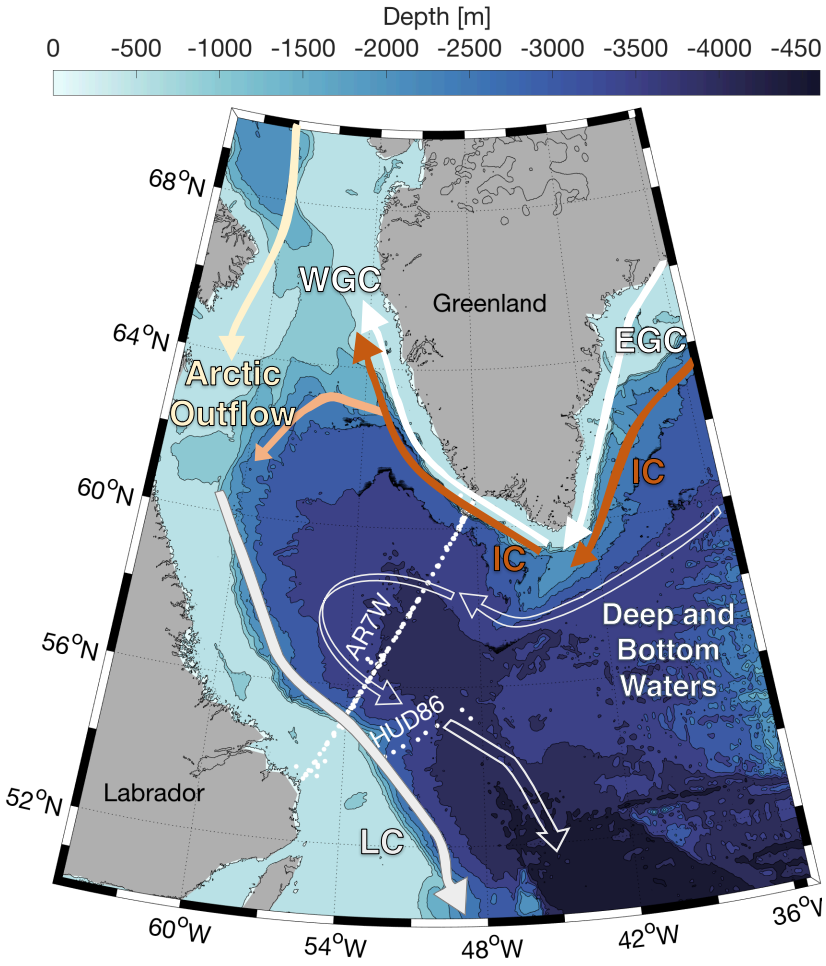

Figure 1.2: Map of the Labrador Sea. The white dots represent stations sampled between 1992 and 2016 along the AR7W line located across the basin, and stations sampled on a southward transect in 1986. LC; Labrador Current. EGC; East Greenland Current. WGC; West Greenland Current. IC; Irminger Current.

1.3.1 Circulation in the Labrador Sea and Labrador Sea Water (LSW) formation

In winter, when cold Arctic air flows on the Labrador Sea, an intense air-sea heat exchange occurs. This, combined with subpolar gyre circulation, results in the formation of an intermediate water mass defined as Labrador Sea Water (LSW) through the process of deep convection. Whereas deep convection has been observed during positive phases of the North Atlantic Oscillation (NAO^+; characterized by cooling and freshening in the Labrador Sea), periods of low convective renewal of LSW were associated to negative phases of NAO (NAO^-, characterized by higher temperature and salinity). Nevertheless this relationship

between LSW renewal and NAO index does not fully explain the variability of deep convection in the Labrador Sea. The onset of deep convection is more complicated, in fact it has been recognized that preconditioning can play an important role in its regulation (*Yashayaev*, 2007) and that LSW renewal can also occur with both little evidence of preconditioning and low NAO index (*Våge et al.*, 2009).

The salinity and temperature signals of the Labrador Sea Water spread across the North Atlantic toward the north-eastern side of the basin, and southward along the western boundary of the North Atlantic. The Labrador Sea circulation is characterized by two cold and relatively fresh boundary currents, the Labrador and West Greenland Currents (LC and WGC) that flow along the Labrador Sea margins. The Labrador Current is formed in the northern and western peripheries of the basin, it is an extension of the Baffin Island Current (originating in the Arctic) which is modified by the West Greenland Current and the Hudson Strait overflow water. This current flows southward along the Labrador shelf/slope exporting cold and fresh water into the North Atlantic. Further off-shore, an inflow of warmer and saltier waters of North Atlantic origin, is found on the eastern side of the basin and undertakes a counterclockwise path. This flow originates in the Irminger Sea and is therefore most commonly defined as the Irminger Current (IC). This current moves along the Western Greenland slope and when reaches the north-east slope it divides in two branches: one moves further North into the Davis Strait and the Baffin Bay, the second deflects westward and can be traced around the Labrador Sea all the way to the west side of the basin. On its path from the eastern to the western coast the Irminger Current turns thinner, cooler and fresher along the Labrador coast (*Yashayaev*, 2007).

The vertical structure of the Central Labrador Sea is characterized by homogenous cold and fresh LSW. This, depending on the depth of convection reached every year, can be generally found between 500 and 2000 m depth (the deepest convection ever observed reached 2400 m in 1994). Below the LSW lies a salty water mass of Atlantic origin called the North East Atlantic Deep Water (NEADW). This water mass originates from the Iceland-Scotland Overflow Water that enters the North Atlantic through the Iceland-Faroe-Scotland Ridge and modifies its characteristics turning into a high saline water due to mixing with upper salty and warm waters (e.g., Subpolar Mode Water). The core of the NEADW[2] is therefore defined as the maximum in salinity below 1500 m. Below the layer

[2]Typical ranges of salinity and temperature for the NEADW are 34.892-34.933 and 2.3-2.8°C, respectively.

of NEADW, a cold, dense and fresh water mass called Denmark Strait Overflow Water (DSOW[3]) is found. This is the densest water mass observed in the Labrador Sea and it enters into the basin from the Greenland Sea after flowing into the Irminger Sea. The core of this water mass is defined as 200 m elevation from the bottom of the basin (*Yashayaev*, 2007).

These water masses have different physical and chemical properties. Indeed they are characterized by different ages (or ventilation ages, as shown by measurement of transient tracers like CFCs (*Azetsu-Scott et al.*, 2005, 2003), but also different inorganic carbon and nutrients content. Because of the multiple pathways and times that these waters take to reach the Labrador Sea, it should be possible to observe different signals of anthropogenic carbon, with older water having lower concentrations compared to younger water masses.

1.3.2 C_{ant} in Labrador Sea

Because of its physical circulation and the formation of LSW, the Labrador Sea represents a direct path for atmospheric gases to the ocean interior (a trap door mode of ventilation as defined in *Bernardello et al.*, 2014; *De Lavergne et al.*, 2014). In particular, it has been shown that a significant portion of the total anthropogenic CO_2 sequestered by the North Atlantic flows through the Labrador Sea (*Tait et al.*, 2000), and an increasing storage of C_{ant} has been observed in the Central part of the basin between 1993 and 1997, with a peculiar vertical structure. The upper water column (between 200 and 1500-2000 m) is characterized by vertically homogeneous high concentrations of C_{ant} (LSW layer). Below this recently ventilated and well mixed convective layer, a minimum in C_{ant} concentrations corresponding to the NEADW is found. Finally, increasing concentrations are observed in the deepest 200 m, within the DSOW (*Tait et al.*, 2000). This vertical structure is closely related to the ventilation time of the different water masses in the basin (i.e., the time elapsed since they were last in contact with the atmosphere). The LSW is a newly ventilated water mass formed every winter in the Central Labrador Sea; it is therefore a "young" water mass and has a relatively high content of anthropogenic CO_2. Similarly the DSOW is also a water mass of recent formation and displays a higher concentration of C_{ant} in the deepest layer of the basin. On the other hand the NEADW was last in contact with the atmosphere earlier than LSW and DSOW, and is therefore characterized by a local C_{ant} minimum (*Tait et al.*, 2000).

[3]Typical ranges of salinity and temperature for the DSOW are 34.858-34.909 and 1.1-1.6°C, respectively

Several prior studies have discussed the capacity of the Labrador Sea to take up and store anthropogenic carbon. Despite the high concentrations of C_{ant} in the Labrador Sea, a study by *Terenzi et al.* (2007) which applied the Transit Time Distribution (TTD) approach to "Classical" Labrador Sea Water (cLSW[4]) in the North Atlantic, suggested that the exchange of CO_2 across the sea surface in the Labrador Sea cannot keep pace with its transport into the ocean interior. This implies that the Labrador Sea is highly undersaturated with respect to C_{ant} in the atmosphere.

Another study by *Steinfeldt et al.* (2009) between 20° S and 65° N in the Atlantic identified the maximum C_{ant} column inventory to be located in the Labrador Sea. Although the inventory of C_{ant} in this whole region has been increasing, tracking the atmospheric increase of CO_2, the authors did not observe the same pattern in correspondence of the LSW over the period studied, which could be explained by a weakening in the rate of LSW formation between 1997 and 2003. The decreased formation of newly ventilated water resulted in an "aging" effect on the water mass which translated into a decreased column inventory of C_{ant} in the western subpolar North Atlantic, but an increased inventory in the eastern part, most likely due to larger export of LSW formed in the western basin into the northeastern region prior to 1997 (*Steinfeldt et al.*, 2009).

Comparable to *Steinfeldt et al.* (2009), finding of a decrease of C_{ant} storage rates of about -2 mol m^{-2} y^{-1}, between the early 1990s and 1997-2006 was also observed in the southern Irminger Sea (*Perez et al.*, 2008). Nevertheless, at the time when these studies were published it was still not possible to define whether the change in column inventory was part of a long-term trend, perhaps associated with climate change, or the result of natural decadal variability in water mass formation. This makes the large availability of data across the Labrador Sea particularly useful to identify the nature of temporal variability from a longer time series.

1.3.3 The Labrador Sea Monitoring Program

A long-term (multi-decadal) monitoring program in the Labrador Sea has been maintained by Fisheries and Oceans, Canada (DFO) - Bedford Institute of Oceanography (BIO). The monitoring program involves annual occupations of a GO-SHIP repeated hydrography section called AR7W (originally started during the WOCE program, and continued during CLIVAR; see Figure 1.2) which crosses the Labrador Sea and that monitors variability

[4]The cLSW is commonly defined as water within a fixed density range of $36.82 \leq \sigma_2 \leq 36.97$ kg m^{-3}

Table 1.1: Summary of monitoring program with years of sampling for each variable used in this study (the monitoring program is ongoing and new observations are available). (S = discrete measurement of salinity; CTD = includes conductivity, temperature and pressure measurements).

	Parameters							
	S	CTD	O_2	NO_3^-	NO_2^-	P_T	Si_T	TA
Year	1992-2016	1992-2016	1992-2016	1992-2016	2012-2016	1992-2016	1992-2016	1995-2016
	DIC	pH	pCO_2	CFC-12	CFC-11	CFC-113	CCl_4	SF_6
Year	1992-2016	2012-2016	2013-2016	1992-2016	1992-2010	1992-2010	1992-2010	2012-2016

in the formation of the LSW (*Kieke and Yashayaev*, 2015) as well as the physical and chemical characteristics of high-latitude-derived water masses that contribute to the North Atlantic Deep Western Boundary Current.

Along this transect a time series from 1992 until present is available for a broad suite of chemical (nitrate, NO_3^-; nitrite, NO_2^-; soluble reactive phosphorus, P_T; silicate, Si_T; chlorofluorocarbons, CFCs; sulfur hexafluoride, SF_6; total alkalinity, TA; dissolved inorganic carbon, DIC; pH and partial pressure of CO_2, pCO_2), physical (Temperature, Salinity, density and velocities) and biological (chlorophyll, zooplankton nets) parameters (see Table 1.1). This large availability of oceanographic variables contributes to this study, allowing the application of several indirect methods to estimate the anthropogenic component of the carbon storage in this basin.

1.4 Thesis Objectives

Even though estimates of C_{ant} from different methods agree on a global scale, conflicting results on the regional uptake, storage and transport of anthropogenic CO_2 still remain (particularly in key regions like the Labrador Sea). Therefore this PhD thesis aims to elucidate the temporal variability of the anthropogenic CO_2 storage in a crucial region of the global ocean and to identify potential decadal to multi-decadal trends, providing a solid base for biogeochemical model validation here. The unusually long time series along the AR7W line provides the opportunity to test the assumption of steady state and the comparison of different approaches in the region. We here present the first multi-decadal estimates of C_{ant} in the Central Labrador Sea between 1993 to 2016 based on two methods: a transient tracers-based method known as the TTD, and a carbon-based method known as eMLR.

We will test two hypotheses: (1) tracer-based (TTD) and carbon-based (eMLR) estimates of C_{ant} concentrations and trends are identical to within the uncertainties of the methods; (2) the increase of C_{ant} in the Labrador Sea explains the observed increase of DIC leaving no room for potential changes in non-anthropogenic components of DIC.

A pre-requisite to assess changes in the inventory, particularly through eMLR, is to assess the quality of the data, therefore in Chapter 2 we assess the internal consistency of the marine carbonate system for those years where over determination is available. This study allows for better understanding of the carbonate system in the context of a long-term monitoring program and for assessing the error propagation in calculating missing carbonate chemistry parameters over the time series. Since only TA and DIC are available throughout the whole time series, we quantify the propagated random uncertainty in pH and pCO_2 calculations for those years where discrete measurements are not available. Differently from other studies we reported the internal consistency at *in situ* conditions of temperature and pressure rather than laboratory ones (important in the context of autonomous measurements performed with sensors).

Despite the crucial role of the Labrador Sea in sequestering C_{ant}, only a few studies have focused on the temporal variability of its accumulation rate (*Rhein et al.*, 2017; *Steinfeldt et al.*, 2009; *Tait et al.*, 2000; *Terenzi et al.*, 2007). Therefore in Chapter 3 we present a thirty year time series of column inventory and storage rates of C_{ant} in central Labrador Sea using a refined TTD method. Thanks to the large availability of data in this region, we

were able to test the validity of two assumptions that this method relies on: (1) constant saturation of transient tracers (often assumed to be 100%), and (2) constant air-sea CO_2 disequilibrium. For this study we extended our time series by including CFC-12 data collected along a transect southward of the AR7W line in 1986 and we used TA and DIC data to obtain pCO_2 between 1992 and 2016. Based on our findings we provide a refined TTD method which accounts for the tracers' saturation variability and, as a result, allows to obtain more accurate estimates of C_{ant} in Labrador Sea. In Chapter 3, we also investigate the temporal variability of C_{ant} concentrations in different water masses and the temporal variability of the C_{ant} storage in the region. Finally, based on the estimates along the AR7W line, we calculate the total inventory of anthropogenic carbon in Labrador Sea.

Chapter 4 focuses primarily on estimating C_{ant} through the eMLR method. The wide range of ocean parameters along the AR7W line allowed to run numerous extended Multiple Linear Regressions. Nevertheless in the chapter we focus on the most basic eMLR which uses temperature, salinity and oxygen as independent variables to model the change in DIC due to the anthropogenic perturbation. In this chapter we seek to understand what sampling frequency is necessary in order to obtain a realistic estimate of the annual average increase of C_{ant} column inventory in the Central Labrador Sea. We test the first hypothesis addressed in the thesis by comparing the increase in C_{ant} column inventories obtained with the eMLR method to that of the TTD method. Further, we estimate the column inventories based on measurements of DIC, which would include both the anthropogenic perturbation as well as any potential natural variability of inorganic carbon. The annual C_{ant} column inventories and the resulting storage rates from the eMLR and TTD are compared to the total change of DIC in Labrador Sea allowing distinction between anthropogenic and potential natural variability of DIC in the region.

CHAPTER 2

THE INTERNAL CONSISTENCY OF THE MARINE CARBON DIOXIDE SYSTEM FOR HIGH LATITUDE SHIPBOARD AND *in situ* MONITORING[1]

2.1 Abstract

Deep convection in the Labrador Sea supplies large amounts of anthropogenic carbon to the ocean's interior. We use measurements of all four measurable CO_2 system parameters made along AR7W (across Labrador Sea) between 2013 and 2015 to assess the internal consistency of the carbonate system, including, as appropriate, conversion to *in situ* temperature (T) and pressure (P). The best agreement between measured and calculated values was obtained through combination of T,P-dependent (pH or pCO_2) and non-dependent (TA or DIC) parameters. Use of the dissociation constants of *Mehrbach et al.* (1973) as refit by *Dickson and Millero* (1987) and *Lueker et al.* (2000) yielded the best internal consistency irrespective of the input parameters used.

A Monte Carlo simulation demonstrated that the propagated uncertainty (i.e., combined standard uncertainty) of calculated parameters of the carbonate system is (a) always larger

[1]Raimondi, L., Matthews, J. B. R., Atamanchuk, D., Azetsu-Scott, K., Wallace, D. W. R. (2019). The Internal Consistency of the Marine Carbon Dioxide System for High Latitude Shipboard and *in situ* Monitoring. *Marine Chemistry*, 213, 49–707. https://doi.org/10.1016/j.marchem.2019.03.001.
Author contribution: I conducted the field work, analyzed the TA, DIC, pH and pCO_2 samples in 2014 and 2015 in collaboration with Stephen Punshon from the Bedford Institute of Oceanography. I led the interpretation of the data and put into writing the manuscript with extensive input from all co-authors. J. B. R. Matthews performed the Monte Carlo simulation analysis.

than the analytical precision of the measurements themselves; (b) strongly dependent on the choice of input parameters and uncertainties; (c) less dependent on choice of the specific set of constants.

For calculation of other parameters of the carbonate system from TA and DIC measurements made throughout the Labrador Sea time-series, the estimated combined standard uncertainty of calculated pCO_2 and pH based on the Monte Carlo simulation is ~ 13 μatm and ~ 0.012 pH units respectively, with accuracy relative to laboratory-based measurement estimated to be between -3 and -13 μatm and 0.002 and 0.007 pH units. Internal consistency especially at *in situ* temperature and pressure conditions is important for rapidly developing sensor-based monitoring programs in the region, including measurement of pH and/or pCO_2 from gliders, profiling floats and moorings. We highlight uncertainty associated with the large pressure effect on pH and pCO_2, and recommend a study of carbonate system internal consistency under deep ocean conditions that addresses pressure effects on calculations.

2.2 Introduction and Background

Over the last 200 years, approximately 40% of the carbon dioxide (CO_2) produced as a result of fossil fuel use and cement production has been absorbed into the ocean through dissolution and reaction with water molecules (*McKinley et al.*, 2017; *DeVries*, 2014; *Le Quéré et al.*, 2018; *Sabine et al.*, 2004) which alters marine carbonate chemistry and pH. These chemical changes reduce the buffer capacity of seawater and decrease the ocean's ability to remove additional anthropogenic CO_2 from the atmosphere. Accumulation of greenhouse gases in the atmosphere is also driving warming of the global ocean as well as freshening in some high latitude regions, which could lead to increased stratification, reduced deep water formation and changes in biological productivity. These can indirectly influence the uptake rates of CO_2.

Monitoring of the oceanic inorganic carbon budget is necessary to keep track of the fate of anthropogenic carbon and monitor the effectiveness of CO_2 emissions reduction policies (*Le Quéré et al.*, 2018). A wide variety of approaches to examining the build-up of excess marine dissolved inorganic carbon are available (*Khatiwala et al.*, 2013; *Sabine and Tanhua*, 2010; *Wallace*, 2001), based on either direct measurements of inorganic

carbon (*Friis et al.*, 2005; *Gruber et al.*, 1996; *Wallace*, 1995), on measurements of tracers which mimic the atmospheric and oceanic history of anthropogenic CO_2 (*Hall et al.*, 2002; *Waugh et al.*, 2006), or use of ocean circulation and biogeochemical models (*DeVries*, 2014; *Gerber et al.*, 2009; *Gruber et al.*, 2009; *Mikaloff Fletcher et al.*, 2006). With the direct measurement approach, it is important to assess accuracy and uncertainty of inorganic carbon data, including thorough consideration of internal consistency across measured parameters.

Furthermore, as *in situ* sensor technology for carbonate chemistry matures there is a new, emerging challenge to ensure consistency between data measured *in situ* with sensors and laboratory-based measurements that can be traced directly to standards and reference materials.

The chemistry of inorganic carbon in seawater is regulated by a system of acid-base equilibria, with three principal equilibrium constants, K_0, K_1 and K_2 (*Dickson et al.*, 2007):

$$K_0 = \frac{[\mathrm{CO2^*}]}{f\mathrm{CO_2}} \tag{2.1}$$

$$K_1 = \frac{[\mathrm{H^+}][\,\mathrm{HCO_3}^-]}{[\mathrm{CO_2}^*]} \tag{2.2}$$

$$K_2 = \frac{[\mathrm{H^+}][\,\mathrm{CO_3}^{2-}]}{[\mathrm{HCO_3}^-]} \tag{2.3}$$

where $f\mathrm{CO_2}$ (the fugacity of carbon dioxide in gas phase), $\mathrm{CO_2}$* (representing a combination of $\mathrm{CO_2}$ and $\mathrm{H_2CO_3}$), $\mathrm{HCO_3}^-$ and $\mathrm{CO_3}^{2-}$ are the carbonate system species and $[i]$ denote concentrations. These are described through four measurable parameters: Total Alkalinity (TA), Dissolved Inorganic Carbon (DIC), Partial Pressure or Fugacity of Carbon Dioxide ($p\mathrm{CO_2}$ or $f\mathrm{CO_2}$) and pH, which are defined by the following equations:

$$\begin{aligned} TA = {} & [\mathrm{HCO_3}^-] + 2\,[\mathrm{CO_3}^{2-}] + [\mathrm{B(OH)_4}^-] + [\mathrm{OH}^-] + ... \\ & + [\mathrm{HPO_4}^{2-}] + 2\,[\mathrm{PO_4}^{3-}] + [\mathrm{SiO(OH)_3}^-] + [\mathrm{NH_3}] + [\mathrm{HS}^-] + ... \\ & - [\mathrm{H^+}]_{\mathrm{free}} - [\mathrm{HSO_4}^-] - [\mathrm{HF}] - [\mathrm{H_3PO_4}] - ... \end{aligned} \tag{2.4}$$

as defined by *Dickson* (1981).

$$DIC = [\mathrm{CO_2}^*] + [\mathrm{HCO_3}^-] + [\mathrm{CO_3}^{2-}] \tag{2.5}$$

$$f\mathrm{CO_2} = \frac{[\mathrm{CO_2}^*]}{K_0} \tag{2.6}$$

where the $f\mathrm{CO_2}$ takes into account the non-ideal behaviour of $\mathrm{CO_2}$, while the $p\mathrm{CO_2}$ is the product of mole fraction and total pressure. These are related through the fugacity coefficient, which represents the ratio of fugacity to partial pressure (*Dickson et al.*, 2007),

$$pH_T = -log[\mathrm{H^+}]_\mathrm{T} \tag{2.7}$$

where T represents the total concentration of the hydrogen ion (pH expressed on total scale).

Using knowledge of solubility and acid-base equilibrium constants it is possible to measure two of the four measurable parameters and calculate the remaining two by solving a system of equations (*Millero*, 2007). In addition, non-measurable ("derived") parameters can be computed including the aragonite and calcite saturation states (Ω_{Ar} and Ω_{Ca}), which are indices of thermodynamic tendency for precipitation (Ω_{Ar} or $\Omega_{Ca} > 1$) and dissolution (Ω_{Ar} or $\Omega_{Ca} < 1$) of these two forms of calcium carbonate ($\mathrm{CaCO_3}$).

In the case when three or four parameters are measured on the same water sample, the carbonate system and its speciation is over-determined. Hence calculated values can be compared with a direct measurement of the same parameter. Although measurements always have an associated error, for the purpose of this paper we will refer to the measured values as being the "true" values, with the level of agreement (or difference) between measured and calculated values referred to as "internal consistency" or "accuracy" of calculations.

Internal consistency depends on how well the equilibrium constants ($\mathrm{K_0}$, $\mathrm{K_1}$ and $\mathrm{K_2}$) describe the carbonate system equilibria. These dissociation constants, which govern

CO_2 solubility and its transformation into carbonate species, have been experimentally determined by multiple studies. K_1 and K_2 have been reported as a function of temperature and salinity based on experiments with both artificial (*Goyet and Poisson*, 1989; *Hansson*, 1973; *Roy et al.*, 1993) and natural (*Mehrbach et al.*, 1973; *Millero et al.*, 2006; *Millero*, 2010; *Mojica Prieto and Millero*, 2002) seawater; while other studies have reported sets of constants based on re-fitting experimental data of others (*Dickson and Millero*, 1987; *Lueker et al.*, 2000). The resulting equations for each constant vary due to differences in the experimental media used, and are valid for different ranges of pressure, temperature and salinity (see Table 1 in *Chen et al.*, 2015, for a summary). Use of any of the sets of constants also involves assumptions concerning the composition of seawater, especially the concentration and acid-base behaviour of inorganic and organic components that contribute to alkalinity. The latter can vary as a result of the contribution of variable amounts and types of organic material ("organic alkalinity"; *Kim and Lee*, 2009), as well as uncertainties and possible geographic variation in borate alkalinity (*Lee et al.*, 2010). Analytical measurement error is non-linearly propagated into the calculations and, together with the choice of carbonate system input parameters, influences the uncertainty of calculated parameters (*Millero*, 2007; *Orr et al.*, 2018).

These sources of uncertainty have implications for the design and operation of monitoring programs aimed at detecting and attributing changes in the ocean's carbonate system. For instance, *Azetsu-Scott et al.* (2010) showed that significantly different values of Ω_{Ar} are obtained when applying different formulations of constants to data from the Canadian Arctic Archipelago and Labrador Sea. It is therefore important to determine which combination of measurable parameters and sets of constants leads to the highest accuracy and precision in calculations of carbon system speciation and derived parameters. The internal consistency can also be used as a quality control tool in the context of a monitoring program where over-determination is achieved over several years (see Discussion below).

Numerous studies have focused on internal consistency of the carbonate system in different regions of the world ocean using different approaches (*Chen et al.*, 2015; *Chierici et al.*, 2004; *Chierici and Fransson*, 2009; *Clayton et al.*, 1995; *Johnson et al.*, 1999; *Jutterström and Anderson*, 2005; *Lee et al.*, 1997, 2000; *Patsavas et al.*, 2015; *Ribas-Ribas et al.*, 2014; *Salt et al.*, 2016; *Wanninkhof et al.*, 1999; *Woosley et al.*, 2017). These studies are summarized in Table 2.1, where we report the region of interest, parameters measured,

the depth range sampled and, where specified by the authors, recommendations for best practices.

2.2.1 Context and Objectives of this study

This study has the goal of assessing the internal consistency of the marine CO_2 system in the context of an ongoing long-term monitoring program in the Labrador Sea. This region is a key location for formation of North Atlantic Deep Water (NADW) and plays a central role in the Atlantic Meridional Overturning Circulation (AMOC). The Labrador Sea is a strong sink for atmospheric CO_2, primarily as a result of biological carbon drawdown in spring and summer (*Körtzinger et al.*, 2008) and the formation and transport of recently-ventilated water masses (i.e., Labrador Sea Water, LSW). Indeed, it is the site of the most intense sink of anthropogenic CO_2 in the world ocean (*DeVries*, 2014). Given this large storage, together with the variability of LSW formation on inter-annual and longer timescales (*Yashayaev and Loder*, 2016), and the potential for future reductions of LSW formation due to increased freshwater input from Greenland (*Böning et al.*, 2016), there is a need for long-term monitoring of oceanic carbon in the region.

A long-term (multi-decadal) monitoring program in the Labrador Sea has been maintained by Canada's Bedford Institute of Oceanography (BIO). This involves annual occupations of a GO-SHIP repeated hydrography section (AR7W) crossing the Labrador Sea (Figure 2.1), and monitoring of variability in the formation of the LSW (*Kieke and Yashayaev*, 2015). Along this transect carbonate chemistry data is available from 1992 until present together with a full suite of chemical, physical and biological parameters (see Figure 2.2). The carbon monitoring program has been based on a high-quality set of laboratory measurements on discrete samples collected from ships, which has included over-determination of the carbonate system since 2012.

As *in situ* measurements of marine CO_2 parameters from sensors mounted on moorings, floats and gliders become more common (*DeGrandpre et al.*, 2006; *Johnson et al.*, 2009; *Körtzinger et al.*, 2008, 2004; *Martz et al.*, 2009; *Riser et al.*, 2016), it is essential to assess the ability of the sensors to resolve ocean carbon-system variability. A further challenge is to relate sensor measurements to those from ships for quality-control purposes (*Johnson et al.*, 2016). It is notable that, at present, suitable *in situ* sensor technology is available only for carbonate system parameters which are pressure and temperature dependent (i.e., pH and pCO_2). Hence relating laboratory measurements (typically made at 1 atmosphere

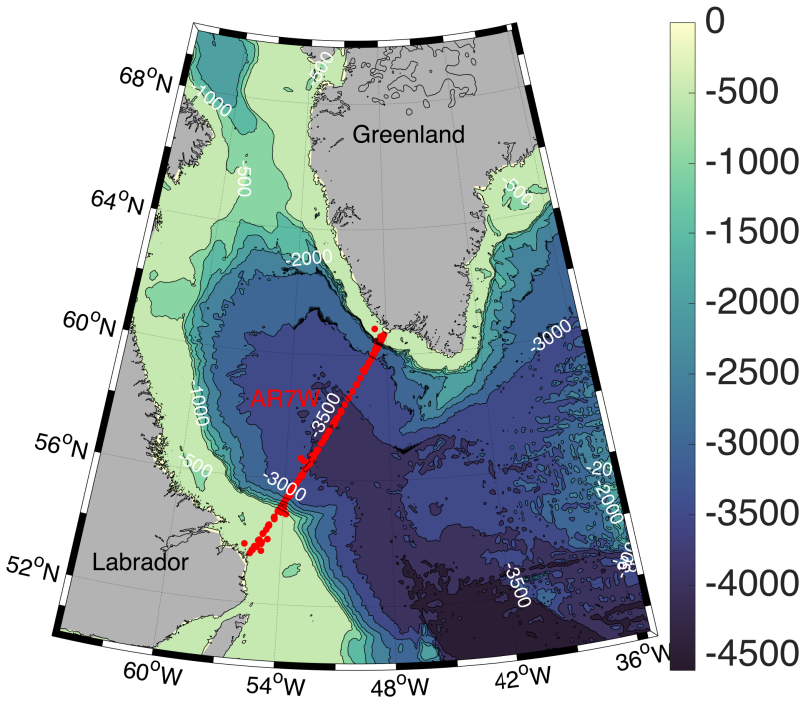

Figure 2.1: Map of the Northwest Atlantic and Labrador Sea, with the stations along the AR7W line indicated by red dots. The color bar shows depth in meters for the bathymetric contours.

pressure and constant temperature) to *in situ* conditions of the interior ocean, requires temperature and pressure corrections using dissociation constants that have not yet been fully characterized or tested. This study identifies potential biases and other issues relevant for planning of *in situ* measurements in this region.

Assessment of the internal consistency of the carbonate system also allows quantification of the uncertainty in pH and pCO_2 calculations for those years where only TA and DIC data are available (see Figure 2.2). Furthermore in this region of strong CO_2 uptake, where the saturation state of calcite and aragonite is likely to change but is not directly measurable, the calculation relies on accuracy of the carbonate system parameter measurements and dissociation constants. As shown in Table 2.1, studies of internal consistency have been conducted in various regions and depth ranges (e.g., surface water only or entire water column) using different sets of parameters (*Chen et al.*, 2015; *Chierici and Fransson*, 2009; *Jutterström and Anderson*, 2005; *Lee et al.*, 1997; *Patsavas et al.*, 2015). These previous studies were performed at laboratory conditions of temperature and pressure, generally

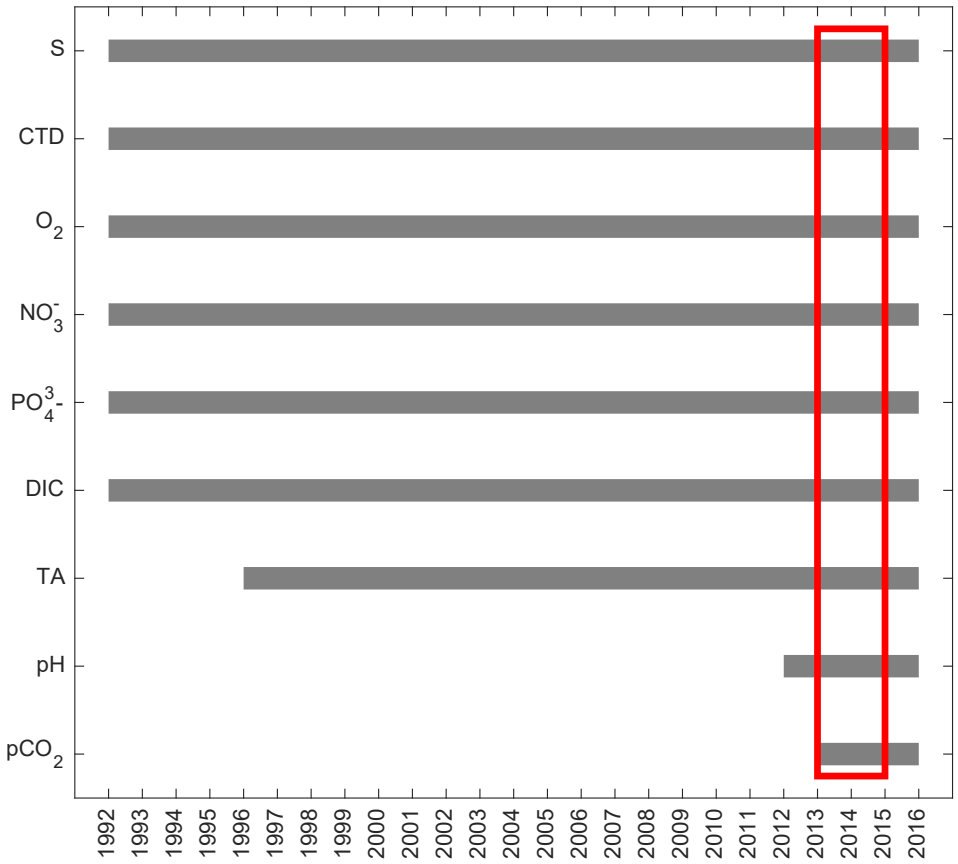

Figure 2.2: Summary of monitoring program with years of sampling for each variable. (S = discrete bottle measurement of salinity; CTD = conductivity, temperature and pressure measurements from the profiling instrument). Red box highlights the years where all four carbonate chemistry parameters are available.

use only one year of data and most do not include a Monte Carlo simulation of uncertainty propagation for carbonate system calculations.

In this study we will present insights into the internal consistency using all four carbonate parameters measured over 3 years in a critical region of the world ocean, including consideration of corrections to *in situ* conditions and Monte Carlo uncertainty propagation to estimate the uncertainty of calculated values (combined standard uncertainty or propagated random uncertainty) from the uncertainty of the input parameters (standard uncertainty or analytical precision).

Table 2.1: Summary of previous works on internal consistency of the carbonate system.

Reference	**Year**	**Region**[2]	**Parameters**[3]	**Depth Range**	**Notes**
Clayton et al. (1995)	1992	EEP	TA, DIC, pH.	Bow lab intake (5 m)	Used constants: M73; H. Recommended couples: (TA,pH) or (DIC,pH).
Lee et al. (1997)	1993	AO	U-fCO_2, fCO_2, pH, TA & DIC	surface fCO_2; water column (pH, TA & DIC)	Recommended constants: M73 when using (pH,TA) or (pH,DIC) to calculate fCO_2. Measurement of pH and fCO_2 were not internally consistent probably due to measurement uncertainty of fCO_2 or values of K_0
Johnson et al. (1999)	1996	AO	U-fCO_2, U-DIC & TA	Surface	Recommended constants: M73
Wanninkhof et al. (1999)	1993 1994 1995	AO PO IO	U-pCO_2, TA & DIC	Surface (pCO_2) Water column (TA and DIC)	Comparison of U-pCO_2 and pCO_2 calculated with (TA,DIC) from surface Niskin bottles. Recommended constants: M73.

Continued on next page

Table 2.1 – *Continued from previous page*

Reference	**Year**	**Region**	**Parameters**	**Depth Range**	**Notes**
Lee et al. (2000)	1990s	AO PO IO	pCO_2, pH, TA& DIC	0-6000 m	Discrete pCO_2 measurements (*Wanninkhof and Thoning*, 1993). Recommended constants: M73 for calculations involving combinations of pH, TA, DIC and fCO_2, TA, DIC at low fCO_2.
Chierici et al. (2004)	1998	ArO	U-pH, U-fCO_2,TA & DIC	Surface (pH and pCO_2) Water Column (TA,DIC)	Used constants: R; Recommended couple: (DIC,pH) or (TA,pH).
Jutterström and Anderson (2005)	1994 1995 1996	ArO	TA, DIC & pH	0-4000 m	One cruise with pH. Recommended constants: R.
Chierici and Fransson (2009)	2005	ArO	TA, pH & fCO_2	Surface	Recommended constants: R. Study of Aragonite and Calcite Saturation State.

Continued on next page

Table 2.1 – *Continued from previous page*

Reference	Year	Region	Parameters	Depth Range	Notes
Ribas-Ribas et al. (2014)	2011	NWESS	U-TA, U-DIC,U-pH U-pCO_2	Surface	TA and DIC from underway supply and surface CTD casts (<5 m). pH and pCO_2 analyzed from the underway inlet only. A Monte Carlo simulation was performed. Best internal consistency of pH with (TA,pCO_2) and (DIC,pCO_2).
Patsavas et al. (2015)	2011 2012	WUS GOM	TA, DIC, pH & fCO_2	0-4000 m	Used constants: L. Study of Aragonite saturation state. Coastal area with presence of organic alkalinity.
Chen et al. (2015)	2010	ArO	TA, DIC & U-pCO_2	Surface (4 m)	Recommended constants: M73; L for calculations of fCO_2 from (TA,DIC). Strong salinity and temperature gradients. Evaluation of the significance of sampling artifacts when comparing underway and CTD.

Continued on next page

Table 2.1 – *Continued from previous page*

Reference	Year	Region	Parameters	Depth Range	Notes
Salt et al. (2016)	2002 2005	NS	TA, DIC,pH & U-pCO_2	0-400 m	Recommended constants: M73; M06. Potentiometric pH. Evidence of presence of organic alkalinity during spring.
Woosley et al. (2017)	2015	AO	TA, DIC,pH & U-pCO_2	Surface (pCO_2) Water Column (TA, DIC & pH)	Recommended constants: M73; L. Poor performance of M02. Correction for *in situ* temperature is considered.

[2]EEP = Eastern Equatorial Pacific; AO = Atlantic Ocean; PO= Pacific Ocean; IO = Indian Ocean; ArO = Arctic Ocean; NWESS = North Western European Shelf Seas; WUS = Western US Coast; GOM = Gulf of Mexico; NS = North Sea.

[3]U- = Underway measurement

2.3 Materials and Methods

2.3.1 Sample Collection and Analysis

The dataset used for this investigation was obtained from three cruises conducted aboard the *CCGS Hudson* during the month of May each year from 2013 to 2015 (HUD2013-008, HUD2014-007 and HUD2015-006) along the GO-SHIP AR7W line (Figure 2.1).

At all stations CTD casts were performed together with collection of samples for all four carbonate parameters (TA, DIC, pCO_2 and pH), nutrients (including nitrate; NO_3^-, nitrite; NO_2^-, soluble reactive phosphorus and silicate; P_T and Si_T), discrete salinity, along with other parameters not used for this study. Samples were collected throughout the water column (0-3600 m) using a rosette equipped with 24 Niskin bottles (12 L) and a SeaBird SBE 911plus CTD unit. Samples for carbon parameters were collected following the standard operating procedures described in *Dickson et al.* (2007). TA and DIC samples were collected in 500 mL borosilicate glass bottles and analyzed on board in 2013. In 2014 and 2015 samples were poisoned with a saturated solution of $HgCl_2$ and stored before being analyzed at the BIO laboratory. The analyses were carried out within 3 months of sample collection. Samples for TA were measured using an open cell potentiometric titration with a full curve Gran end-point determination (*Dickson et al.*, 2007), while DIC was measured by the gas extraction and coulometric method with photometric detection (*Johnson et al.*, 1985). All measurements for TA and DIC were corrected using Certified Reference Materials (CRM batches 126 for 2013; 134 and 139 for 2014; 126 for 2015) provided by A. Dickson of the CRM Laboratory (Scripps Institution of Oceanography, San Diego, USA), which were analyzed every 20 samples (*Dickson et al.*, 2007). For these CRM the assigned values for TA and DIC are within 3 μmol kg^{-1} of their "true" values (*Bockmon and Dickson*, 2015).

For all three cruises, samples for pH were measured at 25°C on-board using a spectrophotometric method (*Clayton and Byrne*, 1993). In 2015, samples were analyzed using purified meta-Cresol purple indicator (*Liu et al.*, 2011), while samples from 2013 and 2014 were analyzed using a non-purified dye but corrected with a factor derived by comparing measurements performed with both purified and unpurified dye. The average offset correction between purified and unpurified dye was 0.015 units. The pH measurements are reported on the total scale (*Marion et al.*, 2011).

Samples for pCO_2 were poisoned and stored, then later analyzed at BIO. Analyses were

Table 2.2: Analytical precision for total alkalinity (TA), dissolved inorganic carbon (DIC), pH, partial pressure of CO_2 (pCO_2), soluble reactive phosphorus (P_T), silicate (Si_T), temperature (T), salinity (S) and pressure (P). The number of samples is n = 476, 486 and 431 for 2013, 2014 and 2015 respectively for all variables except for pCO_2 were the number is n = 47, 68 and 36.

	Analytical Precision								
Year	TA μmol kg^{-1}	DIC μmol kg^{-1}	pH	pCO_2 μatm	P_T μmol kg^{-1}	Si_T μmol kg^{-1}	T $^{\circ}C$	S	P dBar
2013	3.5	1.6	0.002	1.0	0.21	0.09	0.002	0.001	0.1
2014	1.8	1.9	0.002	1.0	0.05	0.18	0.002	0.001	0.1
2015	2.1	3.4	0.002	1.0	0.06	0.02	0.002	0.001	0.1

performed with a head-space equilibration method adapted from *Neill et al.* (1997), in which a sample aliquot (10 mL) was removed and replaced with a head-space gas with 400 ppm CO_2. Samples were then thermally equilibrated at 20$^{\circ}C$ (2013, 2014) or 22 $\pm$ 0.05 $^{\circ}$C (2015). Samples for pCO_2 were collected at the surface for every station and complete profiles were sampled only at select locations (typically at the deepest stations) along the AR7W line (2, 2 and 1 full profile(s) in 2013, 2014 and 2015, respectively). Precision varied from year to year for each parameter, therefore in Table 2.2 we report the analytical precision of all parameters for each year, together with the number of analyzed samples (in table caption).

The precision of TA, DIC and pH is reported as one standard deviation ($\pm$ σ) of the CRM replicates. Precision tests for pCO_2 were run by bubbling seawater with a CO_2 standard gas (400 ppm) followed by measurement of pCO_2 on 17 subsamples, using the procedure described above. The pCO_2 precision is also reported as one standard deviation, based on these 17 replicate analyses.

2.3.2 Calculations of Carbonate Parameters with CO2SYS

Calculations were performed with the MATLAB version of CO2SYS (*Van Heuven et al.*, 2011; *Lewis et al.*, 1998) using eight sets of constants. The constants will be referred to as: R for *Roy et al.* (1993); GP for *Goyet and Poisson* (1989); H for *Hansson* (1973) as refit by *Dickson and Millero* (1987); M73 for *Mehrbach et al.* (1973) as refit by *Dickson*

and Millero (1987); HM for Hansson and Mehrbach as refit *Dickson and Millero* (1987); L for *Lueker et al.* (2000); MPM for *Mojica Prieto and Millero* (2002) and M06 for *Millero et al.* (2006). The more recent constants provided in *Millero* (2010) and *Waters et al.* (2014) were not included in our calculations because the former were formulated using the same data as *Lueker et al.* (2000) and *Millero et al.* (2006) to evaluate the components of the carbonate system in estuarine waters (with salinity and temperature ranges beyond those relevant to our study area), while the latter are not yet implemented in CO2SYS. All calculations used the K_{HSO4} and Total Boron-Salinity formulations of *Dickson et al.* (1990) and *Uppström* (1974), respectively. The use of the latter rather than the value proposed more recently by *Lee et al.* (2010) is justified by the "best-practices" recommendations of *Orr et al.* (2015). In *Orr et al.* (2015) the authors argued that the earlier ratio from *Uppström* (1974) is to be preferred as it is the same used to derive K_1 and K_2 formulations in laboratory determinations by *Mehrbach et al.* (1973).

For each parameter, values were calculated including nutrient data as input variables and using all possible combinations of input (measured) parameters and sets of constants. For instance TA was calculated using (DIC,pH), (DIC,pCO$_2$) and (pH,pCO$_2$) as inputs and all eight sets of constants, thereby generating 24 calculated datasets. Hereafter these different datasets of calculated values will be referred to using an extended version of the notation of *Patsavas et al.* (2015): X(Y,Z)$_k$ represents the parameter X calculated from measured parameters Y and Z using the set of constants represented by the subscript k. For example TA(DIC,pH)$_{M73}$ refers to total alkalinity calculated using DIC and pH as input parameters with the constants of *Mehrbach et al.* (1973) as refit by *Dickson and Millero* (1987).

2.3.2.1 Calculation of *in situ* values for pH and pseudo-potential pCO$_2$

Comparisons of laboratory measurements with *in situ* measurements of pH and/or pCO$_2$, which are made at varying temperatures and (often higher) pressures, as well as the calculation of the *in situ* saturation state of calcite and aragonite, require corrections for temperature and pressure (*Johnson et al.*, 2016). While in CO2SYS the pH can be assessed at *in situ* conditions of both temperature and pressure, the pCO$_2$ is only corrected for *in situ* temperature. No pressure effect on K_0 or on the fugacity coefficient is included for sub-surface values in the software. In fact the combination of the pressure correction terms for K_0 and fugacity coefficient increases exponentially with increasing total pressure

(atmospheric + hydrostatic). However in CO2SYS the total pressure is considered to be equal to the atmospheric pressure (1 atm) also for sub-surface conditions, meaning that no correction is applied for *in situ* values of pressure. *Orr and Epitalon* (2015) recommend to refer to the pCO_2 values corrected for *in situ* temperature but with no pressure correction as "pseudo-potential pCO_2". From here on all the pCO_2 data presented in this work refer to pseudo-potential conditions.

We converted our pH and pCO_2 measurements from the laboratory to *in situ* and pseudo-potential conditions, respectively, using a two-step procedure. Because our laboratory measurements of pH and pCO_2 were performed at 25°C, and 20 or 22°C, respectively, the first step was to convert all measurements to a common laboratory temperature of 25°C. Values of pCO_2 at the temperature of equilibration were converted to pCO_2 at 25°C by first calculating TA from DIC and pCO_2 at 20°C (or 22°C) and using these computed TA values with measurements of perturbed DIC (i.e., accounting for outgassing during pCO_2 equilibration) as inputs to CO2SYS (*Neill et al.*, 1997; *Patsavas et al.*, 2015). All laboratory-based measurements were converted using CO2SYS (and all eight sets of constants) to *in situ* temperature and pressure (for pH) and *in situ* temperature and 1 atmosphere pressure (for pCO_2, see above). Hereafter these *in situ* values of pH and pseudo-potential pCO_2 will be referred to as the measured values.

Figure 2.3 presents vertical profiles of pH and pCO_2 for both laboratory, *in situ* and pseudo-potential conditions, respectively. It is immediately noticeable that the corrections to *in situ* conditions are substantial and vary considerably due to the differing temperature dependencies of each set of constants. There is no corresponding variation for the pressure correction because the pressure dependence of the constants has been measured only once by *Culberson and Pytkowicz* (1968), with their results adopted for use with all of the sets of constants in the literature. For calculations of *in situ* pCO_2 the pressure dependence of K_0 was formulated according to *Weiss* (1974), using equations 3 and 4 in *Orr and Epitalon* (2015).

The *in situ* values of pH and pseudo-potential values for pCO_2 also varied depending on which parameters they were paired with for calculation at *in situ* conditions. For data collected in 2015, the *in situ* pH values obtained with (DIC,pH), (TA,pH) and (pH,pCO_2) ranged between 7.995 and 8.025, 7.977 and 8.003, 7.963 and 7.992 respectively, across the full depth range and eight sets of constants. Similarly, pseudo-potential pCO_2 for 2015

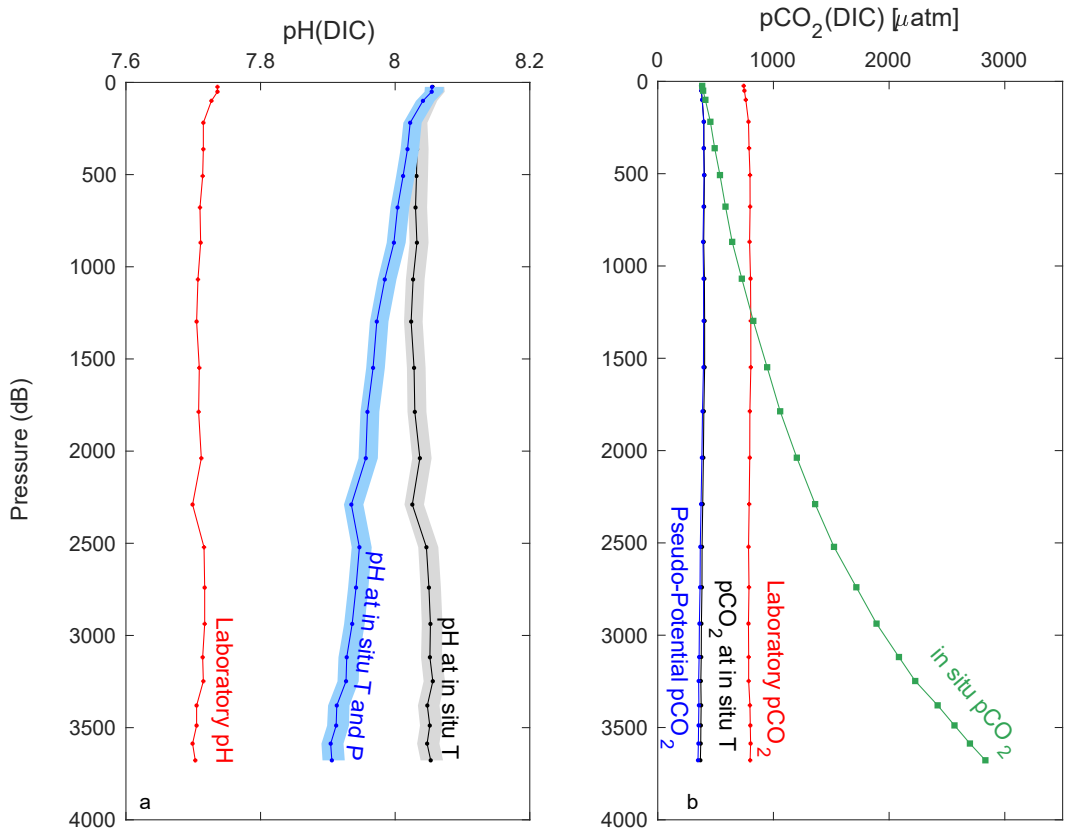

Figure 2.3: Vertical profiles of pH and pCO_2 from central Labrador Sea. The red lines represent measurements of pH and pCO_2 at laboratory conditions of temperature and pressure. The black lines represent values calculated with M73 constants and DIC as the second input parameter and corrected for *in situ* temperature alone. The blue lines represent values calculated with M73 constants and DIC as the second input parameter and corrected for both *in situ* temperature and pressure (for pH), and for *in situ* temperature but no pressure correction (for pCO_2; i.e., pseudo-potential pCO_2). The grey and light blue shaded areas represent the range obtained when the correction was applied with the dissociation constants that displayed the smallest (HM) and biggest correction (R). In panel b the green line represents the pCO_2 at *in situ* conditions of temperature and pressure including the pressure effect on K_0 (*Orr and Epitalon*, 2015; *Weiss*, 1974). Note that the grey and blue shaded areas do not include the uncertainty in the *in situ* correction for the M73 constants.

obtained with the pairs (DIC,pCO_2), (TA,pCO_2) and (pH,pCO_2) varied between 317.5 and 345.3, 320.4 and 347.7, 323.7 and 350.7 μatm.

This means that for comparison of measured and calculated values with different K_1 and K_2 (eight sets selected) and different input couples (3 couples), 24 sets of measured pH and pCO_2 values at *in situ* and pseudo-potential conditions were available. *Woosley et al.* (2017) chose to average across *in situ* values corrected using different sets of constants in order to remove any bias that might result from the use of a single set of constants. We assessed if the differences among these 24 sets of measured pH and pCO_2 values were statistically significant by running an n-way ANOVA test (not shown). We found that the differences were statistically insignificant ($p < 0.005$), and thus any of these sets could be used as our measured *in situ* and pseudo-potential values of reference. We chose to use the values of pH and pCO_2 at *in situ* and pseudo-potential conditions, obtained with (DIC,pH) and (DIC,pCO_2), respectively and with M73 constants. This is consistent with previous recommendations for pCO_2 calculations (*Johnson et al.*, 1999; *Wanninkhof et al.*, 1999; *Millero et al.*, 2002; *Chen et al.*, 2015) but also justified by values from M73 falling close to the average obtained from all constants (see Figure 2.3).

2.3.2.2 Comparison of measured and calculated values

We analyzed differences between measured values and the corresponding calculated values, which we hereafter refer to as residuals (i.e., measured minus calculated) and represent as $\Delta X(Y,Z)_k$, using the notation introduced in Section 2.3.2. We assume implicitly that measurements represent the "true" value of a parameter, and therefore that small absolute values of ΔX indicate an accurate calculation. The standard deviations of ΔX are representative of the spread of these residuals, while the uncertainty in our calculated values (i.e., the combined uncertainty) was assessed using a Monte Carlo simulation.

2.3.3 Monte Carlo Simulation

Following *Juranek et al.* (2011) and *Legge et al.* (2015), we conducted a Monte Carlo uncertainty propagation analysis with CO2SYS to derive computational uncertainties for our calculated values. This involved varying the values of both input parameters and internal CO2SYS variables by randomly sampling from normal distributions characterizing

their uncertainties [4]. Specifically, we accounted for measurement precision in the input carbonate and auxiliary (T, S and nutrients) parameters, uncertainties in the K_1 and K_2 formulations for each set of constants (using estimates from the corresponding papers), and uncertainties in the K_0, K_B, K_W and K_{Ar} formulations used (again using reported uncertainties).

The analytical precisions are presented in Table 2.2, and in the Appendix A.2 we provide a detailed description of the method together with a complete list of the standard uncertainties used. As described in Appendix A.2 we found that a large number of random samples are required in order for the Monte Carlo simulations to converge. We used 100,000 random samples and compared the resulting estimates for calculated parameters against our corresponding analytical precision for them.

2.4 Results

Internal consistency of a carbonate system parameter X varies depending on the choice of input parameters and dissociation constants. Figures 2.4 through 2.7 present the distribution of residuals (ΔX) for DIC, TA, pCO_2 and pH respectively, calculated with data from 2015. Each figure shows residuals for the three combinations of input parameters (panels a, b and c), as well as a summary panel (panel d). Tabulated values of the residuals for all three years and their statistics are presented in an Appendix (Tables A1 to A5).

The plots generally show that calculations of the four parameters are more strongly dependent on the choice of input pair of carbonate system variables than on the choice of constants. The different vertical scales used in the plots of residuals show that some couples yield exceptionally consistent values (e.g., DIC,pH and TA,pH) while others lead to high inaccuracy (e.g., pH,pCO_2).

Further, the distributions show that use of a "non-mixed" couple (two temperature (T) and pressure (P) dependent parameters (e.g., pH,pCO_2) or two T,P-independent parameters (e.g., TA,DIC) as input, results in calculated values that are generally less accurate and with higher standard deviations than those obtained using a "mixed" couple (one T,P-dependent and one T,P-independent parameter; e.g., DIC,pH).

[4]These normal distributions were characterized by a mean equal to the measured value for input parameters, and by a standard deviation equal to the analytical precision (from Table 2.2) or reported precision (from Table A7), respectively

The residual distributions revealed relatively poor agreement between measured and calculated values when using sets of constants that were determined in artificial seawater (ASW). Among the constants assessed in natural seawater (SW), M73, L and M06 more commonly produced accurate calculations, as shown by average residuals close to zero. As expected, values calculated using the M73 and L constants are closely comparable since both are based on the experimental values determined by *Mehrbach et al.* (1973). In most cases these two sets also perform similarly to M06. Among all couples the results obtained with H, R and GP were always the poorest, in particular H emerged as one of the sets that produced the poorest calculations when the couples (TA,DIC) and (pH,pCO_2) were employed, while R and GP were the poorest with almost all other combinations.

When TA measurements from 2014 were used in calculations, some results contradicted those from the other two years (see Tables A1 to A4). For instance, average residuals closer to zero were obtained with ASW-derived constants when calculating DIC with both (TA,pH) and (TA,pCO_2) instead of with M73, L and M06 constants for the data from 2013 and 2015. Similarly the best internal consistency in 2014 was yielded by ASW-derived constants for calculations of TA when using both (DIC,pH) and (DIC,pCO_2). Calculations of pCO_2 with (TA,DIC) consistently produced positive average residuals with 2014 data, contrary to results obtained with data from 2013 and 2015. These discrepancies suggested that the TA dataset from 2014 was biased relative to the other years, and a comparison based on internal consistency suggested that a correction of ~ 10 μmol kg^{-1} should be applied to TA values from 2014. This was confirmed using secondary quality control with other data from the region following the GLODAPv2 procedure for cross-over analysis (*Olsen et al.*, 2016, Supplementary Figure A.1) which gave an offset of 12.2 μmol kg^{-1} . The TA data with this offset subtracted are used in the following sections to discuss only the inter-annual variability of the internal consistency (see Table A5).

In the following subsections we separately discuss results for each carbonate system parameter. We describe results from calculations with each couple of input parameters emphasizing their accuracy and standard deviation, and identify the dissociation constants that produce the best and worst results and conclude with an inter-annual comparison. We show only data from 2015 in Figures 2.4 to 2.7 due to the offset in TA for 2014 and because better control of equilibration temperature was achieved for pCO_2 measurements in 2015 compared to 2013 (S. Punshon *pers. comm.*). Nevertheless results from 2013 and

2015 data generally show agreement for all four parameters (see Tables A1 to A4).

2.4.1 Internal Consistency for DIC

The DIC residuals for all three years are reported in Table A1 and residuals for 2015 data are shown in Figure 2.4.

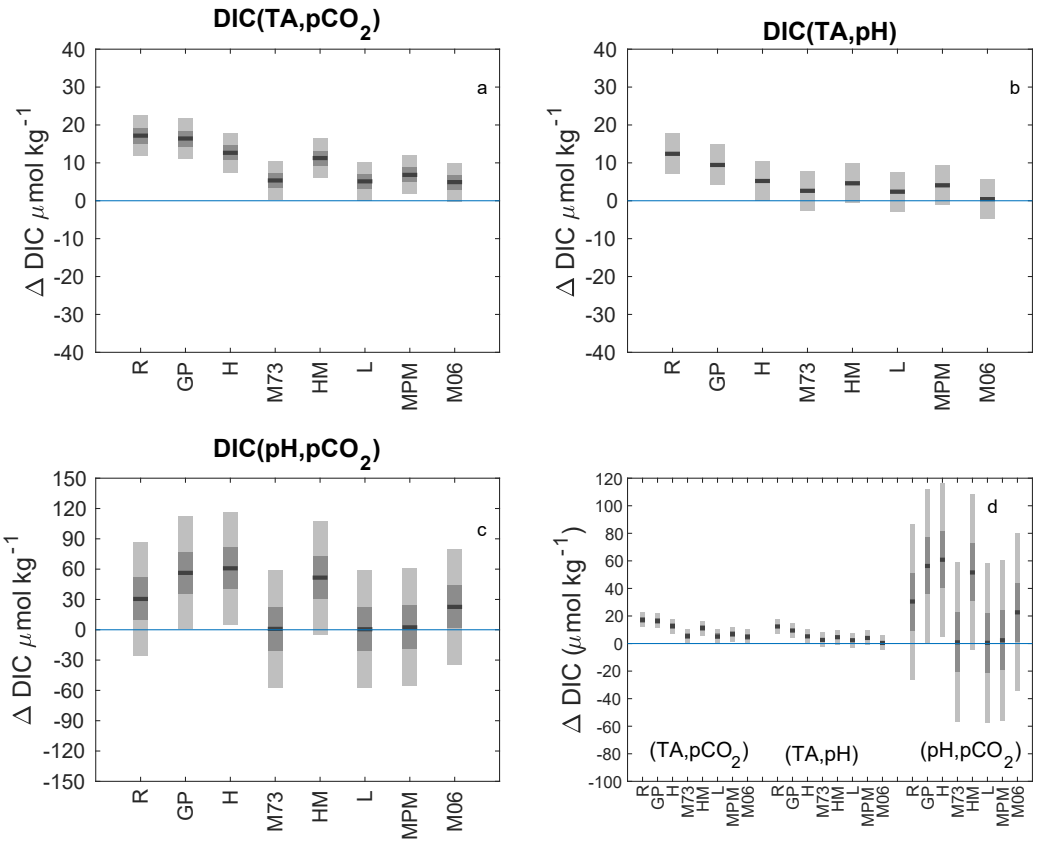

Figure 2.4: ΔDIC (measured DIC-calculated DIC) obtained by calculating DIC with each of the three possible couples of input parameters and eight sets of constants, then calculating the difference with the measured values. The plots include mean values of ΔDIC (black line), standard error of the mean with 95% confidence intervals (dark grey), and standard deviations (light grey). The data represented are from the *CCGS Hudson* cruise in 2015.

Calculations with all couples of input parameters generated DIC average residuals that are exclusively positive (Figure 2.4), meaning that calculated values are underestimated compared to laboratory measurements. The couples (TA,pCO_2) and (TA,pH) produced overall good accuracy (ΔDIC between 1 and 17 μmol kg^{-1} for the former couple and

between -1.5 and 12.4 for the latter, depending on choice of constants and year of measurement; see Table A1) with low standard deviations of residuals ($\sim$ 4-6 μmol kg^{-1}). The calculations obtained from (pH,pCO$_2$) were the most variable, with average ΔDIC ranging from 0 to 68 μmol kg^{-1} and with much larger standard deviations compared to the other couples ($\sim$ 28 μmol kg^{-1} in 2013 and 58 μmol kg^{-1} in 2015). The large differences obtained with the three couples of input parameters is represented by the different vertical scales used for panels a, b and c of Figure 2.4 and summarized in panel d.

The best agreement between laboratory measurements and calculations was achieved when all couples were used in combination with the M73, L or M06 constants. Calculations carried out with the constants of R, GP, H and HM were less accurate.

The internal consistency results for DIC were consistent across all couples for datasets from years 2013 and 2015. After the offset in TA in 2014 was corrected for (see Table A5 for results from corrected values) the average residuals obtained using (TA,pH) agreed with the other years to within 2 μmol kg^{-1} . For the (TA,pCO$_2$) couple the average residuals for the 2015 dataset were within 5 μmol kg^{-1} of those for 2013 and within 8 μmol kg^{-1} for the corrected 2014 values. The couple (pH,pCO$_2$) showed higher inter-annual variability with good agreement between 2013 and 2015, but pronounced differences in 2014 (with averaged residuals that ranged between -26.9 and 36.5 μmol kg^{-1}). Overall the best results for DIC calculations in all years were obtained with the (TA,pH) couple and use of the M73, L and M06 constants.

2.4.2 Internal Consistency for TA

Statistics for the TA residuals are reported in Table A2 (with statistics for residuals computed with corrected TA for 2014 given in Table A5). Data from 2015 are shown in Figure 2.5.

Negative residuals of TA were obtained overall with both (DIC,pCO$_2$) and (DIC,pH) indicating consistent overestimation of calculated TA (Figure 2.5), with average ΔTA ranging between $\sim$ -0.5 and -19.7 μmol kg^{-1} depending on choice of constants and year. The residuals from these couples were also characterized by a low standard deviation ($\sim$ 5-6 μmol kg^{-1}) no matter which set of constants was used.

The (pH,pCO$_2$) couple produced both positive and negative average residuals of TA (Figure 2.5c). It yielded the worst accuracy of calculations, as shown by high absolute values of the average residuals (between -8.8 and 67.3 μmol kg^{-1} depending on year and

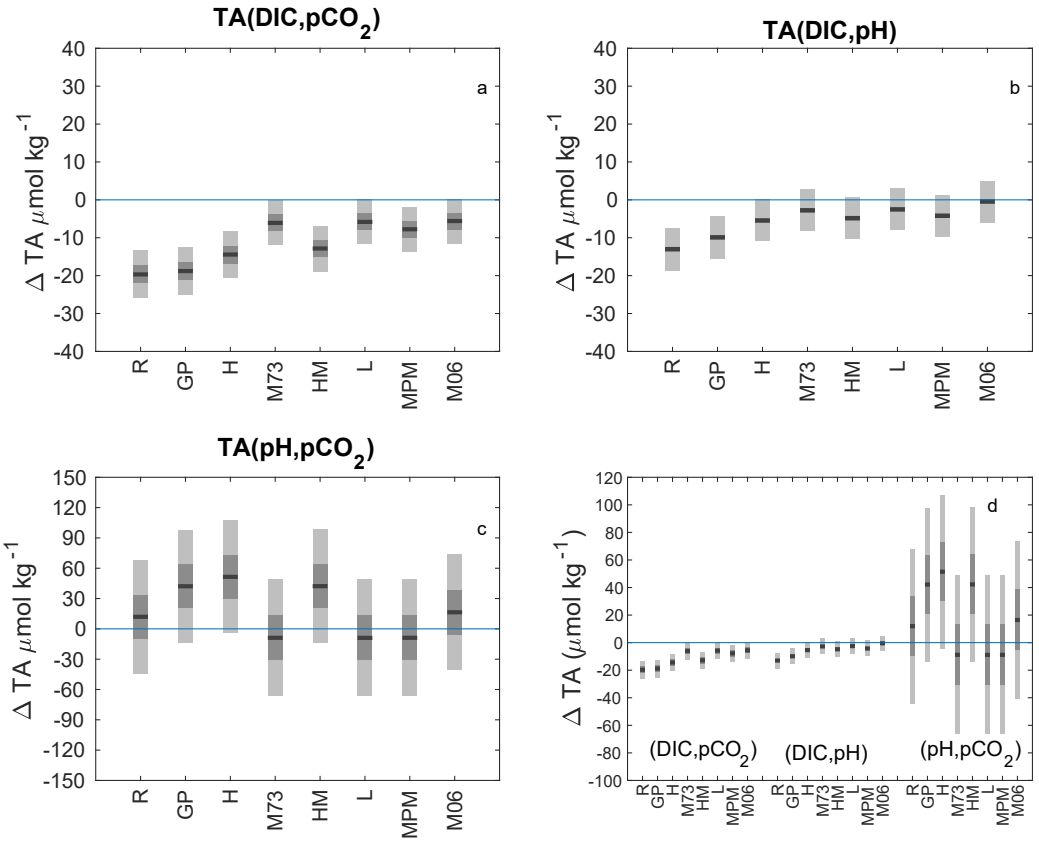

Figure 2.5: ΔTA (measured TA-calculated TA) obtained by calculating TA with each of the three possible couples of input parameters and eight sets of constants, then calculating the difference with the measured values. The plots include mean values of ΔTA (black line), standard error of the mean with 95% confidence intervals (dark grey), and standard deviations (light grey).

constants) and very high standard deviations ($\sim$ 30 μmol kg^{-1} in 2013 and $\sim$ 56 μmol kg^{-1} in 2015).

For all couples the most accurate calculations were produced in combination with M73, L and M06, while the constants from R and GP yielded the worst accuracy.

Generally good inter-annual agreement was observed among the 2013, 2015 and corrected 2014 data [5]. The best accuracy overall was obtained with (DIC,pH) although with the corrected 2014 TA data, the best internal consistency was obtained with (DIC,pCO$_2$). The couple (DIC,pH) produced smaller absolute residuals of ΔTA in 2013 than in 2015 with 3 μmol kg^{-1} better accuracy on average. Different sets yielded the best match for different

[5] See Tables from A2 and Figure 2.5

years, with comparable values obtained from M73, L and M06. Similarly, (DIC,pCO_2) performed best with M73, L and M06 in all three years. On the other hand, M06 gave poorer results compared to M73 and L with (pH,pCO_2) as the input parameters.

2.4.3 Internal Consistency for pCO_2

Statistics of pCO_2 residuals for all three years are reported in Table A3 while Figure 2.6 shows results for 2015. Calculations of pCO_2 with (TA,pH) and (DIC,pH) produced

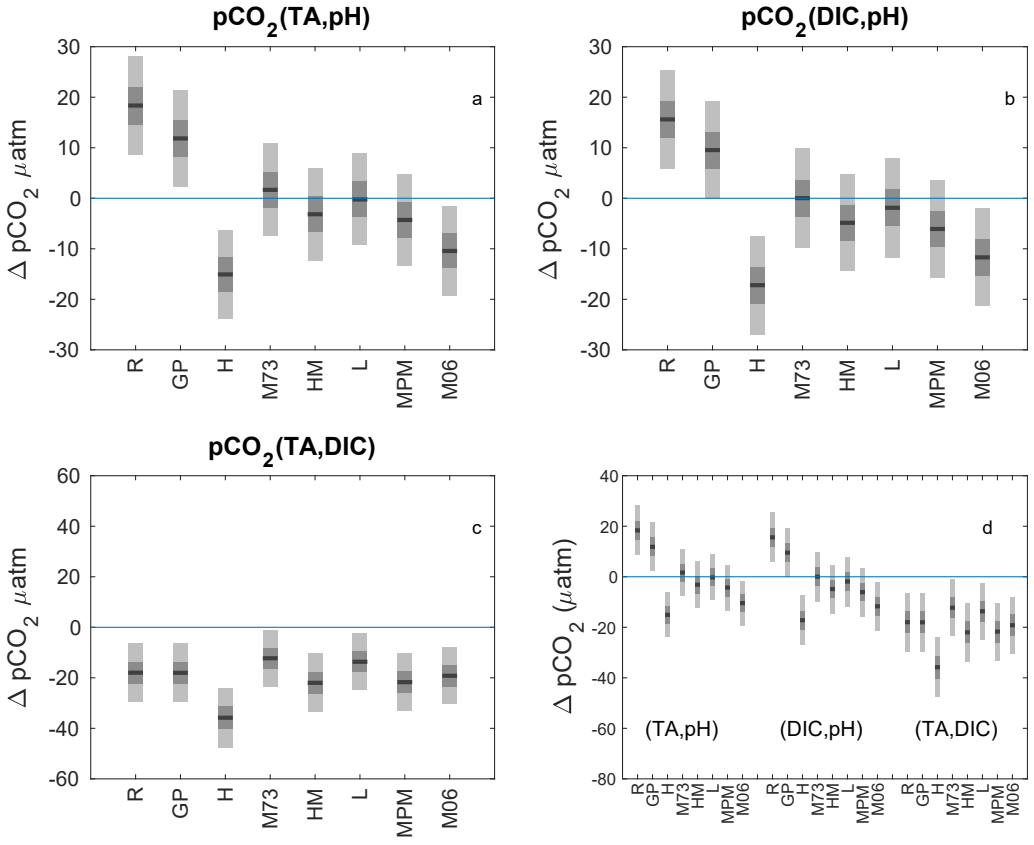

Figure 2.6: ΔpCO_2 (measured pCO_2-calculated pCO_2) obtained by calculating pCO_2 with each of the three possible couples of input parameters and eight sets of constants, then calculating the difference with the measured values. The plots include mean values of ΔpCO_2 (black line), standard error of the mean with 95% confidence intervals (dark grey), and standard deviations (light grey).

average residuals close to zero with several sets of constants and that ranged from $\sim$ -15 and $\sim$ 18 μatm depending on measurement year and choice of constants. For both couples the residuals displayed relatively low standard deviations ($\sim$ 6 and 10 μatm), that were uniform across the sets of constants.

Values of ΔpCO_2 (measured pCO_2-calculated pCO_2) obtained from the couple (TA,DIC) showed consistent overestimation (Figure 2.6c) and the calculations performed with this couple produced the poorest agreement of all, with average ΔpCO_2 ranging between -3.1 and -35.8 μatm. On the other hand, standard deviations were similar to those obtained from other couples ($\sim$ 12 μatm).

Despite the different levels of agreement among the couples and sets of constants, those that provided the best overall calculations of pCO_2 were always M73 and L, in agreement with previous studies where M73 was suggested as the best choice for pCO_2 calculations (*Johnson et al.*, 1999; *Wanninkhof et al.*, 1999; *Millero et al.*, 2002; *Chen et al.*, 2015).

The constants that led to the poorest agreement were R, GP and H. Note that whereas for calculation of DIC and TA the constants of M06 were amongst the best choices, this was not the case for calculations of pCO_2.

Results of internal consistency from 2014 with corrected TA data were similar to those in 2013 and 2015. Overall, we have most confidence in the accuracy of pCO_2 data from 2015 (see above). The couples (TA,pH) and (DIC,pH) paired with the SW-derived constants of M73 and L produced, on average, accurate estimates. On the other hand, the ASW-derived constants of R, GP and H resulted in poorer agreement. Different results were, however, observed for (TA,pH) in 2014 despite the TA data correction. For instance the sets of constants from HM and MPM resulted as the best choices instead of M73 (see Table A5).

2.4.4 Internal Consistency for pH

The averages and standard deviations for pH residuals for all years are reported in Table A4 while Figure 2.7 presents the results of the internal consistency analysis for data from 2015.

Comparisons of measured pH with values calculated from the couple (TA,pCO_2) and (DIC,pCO_2) showed generally good agreement, with the average residuals often very close to zero irrespective of choice of constants. The only sets of dissociation constants that produced consistently negative pH, and therefore overestimates, were the ASW-derived constants of R and GP (Figure 2.7). Overall these couples produced accurate results (average ΔpH ranging between -0.028 and 0.013 units depending on choice of constants and year). The standard deviations of residuals were similar across all constants (between $\sim$ 0.006 and 0.012). The best calculations were obtained with M73 and L and in contrast to other calculations, good accuracy was also obtained using H. On the other hand, calculated

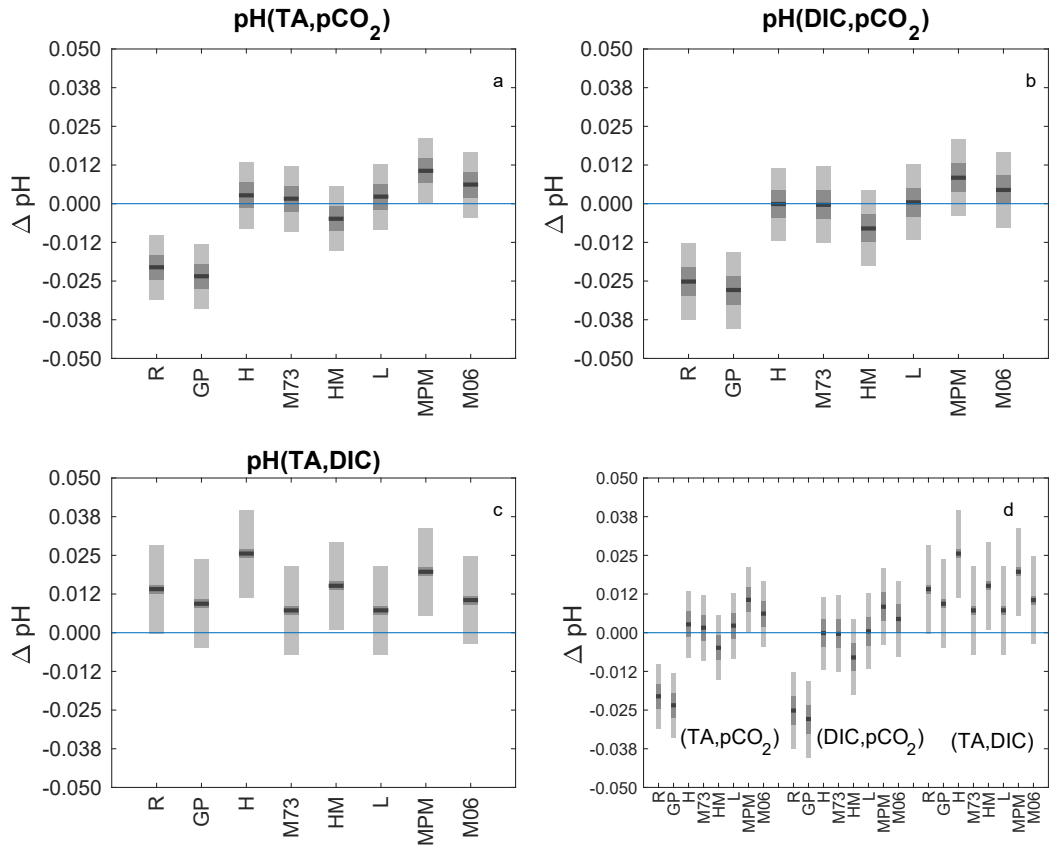

Figure 2.7: ΔpH (measured pH-calculated pH) obtained by calculating each parameters with the three possible couples of input parameters and eight sets of constants, then calculating the difference with the measured values. The plots include mean values of ΔpH (black line), standard error of the mean with 95% confidence intervals (dark grey), and standard deviations (light grey).

and measured values of pH from these couples showed poor agreement with R and GP.

Contrary to other couples that did not show a consistent pattern of the residuals across constants, the (TA,DIC) couple exhibited consistently positive values of average residuals, hence a systematic underestimation of pH (Figure 2.7c). The accuracy of calculations with this couple was comparable to that of the previously discussed couples with average ΔpH ranging between 0.002 and 0.026 pH units for the different years. Slightly higher standard deviations of residuals were observed with these input parameters ($\sim$ 0.015). In contrast to the other two couples, (TA,DIC) produced worse accuracy of calculations with constants from H and MPM.

Results from all three years (with the corrected TA data for 2014) showed very similar

results for all couples and constants. For couples including pCO_2, M73, L and H achieved the best accuracy of calculations, whereas use of R and GP resulted in pH residuals of order 0.01 or larger (see Tables A4 and A5).

2.4.5 A Monte Carlo simulation to study the uncertainty propagation in CO2SYS calculations

We used Monte Carlo (MC) simulation to obtain the propagated random uncertainty for values calculated with CO2SYS and then compared these with our analytical precision estimates for the measured values (see Table 2.2). In Figures 2.8 to 2.11 we present four summary plots (hereafter called "half-target plots" because the uncertainty is always non-negative) that show combined uncertainty, as determined by Monte Carlo simulation (propagated random uncertainty), vs accuracy of calculations, as given by the average of residuals, ΔX. Because the absolute value of residuals and MC simulation results were very similar for both 2013 and 2015, data are reported as the average of the results from these two years. We did not use the results from 2014 for this exercise due to the previously discussed offset in the TA measurements in that year. On these plots, an ideal result would lie at the origin of the axes, where calculated values would be both accurate (low X) and with low combined uncertainty.

For combined uncertainty, the half-target plots show that the choice of input couple is more important than the choice of dissociation constants. Uncertainty can vary significantly between different couples for computed DIC and TA (up to $\sim$ 90 μmol kg^{-1} between different couples). This difference in uncertainty among the couples is observed also for pH and pCO_2 calculations, although to a lesser extent (up to $\sim$ 0.007 units and $\sim$ 2-4 μatm between the couples with the lowest and highest uncertainty, respectively). Combined uncertainties for DIC and TA were considerably higher for the non-mixed couple (pH,pCO_2) compared to mixed couples and similarly the non-mixed couple (TA,DIC) produced a higher uncertainty for pCO_2 calculations. An important exception is pH, for which the non-mixed couple (TA,DIC) gave the lowest combined uncertainty.

For accuracy of calculations, the half-target plots show that choice of input parameters again has a strong impact on results, but more so than for combined uncertainty, the accuracy of calculations can also be strongly affected by choice of dissociation constants. Calculations for DIC and TA more commonly resulted in poor accuracy when

using (pH,pCO_2), whereas calculations performed using (DIC,pH), (DIC,pCO_2), (TA,pH) and (TA,pCO_2) gave generally accurate results. Nevertheless, certain dissociation constants were accurate on average even with use of a mixed couple (e.g., (pH,pCO_2)$_L$ and (pH,pCO_2)$_{M73}$).

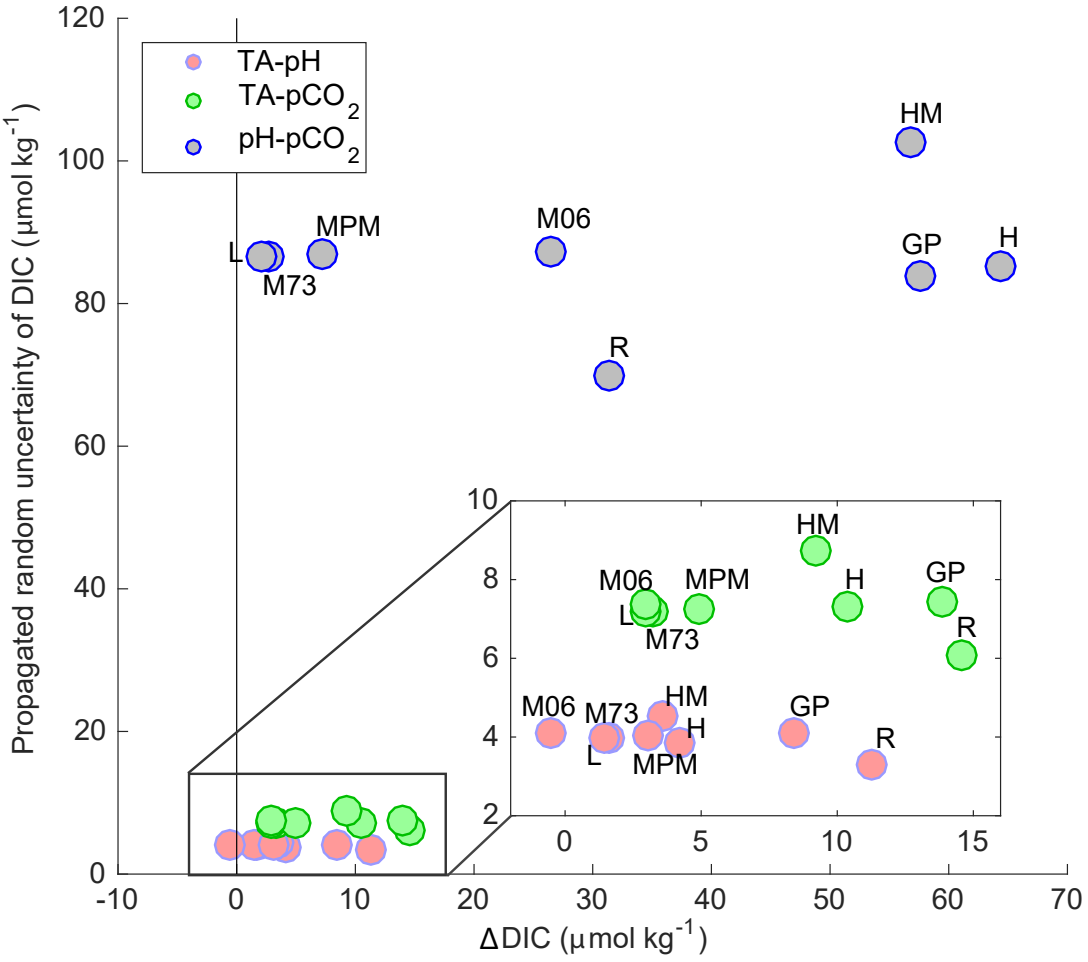

Figure 2.8: Half-target plot for the DIC calculations. The x-axis represents the accuracy of DIC calculations through CO2SYS as the average difference between measured and calculated values (ΔDIC) from the three couples of input parameters (TA-pH, TA-pCO_2 and pH-pCO_2). On the y-axis, we report the propagated random uncertainty associated with the computed DIC values obtained from the Monte Carlo simulation. The inset represents a zoom-in of the accuracy and propagated random uncertainty obtained with the couples (TA,pCO_2) and (TA,pH).

DIC. For DIC (Figure 2.8) the most accurate results were obtained using the couple (TA,pH) with average DIC residuals ranging between -0.5 and 11.3 μmol kg^{-1}. With this

couple, the constants that produced the best accuracy of calculations were M73, L and M06. The couple (TA,pH) also produced the lowest uncertainty, with combined uncertainty ranging between 3-4 μmol kg^{-1}, and no strong differences among the different sets of constants.

The couple (TA,pCO$_2$) also produced accurate results, although slightly less accurate than (TA,pH), using L, M73 and M06. The combined uncertainty (considering only random input uncertainties) for (TA,pCO$_2$) was higher than for (TA,pH) with combined uncertainties of $\sim$ 6-9 μmol kg^{-1}.

The couple (pH,pCO$_2$) had the worst accuracy of calculations, although with small average residuals for M73, L and MPM whereas, unlike with the other couples, M06 gave the worst internal consistency. The uncertainty of the (pH,pCO$_2$) couple was, however, the highest of all, with minimum and maximum combined uncertainties of 69.8 and 102.7 μmol kg^{-1} for R and HM respectively and use of most constants resulting in uncertainty $\sim$ 85 μmol kg^{-1}.

Among the more accurate combinations the overall best were DIC(TA,pH)$_L$ and DIC(TA,pH)$_{M06}$. Although use of R exhibited the lowest uncertainty it also gave the worst internal consistency with DIC(TA,pH) and DIC(TA,pCO$_2$). With the Monte Carlo simulation we identified that calculations of DIC could achieve precision of 3.3 μmol kg^{-1}, but that the analytical precision was generally still higher than the propagated random uncertainty (see Table 2.2).

TA. The best-accuracy calculations of TA were obtained with the couple (DIC,pH). The constants that produced the most accurate results with this couple were again M06, L and M73 (Figure 2.9). This couple also had the lowest uncertainty for calculation of TA, with combined uncertainties ranging between $\sim$ 3-5 μmol kg^{-1}. This small range of uncertainty shows that the choice of constants does not strongly affect the combined uncertainty of the calculations.

The couple (DIC,pCO$_2$) also produced accurate calculations. As for (DIC,pH) the constants that produced the smallest residuals were M06, L and M73. This couple also yielded low combined uncertainties of $\sim$ 7-10 μmol kg^{-1} (for R and HM, respectively) although most of the constants resulted in combined uncertainty of $\sim$ 8 μmol kg^{-1} .

Use of the couple (pH,pCO$_2$) resulted in the poorest accuracy for TA calculations. As with calculations of DIC, (pH,pCO$_2$) produced better accuracy, on average, when combined

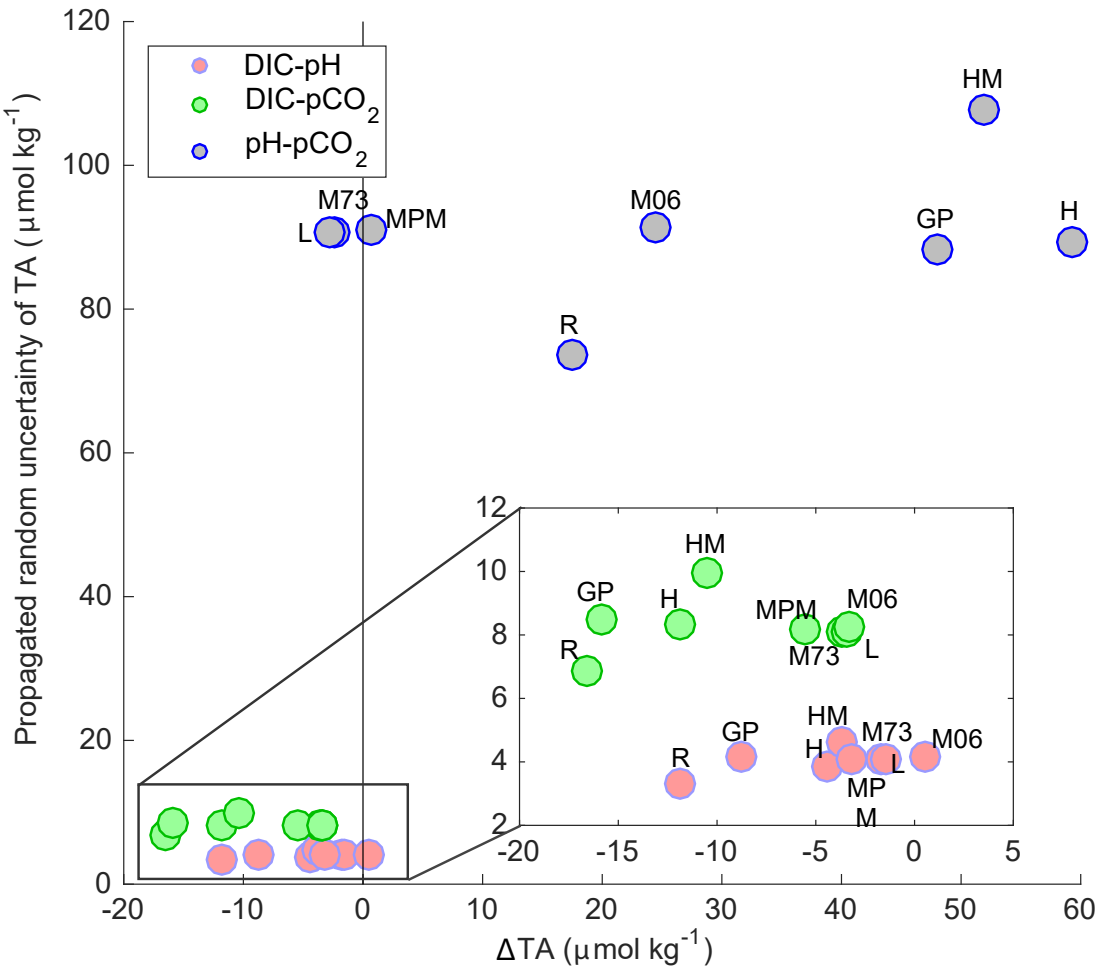

Figure 2.9: Half-target plot for the TA calculations. The x-axis represents the accuracy of TA (ΔTA) from the three couples of input parameters (DIC-pH, DIC-pCO_2 and pH-pCO_2). On the y-axis we report the uncertainty associated with TA calculations (MC Uncertainty). The inset represents a zoom-in of the accuracy and propagated random uncertainty obtained with the couples (DIC,pCO_2) and (DIC,pH).

with the constants of M73, L and MPM (while again M06 resulted in worse accuracy). Also similar to the DIC results, this couple gave the highest uncertainty for TA calculations, with combined uncertainties of $\sim$ 73-108 μmol kg^{-1} (for R and HM respectively) with most of the constants giving uncertainty of $\sim$ 90 μmol kg^{-1}.

Overall the best results in terms of both the accuracy and uncertainty of calculations were obtained with TA(DIC,pH)$_{M06}$. Use of M73 and L also produced accurate results with low combined uncertainty. Although computed TA values can have propagated random uncertainty as low as 3.3 μmol kg^{-1}, the propagated random uncertainties obtained were

still higher than the analytical precision (see Table 2.2).

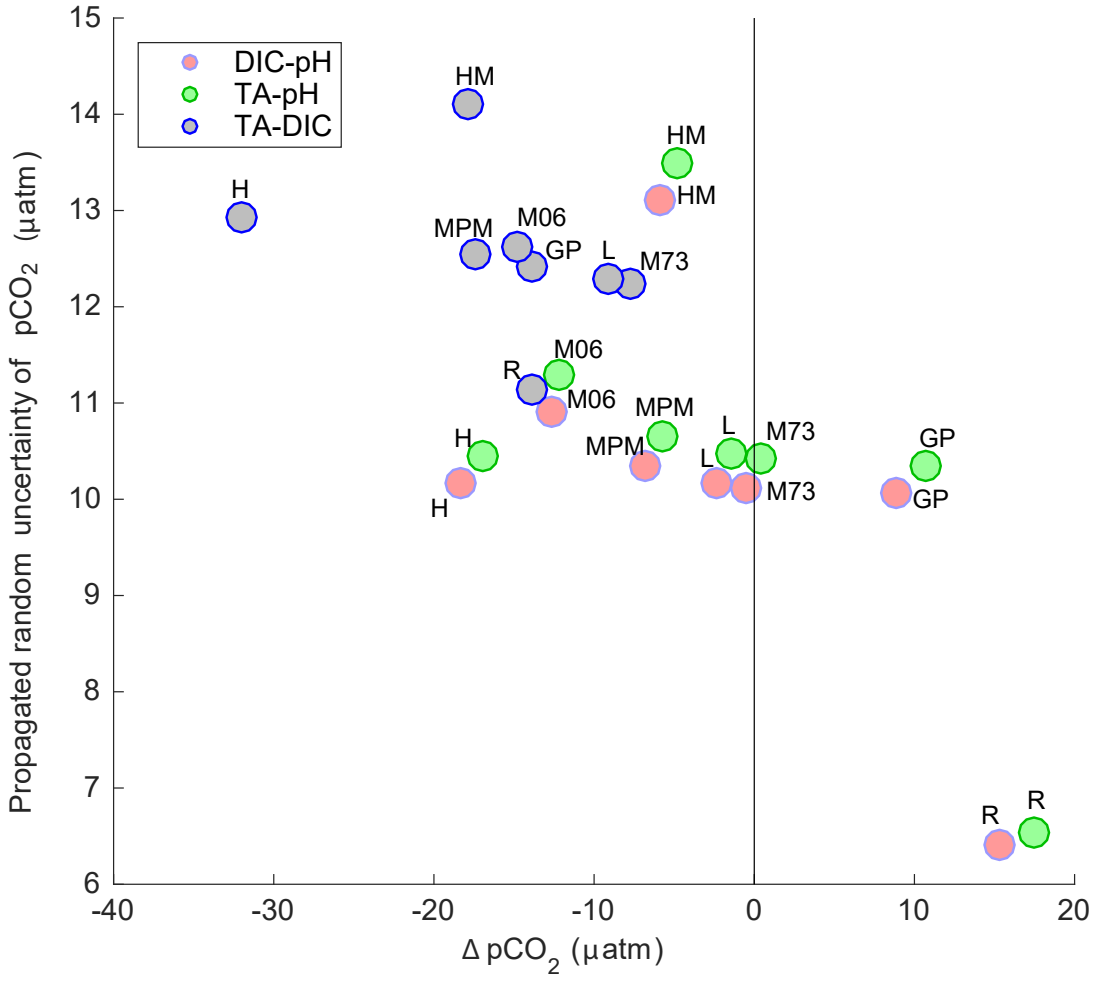

Figure 2.10: Half-target plot for the pCO_2 calculations. The x-axis represents the accuracy of pCO_2 calculations (ΔpCO_2) from the three couples of input parameters (DIC-pH, TA-pH and TA-DIC). The y-axis reports the propagated random uncertainty associated with the calculations of pCO_2.

***p*CO$_2$.** The half-target plot for pCO_2 (Figure 2.10) shows a different pattern than for DIC and TA. The results from different couples are closer together implying that choice of input parameters does not have as strong an impact.

The couples (DIC,pH) and (TA,pH) gave similar results for both the accuracy and combined uncertainty of calculations. For both couples the constants that produced the best internal consistency were M73 and L. The combined uncertainty of the calculated values obtained with both (DIC,pH) and (TA,pH) ranged between 6.5 and 13.5 μatm for R and HM, respectively. While the constants of R and HM marked the bounds of uncertainty,

other constants produced similar combined uncertainties of $\sim$ 10 μatm.

Overall the couple (TA,DIC) was less accurate and also gave pCO$_2$ calculations with the highest combined uncertainty of 11.1 and 14.1 μatm for R and HM, respectively. Other constants produced a combined uncertainty of 12-13 μatm. The spread across the (TA,DIC) results is smaller than for (DIC,pH) and (TA,pH), for both accuracy and uncertainty of calculations. The accuracy with (TA,DIC) varied by $\sim$ 24 μatm between the worst and best set of constants, whereas the range of accuracy was larger ($\sim$ 34 μatm) with use of (DIC,pH) and (TA,pH).

The spread of uncertainties with use of the couples (DIC,pH) and (TA,pH) ($\sim$ 7 μatm for both) was also larger than with (TA,DIC) (3 μatm), so that the choice of constants was also slightly more important for these two couples than for (TA,DIC). Overall we find that the best combination for calculating pCO$_2$ is (DIC,pH)$_{M73}$, although we note also that the combined uncertainty from this combination ($\sim$ 10 μatm) is 10-fold larger the analytical precision (see Table 2.2).

pH. Calculations of pH with (DIC,pCO$_2$) and (TA,pCO$_2$) as input parameters produced similar results, both in terms of internal consistency and uncertainty (Figure 2.11). The best accuracy of calculations using (DIC,pCO$_2$) was achieved with L and M73 constants. The combined uncertainty with this couple ranged between 0.015 (R) and 0.024 (HM), with all other constants giving a pH combined uncertainty of $\sim$ 0.019 units. The couple (TA,pCO$_2$) yielded similar results for accuracy and uncertainty of calculations, with a comparable spread across the different dissociation constants.

On the other hand, the couple (TA,DIC) yielded worse accuracy but lower combined uncertainty in pH computations. As with the other couples, the constants of L and M73 gave the smallest average residuals. In contrast to the results for pCO$_2$, the couple (TA,DIC) gave the lowest uncertainty for pH, with combined uncertainties ranging between 0.011 (R) and 0.013 (HM) units. Although the standard deviations of residuals for this couple were slightly higher than for the others, the Monte Carlo analysis gave lower uncertainties. As was observed for pCO$_2$ the spread across the (TA,DIC) results was smaller than for (DIC,pCO$_2$) and (TA,pCO$_2$), in terms of both accuracy and uncertainty of pH calculations.

Overall, the best results across all three couples were obtained with (DIC,pCO$_2$)$_L$, (DIC,pCO$_2$)$_{M73}$, and with (TA,pCO$_2$)$_{M73}$ and (TA,pCO$_2$)$_L$. The couple (TA,DIC)$_{M73}$ gave worse accuracy of calculations but also lower combined uncertainty (0.012) compared

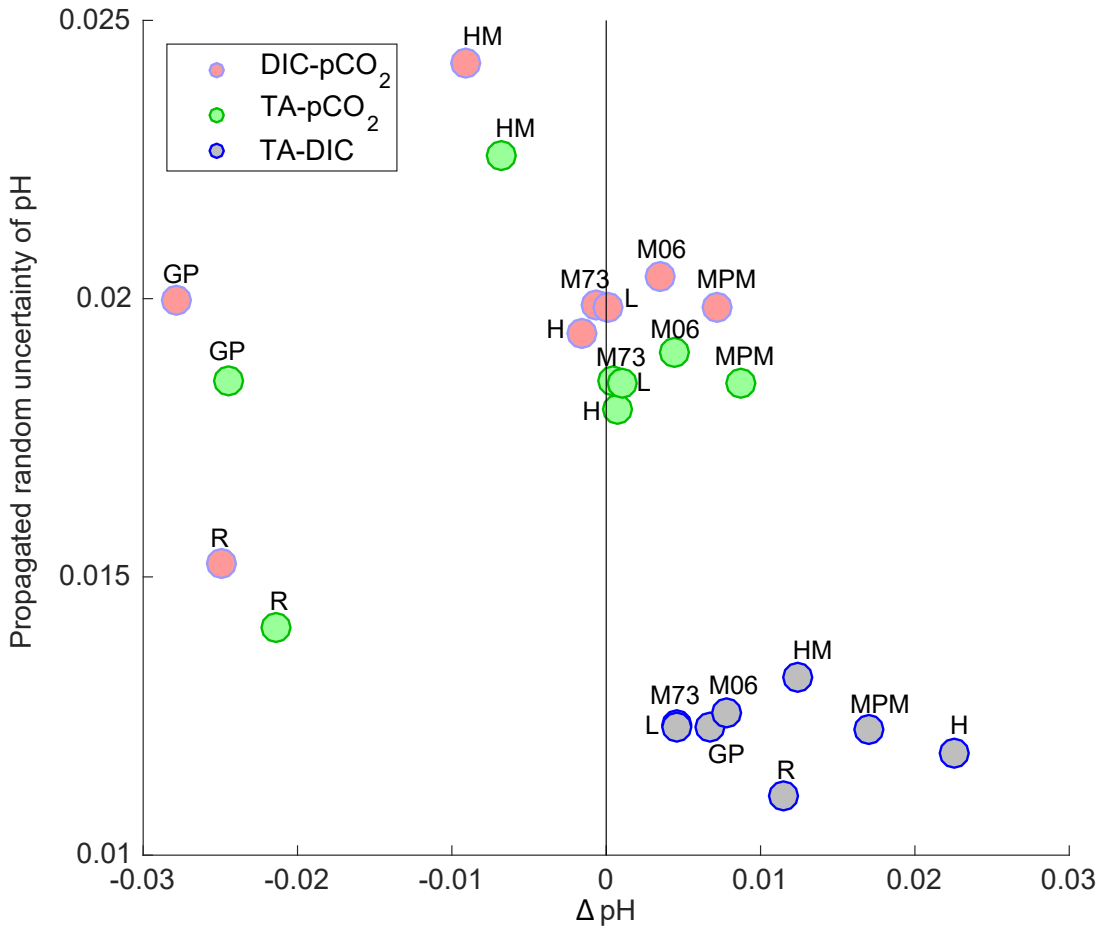

Figure 2.11: Half-target plot for the pH calculations. The x-axis represents the accuracy of pH (ΔpH) from the three couples of input parameters (DIC-pCO_2, TA-pCO_2 and TA-DIC). On the y-axis we report the propagated random uncertainty associated with the pH calculations.

to the other combinations with M73. As with pCO_2, the analytical precision of pH was around an order of magnitude better than the uncertainty of its calculated values.

2.5 Discussion

2.5.1 General findings and recommendations on input parameters and constants

In this study we identified the combinations of input parameters and sets of constants that work best for the calculation of each measurable carbonate parameter in the Labrador Sea. Generally, the best results were given by couples that pair a T,P-dependent parameter

(pH or pCO_2) with a non-dependent one (TA or DIC). Conversely, use of couples that used two T,P-dependent or independent parameters (i.e., pH,pCO_2 or TA,DIC) yielded poorer results, although some exceptions were found (e.g., low combined uncertainty when calculating pH from (TA,DIC)). The poorer performance of (pH,pCO_2) reflects the fact that pH and pCO_2 are closely correlated and therefore do not serve as effective, independent constraints. Furthermore the intermediate steps required to first obtain these two parameters at 25°C before calculating DIC and TA (see section 2.3.2.1), introduce additional uncertainty propagation through CO2SYS.

For (TA,DIC) we examined whether the relatively poor accuracy achieved could be due to organic bases that would be included in measured values of TA but not accounted for in CO2SYS. Given that the contribution of these species might more likely occur during intense primary production, we isolated TA residuals obtained from the bloom area that occurs along the eastern side of the basin. We selected only ΔTA values from the upper 30 meters of the water column along the Greenland coast and plotted these values against the measured Total Alkalinity (not shown). We found no evidence of the presence of organic bases, which would have appeared as a consistent positive offset between measured and calculated values. A further reason why the presence of organic bases is probably not the cause for the worse accuracy of the (TA,DIC) couple is that other calculations involving TA (coupled with either pH or pCO_2) did not show a similarly poor performance in calculations with CO2SYS.

The combinations (pH,pCO_2)$_{M73}$ and (pH,pCO_2)$_L$ were found to exhibit low average residuals for computed TA and DIC, even though they use two T,P-dependent parameters. However, the Monte Carlo simulation found that these combinations produced the highest combined uncertainty by far (almost twenty times higher than other couples), and therefore should not be used for calculation of TA and DIC.

While the use of (TA,DIC) as input parameters produced the highest uncertainty for calculation of pCO_2, the opposite was found for pH. Indeed for pH, the (TA,DIC) couple produced the lowest propagated random uncertainty, no matter the constants chosen, although the accuracy of calculations was worse.

In general, we found that, regardless of input couple, M73 and L yielded the best internal consistency for all inorganic carbon parameters. In contrast, use of ASW-derived constants like R, GP and H produced poorer consistency. Our results agree with some of

Table 2.3: Recommended couples of input parameters and dissociation constants to obtain the most accurate and precise calculations of each carbonate system parameter based on the Labrador Sea dataset. The accuracy of calculations is reported for each of the three best sets of constants while the uncertainty is given as a single indicative value since there was very little difference observed with the three best sets of constants. All values of DIC and TA are reported as μmol kg^{-1} , pCO$_2$ as μatm. The recommended combinations of input parameters and sets of constants are valid for ranges of temperature and salinity between -1.7° and 5.2°C, and between 32.3 and 35.0, respectively.

Calculated	**Couple**	**Constants**	**Accuracy**	**Uncertainty**
DIC	(TA,pH)	M73/L/M06	-1.6/-1.4/-0.5	$\sim$4
TA	(DIC,pH)	M73/L/M06	-1.7/-1.5/0.5	$\sim$4
pCO$_2$	(DIC,pH)	M73/L	-0.5/-2.3	$\sim$10
pH	(TA,pCO$_2$)	H/M73/L	0.001/0.000/0.001	$\sim$0.02

the internal consistency literature but contrast with other studies. In particular *Chierici and Fransson* (2009) found good internal consistency for fCO$_2$ in the Arctic Ocean using (TA, pH) in combination with R, while a later study in the same region by *Chen et al.* (2015) concluded that the best internal consistency for fCO$_2$ was obtained with (TA,DIC) and M73 constants. In the cases where (TA,pH) or (TA,DIC) are used as the input couple our data show best agreement between measurements and calculated pCO$_2$ values with M73. This discrepancy with *Chierici and Fransson* (2009) is probably due to the wider range of temperatures encountered in the Arctic region compared to our study area, and perhaps a better performance of R constants at lower temperatures.

Further, we found that constants derived using natural rather than artificial seawater nearly always yielded better internal consistency. However some exceptions were found, in particular pH(DIC,pCO$_2$)$_H$ and pH(TA,pCO$_2$)$_H$ displayed small average residuals, which were comparable to those obtained using M73 and L.

Our Monte Carlo simulations show that the combined uncertainty is higher than analytical precision for all four carbonate parameters. Further, we found that the choice of constants is less critical for combined uncertainty than the choice of input parameters, as most constants showed similar combined uncertainties for the same couple. Despite this, the constants R and HM always produced the lowest and highest combined uncertainty, respectively, for all input couples and all parameters calculated.

In Table 2.3 we summarize our recommendations on the couples of input parameters and sets of constants to be used in calculations of each carbonate parameter in the Labrador Sea together with the accuracy and uncertainty obtained with these combinations.

2.5.2 Residuals as a function of temperature and salinity

Since dissociation constants are sensitive to temperature and salinity we investigated the possible dependency of the internal consistency on these two variables. The residuals for each parameter were fitted with a linear model to determine whether there is a significant relationship with temperature and salinity. We found no significant relationships, with none of the linear regressions exhibiting a high r-squared value and the p-values being <0.05. In the supplementary Figure A.2 we show as an example the DIC residuals for 2015 plotted against temperature (left panels) and salinity (right panels). The lack of correlation might be a consequence of the relatively narrow ranges of temperature and salinity encountered in the Labrador Sea [6], which are smaller than those reported for other regions (e.g., the Arctic Ocean from *Chen et al.* (2015)). All our samples have salinities within the valid ranges of the dissociation constants assessed and only a few had temperatures lower than the valid range (fewer than 20% and 10% of samples had a temperature below $2°C$ and $0°C$, respectively).

2.5.3 Saturation state of Aragonite (Ω_{Ar})

We also assessed the impact of the choice of carbonate system parameters and constants on calculation of the saturation state of Aragonite, the orthorhombic mineral form of $CaCO_3$. Previously *Patsavas et al.* (2015) reported that the calculations of *in situ* aragonite saturation state (Ω_{Ar}) near the saturation horizon can show differences on the order of 10% between calculations performed with the couple (TA,DIC) compared to those using (pH,fCO_2), (DIC, fCO_2) and (DIC,pH). They therefore recommended using a couple with pH or fCO_2 in order to better predict future changes of Ω_{Ar}. We performed calculations of Ω_{Ar} with the same couples listed in their study. In this case the $\Delta\Omega_{Ar}$ or "residual" of Ω_{Ar} represents the difference between the saturation state value obtained from a couple combined with M73 minus the saturation state obtained from another couple also calculated with M73 (e.g., $\Delta\Omega_{Ar} = \Omega_{Ar}(\text{TA,DIC})_{M73} - \Omega_{Ar}(\text{DIC,pH})_{M73}$). Our results are summarized in Figure 2.12 (data are reported in Table A6).

[6]The Labrador Sea ranges of salinity ($\sim$ 32-35) are here defined narrow in comparison to those reported for the Arctic Ocean by *Chen et al.* (2015) (25.8-33.1 in surface water) as well as in comparison to the

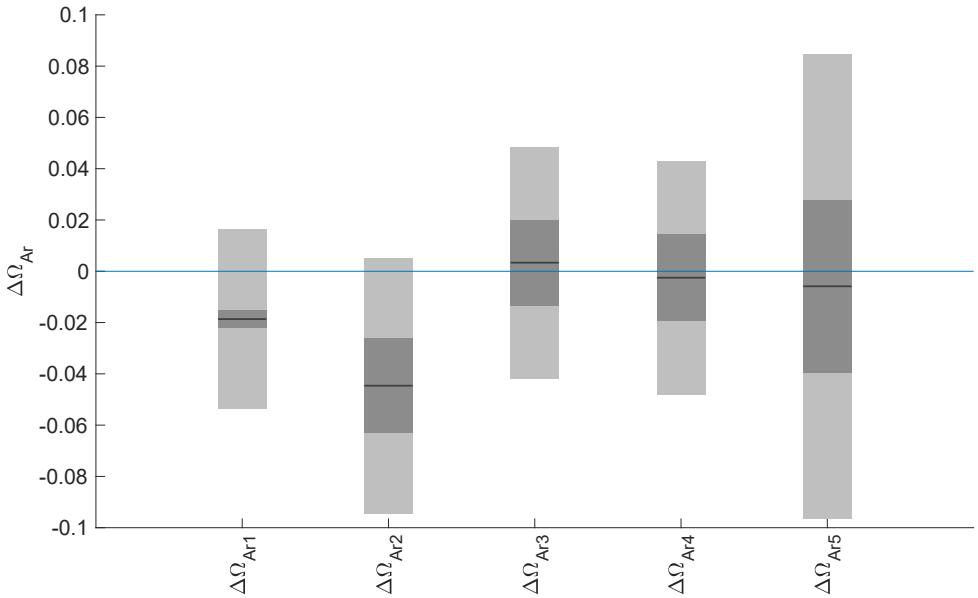

Figure 2.12: Relative differences in calculated aragonite saturation state ($\Delta\Omega_{Ar}$) using different couples of carbonate parameters. The x-axis labels represent $\Delta\Omega_{Ar1}$ = Ω_{Ar}(TA,DIC)-Ω_{Ar}(DIC,pH); $\Delta\Omega_{Ar2}$ = Ω_{Ar}(TA,DIC)-Ω_{Ar}(DIC,pCO$_2$); $\Delta\Omega_{Ar3}$ = Ω_{Ar}(DIC,pCO$_2$)-Ω_{Ar}(DIC,pH); $\Delta\Omega_{Ar4}$ = Ω_{Ar}(pH,pCO$_2$)-Ω_{Ar}(DIC,pH); $\Delta\Omega_{Ar5}$ = Ω_{Ar}(pH,pCO$_2$)-Ω_{Ar}(DIC,pCO$_2$). The closer to the zero reference line, the closer the agreement between couples of input parameters.

Using our Monte Carlo analysis we investigated whether the couple (TA,DIC) yields higher uncertainty compared to other couples of input parameters. We found that the highest uncertainty was associated with couples including pCO$_2$ (see Figure 2.13), while (TA,DIC), despite giving higher residuals (see Figure 2.12), did not exhibit higher uncertainties than other couples, including those with pH. The standard uncertainties propagated through the Monte Carlo simulation for all couples and constants produced combined uncertainties of $<$0.1, indicating that the choice of input parameters can influence uncertainty of calculations to a maximum of 10% when Ω=1.

Similar to *Patsavas et al.* (2015) we find that the couples with the lowest average differences are (DIC,pH), (DIC,pCO$_2$) and (pH,pCO$_2$), while the largest average differences occur with (TA,DIC). Nevertheless, we emphasize that agreement between certain couples

salinity ranges used to determine the dissociation constants of carbonic acid in SW and ASW (0-50).

and not others (see all $\Delta\Omega_{Ar}$ where (TA,DIC) couple is used) does not signify better accuracy. Indeed no conclusions can be drawn regarding the accuracy of aragonite saturation state calculations as no direct determinations of this derived parameter are available.

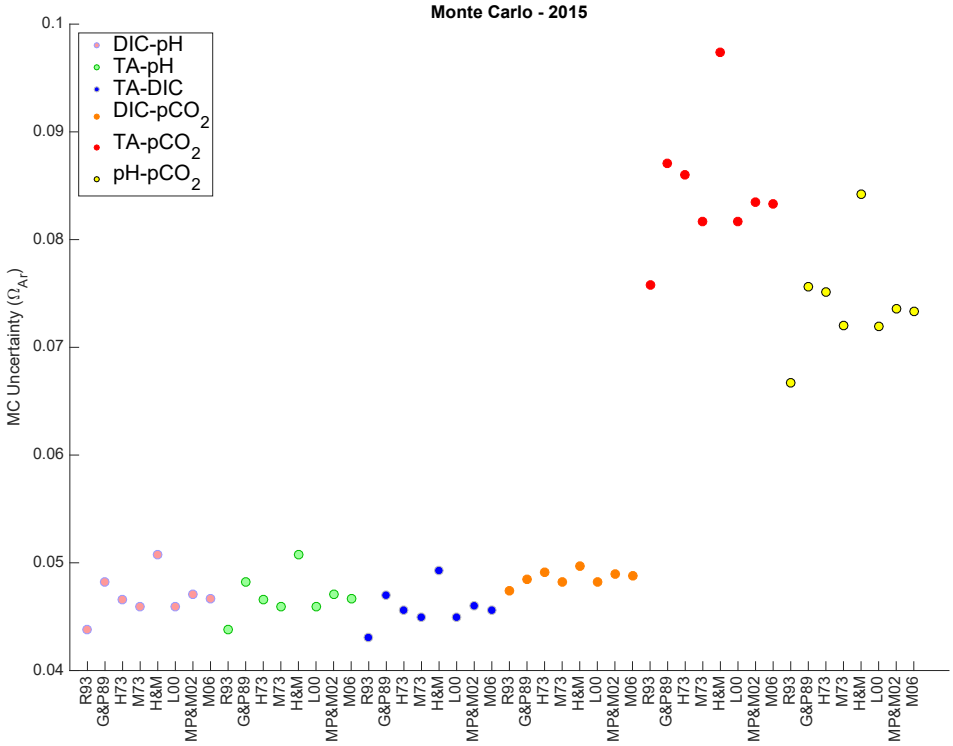

Figure 2.13: Uncertainty in calculated Ω_{Ar} obtained from the Monte Carlo simulation using different couples of input parameters and sets of constants for the year 2015.

2.5.4 Implications for comparison of laboratory and sensor measurements

As noted in the Introduction, data obtained from *in situ* pH and pCO_2 sensors are of growing importance. Typically, such sensors are calibrated in the laboratory as a function of both temperature and pressure prior to deployment. However overall quality control also relies on comparison of *in situ* sensor-based measurements with conventional measured or calculated values of pH derived from shipboard or laboratory measurements on discrete water samples conducted at laboratory temperature and pressure (see *Johnson et al.* (2016) and *Williams et al.* (2017) for review). Hence, the quality assurance procedures require correction of carbonate system parameters to *in situ* temperature and pressure conditions as described in section 2.3.2.1, as well as other aspects related to internal consistency.

Johnson et al. (2016) report short-term consistency between *in situ*, sensor-based measurements of pH and shipboard measurements corrected to *in situ* conditions (0-1000 m depth) averaging 0.00 ± 0.011. However, a systematic depth-dependence to the offset between *in situ* and laboratory-measured pH values was observed which reached 0.01 at 1000 meters. It was noted that this depth-dependent offset is within the uncertainty of the pressure-dependence of the carbonate system constants. However it could, of course, also conceivably be a consequence of inaccuracy in a sensor's pressure-coefficient. With our present, very limited knowledge of the pressure-dependence of the carbonate system equilibrium constants (see section 2.3.2.1) it is not possible to definitively assign such offsets to either: a) *in situ* measurement error, or b) uncertainties in extrapolation of measurements made at laboratory conditions to the conditions of the deep ocean.

Comparisons of *in situ* measurements in deep water (i.e., at high pressure) with shipboard measurements on deep water samples (1000-2000 m) are also used to correct for post-deployment sensor drift (*Johnson et al.*, 2016; *Williams et al.*, 2017). An assumption is that trends of sensor-determined pH diagnosed with this approach reflect changes in the sensor's reference potential (*Johnson et al.*, 2016), with the implicit assumption that a sensor's pressure coefficient, f(P), does not change. A second key assumption is that the pH of samples collected at depths >1000 m, after adjustment for variations of carbon-correlated parameters such as T, S and O_2, is invariant relative to the magnitude of a carbonate system "signal" of interest in overlying waters. The former assumption has not, to the best of our knowledge, been tested to-date. The latter assumption is justifiable in slowly-ventilated regions of the World Ocean (e.g., the North Pacific), but not necessarily in locations such as the Labrador Sea where temporal changes of carbonate system parameters, due to variability of anthropogenic CO_2 and variable "pre-formed" conditions at the sea surface, can impact water at all depths. In the Labrador Sea, the decadal pH change at 1500 meters is comparable to that at the sea surface (ca. -0.01 per decade, *unpublished data*) and deep water spatial variability is also considerable, due to the existence of multiple water masses with differing ventilation and formation histories.

A key application for *in situ* measurement of pH from profiling floats is to determine the pCO_2 of surface waters in order to estimate air-sea pCO_2 fluxes (*Williams et al.*, 2017). This generally requires estimation of a second carbon system parameter based on a "proxy"-variable that can be measured *in situ*. Total alkalinity is commonly the chosen second

parameter and is estimated from regional regressions of alkalinity with salinity determined with shipboard surveys. Based on a detailed uncertainty analysis, *Williams et al.* (2017) estimated an uncertainty of $\pm$ 11 μatm for near-surface *in situ* pCO_2 calculated from *in situ* pH measurements made on profiling floats in the Southern Ocean. They noted that "an unknown bias may be introduced to the float pH data during the quality control process as a result of the uncertainties in the effect of pressure on the carbonate system equilibrium constants, which has been measured only once (*Culberson and Pytkowicz*, 1968)". The considerable magnitude of this uncertainty for pH is clear from Figure 2.3 which also shows that the pressure effect on *in situ* pCO_2 is very strong.

Given the rapidly growing importance of *in situ* measurement of pH and calculation of *in situ* pCO_2, and the role of deep water comparisons for quality control of these data, a concerted effort is required to reduce uncertainty in comparison of shipboard and *in situ* measurements of the carbonate system. This should include laboratory measurements of the pressure effect on seawater pH to update the only study by *Culberson and Pytkowicz* (1968) which is now obsolete (*Johnson et al.*, 2016). The importance of accurate representation of pressure effects on the constants will grow as platforms such as biogeochemical Argo floats are adapted to profile into the deepest waters of the ocean, similar to the 6000m depths envisioned for the "Deep Argo" program (*Jayne et al.*, 2017). However, the history of laboratory study of carbonate system dissociation constants suggests that empirical field studies of carbonate system internal consistency within the deep ocean, including consistency with *in situ* sensor measurements of both pH and pCO_2, will also be required for the real-world validation of laboratory studies.

We suggest that a subset of future GO-SHIP cruises and/or other deep-ocean surveys (such as the Labrador Sea monitoring program) should include vertical profiling of both pH and pCO_2 using laboratory-calibrated *in situ* sensors in addition to the laboratory-based analysis of full-depth profiles of DIC, TA, pH and pCO_2. We note that current Standard Operating Procedures for laboratory-based determinations of pCO_2 and pH call for measurements at standard temperatures that are close to laboratory temperature (e.g., 20$^\circ C$ or 25$^\circ C$). This recommendation was made largely for practical reasons connected with the ease- and reliability of sample temperature control, and because earlier carbon-system surveys were not designed for calibration of *in situ* sensors but rather for determining global distributions of DIC and TA for which a specific temperature of

measurement of pH and pCO_2 was not important.

However as seen in Figure 2.3, and noted by *Williams et al.* (2017) and *Orr and Epitalon* (2015), conversion of laboratory-based measurements to *in situ* conditions, for calibration adjustment of *in situ* pH and pCO_2 measurements, involves large corrections, the uncertainty of which is not yet fully known. Whereas routine laboratory measurements at deep ocean pressures remain impractical, we suggest consideration should be given to including measurements of discrete pH and pCO_2 at standard temperatures closer to deep ocean temperatures in future surveys. This would minimize one source of uncertainty involved in comparing *in situ* and laboratory-based measurements. Such a program of combined sensor and laboratory-based measurements from deep ocean surveys would provide data that can validate approaches used to inter-relate observed carbon system parameters at depth within the ocean.

2.6 Conclusions

Based on an assessment of internal consistency of the marine carbonate system in the context of a long-term monitoring program in the Labrador Sea, we emphasize the following main points:

The choice of carbonate parameters to be measured is crucial since this strongly affects both accuracy and uncertainty of parameters that are computed from them. In particular, we find that a mixed combination of parameters, with one T,P- independent and the other T,P-dependent is preferred. Especially the use of (pH,pCO_2) should be avoided as poor accuracy and high combined uncertainty of calculated TA and DIC are obtained from these parameters.

For a given couple of input parameters, the choice of equilibrium constants can also be very important for accuracy. Overall we find that the constants of *Mehrbach et al.* (1973) (M73) as refit by *Dickson and Millero* (1987) and *Lueker et al.* (2000) (L) give accurate results with low combined uncertainty for all four measurable parameters of the carbonate system with the dataset from Labrador Sea.

For our dataset, calculations using a mixed couple involving measurement of pH results in better accuracy and lower combined uncertainty for computed parameters than use of pCO_2. Further, we recommend DIC over TA when possible due to the improved accuracy obtained with use of this parameter in mixed couples. DIC is also preferable because it is

a direct measurement of carbon content, while measurements of TA could include poorly characterized contributions from, for example, organic acids.

Comparisons of internal consistency between different years revealed differences which helped identify a bias in TA for the 2014 dataset. Hence, knowledge of internal consistency and over-determination of the carbonate system is useful for quality control in long-term monitoring programs.

The couples that gave the best consistency with observations were: (TA,pH) for calculation of DIC and (DIC,pH) for calculation of both TA and pCO_2. For calculation of pH, all couples produced generally good internal consistency however the (TA,DIC) couple gave the lowest combined uncertainty. Hence, for those years of the AR7W time series for which only TA and DIC were measured, we estimate that pH can be calculated with an accuracy of <0.007 and a combined uncertainty of <0.011 (with use of M73 or L constants).

Our Monte Carlo simulation showed that the choice of input couples can affect the uncertainty of aragonite saturation state calculations to a maximum value of 0.1. Whenever the couple (TA,DIC) is used higher residuals of Ω_{Ar} are observed, nevertheless no conclusions concerning accuracy can be drawn from these results as no direct determinations of Ω_{Ar} are available.

Internal consistency at *in situ* conditions of T and P is increasingly important in the context of autonomous oceanographic measurement of pH and/or pCO_2 (e.g., from gliders, Argo floats, moorings) and for model validation. However this is limited by current uncertainty concerning pressure effects on the constants. A new experimental investigation of the pressure effect on carbonate system dissociation constants and CO_2 solubility is required. We suggest that this should be validated with an intensive assessment of the internal consistency of carbonate system measurements within the deep ocean interior. This should include systematic comparison of laboratory-based measurements with measurements made *in situ*, of both pH and pCO_2, and could make use of shipboard programs such as the Labrador Sea monitoring discussed here.

CHAPTER 3

A 30 YEARS TIME SERIES OF TRANSIENT TRACER-BASED ESTIMATES OF ANTHROPOGENIC CARBON IN THE CENTRAL LABRADOR SEA [1]

3.1 Abstract

We use a 30-year time series (1986-2016) of dichlorodifluoromethane (CFC-12) concentrations with a refined Transit Time Distribution method (TTD), to estimate the temporal variation of anthropogenic carbon (C_{ant}) in the Central Labrador Sea.

We determined that the saturation of CFC-12 and sulfur hexafluroide (SF_6) in newly-formed Labrador Sea Water had departed significantly from 100% and varied systematically with time. Multiple linear regression of the time-varying saturation, with the tracer's atmospheric growth rate and the wintertime mixed layer depth as independent variables, allowed reconstruction of the saturation history of CFC-12 and SF_6 in wintertime surface waters, which was implemented in the TTD method.

[1] Raimondi, L., Tanhua, T., Azetsu-Scott, K., Yashayaev I., Wallace, D. W. R. (2021). A 30 years time series of transient tracer-based estimates of anthropogenic carbon in the Central Labrador Sea. *Journal of Geophysical Research: Oceans*, e2020JC017092. https://doi.org/10.1029/2020JC017092. Author contribution: I conducted the field work, analyzed the TA, DIC samples in 2014, 2015 and 2016 in collaboration with Stephen Punshon from the Bedford Institute of Oceanography. Tanhua T. provided extensive support with the TTD method. Yashayaev I. provided the MLD data and supported with the water masses definitions. I led the interpretation of the data and wrote the manuscript with extensive input from all co-authors.

Use of the time-varying saturation for CFC-12 gave C_{ant} concentrations ~ 7 μmol kg^{-1} larger than estimates obtained assuming a constant saturation of 100%. The resulting C_{ant} column inventories were $\sim 20\%$ larger and displayed lower interannual variability compared to conventional TTD-based estimates.

The column inventory of C_{ant} increased at an average rate of 1.8 mol m^{-2} y^{-1} over the 30-year period. However, the accumulation rate of C_{ant} was higher than this average in the early 1990's and since 2013 whereas inventories remained almost unchanged between 2003 and 2012. The variation in the C_{ant} accumulation rate is shown to be linked to temporal variability in the relative layer thickness of the annually ventilated Labrador Sea Water and the underlying Deep Intermediate Water.

The non-steady C_{ant} accumulation highlights the importance of sampling frequency, especially in regions of variable deep mixing and high carbon inventories, and potential misinterpretation of C_{ant} dynamics.

3.2 Introduction

The change in oceanic total dissolved inorganic carbon (DIC) concentrations relative to pre-industrial values, due to human mobilization of carbon over the past 250 years, is defined as "excess" or "anthropogenic" carbon dioxide *Wallace* (Excess CO_2 or C_{ant}; 2001). This C_{ant} represents only a small fraction of the total dissolved CO_2, and therefore difficulties are encountered in distinguishing the anthropogenic perturbation from the predominant natural signal. This is further complicated by spatial and temporal variability of the oceanic sink for anthropogenic CO_2 (*Gruber et al.*, 2019b,a).

Here we take advantage of a long time series of transient tracers (CFC-12 and SF_6) in the Central Labrador Sea, a region with high integrated column inventory of C_{ant}, to explore the temporal variability of tracer-based estimates of C_{ant} in this key region of the world's ocean for gas uptake and transport.

Methods to estimate C_{ant} in the ocean can be classified in four main categories (see *Sabine and Tanhua*, 2010, for a review): (1) back-calculation approaches (e.g., ΔC^*; *Gruber et al.*, 1996) that separate observed Dissolved Inorganic Carbon (DIC) from the pre-industrial preformed DIC based on estimation of changes due to remineralization of organic matter and dissolution of calcium carbonate; (2) decadal change methods based on repeat observations (e.g., the extended multiple linear regression (MLR), eMLR; *Friis*

et al., 2005) that identify C_{ant} by measuring differences between surveys completed in the same location but at different times; (3) model-based approaches (e.g., Ocean Circulation Inverse Model (OCIM); *DeVries*, 2014) that can be used to assess the air-sea flux of C_{ant} by simulating ocean mixing, circulation and biogeochemistry; (4) tracer-based approaches (the Transit Time Distribution or TTD method; *Waugh et al.*, 2006) that use transient tracers to estimate the age of a water sample and, from that, deduce its C_{ant} content based on the history of CO_2 in the atmosphere and surface water.

An important underlying assumption of most applications of these methods is that large-scale ocean circulation (e.g., ventilation of the ocean interior) is invariant over the timescale of the C_{ant} increase being considered. This steady-state assumption is particularly questionable for high latitude regions, such as the Labrador Sea considered here, where deep water formation displays strong interannual to decadal variability (e.g., *Yashayaev and Loder*, 2017). Relatively few observation-based studies have addressed the validity and significance of this assumption and examined the temporal variability of C_{ant} accumulation (e.g., *Carter et al.*, 2017; *Steinfeldt et al.*, 2009; *Tanhua and Keeling*, 2012; *van Heuven et al.*, 2011), likely because few, suitable, temporally-resolved datasets are available. Similarly, modelling studies (e.g., *Goodkin et al.*, 2011) have highlighted how errors in the ocean transport and dynamics of a model can directly affect the prediction of carbon cycle variables (e.g., air-sea CO_2 flux and C_{ant} uptake).

The Northwest Atlantic Ocean (together with the Mediterranean Sea; *Schneider et al.*, 2010) has been shown to have amongst the highest vertically integrated concentrations of C_{ant} (*DeVries*, 2014; *Khatiwala et al.*, 2009, 2013; *Sabine et al.*, 2004; *Waugh et al.*, 2006) in the global ocean. The Labrador Sea, in particular, is the source of Labrador Sea Water (LSW) which, together with underlying dense waters from the Denmark Strait and Iceland-Scotland Overflows, forms NADW and therefore plays a central role for ventilating the deep ocean interior. It has previously been shown that a significant portion of the total C_{ant} that is ultimately sequestered by the North Atlantic flows through the Labrador Sea basin (*Tait et al.*, 2000).

The formation of water masses by deep convection provides a direct path for atmospheric gases, including C_{ant}, to be exchanged with the ocean interior and has been referred to as a "trap door" mode of ventilation (*Bernardello et al.*, 2014; *De Lavergne et al.*, 2014). In contrast to the suppression of deep convection by a strengthening halocline in the Weddell

Gyre described by *Bernardello et al.* (2014) and *De Lavergne et al.* (2014), Labrador Sea Water formation continues today, but is highly variable on interannual and longer timescales (*Yashayaev and Loder*, 2016, 2017). Further, model projections suggest there is potential for significant future reductions of convection depth and LSW formation in response to increased freshwater input from Greenland (*Böning et al.*, 2016).

Here we present and interpret a time series of annual, tracer-based estimates of column inventories and storage rates of C_{ant} in the Central Labrador Sea over a thirty year period, from 1986 to 2016. The estimates are obtained with a refined version of the TTD method applied to data collected from a long-term monitoring program conducted along the WOCE/CLIVAR/GO-SHIP repeated hydrography line AR7W. The extensive time series data available along this hydrographic transect enable us to test and/or refine two of the assumptions typically applied when using the TTD method: (a) constant (usually 100%) saturation of the transient tracers and (b) constant air-sea CO_2 disequilibrium (*Matsumoto and Gruber*, 2005).

Relatively few studies have focused on the spatial distribution and potential for non-steady-state behavior of C_{ant} in this region. Using the ΔC^* method (*Gruber et al.*, 1996), *Tait et al.* (2000) provided the first description of the vertical distribution of C_{ant} in the Labrador Sea. This was followed by several studies which discussed the capacity of Labrador Sea to take up and store C_{ant}. For example, *Terenzi et al.* (2007) applied the TTD approach to "Classical" Labrador Sea Water[2] in the North Atlantic, and suggested that, despite the high concentrations of C_{ant} in Labrador Sea, the exchange of CO_2 across the sea surface in the Labrador Sea cannot keep pace with its transport into the ocean interior. This implied that the Labrador Sea is highly undersaturated with respect to C_{ant} in the atmosphere.

Another TTD-based study by *Steinfeldt et al.* (2009) between 20°S and 65°N in the Atlantic identified that the maximum C_{ant} column inventory was located in the Central Labrador Sea. A basin-wide decrease of the inventory within LSW was inferred between 1997 and 2003, which was explained by a temporary weakening in the rate of LSW formation and warming of the intermediate-depth waters during this period.

At the time when these studies were published it was still not possible to define whether apparent changes in column inventory were part of a long-term trend, or the result of

[2]See definition provided in Section 1.3.2

natural (e.g., decadal) variability in water mass formation. The unusual availability of a long time series of data from the Labrador Sea makes this area particularly valuable for identification of the nature of temporal variability in C_{ant} uptake.

3.3 Materials and Methods

3.3.1 Data

To calculate the C_{ant} with the TTD method we selected tracers and hydrographic data along a WOCE/CLIVAR/GO-SHIP repeated hydrography section (AR7W; Figure 3.1) that crosses the Labrador Sea, and that has been maintained by the Bedford Institute of Oceanography (BIO), Fisheries and Oceans, Canada (DFO). During these expeditions (occurring under the Atlantic Zone Off-Shore Monitoring Program [AZOMP] in recent years) samples for hydrographic, chemical and biological parameters were collected every spring-summer along this transect (typically in May, but occasionally in June or July). For a more detailed list of the parameters measured along this section see *Raimondi et al.* (2019) and AR7W cruise reports at `https://cchdo.ucsd.edu/`.

Measurements of CFC-12 from 1992 to 2011 were subject to a secondary quality control and compiled in the GLODAPv2 data product (*Olsen et al.*, 2016). For the years between 2012 and 2016 we performed the secondary quality control using the toolbox of *Lauvset and Tanhua* (2015). We also included early CFC-12 data collected in 1986 along a transect located slightly to the south of the AR7W line (*Wallace and Lazier*, 1988, see Figure 3.1), which extends our dataset over three decades. Sampling of SF_6 started in 2012 and annual data are available up to 2016. In *Azetsu-Scott et al.* (2005) and *Punshon et al.* (2016) a detailed description on the analytical procedures used to measure CFC-12 and SF_6 is provided.

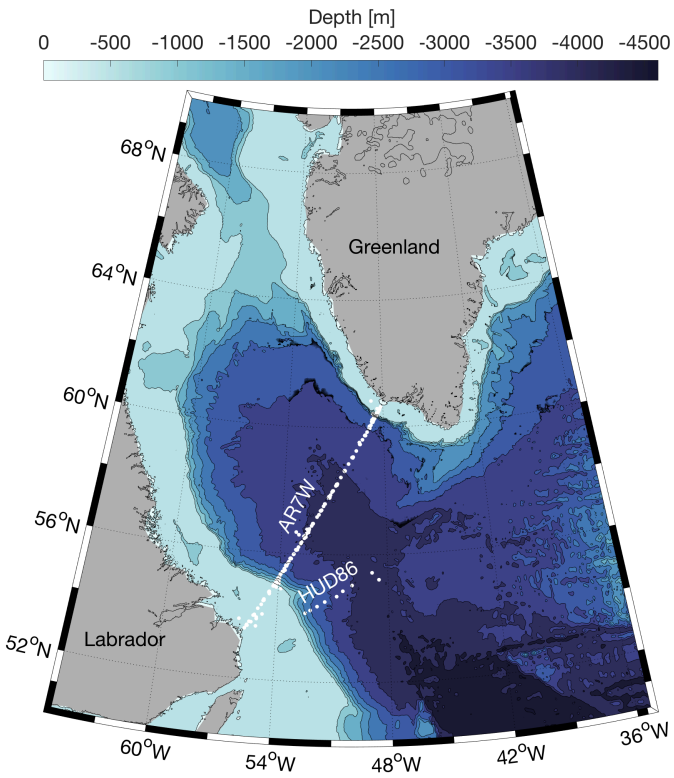

Figure 3.1: Map of the Labrador Sea with locations of the stations occupied during the Atlantic Zone Off-Shelf Monitoring Program (AZOMP) along the AR7W section between 1992 and 2016, and during the Hudson cruise in 1986 (southernmost stations).

3.3.2 TTD Method

We estimated the annual inventory of C_{ant} in the Central Labrador Sea between 1986 and 2016 using a refined version of the Transit Time Distribution (TTD) method (*Hall et al.*, 2002, 2004; *Waugh et al.*, 2006). The TTD provides a statistical description of the age distribution of a water mass within the ocean interior (where age refers to time elapsed since a parcel of water left contact with the atmosphere within the surface mixed-layer of an isopycnal outcrop region). If water is transported into the ocean interior by advection only, a water mass could be described by a single age or "transit time", but generally mixing of water parcels with different "ages" occurs so that a water mass has a distribution or spectrum of ages. As shown by *Holzer and Hall* (2000), the concentration within the ocean interior of a dissolved substance subject to time-variable surface water concentrations (such as transient tracers and C_{ant}) is given by:

$$c(t,r) = \int_0^\infty c_0(t-t')G(t',r)dt' \tag{3.1}$$

where c(t,r) is the concentration of the dissolved constituent within the ocean interior at time t and position r, $c_0(t)$ is the constituent's surface water concentration as a function of time, and G(t',r) is the age distribution in the form of a Green's function that describes the propagation of surface boundary conditions into the ocean interior (*Waugh et al.*, 2006). This distribution is commonly defined by an Inverse Gaussian Function (eq.3.2) characterized by a mean Γ and a width Δ.

$$G(t') = \sqrt{\frac{\Gamma^3}{4\Pi\Delta^2 t'^3}} \cdot exp\left(\frac{-\Gamma(t'-\Gamma)^2}{4\Delta^2 t'}\right) \tag{3.2}$$

The transport of water that delivers the time-variable tracer (or C_{ant}) to a certain location is characterized by the mixing of water parcels with different ages and, possibly, different source locations. The concentration of C_{ant} in the ocean interior can be estimated based on knowledge of the TTD and of the corresponding surface water concentration history of C_{ant}. The latter is obtained from the time-history of atmospheric CO_2 mixing ratios, the solubility of carbon dioxide and knowledge of the water mass' preformed alkalinity (TA_0; i.e., the total alkalinity [TA]of a water mass at the time it lost contact with the atmosphere). The TTD parameters, Δ and Γ, are constrained using concentrations of transient tracers such as CFC-12, CFC-11, CFC-113, CCl_4 and SF_6 and other tracers (e.g., ^{129}I; *Smith et al.*, 2016). The ratio of width (Δ) to mean age (Γ) reflects the relative strength of diffusive to advective transport processes that connect the ocean surface to the ocean interior. Its value is generally constrained empirically by comparing mean ages obtained from different tracers with different surface water concentration histories. Purely advective transport would have a $\Delta/\Gamma = 0$ and higher ratios correspond to increasing contributions of mixing to the overall tracer transport. For the Labrador Sea, we constrained Γ and Δ using CFC-12 and SF_6 data.

Although the TTD method accounts for effects of mixing of water with different ages on tracer and C_{ant} concentrations, its use involves a number of simplifying assumptions (see *Waugh et al.*, 2006, for a review). The first is assumption of constant saturation of surface waters (usually 100%) relative to the time-varying atmospheric concentrations of the transient tracer gases such as chlorofluorocarbons (CFCs) used to estimate the TTDs. An implication is that if the true saturation is lower than the assumed value, mean ages will be over-estimated and lower concentrations of C_{ant} will be inferred for the ocean interior. Previous studies showed that CFCs can be significantly under-saturated in newly-formed

Labrador Sea Water (*Azetsu-Scott et al.*, 2003; *Wallace and Lazier*, 1988), and dissolved oxygen also does not reach equilibrium during deep convection (*Atamanchuk et al.*, 2020; *Koelling et al.*, 2017).

The constant 100% saturation assumption was partially relaxed in the work of *Terenzi et al.* (2007) where they allowed under-saturation of the transient tracer by scaling the atmospheric history of CFC-11 to match values observed in the Labrador Sea. This scaling produced a saturation of 66%, consistent with previous observations of 60% by *Wallace and Lazier* (1988) and 70% by *Smethie Jr and Fine* (2001), nevertheless this value was held constant in *Terenzi et al.*'s approach.

In the case of CFCs, under-saturation of wintertime deep mixed layer is likely to have been more pronounced during periods when the rate of increase of CFCs in the atmosphere was fastest (i.e., up to 15% year^{-1} in the period between 1960s to early 1990s). Under-saturation of a tracer at the time of water mass formation is also likely to be influenced by the depth of wintertime convection (*Haine and Richards*, 1995). The deeper the convection, the larger the volume of water that must be equilibrated (via gas exchange) with the altered atmospheric concentration of the tracer gas. Deep convection involves entrainment of older, sub-surface water masses, typically with lower concentrations of transient tracers, which dilute tracer gas concentrations in the surface layers that are exposed to the atmosphere (*Azetsu-Scott et al.*, 2005; *Tanhua et al.*, 2008). Consideration of both mechanisms suggests that under-saturation of transient tracers is likely to be variable in regions of deep convection such as the Labrador Sea.

A second key assumption when applying the TTD method to C_{ant} estimation, is that the air-sea CO_2 disequilibrium has remained constant over time. Violation of this assumption might be expected given relatively long gas equilibration timescale for CO_2 (ca. 1 year) and consequent possibility that deep winter mixed-layers, that are exposed to the atmosphere for periods of weeks to months, fail to keep pace with the increase of atmospheric pCO_2 (*Takahashi et al.*, 1997). On the other hand, the growth rate of CO_2 in the atmosphere has been steadier than that of transient tracers. Contrary to the impact of the assumption concerning tracer gas saturation discussed above, this assumption of constant CO_2 disequilibrium may typically lead to overestimation of C_{ant} concentrations.

3.4 Adaptation and Application of the TTD Method to the Labrador Sea

3.4.1 Influence of Variable Surface Tracer Saturation to the C_{ant} Estimate

The Labrador Sea is one of the few major water-mass formation regions where historical time series of transient tracer concentrations are available with annual resolution extending over several decades. Using data from the repeated occupation of the AR7W line in May or June of each year, we reconstructed the time-varying saturation for the time of water mass formation (typically late February or March; *Yashayaev and Loder*, 2016; *Yashayaev*, 2007). We assumed that water lying between the seasonal thermocline (>200 metres [m] depth) and the maximum mixed layer depth (MLD) in the Central basin best represents the water that was in contact with the atmosphere during winter. This layer is hereafter referred to as Labrador Sea Water (LSW). The gas saturation for each year of the time series was obtained by averaging the measured concentrations of CFC-12 and SF_6 in this LSW layer and converting these to percent-saturation based on the contemporary atmospheric mixing ratios (hereafter, the percent-saturations obtained in this way are referred to as "observed saturations").

Using a least squares method, we modelled interannual variations of the observed saturation of CFC-12 and SF_6 tracer gases at the time of convection as a function of (a) the annual rate of increase of the tracer gas's atmospheric mixing ratio and (b) the interannually-varying maximum depth of wintertime convection.

The atmospheric histories of both CFC-12 and SF_6 are well constrained. The CFC-12 atmospheric history has been reconstructed using records of production and release data from manufacturers prior to 1979 and from direct measurements after 1979 (*Prinn et al.*, 2000; *Walker et al.*, 2000). The SF_6 input function is based on production estimates dating back to 1953 and direct measurements since then (*Bullister*, 2017). The annual variation of the maximum MLD can be estimated from measurements of temperature and salinity which have been carried out in the Central Labrador Sea since the 1930s (*Yashayaev and Loder*, 2016). The MLD was assessed through the methodology described in *Yashayaev and Loder* (2016) and using ship-board and Argo floats data collected by Fisheries and Oceans Canada (*Yashayaev and Loder*, 2017). Using the wintertime surface heat-loss and the observation-based estimates of MLD, a linear regression was obtained to parameterize

the MLD for years prior the early 2000's, when Argo floats data started complementing the AR7W line observations (see section B.2 of the Supplementary Material for a detailed description of the approach). We use model MLD-4 for our calculations as this was closest to the observed MLD, and closest to the average MLD value of the four models. The regression coefficients obtained for years of observations were then used to model the saturation back to 1945 (see Figure 3.2).

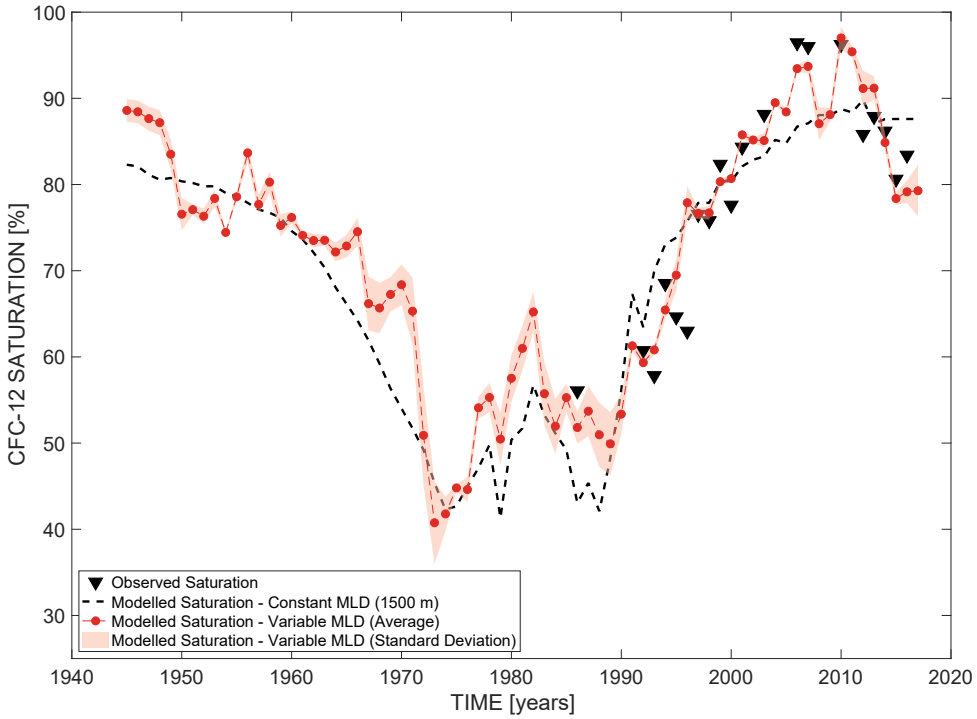

Figure 3.2: Modelled CFC-12 saturation during wintertime conditions in central Labrador Sea. The black triangles represent the observed saturations from 1986 to 2016. The dashed line represents the modelled saturation when the maximum MLD is assumed to be constant at 1500 m. The dots and shaded area represent the average modelled saturation and the standard deviations obtained with a MLR involving the first derivative of the atmospheric input function and different realizations of the maximum MLD from a conceptual model (see Supporting Information).

We used MLR of observed saturations to estimate the saturation of CFC-12 and SF_6 for years before the tracers were measured. The dependent variable was the observed saturation for the years 1986 to 2016 and 2012 to 2016 for CFC-12 and SF_6, respectively, and the independent variables were the first derivative of the atmospheric input function

and the maximum MLD for the same years:

$$sat(LSW)(\%) = a + b \cdot \frac{dC}{dt} + c \cdot MLD \tag{3.3}$$

where dC/dt represents the (annual) rate of increase of the tracer's atmospheric mixing ratio and MLD is the maximum MLD in meters.

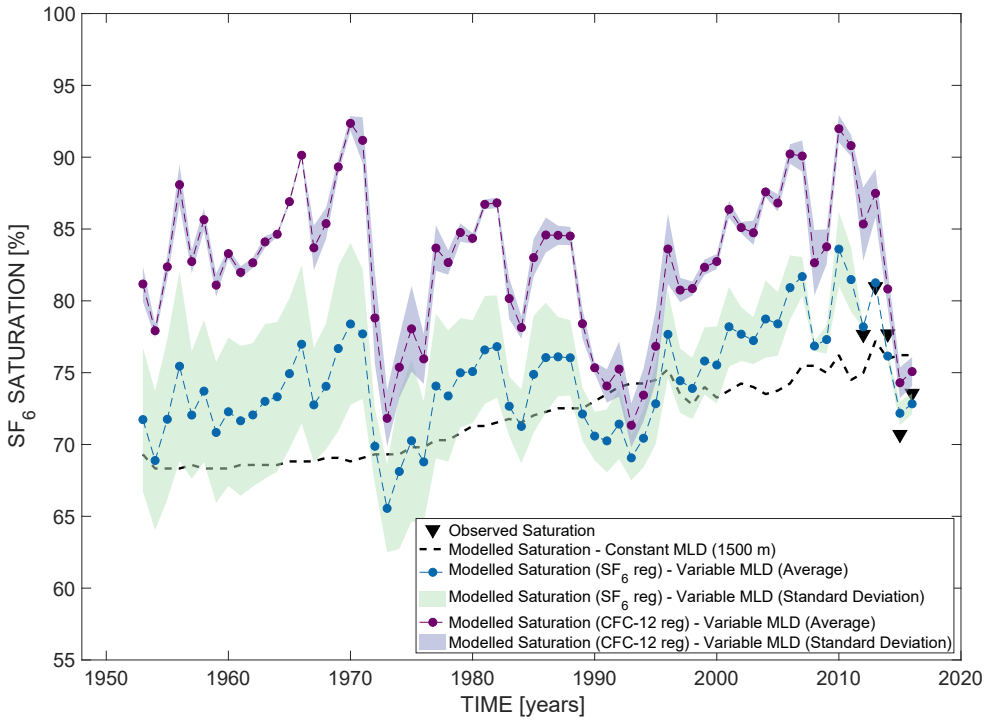

Figure 3.3: Modelled SF_6 saturation during wintertime in the Central Labrador Sea. The triangles represent the observed SF_6 saturations. The dashed line represents the SF_6 saturation obtained with an MLR and a constant MLD of 1500 m. The blue dots and shading represent the average saturations and their standard deviations, respectively, obtained from the MLR performed with the SF_6 observations and the four realizations of maximum MLD. Finally, the purple dots and shading represent the average SF_6 saturations and standard deviations from the MLR performed using the regression coefficients obtained from the CFC-12 observations.

We modelled the saturation of SF_6 using both a MLR based on the 5 years of SF_6 observations, as well as using regression coefficients from the MLR obtained with the CFC-12 observations (see Figure 3.3). The latter approach is justified because the two tracers shared quasi-exponential atmospheric histories and similar controls on air-sea

exchange and uptake. We applied the regression coefficients obtained from the CFC-12 regression with the MLD time-series data and the first derivative of the SF_6 atmospheric history.

Saturation variations were largely determined by the atmospheric growth rate (the root mean square error [RMSE] of the regressions using MLD alone, atmospheric growth rate alone and both atmospheric growth rate and MLD as independent variables were 9.6, 7.9 and 5.2%, respectively). A comparison of saturations reconstructed with a time-varying MLD (dots in Figures 3.2 and 3.3), showed that year-to-year variation of the MLD had only a small contribution of up to 17% and 12% to the overall variability of CFC-12 and SF_6 saturations, respectively. Years with saturations higher than values obtained with the constant 1500 m MLD, indicate that the actual MLD was a shallow one (e.g., 1960-1970, 2000-2010) while lower saturations indicate years with deeper convection (e.g., 2013-2016 see Figure B.2).

The modelled saturations of both CFC-12 and SF_6 were then used to reconstruct the wintertime surface history of the tracers effective mole fraction corrected for non-equilibrium conditions in central Labrador Sea using equation 3.4.

$$X_{eff}(t) = \frac{(X_{atm}(t) \cdot sat_{LSW}(t))}{100} \tag{3.4}$$

where X_{eff} is the effective mole fraction (ppt) of either CFC-12 or SF_6 in air that is in equilibrium with the contemporary, wintertime surface water concentrations, X_{atm} is the tracer's atmospheric mole fraction and sat_{LSW} is the saturation calculated for newly-formed LSW in each year using the MLR (equation 3.3). These calculated histories for surface water were implemented in the TTD routine so that the mean age calculation would account explicitly for the time-varying saturation of CFC-12 and SF_6. Figure 3.4 shows the resulting reconstructed surface histories of CFC-12 (panel a) and SF_6 (panel b) together with the atmospheric input functions of the two tracers. In Figure 3.4 it is noticeable that, when time-varying saturation in taken into account, both CFC-12 and SF_6 deviate significantly from the atmospheric input functions. Therefore, a large and time dependent bias is introduced when the traditional TTD approach (with assumed constant saturation of 100%) is applied to waters ventilated in the Labrador Sea.

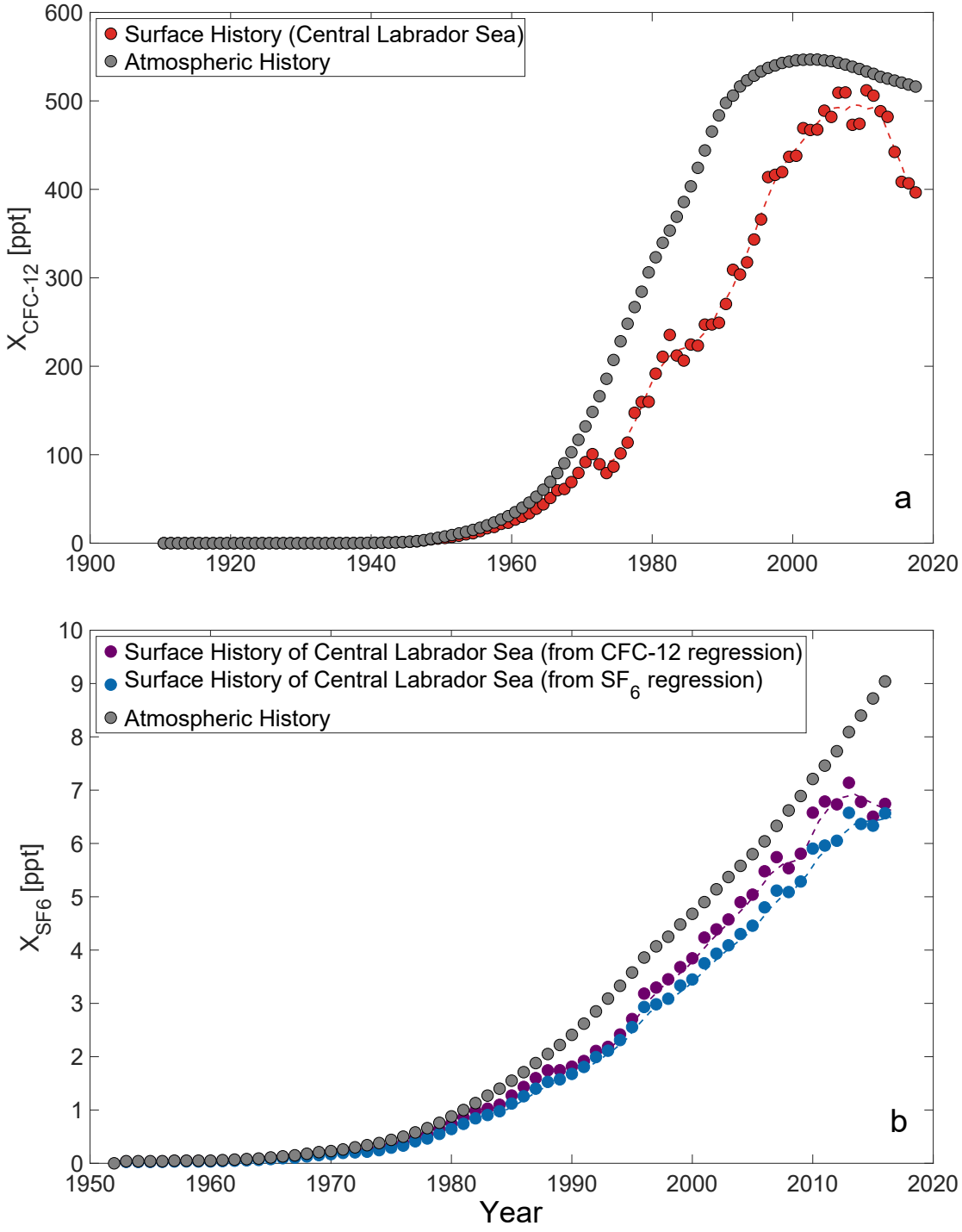

Figure 3.4: Panel a) Comparison between the atmospheric history (grey dots) and the Central Labrador Sea wintertime surface history (red dots) of the X_{CFC-12} (see equation 3.4). The dashed line represents the Smoothed function (moving average filter) of the surface history. Panel b) Comparison between the atmospheric history (grey dots); the Central Labrador Sea wintertime surface history of X_{SF6} obtained by applying the regression coefficients from a MLR using CFC-12 observed saturations to the SF_6 input function (purple dots) and through a MLR using observed saturations of SF_6 instead (blue dots). The dashed lines represent the smoothed functions of both surface histories of X_{SF6}.

3.4.2 Time-Variation of pCO_2

A second key assumption of the TTD approach is that the air-sea disequilibrium of CO_2 has remained constant over time. Although direct measurements of near-surface pCO_2 are not available for most of the time series, measurements of DIC and TA have been made since 1996 and allow pCO_2 to be calculated (see *Raimondi et al.*, 2019, for description of carbonate chemistry data). For some years of the time series, TA was either not measured (from 1992 to 1995) or excluded from the GLODAPv2 data product (*Olsen et al.*, 2016) due to lower quality of the measurements (1998-2000, 2002, 2006 and 2007). Because TA is not expected to vary systematically over time, we used a regional Salinity-Alkalinity relationship based on all available data to calculate TA for the years when TA measurements were not available (TA = 41.25 $\times$ Salinity + 862.41; R^2 = 0.85).

Using the MATLAB version of the CO2SYS software (*Lewis et al.*, 1998; *Van Heuven et al.*, 2011) we calculated pCO_2 using the equilibrium constants from *Mehrbach et al.* (1973) as refit by *Dickson and Millero* (1987) and including measurements of salinity (S), temperature (T), pressure (P), soluble reactive phosphorus (P_T) and silicate (Si_T). From these calculated values of pCO_2 we selected only those belonging to the LSW layer and compared average values obtained for this water mass (hereafter referred to as $pCO_{2(LSW)}$) to mean values of wintertime atmospheric pCO_2 (January to April) reported from the ICE station in Iceland (*Dlugokencky et al.*, 2019).

Figure 3.5 presents average values of wintertime atmospheric pCO_2 ($pCO_{2(atm)}$) and $pCO_{2(LSW)}$ over the period of measurement. Note that the calculated $pCO_{2(LSW)}$ values from (TA,DIC) agree well with independent estimates from moored sensors available in the region (red markers in Figure 3.5).

Although there is larger interannual variability in the oceanic pCO_2, we cannot determine whether this is representative of a time-varying air-sea disequilibrium because of the uncertainty associated with the calculated pCO_2 values. The root mean square error (RMSE) for a linear regression of $pCO_{2(LSW)}$ against time was 7.7 μatm which is smaller than the propagated random uncertainty associated with calculating pCO_2 from (TA,DIC) which has been estimated previously to be $\sim$ 12 μatm (*Raimondi et al.*, 2019). Hence the variability of $pCO_{2(LSW)}$ in Figure 3.5 is consistent with the combined random uncertainty of the dissociation constants and carbonate system measurements used in calculating pCO_2.

The rates of increase of atmospheric and Labrador Sea Water pCO_2 between 1996 and 2016 were 2.2 and 2.3 μatm y^{-1}. A t-test, performed following recommendations from *Andrade and Estévez-Pérez* (2014), shows that the two slopes are not significantly different from each other (α = 0.05). We therefore conclude that $pCO_{2(LSW)}$ tracks the atmospheric increase and that there is no evidence for a time-varying air-sea disequilibrium over the period of measurement. This suggests that a constant disequilibrium assumption for pCO_2 is appropriate for use with the TTD method in this region, over this time-period.

This finding is consistent with the time evolution of the air-sea CO_2 surface disequilibrium obtained from a model simulation (*Matsumoto and Gruber*, 2005) which also showed little divergence between atmosphere and ocean over the years when our data were collected ($\sim$ 0.5 μmol C kg^{-1}, equivalent to approximately 1 μatm). It is likely that a longer time series would be required to detect any trend in air-sea CO_2 disequilibrium that is necessary to derive a larger uptake of CO_2.

3.4.3 Constraints on Mixing Conditions (selection of Δ/Γ)

In contrast to some other indirect approaches of C_{ant} estimation, the TTD method accounts for water mass mixing using the Δ/Γ ratio (a measure of the breadth of the TTD). As stated in *Waugh et al.* (2006), two tracers with sufficiently different time histories can be used to constrain Δ and Γ. If a Δ/Γ ratio is representative of mixing conditions, the same mean age should be obtained from the different tracers. We therefore simulated mean ages based on CFC-12 and SF_6 concentrations and varied the Δ/Γ ratio between 0.4 and 2.0. We then selected the most appropriate Δ/Γ ratio based on the overall agreement of the mean ages obtained with the two tracers (see Figure B.1).

We performed this Δ/Γ selection by plotting the ratio of CFC-12-derived to SF_6-derived mean ages versus the SF_6-derived mean ages. Due to recently decreasing concentration of CFC-12 in the atmosphere (see Figure 3.4 panel a), we excluded recently formed water masses for which a consistent positive bias in CFC-12-derived mean ages was observed. We performed a linear regression using only mean ages for which SF_6 values were $<$6 ppt, corresponding to the time period when the CFC-12 atmospheric concentration was

[3]To convert mixing ratios (ppm) into pCO_2 (μatm) we used the air pressure with water vapour correction. The wintertime air pressure was obtained by selecting the monthly mean values of sea level NCEP air pressure throughout the convection period (from January until March) for each year (reanalysis product downloaded at `https://psl.noaa.gov`). For the water vapour correction a MATLAB function provided by Prof. Roberta Hamme was used instead (downloaded at `https://web.uvic.ca/~rhamme/vpress.m`).

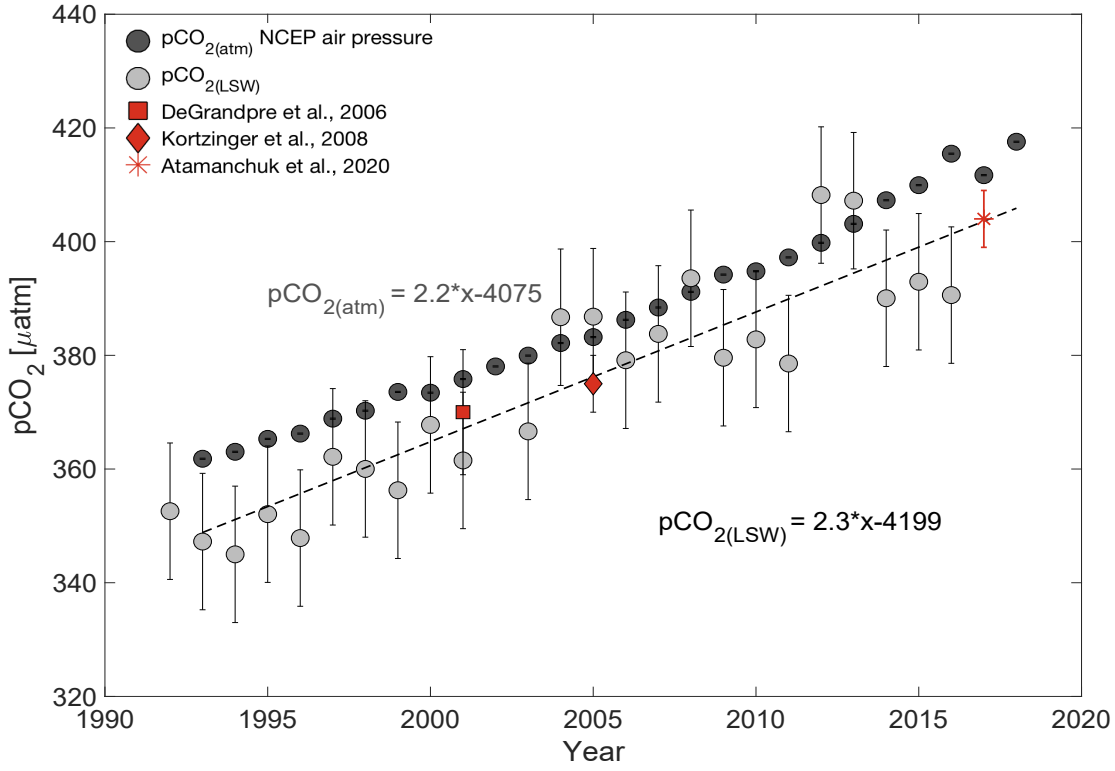

Figure 3.5: Average atmospheric pCO_2 and $pCO_{2(LSW)}$ values from 1992 to 2016. The atmospheric pCO_2 is a wintertime average obtained from the Iceland station data (Storhofdi, Vestmannaeyjar). The Seawater pCO_2 was calculated using (TA,DIC) as input couple in CO2SYS and averaged for the central region of Labrador Sea between seasonal thermocline and maximum MLD of each year. A S-TA relationship was obtained using our time series and then applied for those years where TA was either missing or excluded from the GLODAPv2 data. The atmospheric values of pCO_2 in μatm was obtained using NCEP values of air pressure for this region [3]. The red square, diamond and asterisk markers represent previous estimates of pCO_2 in the region within 200 m depth by *Atamanchuk et al.* (2020); *DeGrandpre et al.* (2006); *Körtzinger et al.* (2008), respectively.

lower than the contemporary CFC-12 concentration. The selection was performed based on the coefficients of this regression and the average distance of the data from a reference line (black line in supplementary Figure B.1 with intercept of 1 and slope of 0). The most representative ratio would be that with a slope close to 0, an intercept close to 1 and the lowest average distance of the data point from the reference line. From this analysis, the Δ/Γ ratios that best represent the mixing conditions was 1.8.

3.4.4 Calculation of C_{ant} Concentrations and Inventories

The mean ages derived from this refined TTD approach were used together with the surface history of C_{ant} (obtained from atmospheric pCO_2 data and equilibrium constants) to obtain estimates of anthropogenic carbon along the AR7W line. Using the surface concentration histories of CFC-12 and SF_6 with variable saturation derived from the multiple linear regression, assuming constant disequilibrium for CO_2 and the Δ/Γ value selected in the previous section (Δ/Γ = 1.8), the C_{ant} concentration was calculated as:

$$C_{ant}(r,t) = \int_0^\infty C_{ant,0}(t-t')G(r,t')dt' \tag{3.5}$$

where $C_{ant,0}$ (t) is the surface concentration of C_{ant} and G(r,t') is the age spectrum obtained from the tracers. The C_{ant} concentrations were then interpolated using objective mapping (*Roemmich*, 1983) onto a standard grid to assist with calculation of inventories for comparison between years. In order to calculate column inventory for the Central Labrador Sea (defined here as the portion of the AR7W line with bottom depth >3300 m; *Yashayaev*, 2007), the gridded values of C_{ant} from the objective mapping (spatial resolution of 5 km), were averaged horizontally for 5 m depth intervals. An average C_{ant} profile was then integrated vertically to obtain a column inventory as follows:

$$I_{C_{ant}} = \int_0^{max(depth)} C_{ant,0} \times \rho \;\; dz \tag{3.6}$$

where $I_{C_{ant}}$ stands for column inventory of C_{ant}, C_{ant} is in mol kg^{-1}, ρ is the *in situ* density (kg m^{-3}). The integration was performed by using 5 m intervals.

In order to demonstrate the significance of the constant saturation assumption of tracers and the choice of Δ/Γ, we estimated C_{ant} using both a constant and a time-varying saturation for all Δ/Γ values listed earlier (see Results section). Finally, from the column inventories calculated for each year of the time series we calculated the storage rate (SR)

in the Central Labrador Sea over three decades (in mol m^{-2} y^{-1}).

3.5 Results

In this section, we present results of C_{ant} concentrations obtained using the TTD method with CFC-12 data, for both a constant (100%) and a time-varying saturation (presented in section 3.4.1). Results of C_{ant} obtained using the TTD method with SF_6 are provided in the supplementary material (section B.3).

3.5.1 Sensitivity of C_{ant} Estimates to the Saturation of CFC-12

Use of a time-varying CFC-12 saturation for TTD calculations resulted in higher estimated C_{ant}, with average differences from the conventional TTD approach of $\sim 7 \pm 1.5$ μmol kg^{-1}. This translated into column inventories that were 19.2 to 39.7 mol m^{-2} higher when estimated with the refined TTD approach, compared to estimates based on the conventional assumption of constant (100%) saturation. In Figure 3.6 we show column inventories of C_{ant} calculated with both time-varying ($C_{ant(VS)}$; where the subscript VS denotes variable saturation) and constant saturations ($C_{ant(CS)}$; where CS denotes constant saturation) for Δ/Γ = 1.8.

With the constant saturation assumption, the $C_{ant(CS)}$ inventory estimates increased from 72.3 to 148.6 mol m^{-2} between 1986 and 2016, whereas the increase was from 112.0 to 181.4 mol m^{-2} when the variation of the tracer's saturation over time was accounted for. Hence, the storage rate with time-variable saturation was slightly smaller than with the traditional-TTD approach (1.8 and 2.1 mol m^{-2} y^{-1}, respectively) but still within its uncertainty.

Use of a time-varying saturation also reduced the interannual variability (or scatter) around the long-term rate of increase, as given by the regression line (RMSE of 5.7 and 3.7 mol m^{-2} y^{-1} using constant and time-varying saturations, respectively). The column inventory for the first year of the time-series, 1986, falls noticeably closer to the regression line when calculated with a time-varying saturation. Both approaches indicate a slow-down in the rate of increase in the early 2000s, but only the $C_{ant(VS)}$ results indicate a rapid increase in the latest years of the time series (see Figure 3.6): a result which is also obtained using SF_6 (see section B.3 of supplementary material). In fact we found that when accounting for time-varying saturation, the C_{ant} estimates based on CFC-12 agree

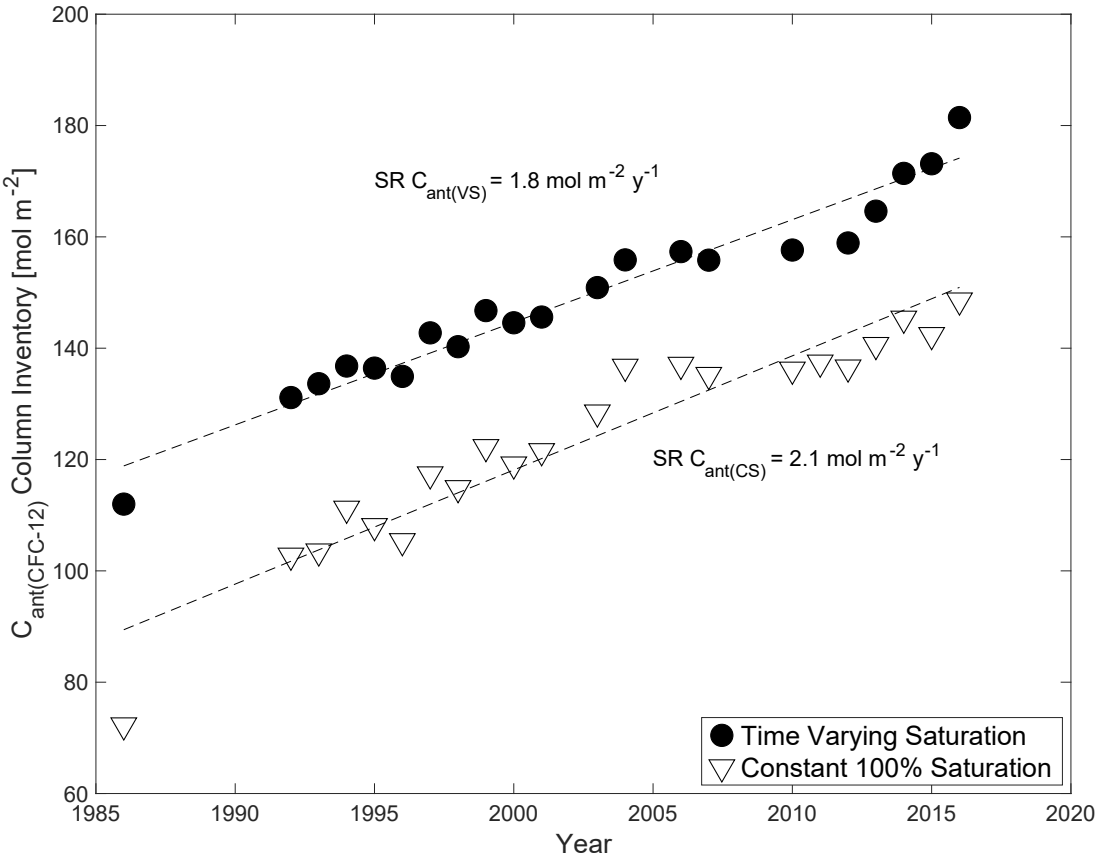

Figure 3.6: Column inventory of C_{ant} in the Central Labrador Sea obtained from mean ages calculated using a constant CFC-12 saturation assumption (triangles) and the column inventory obtained from our refined TTD method with Δ/Γ = 1.8 (black dots). Here CS and VS stand for constant and variable saturation, respectively. We also report the slope of the regressions which represent the storage rates (SR; in mol m^{-2} y^{-1}).

better with those based on SF_6 (see Figure B.5), which is a more reliable tracer for recent years compared to CFC-12 due to decreasing atmospheric concentrations of the latter.

3.5.2 Sensitivity of C_{ant} Estimates to the Selection of Δ/Γ

Figure 3.7 presents C_{ant} column inventories for the Central Labrador Sea from 1986 to 2016 (black dots) that are averages of values calculated with the refined TTD method with CFC-12 data and using the full range of Δ/Γ ratios discussed in section 3.4.3. The average column inventories increased from 114 to 182 mol m^{-2} over 30 years. The standard deviation of the inventories obtained with this range of Δ/Γ is represented by the shaded area in Figure 3.7 and varies between 0.6 and 2.5 mol m^{-2} in different years. This suggests that the choice of Δ/Γ does not dramatically affect the column inventory estimates. Indeed,

the choice of Δ/Γ can lead to percent differences between a minimum of -4.5% and a maximum of 0.4% in C_{ant} concentrations compared to the reference concentrations obtained with Δ/Γ = 1.8 (see Table B1). This translated into a maximum difference of $\sim$ 1.2% in column inventory estimates using different ratios. We note that *Hsieh* (2016) suggested that the Δ/Γ ratio should be variable over time to better represent the different mixing conditions at times of intense and weak convection. However our results show that the choice of Δ/Γ will not dramatically affect our estimates of C_{ant} column inventories and therefore, for this study, the Δ/Γ ratio was held constant over time.

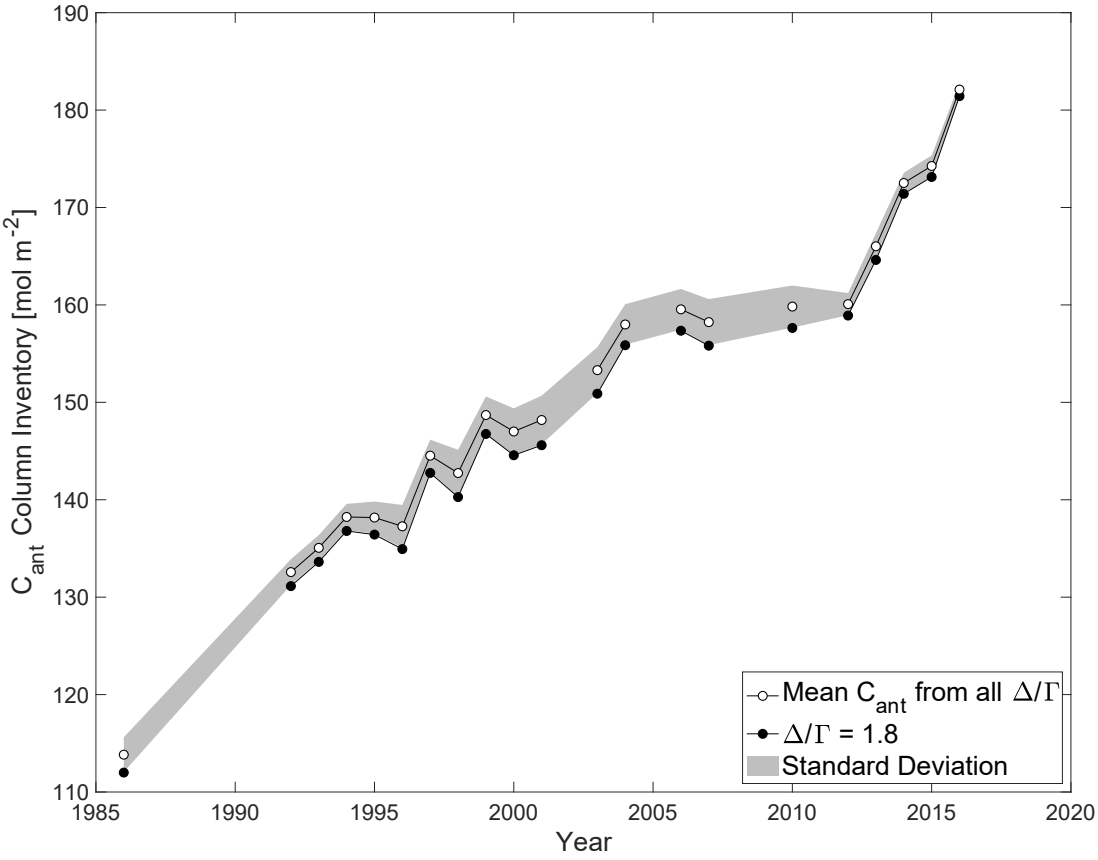

Figure 3.7: Average column inventories of C_{ant} in the Central Labrador Sea from 1986 to 2016 obtained from CFC-12 (white dots). These averages were calculated using C_{ant} estimates obtained from a wide range of Δ/Γ (0.4-2.0) and time variable saturation. The shaded area represents the standard deviation obtained for the range of Δ/Γ. For reference, we also report the column inventories obtained with the selected Δ/Γ of 1.8 (black dots).

3.5.3 Distribution of C_{ant} in Major Water Masses

Below the seasonal thermocline (i.e.,>200 m depth) the vertical structure of the Central Labrador Sea is dominated by a homogeneous cold and fresh layer defined as LSW. Depending on the depth of convection reached every year, the lower limit of the LSW layer can be usually found between 500 and 2000 m depth, with the deepest convection ever observed reaching as deep as 2400 m in 1993 and 1994 (*Yashayaev*, 2007; *Yashayaev and Loder*, 2016). Below the LSW lies the more saline North East Atlantic Deep Water (NEADW) which originates from the Iceland-Scotland Overflow Water that enters the North Atlantic through the Iceland-Faroe-Scotland Ridge and becomes more saline due to mixing with overlying salty and warm Atlantic waters (thermocline water in the lower limb of the Subpolar Mode Water and North Atlantic Current) that add characteristic salt to the mix (*Yashayaev and Dickson*, 2008). Below the NEADW layer, lies the cold, dense and less saline Denmark Strait Overflow Water (DSOW). This is the densest water mass observed in the Labrador Sea and the entire Subpolar North Atlantic (SPNA). It originates from the Denmark Strait Overflow and enters the basin from the Greenland Sea via the Irminger Sea (*Yashayaev*, 2007).

We identified these water masses based on either their time-varying or fixed density ranges (σ_2 [4]; for LSW and NEADW, respectively) or depth range (for surface water and DSOW), and calculated both the average C_{ant} concentrations and the individual contributions to the total column inventory of these water masses (see supplementary Table B2 and Table B3 for water masses definitions, some of which have varied over time). As a further step we identified the contribution to the total C_{ant} column inventory of a body of water here referred to as Deep Intermediate Water (DIW). This water mass is a mixture of LSW, NEADW, Icelandic Slope Water (*Yashayaev and Loder*, 2017) and other intermediate and deep-water masses of the SPNA. The DIW is the product of modification and transformation of a deep-reaching and dense class of LSW formed between 1987 and 1994, possibly with smaller, occasional additions of dense water formed in subsequent years. The aging of this old class of LSW ($LSW_{1987-1994}$ in *Yashayaev*, 2007) is reflected in the steady loss of its original high freshwater and oxygen signatures, which eventually determined DIW to be almost indistinguishable from NEADW. Similarly to new LSW formation, the DIW shows strong temporal variability of its layer thickness (see Figure 3.9

[4] σ_2 = potential density anomaly references to 2000dbar.

panel d).

In Figure 3.8, we present selected C_{ant} sections from 1986, 1996, 2006 and 2016 to illustrate the multi-decadal increase and deep penetration of C_{ant} throughout the Labrador Sea (for the full time series we refer to the animation provided as supplementary material). The sections, are similar to the vertical distribution of C_{ant} described by *Tait et al.* (2000). The highest concentrations of C_{ant} are found, by definition, in the surface layer ($<$200 m) which is underlain by a relatively homogeneous layer of high concentrations extending down to 1500-2000 m (this is the layer of water that is primarily ventilated in Labrador Sea). The depth range of the older NEADW (2400-3400 m) is marked by a minimum in C_{ant} concentrations whereas an increase in concentrations within 200 m above the seabed, reflects the presence of more recently ventilated DSOW.

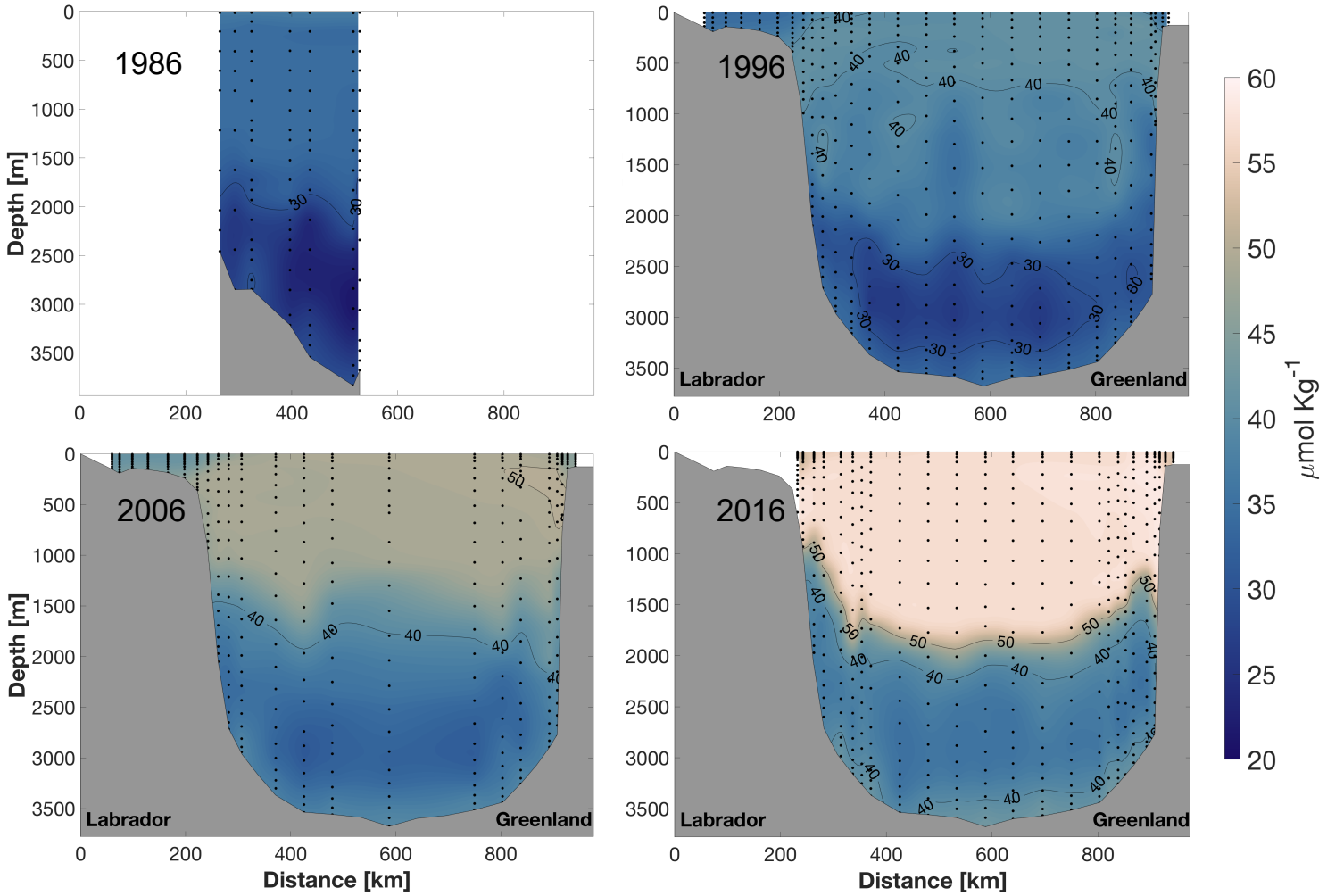

Figure 3.8: Sections of C_{ant} along the AR7W line (except for data in 1986 which were collected further south) obtained from the refined TTD method. The sections show the strong increase and deep entrainment of C_{ant} in Labrador Sea.

3.6 Discussion

3.6.1 Interannual Variability of C_{ant} in Major Water Masses

In Figure 3.9 (panel a) we present the temporal variation of the average and standard deviation of the C_{ant} concentrations in the major water masses discussed in the previous section. Between 1986 and 2016, the average C_{ant} concentration of LSW increased by 22 μmol kg^{-1}, whereas notably smaller increases were observed in the other water masses (13 μmol kg^{-1} in both DIW and NEADW; 12 μmol kg^{-1} in DSOW). This implies that the rate of increase of the annual mean C_{ant} concentrations is the fastest in LSW (at 0.8 μmol kg^{-1} y^{-1}), showing that this is the water mass that primarily drives the overall variability of C_{ant} around the longterm (multi-decades) trend observed in the region. The DIW showed an overall temporal increase similar to that of NEADW and DSOW, but also showed higher interannual variability in C_{ant} concentrations as with LSW (see Figure 3.9 panel a).

As noted earlier, the DIW is primarily composed of LSW left over from previous years of strong convection, and not just $LSW_{1987-1994}$, and was therefore originally characterized by high concentrations of C_{ant}. Nevertheless, while LSW is ventilated from the surface every year and therefore exposed to increasing C_{ant} concentrations, the DIW becomes progressively older, explaining why its rate of increases of C_{ant} is similar to that of NEADW.

Both the annual mean concentrations and rate of increase of C_{ant} are higher in DSOW than in NEADW (Figure 3.9 panel a). This is explained by the more recent ventilation of the former and by the stronger transformation and modification the NEADW undergoes when arriving into the Labrador Sea (*Yashayaev and Dickson*, 2008). Further a smaller fraction of annual addition of the original overflow water mixes into NEADW compared to DSOW.

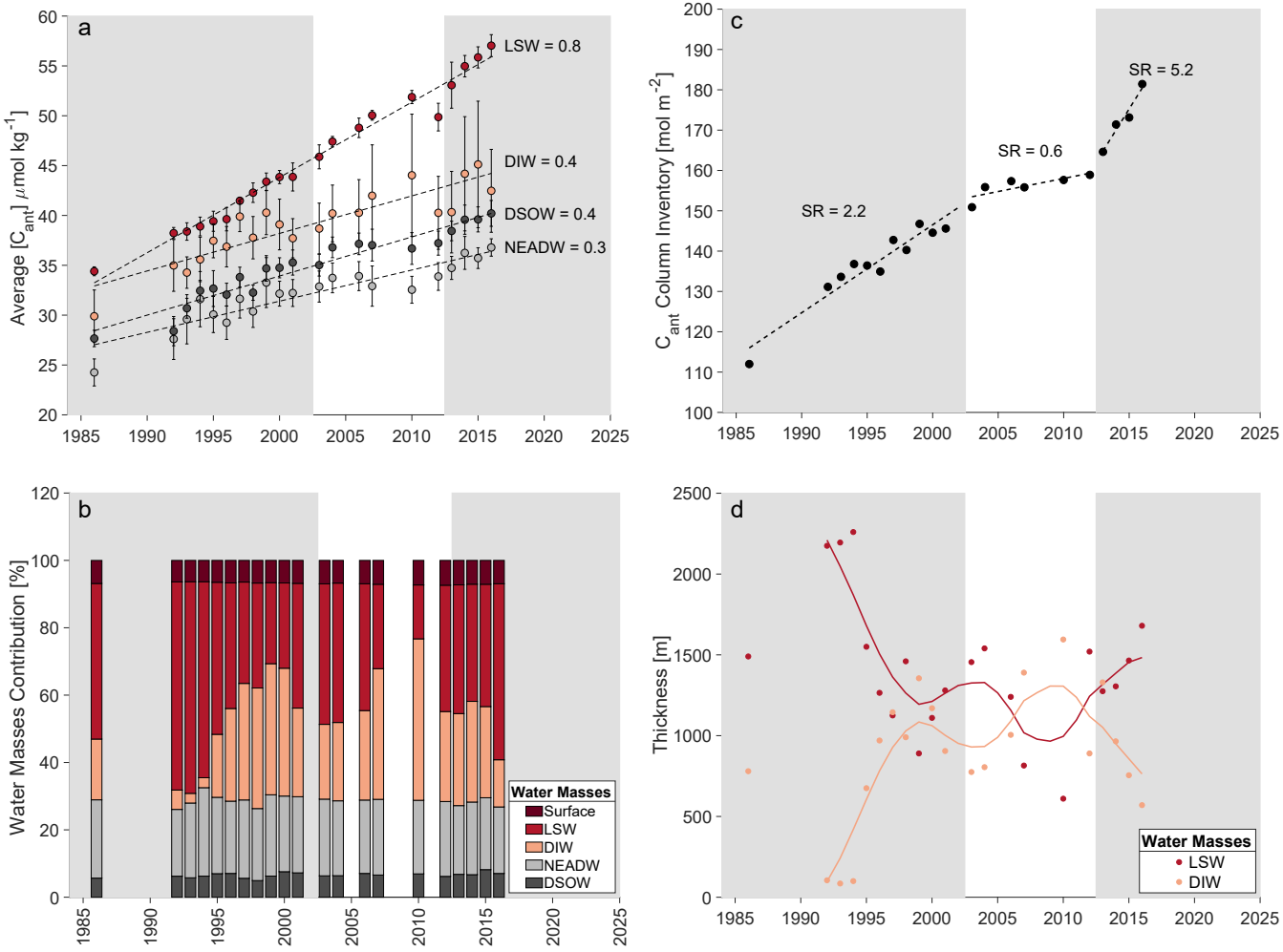

Figure 3.9: Caption in the next page.

Figure 3.9: (Previous page.) Panel a) Average C_{ant} concentrations and standard deviations in LSW, DIW, NEADW and DSOW in the Central Labrador Sea between 1986 to 2016. Next to each water mass we report the rate of increase of the average concentration in μmol kg^{-1} y^{-1} (i.e., slopes of the regressions). Panel b) Breakdown of the percent contribution of different water masses to the C_{ant} column inventory in the Central Labrador Sea. Panel c) Time evolution of C_{ant} column inventories from 1986 to 2016 with regressions for three periods. Note that SR represents the slope of each of the three regressions (in mol m^{-2} y^{-1}). Panel d) Time evolution of the LSW and DIW layer thickness between 1986 and 2016, dots represent absolute values, solid line represent smoothed 5 years running means. All four panels show time periods with shaded background. The shaded areas represent periods of intermediate and fast rate of C_{ant} accumulation, on the other hand the white area represents a period of slow C_{ant} accumulation rate.

In Figure 3.9 panel b we present the percentage contributions of the four main water masses, as well as the surface water, to the C_{ant} column inventory of the Central Labrador Sea over time. The figure shows that NEADW and DSOW, which are ventilated outside the Labrador Sea, display a stable contribution to the total inventory. On the other hand, LSW and DIW, which both are ventilated, at least partially, in the Labrador Sea, show large variability in their relative contributions. Whereas LSW's contribution dominated the column inventory in the early 1990s and in the most recent years, DIW contributed significantly during the intervening years, reflecting the decreased LSW layer thickness. The LSW and DIW exhibited stronger interannual variability of their contribution to the C_{ant} column inventory due to changes in their relative layer thickness (see Figure 3.9 panel d), this is reflected by wider ranges of percent contribution for LSW and DIW (between 16-63% for LSW, 3-48% for DIW) compared to narrower ranges for NEADW and DSOW (20-26% for NEADW and 5-8% for DSOW).

3.6.2 Non-Steady Accumulation of C_{ant} in Central Labrador Sea

The time series of C_{ant} column inventory (Figure 3.6) shows that the increase in column inventory is not steady over time. In particular we observed three distinct periods: 1986-2002, 2003-2012 and 2013-2016 (see Figure 3.9 panel c). We find that whereas the first and third periods were characterized by intermediate and fast increase of C_{ant} column inventory respectively (2.2 and 5.2 mol m^{-2} y^{-1}), the period between 2003-2012 was characterized by a low accumulation rate (0.6 mol m^{-2} y^{-1}). This accumulation rate was not significantly different than zero therefore indicating that the C_{ant} column inventory remained constant at this time.

During the first period (between 1986 and 2001) the average C_{ant} concentrations of LSW and DIW displayed differences <5 μmol kg^{-1} (see Figure 3.9 panel a). During this time, the Labrador Sea experienced both deep (1992-1995) and intermediate (1996-2002) convection, which was responsible for a shift from a LSW-dominated water column to one that was equally partitioned between LSW and DIW (see Figure 3.9 panel d). During this first period, the average concentrations of C_{ant} were the lowest throughout the time series and not very different in these two water masses, therefore the relative proportion of the two water masses did not matter to the extent it did in later years of the time series. Further, whereas the rate of increase of C_{ant} average concentrations in DIW at this time (0.6 μmol kg^{-1} y^{-1} between 1986 and 2002) was the same as that observed toward the end of the time series (0.7 μmol kg^{-1} y^{-1} between 2013-2016), the rate of increase in the LSW during this first period (0.7 μmol kg^{-1} y^{-1} between 1986 and 2002) was considerably lower than what was observed toward the end of the time series (1.3 μmol kg^{-1} y^{-1} between 2013-2016). As a result, we observed only an intermediate storage rate of C_{ant} despite this being the period when the deepest convection was observed.

Starting in 2003, and continuing for the remainder of the time series, we observed a divergence of the LSW and DIW C_{ant} concentrations, with LSW displaying progressively higher average concentrations than DIW (see Figure 3.9 panel a). During this second period of our time series (between 2003 and 2012), the formation of LSW became progressively shallower and the DIW became the main water mass contributing to the total inventory of C_{ant}. The combination of lower formation of LSW, the consequent predominance of DIW (see Figure 3.9 panel d), the much lower concentrations of C_{ant} displayed in DIW compared to LSW and the lowest rate of increase of C_{ant} in both water masses (0.5 and 0.3 μmol kg^{-1} y^{-1}, for LSW and DIW, respectively), resulted in the low accumulation observed between 2003-2012 (see Figure 3.9 panel c).

During the third period (between 2013 and 2016), there was renewed formation of LSW, and this time the water mass displayed large average concentrations of C_{ant} (which were larger than the concentrations observed in the DIW layer) and the highest rate of increase observed (1.3 μmol kg^{-1} y^{-1}). The increase in the thickness of the LSW layer coupled with its high C_{ant} concentrations, resulted in the fastest accumulation rate of C_{ant} observed over the 30-year time series (see Figure 3.9 panel c).

Therefore, we find that the combination of variability in the relative layer thickness

of LSW and DIW and their average C_{ant} concentrations leads to significant multi-year variability in the rate at which C_{ant} is stored in the Labrador Sea.

This is consistent, overall, with the findings of *Steinfeldt et al.* (2009), that C_{ant} accumulation in LSW is not steady over time. Nevertheless, whereas they detected a slow-down of C_{ant} accumulation in LSW throughout the northwest Atlantic between 1997 and 2003, our study demonstrates a period of slow-down in C_{ant} accumulation within the Central Labrador Sea (the formation region for LSW) that starts in 2003 and continued until 2012.

There are several potential reasons for this apparent discrepancy between our findings and those of *Steinfeldt et al.* (2009). For example, the lower-than-expected accumulation between 1997-2003 in the *Steinfeldt et al.* study might have been caused by their assumption of constant saturation of transient tracers when estimating C_{ant} . Alternatively, the very significant differences in the temporal and, especially, spatial distribution of the data used in the two studies complicates any comparison of the two estimates. Our study has high temporal resolution, but is confined to the immediate formation region of LSW, whereas *Steinfeldt et al.* (2009) compare only two "snapshots" of C_{ant} distributions, but those snapshots involve LSW that is distributed throughout the Sub-polar Gyre of the North Atlantic.

Our saturation reconstruction (Figures 3.2 and 3.3) shows that the period between 1997 and 2003 addressed by *Steinfeldt et al.* (2009) was characterized by strong undersaturation of both CFC-12 and SF_6, implying that CFC-11, which was used to estimate C_{ant} in 1997 in their work, was likely also undersaturated. While the possibility of undersaturation was taken into account by *Steinfeldt et al.* (2009), using values between 65% and 100% depending on the density layer, the saturation values were held constant over time. Applying a constant 65% saturation to the calculation of C_{ant} inventories along the AR7W line, increases our estimates by 12% for 1997 and 18% for 2003, compared to estimates based on an assumed constant saturation of 100%, bringing our estimates closer to those reported in *Steinfeldt et al.* (2009). Nevertheless, our C_{ant} column inventory estimates for the Central Labrador Sea in 1997 are significantly lower ($\sim$ 10-40 mol m^{-2}) than those reported in Figure 5 of *Steinfeldt et al.* (2009), irrespective of whether we use a time-varying or a constant 65% saturation. For this reason, we do not see a slow-down in C_{ant} accumulation until later in the time series.

It is important to emphasise that the slow-down in C_{ant} storage rate was only temporary

(ca. 10 years) and not representative of the overall trend throughout the three decades. In particular we observed a recovered fast storage rate in the latest years of the $C_{ant(VS)}$ time series (note that this would not have been observed if a constant 100% saturation had been assumed) which corresponds with renewed deep winter convection during this period (*Yashayaev and Loder*, 2016).

Rhein et al. (2017) reported C_{ant} estimates based on the TTD method for the Central Labrador Sea between 1992 and 2016, however in contrast to this study they only considered constant saturation of CFC-12. Further, *Rhein et al.* (2017) assessed the C_{ant} inventory in two adjacent density layers: the upper LSW (uLSW) and deep LSW (dLSW) as defined in *Stramma et al.* (2004), however this partitioning of the upper-to-intermediate water column into two density layers does not necessarily reflect the time evolution of newly formed LSW and the associated LSW classes (*Yashayaev*, 2007; *Yashayaev and Loder*, 2016, 2017). Our approach was to define water masses as water with homogeneous property distributions, with LSW defined following *Yashayaev* (2007), and later revisited in *Yashayaev and Loder* (2016, 2017), and NEADW and DSOW defined as in *Yashayaev and Dickson* (2008). For comparison purposes in Supplementary Figures B.3 and B.4, we have also reported results using the uLSW and dLSW layer definitions.

Overall our C_{ant} estimates are comparable to those reported in Figure 3b of *Rhein et al.* (2017), even though some discrepancies are to be expected due to the use of the refined TTD method in our study. The slow-down in C_{ant} storage rate that we observed between 2003 and 2012 appears to be consistent with findings in *Rhein et al.* (2017). These authors report that the C_{ant} inventory in the LSW layer (uLSW + dLSW) in 2007-2010 was lower than the value projected based on data from 1996 to 1999 and assuming no changes in ventilation had occurred. This difference was attributed to a decrease in ventilation rate and supported by a decrease in the fraction of LSW younger than 20 years (see Figure 5 in *Rhein et al.*, 2017).

We show that the decreasing thickness of LSW between 2003-2012, and increased thickness of DIW due to transformation of old LSW into DIW (which is characterized by low C_{ant} concentrations), not only affects the C_{ant} inventory of the LSW but also the overall accumulation of C_{ant} in the Central Labrador Sea, as demonstrated by the lack of column inventory increase during this second period of the time-series.

Using the same GLODAPv2 data product *Gruber et al.* (2019b) provided global estimates of decadal changes in C_{ant} between the JGOFS/WOCE era (1982-1999) and the GO-SHIP era (2000-2013) based on their eMLR(C^*) approach. From this study, it emerged that the Labrador Sea has experienced an increase of $\sim$ 15 mol m^{-2} over the period 1994-2007, which corresponds to a storage rate of 1.15 mol m^{-2} y^{-1}. Our C_{ant} estimates showed an increase of 19 mol m^{-2} in column inventory based on the difference between these two years which, when divided by the number of years elapsed results in a storage rate of 1.46 mol m^{-2} y^{-1}. On the other hand, if we use the annual estimates and calculate the storage rate as the slope of a linear regression for this time period we find a storage rate of 1.8 mol m^{-2} y^{-1} instead. Both of these approaches assume a steady linear increase in C_{ant} column inventories, which we have shown is unlikely in Labrador Sea where the storage rate can change significantly over short periods of time.

The differences between these accumulation rates can potentially be related to the different methodologies applied to estimate C_{ant} and the different time resolution of the two studies. Whereas we used a tracer-based approach (the TTD method), *Gruber et al.* (2019b) used the eMLR(C^*) method which is based on DIC measurements as well as other oceanographic variables (i.e., temperature, salinity, nutrients etc). As mentioned previously we know that while on a global scale these methods can produce estimates that agree within their uncertainties, disagreements can occur on a regional scale (*Khatiwala et al.*, 2013).

Further, the discrepancies between accumulation rate estimates highlights the importance of sampling frequency and the assumption of steady linear increase of C_{ant}, especially in highly variable regions like the Labrador Sea. While for most of the world oceans sampling at a decadal frequency allows to track the uptake and inventory of anthropogenic carbon (*Sloyan et al.*, 2019), we show here that this is most likely not the case for the Labrador Sea. Depending on the years analyzed, conclusions on the accumulation of anthropogenic carbon in Labrador Sea could be significantly biased depending on the temporal sampling resolution.

3.7 Conclusions

In this study we calculated annual estimates of column inventory and the multi-decadal, average storage rate of anthropogenic carbon in the Labrador Sea using a refined version

of the tracer-based, TTD approach from 1992 to 2016 and extended further to 1986.

We analyzed the validity of two assumptions used conventionally with the TTD approach: the transient tracers' constant saturation (often assumed to be 100%); and constant air-sea CO_2 disequilibrium.

The saturation of CFC-12 and SF_6 over time was reconstructed using a multiple linear regression approach with the rate of increase of the tracers' atmospheric mixing ratios (first derivative of the atmospheric input functions) and maximum mixed layer depth as independent variables. We found that the atmospheric input function was the most important controlling factor of the tracers' saturation. Both CFC-12 and SF_6 were under-saturated in wintertime surface waters throughout the three decades of observations in this region so that a significant bias can be introduced if the TTD method is applied assuming constant 100% saturation. Our refined TTD method, accounting for a time variable saturation of transient tracers, resulted in higher column inventory estimates (18% difference on average) and slower storage rates (17% lower storage rate) than the conventional approach (see Figure 4.6). Accounting for time-varying saturation also led to better agreement between C_{ant} column inventories estimated through CFC-12 and SF_6 compared to when using a constant 100% saturation.

With regard to the second assumption of the TTD method, values of pCO_2 calculated from our measurements showed that, for the time-period of observations, a constant air-sea CO_2 disequilibrium is an adequate assumption in this region.

Hence this study shows the critical importance of assumptions when using indirect, tracer-based approaches to estimate the concentration of C_{ant}. As noted previously (*Wallace*, 1995, 2001; *Waugh et al.*, 2006), CFCs are not an exact analog or proxy for a reactive, high-solubility gas like CO_2, so testing of assumptions and approaches can be key to inferences of C_{ant} behaviour.

With this refined TTD method, we estimated an overall increase of 69 mol m^{-2} in the average column inventory in the Central Labrador Sea between 1986 and 2016 resulting in an average storage rate of 1.8 mol m^{-2} y^{-1} (roughly three times the global average accumulation rate estimated by *Gruber et al.*, 2019b). However, the accumulation rate was not steady over time. A slowdown in the accumulation of anthropogenic carbon was observed between 2003 and 2012 in the Central Labrador Sea (SR = 0.6 mol m^{-2} y^{-1}). Nevertheless, the slowdown was temporary, and an increase in column inventories was

re-established between 2013 to 2016 at a faster pace (SR = 5.2 mol m^{-2} y^{-1}) compared to that observed in the 1990s (SR = 2.2 mol m^{-2} y^{-1}).

These variations in the accumulation rate of C_{ant} were associated with changes in the annual depth of convection and therefore with differences in the mean C_{ant} concentrations in LSW and DIW. In particular, 2003-2012 slow-down in C_{ant} accumulation was associated with shallower LSW formation and a predominance of DIW with lower mean C_{ant} concentrations than LSW, at that time.

The non-steady accumulation of C_{ant} in the Labrador Sea highlights the importance of sampling frequency in highly variable regions like the Labrador Sea. In fact while decadal repeated occupations of oceanographic sections allow the overall increase of the C_{ant} column inventory to be observed (*Gruber et al.*, 2019b; *Sabine et al.*, 2004), important interannual and sub-decadal variability can be missed with this sampling frequency. The arbitrary selection of sampling years could lead to misinterpretation of anthropogenic carbon dynamics in regions like the Labrador Sea, for example when the two years sampled happened to be extremely divergent from the overall, long-term trend. Further with this study we have shown the importance of long time series in testing assumptions of methodologies used to estimate C_{ant}.

Accounting for the whole Labrador Sea (here defined as the region between 52-66°N and 42-65°W), using a gridded bathymetry and assuming that the C_{ant} concentrations measured along the AR7W line are spatially uniform throughout, we estimated the total inventory of anthropogenic carbon stored in this region. This inventory has increased from 0.9 to 1.5 Pg C between 1986 and 2016, meaning that the Labrador Sea, despite representing only 0.1% of the world's ocean volume, stores $\sim$ 1% of the global inventory of C_{ant} (compared to the "best-estimate" inventory of 155 Pg C reported by *Khatiwala et al.* (2013)). This estimated total inventory of C_{ant} for the Labrador Sea is equivalent to $\sim$ 11% of Canada's total CO_2 emissions between 1992 and 2016 (*Environment & Climate Change Canada*, 2020).

CHAPTER 4

NATURAL AND ANTHROPOGENIC CARBON VARIABILITY IN THE CENTRAL LABRADOR SEA[1]

4.1 Abstract

In this Chapter a small subset of the large suite of oceanographic parameters measured along the AR7W transect is used to estimate concentrations and column inventories of anthropogenic carbon (C_{ant}) in the Central Labrador Sea by means of the extended Multiple Linear Regression (eMLR). Thanks to the high temporal resolution (annual observations) of our time series, we also explored the impact of sampling frequency on the estimation of C_{ant} accumulation rates in this region by applying the eMLR with different time intervals.

We found that while an annual temporal resolution of the observations is not necessary to obtain a realistic average annual increase of C_{ant} over one to two decades, misleading accumulation rates could be estimated depending on the starting year selected.

The analysis was further extended into a comparison between the C_{ant} estimates based on the eMLR and the Transit Time Distribution methods (TTD; presented in Chapter 3) as well as to direct observations of Dissolved Inorganic Carbon (DIC) along the transect. The latter comparison was performed in order to understand whether changes in dissolved inorganic

[1]Raimondi, L., Boteler C., Wallace, D. W. R. Natural and anthropogenic carbon Variability in the Central Labrador Sea, *in preparation*.
Author contribution: I conducted the field work, analyzed the carbonate system's samples in 2014, 2015 and 2016 in collaboration with Stephen Punshon from the Bedford Institute of Oceanography. I led the interpretation of the data and put into writing this Chapter. Boteler C. closely collaborated on the development of the statistical tests to compare accumulation rates and performed the statistical analysis. Wallace D. W. R. provided extensive support on the eMLR method.

carbon between 1993 and 2016 were exclusively due to the C_{ant} invasion or if some natural variability of DIC is associated to this signal. While results of C_{ant} accumulation rate from the eMLR method excluded any contribution of natural variability of DIC in its increase, results of the TTD-based accumulation rate contradicted the results of the eMLR.

All three methods to estimate the change in DIC showed that a non-steady accumulation of C_{ant} occurs in this region. Nevertheless, depending on the method applied, very different interpretation of the timing of increase and/or duration of periods of fast and slow rate of increase can be deduced and therefore potentially erroneous conclusions could be drawn on the role of the Labrador Sea in C_{ant} sequestration.

Differences between the inventories obtained based on the eMLR and TTD methods as well as the annual increase of C_{ant} concentrations in Labrador Sea's main water masses, revealed potential bias in the C_{ant} estimates with the TTD method associated with the assumed tracers' saturation history for Denmark Strait Overflow Water (DSOW) and North East Atlantic Deep Water (NEADW). By accounting for a time-lag in the saturation histories of these two water masses (i.e., considering that these water masses have different ventilation histories compared to waters ventilated in the Labrador Sea), we estimated differences in CFC-12 percent saturation compared to the LSW that ranged between -15 and +28% and between -10 and +36% for DSOW and NEADW, respectively. We found that differences in saturations of this magnitude could lead to over- or underestimation of the combined contribution of DSOW and NEADW to the total column inventory of C_{ant} in the order of ~ 4 to ~ 13 mol m^{-2}.

4.2 Introduction

It is estimated that approximately 160 Pg of anthropogenic carbon (C_{ant}) was taken up by the ocean since the beginning of the industrial era until 2010 (*Gruber et al.*, 2019b; *Khatiwala et al.*, 2013; *DeVries*, 2014). Large quantities of this C_{ant} are found at high latitudes, in particular the North West Atlantic has been identified as one of the regions with the highest integrated column inventories of C_{ant} in the world's ocean (*DeVries*, 2014; *Gruber et al.*, 2019b; *Sabine et al.*, 2004).

As highlighted in previous chapters, the Labrador Sea plays a key role in the transport and storage of gas in the North West Atlantic. Wintertime convection represents a direct pathway through which gases can move from the atmosphere and upper water-column into

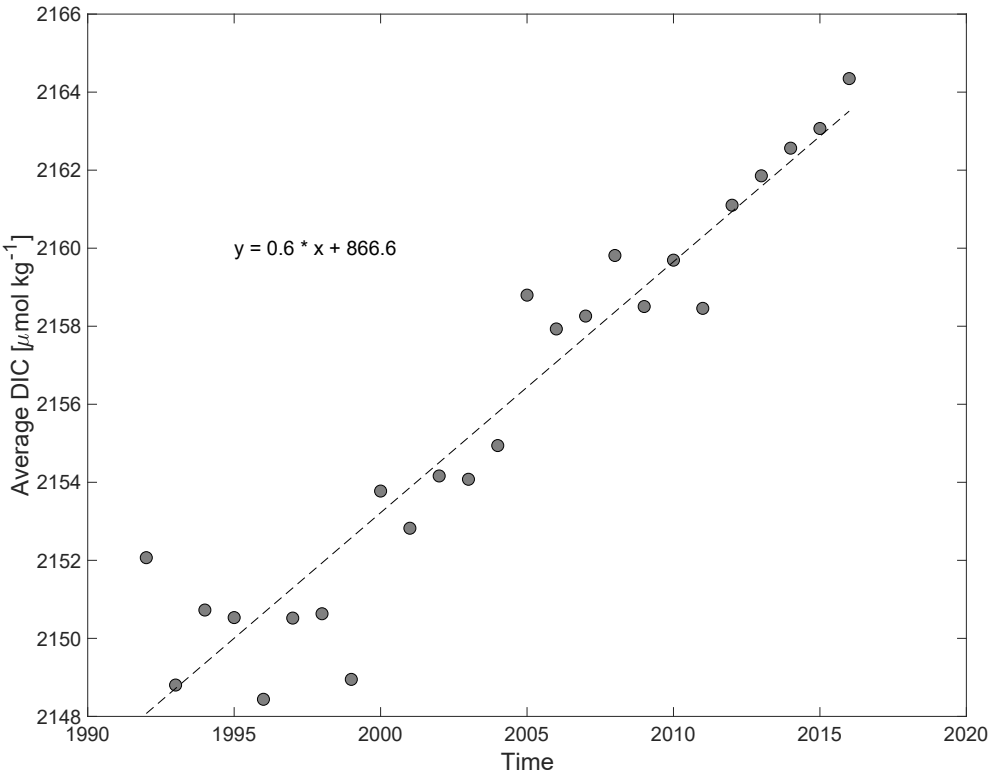

Figure 4.1: Average full water-column concentrations of DIC measured in the Central Labrador Sea between 1992 and 2016 along the AR7W line.

the deep ocean interior. Oxygen and chlorofluorocarbons (CFCs), among other gases, can be found in high concentrations throughout the full water column in this region. Similarly, the anthropogenic carbon signal can be detected down to the bottom of this basin (see Chapter 3 as well as *Rhein et al.*, 2017; *Steinfeldt et al.*, 2009; *Tait et al.*, 2000).

A significant increase in DIC concentrations in the Labrador Sea was observed from measurements performed along the AR7W line since the early 1990s by *Tait et al.* (2000) and is still occurring today. In Figure 4.1 we show that full water-column average DIC concentration in Central Labrador Sea has increased at a pace of 0.6 μmol kg^{-1} y^{-1} between 1992 and 2016. Based on this slope (obtained from a linear regression) we estimated a total average increase of 14.4 μmol kg^{-1} when considering the 24 years of observations. These changes in observed DIC (C_{obs}) concentrations are potentially associated to either increasing C_{ant} concentrations, temporal variability of natural carbon

(C_{nat}) or both. Therefore the signal in DIC can be described as:

$$C_{obs} = C_{ant} + C_{nat} \tag{4.1}$$

and, as a consequence, temporal changes in these pools (difference between two time periods) can be described as:

$$\Delta C_{obs} = \Delta C_{ant} + \Delta C_{nat} \tag{4.2}$$

In Chapter 3 we presented a refined TTD method, which accounts for time-varying saturation of transient tracers (i.e., CFC-12 and SF_6) to estimate the mean age of the water, therefore allowing more accurate estimate of C_{ant} concentrations. Despite accounting for the time-varying saturation of CFC-12 and SF_6, the refined approach does not address the main potential flaw of the TTD method: the C_{ant} signal is derived, indirectly, using gases that have very different solubilities, biogeochemical behaviours, input histories and atmosphere-ocean equilibration times compared to CO_2. For example, unlike CO_2, CFCs and SF_6 are not transported by the biological pump.

Using the TTD method we already inferred that a substantial increase in anthropogenic CO_2 has occurred in the Labrador Sea (with column inventories increasing at a pace of ~ 1.8 mol m^{-2} y^{-1} between 1986 and 2016). Nevertheless, acknowledging the indirect, "proxy"-nature of the TTD method and because of the wide range of ocean parameters measured along the AR7W line (DIC, oxygen and nutrients among others), we can assess the contribution of C_{ant} to the overall DIC increase using alternative approaches based more directly on carbon measurements. In this Chapter we focus on the application of the extended Multiple Linear Regression (or eMLR) method as well as the overall increase of DIC along the AR7W line between 1993 and 2016.

The comparison of the TTD and eMLR methods allows verification of whether estimates of C_{ant} column inventories are the same regardless of the method used. These two methods cannot, however, identify the variability of DIC due to other factors (e.g., increased or decreased biological activity, changes in total alkalinity and therefore buffering capacity). The availability of long term measurements of DIC along AR7W offers the opportunity to elucidate whether changes in DIC are solely due to the anthropogenic CO_2 invasion (assessed with the eMLR and TTD methods) or if there is natural variability captured in

the DIC signal which can be estimated from the difference between DIC inventories and the C_{ant} inventories obtained with either the TTD or eMLR methods (see Equation 4.1).

Therefore the goals of this chapter are: (1) to estimate C_{ant} using the eMLR method; (2) to assess the impact of different sampling intervals in order to guide the planning of future observations in the region (see section 4.3.2); (3) to compare these estimates to those obtained with the TTD method; and (4) to compare the overall DIC increase observed in the Central Labrador Sea with the estimates of C_{ant} accumulation.

4.3 Materials and Method

4.3.1 The Multivariate Time Series method and its Extended Version

The *Multivariate Time Series* method was introduced by *Wallace* (1995) as a means to estimate the temporal increase of C_{ant} based on repeated measurements. The original method was developed to compare historic and recent data collected in a specific region of interest. The method uses a data set of chemical and hydrographic variables of a first occupation to obtain a predictive equation for DIC using a multiple linear regression (MLR). The observed change in the residuals between predicted DIC using the MLR and the measured DIC of a second re-occupation is assumed to provide a measure of the anthropogenic carbon increase between the two sampling years. The method relies on many assumptions, including: 1) a multi-parameter linear model can describe the distribution of DIC within the region analyzed; 2) the natural variability of DIC can be accounted for by its multiple correlation with independent parameters; 3) this underlying relationship between the independent parameters and DIC does not change over the time period between the surveys. In other words, values of the independent parameters can change over time but their underlying correlation with natural variations of DIC does not.

The choice of independent parameters is rather subjective (*Plancherel et al.*, 2013; *Thacker*, 2012) and often dependent on the availability and quality of data. These variables should include information about: the thermodynamics of the carbonate system, the stoichiometry of the biological pump and the characteristics of the CO_2 system in regions with different biogeochemistry.

A later approach, introduced by *Friis et al.* (2005), extends the *Multivariate Time Series* method by developing the predictive equations between DIC and other parameters for two data sets collected at different times in the same location. This method is called

extended Multiple Linear Regression (eMLR). In this case the signal of C_{ant} is represented as the difference between the coefficients of two predictive relations obtained from two occupations of the same (or geographically close) hydrographic transect. To apply the eMLR method, the DIC of the first occupation of the transect or region under study is used to estimate a multiple linear regression model of DIC using independent physical and chemical properties that meet the prerequisites stated above. The form of this regression is as follows:

$$DIC_{MLR,t_1} = a_1 + b_1 x_{1,t_1} + c_1 x_{2,t_1} + d_1 x_{3,t_1} + e_1 x_{4,t_1} + \varepsilon_1 \tag{4.3}$$

where the subscript 1 refers to the first cruise, x_{i,t_1} refers to the independent parameters, letters (a, b, c, d and e) are the regression coefficients and ε_1 are the normally distributed errors. A second multiple linear regression is then calculated for the DIC at time t_2 (i.e., on a second cruise available for the same transect):

$$DIC_{MLR,t_2} = a_2 + b_2 x_{1,t_2} + c_2 x_{2,t_2} + d_2 x_{3,t_2} + e_2 x_{4,t_2} + \varepsilon_2 \tag{4.4}$$

The anthropogenic signal is then obtained as the change in DIC between t_1 and t_2, and calculated by subtracting the coefficients of the two models and applying these new coefficients to variables measured at t_2:

$$\begin{aligned} DIC_{eMLR(t_1,t_2)} =& (a_2 - a_1) + (b_2 - b_1)x_{1,t_2} + (c_2 - c_1)x_{2,t_2} + \\ &+ (d_2 - d_1)x_{3,t_2} + (e_2 - e_1)x_{4,t_2} \end{aligned}$$

where DIC_{eMLR} is interpreted to represent the change in DIC due to C_{ant} invasion between the two surveys (ΔC_{ant}).

The eMLR method, compared to other back-calculation methods, can remove the natural signal of DIC variability by considering changes in biological production and respiration, calcium carbonate production and dissolution, and circulation patterns, but does not rely on specific Redfield ratios and constant CO_2 or tracer disequilibrium with the atmosphere. The eMLR approach minimizes the propagation of measurement error associated with each independent parameter because the error goes into the prediction twice (once for the regression of the first cruise and again for the regression obtained for the second one).

Unlike the TTD method, the eMLR is not dependent on transient tracers and can provide, for example, a better representation of the C_{ant} distribution in deeper waters where there may be no CFC-12 or SF_6, but which may still contain anthropogenic CO_2 (note that this does not occur in the Labrador Sea, where recently ventilated water is present at the bottom of the basin, i.e., DSOW).

Nevertheless, many caveats are also associated with the eMLR method (*Goodkin et al.*, 2011; *Levine et al.*, 2008; *Plancherel et al.*, 2013; *Thacker*, 2012). For instance the assumption of linearity between DIC and other independent parameters is not necessarily valid in surface waters, where the relationships with DIC may not be linear due to seasonally varying air-sea gas exchanges (this problem is often avoided by removing surface data prior to performing the multiple linear regressions). Further, the eMLR method assumes that the independent parameters are not correlated with one another which is often not the case. For instance alkalinity and salinity have a strong linear relationship to one another, therefore collinearity occurs when these are both used as variables to predict DIC.

For most regions of the ocean, the availability of observations of multiple variables in different years and decades is a strong limitation of this method. However, the AR7W is one of the very few locations in the world's ocean where this issue is not encountered.

The wide range of ocean parameters measured along the AR7W line throughout this multi-decadal time series allows for numerous variants of the extended Multiple Linear Regressions technique to be applied using different combinations of independent variables. Nevertheless in this Chapter, we will focus on one of the most simple eMLR which uses only potential temperature (θ), salinity (S) and dissolved oxygen (DO) as independent variables.

4.3.2 eMLR with Variable Time Intervals

Because *in situ* measurements of oceanographic parameters are sparse in space and time, *Goodkin et al.* (2011) investigated the robustness of ΔC_{ant} estimates obtained using the eMLR approach. They compared anthropogenic carbon estimates from ocean model simulation to results obtained with the eMLR approach (using model outputs of DIC and temperature, salinity, dissolved oxygen, phosphate and alkalinity as independent variables). They found that, contrary to what is typically assumed by the eMLR method (and for other C_{ant} estimation methods based on *in situ* observations), changes in climate and ocean chemistry will affect the relationship that DIC has with other oceanographic parameters

which can result in significant bias in the eMLR based estimates when this is applied beyond a time interval of 2 to 4 decades. Therefore the authors suggest that the eMLR should not be applied for observations more than 40 years apart and recommend that field measurements be repeated at a decadal frequency.

While for most of the world ocean the eMLR applied to datasets collected one or two decades apart might provide a good representation of carbon accumulation, in the Labrador Sea decadal sampling frequency might lead to misinterpretation due to the non-steady accumulation of C_{ant} that this region experiences (as shown in Chapter 3). While *Goodkin et al.* (2011) recommended measurements be performed at a decadal frequency based on analysis of model output, the Atlantic Zone Off-Shore Monitoring Program (AZOMP) provides one of the very few datasets where we can use observations to test whether finer time resolution is required in order to understand the variability of carbon.

Here, we apply the eMLR based on θ, S and DO (using only data >300 m depth to remove potential non-linearity between DIC and the independent variables) to obtain an estimate of DIC changes due to C_{ant} invasion using different time intervals between the two regressions. Although observations along the AR7W line are available starting in 1992, these data are excluded because only half of the transect was sampled that year. Therefore only data between 1993 and 2016 are included in this analysis. Because the annual observations extend over 24 years, we performed eMLRs with all possible combinations of starting and ending year, nevertheless in the results section we will focus primarily on comparisons of eMLRs performed with time intervals of 1, 5, 10 and 20 years (Figure 4.2).

For instance when considering the C_{ant} accumulation rate between 1993 and 2003, we could calculate the ΔDIC_{eMLR} using AR7W reoccupations that occurred 1 year apart (i.e., 1993-1994, 1995-1996, 1997-1998...2002-2003), or 5 years apart (i.e., 1993-1998, 1998-2003) and finally 10 years (i.e., 1993-2003) apart. These accumulations can be written as:

$$\begin{aligned} \Delta DIC^{1yr}_{eMLR(1993,2003)} &= DIC_{eMLR(1993,1994)} + DIC_{eMLR(1994,1995)} + \\ &+ DIC_{eMLR(1995,1996)} + ... + DIC_{eMLR(2002,2003)} \end{aligned} \tag{4.5}$$

or

$$\Delta DIC^{5yr}_{eMLR(1993,2003)} = DIC_{eMLR(1993,1998)} + DIC_{eMLR(1998,2003)} \quad (4.6)$$

or

$$\Delta DIC^{10yr}_{eMLR(1993,2003)} = DIC_{eMLR(1993,2003)} \quad (4.7)$$

First the C_{ant} concentration changes were obtained at the sampling locations along the transects using the eMLRs (in this example we will have 13 estimates of DIC_{eMLR}: 10 for the year-to-year time interval, 2 for the 5-year time interval and 1 for the 10-year time interval). We then interpolated the resulting estimates along the AR7W transect, selected the values from the central portion of the basin and calculated the average column inventory for that region (following the routine presented in section 3.4.4). Because these inventories represent only the changes that occurred between re-occupation of the transect, we report the overall increase in column inventory of ΔDIC_{eMLR} as cumulative sum from the reference year (starting year) to the end year of the time period selected. These calculations were performed with all possible starting years for time periods that had a moving window of 5, 10 and 20 years (see schematic in Figure 4.2), which produced a set of time series that we use in our subsequent analysis.

As mentioned earlier, our eMLR time series product allows us to identify what sampling frequency is necessary to obtain an accurate estimate of the C_{ant} accumulation rate. Another issue that can be addressed with the time series, is whether selection of different starting years for the same time intervals can affect our estimates of C_{ant} accumulation rate.

To address these questions we need a statistical test to compare the slopes obtained from different eMLRs. First we selected several time periods (5, 10 and 20 years) and ran eMLRs with different time intervals (year-to-year, 5, 10 and 20 years) within each, which resulted in the slopes presented in Table 4.1. Then we performed two different tests: one to compare the slopes obtained with different time intervals and another to compare slopes for the same time intervals with different starting years.

4.3.2.1 Comparison among eMLRs with Variable Time Intervals

To compare results from the eMLRs with different time intervals we performed linear regressions with interaction terms. For this analysis we defined each time interval as a factor (category) and selected the factor with the largest time interval within a time period

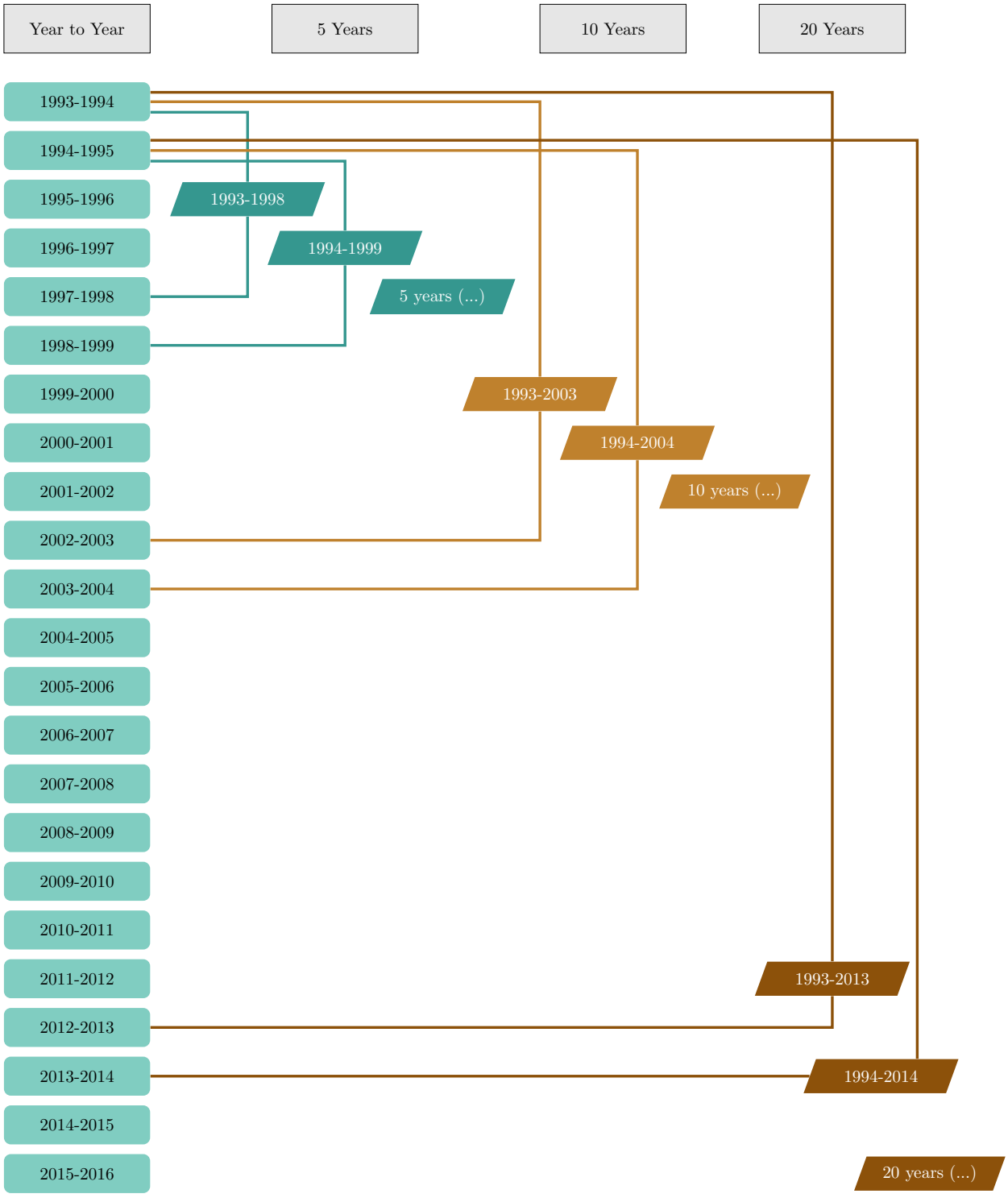

Figure 4.2: Schematic of the different time intervals used to perform the eMLR. Two examples are given for each time interval while the 5, 10 and 20 years (...) indicate that the analysis has been repeated for all possible starting year.

as the reference factor (e.g., for the time period 1993-1998 the 5-year time interval would be the reference factor and the year-to-year time interval would be the comparison factor; for the time period 1993-2003, the 10-year time interval would be the reference factor and the year-to-year and 5-year time intervals would be comparison factors, and so on).

In these linear regressions, the differences between the regression coefficients of the reference (α_i and β_i for intercept and slope, respectively) and comparison factors (α_j and β_j) represent the interaction terms ($\alpha_{i:j}$ and $\beta_{i:j}$). Since the goal is to determine whether using eMLRs with different time intervals leads to a different accumulation rate of C_{ant} within the time period selected, we focus on comparison of slopes and disregard the differences in intercepts (though, as shown in Equation 4.8, the regressions were performed including intercepts). The difference in average annual slope (storage rate or accumulation rate) between the 20-year and 10-year time intervals would be reported as $\beta_{20:10}$, while the difference in average annual slope between the 20-year and the year-to-year time intervals would be reported as $\beta_{20:1}$ (see the illustration of slope differences in Figure 4.3). Using a t-test, we verify whether the difference between slopes of each comparison factor and the reference factor is significantly different than zero (this was assessed with the p-value for the interaction factor at a significance level of α = 0.05, with the p-value taken from the t-distribution with N-p degrees of freedom, where N is the number of time series points and p is the number of parameters estimated). The equation for these linear regressions with interaction terms would be in the form of:

$$\begin{aligned} Cumulative \\ \Delta DIC_{eMLR} \end{aligned} = \alpha_{20} + \beta_{20}t + \alpha_{20:10} + \beta_{20:10}t + \alpha_{20:5} + \beta_{20:5}t + \alpha_{20:1} + \beta_{20:1}t + \epsilon \tag{4.8}$$

where α represents the intercepts, β represents the slopes and the subscripts with colon represent the difference in coefficients between the different factors (i.e., interaction terms).

It is important to highlight that some regressions were performed on time series that only included two data points (i.e., the reference factors for each time period). While it would not be possible to verify any statistical robustness on these time series individually (the degrees of freedom are = 0 and the standard error of regression cannot be assessed, therefore precluding the feasibility of its individual t-test), this is possible when included in the interaction analysis. In fact, whereas the slopes and intercepts are assessed for each

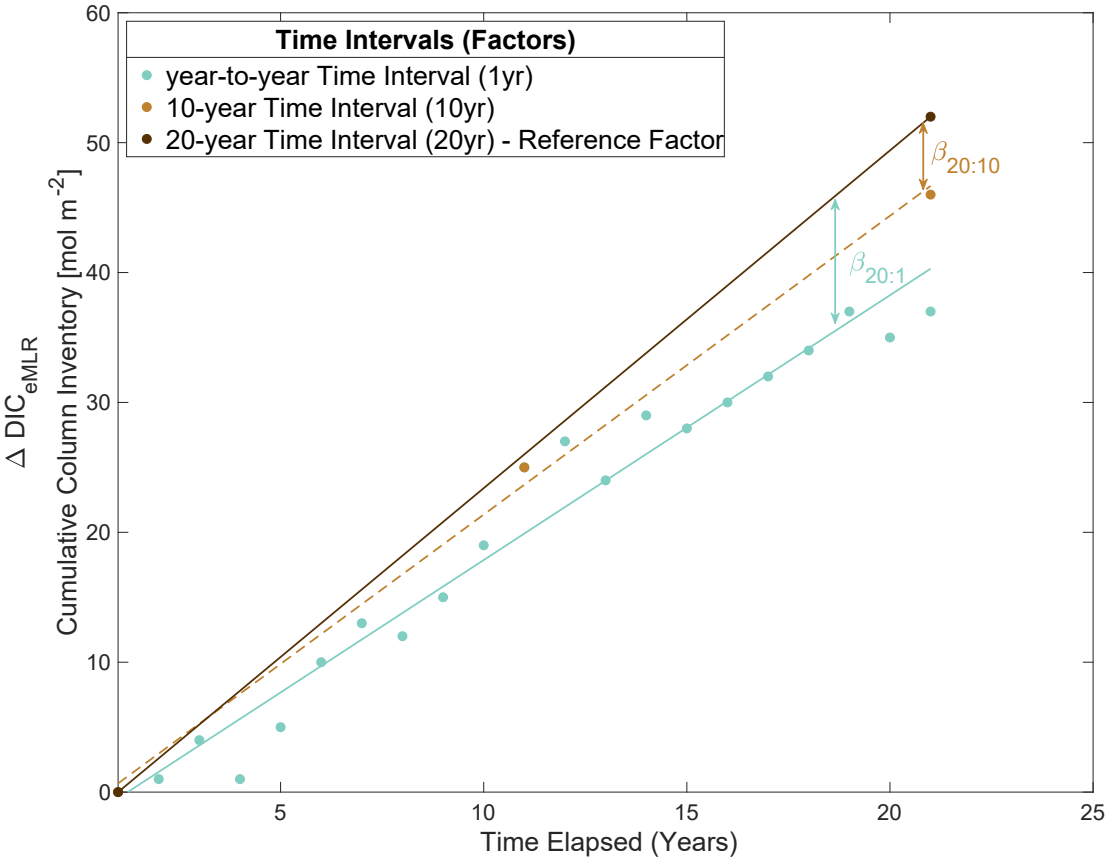

Figure 4.3: Illustration of the method used to compare the eMLRs with different time intervals. In the graphic the time period selected is 20 years therefore the reference factor is the eMLR performed with 20-year time interval and the comparisons factors are the year-to-year and the 10-year time intervals. Note that in this plot (and in the following ones), only regressions of the reference factor and those statistically different from it are drawn as solid lines. If no difference is found the regression lines are drawn with a dashed line.

individual factor, the standard error calculation is based on all data points regardless of their category. While this solves the problem of degrees of freedom in the comparison of different time intervals (i.e., comparison of the slopes reported on each row of Table 4.1), it does not apply in the context of comparison of the same time intervals with different starting years (i.e., comparisons within each sub-column in Table 4.1).

4.3.2.2 Comparisons Among eMLRs with the same Time Intervals but Different Starting Year

When comparing eMLRs with the same time interval but different starting years, all of the slopes will be obtained based on only two data points. A further complication for this second comparison lies in the selection of the reference factor.

With these complications in mind, we opted to use a different approach for this second comparison. We make use of independent t-tests between the slopes calculated for the same time interval but different starting years. In this case we selected the regressions with highest, lowest and median values of the slope as three possible reference factors (an exception is the 20-year time interval for which four slopes were available and therefore we used only the highest and lowest slopes). In these tests the null hypothesis (H_0) is that each slope obtained using eMLRs with the same time interval but different starting years are equal to the reference factors. The alternative hypothesis (H_a) is that comparison and reference slopes are significantly different from each other.

Adapting a statistical test presented in *Andrade and Estévez-Pérez* (2014) to this application, we first assessed whether a simple t-test or a Welch t-test should be used. To compare two slopes with a simple t-test using a pooled variance, the regression variances (or squared standard errors of regression or mean squared error; MSE) must be equal and therefore belong to the same population. If this is not true a Welch t-test should be used instead. Therefore as a first step we calculated the regression variances for the reference and comparison factors. In our case the slopes were calculated from two data points, each of which was obtained from an eMLR that, in turn, involved two linear regressions. Therefore when calculating our regression variances we need to account for the four regressions used to perform the two eMLR (one eMLR for the reference and one for the comparison factor). The regression variances for each of the four regressions were obtained with the

following equation:

$$s_i^2 = MSE_i = \frac{SSE_i}{df_i} = \frac{\sum(\epsilon_i^2)}{n_i - 4} \tag{4.9}$$

where i represents each one of the regressions used to perform the two eMLRs and ϵ_i (also written as SSE_i) represents their sum of squares of errors. For each eMLR, the combination of squared standard errors for the two regressions is indicated by s_{ij}^2 and is calculated with the following equation:

$$s_{ij}^2 = \frac{1}{\Delta t^2}(s_i^2 + s_j^2) = \frac{SSE_i}{\Delta t^2(n_i - 4)} + \frac{SSE_j}{\Delta t^2(n_j - 4)} \tag{4.10}$$

where df are the degrees of freedom calculated as the number of observations (of θ, S and DO used to perform the original regressions of the eMLR) minus the number of regression parameters estimated, and Δt is the time interval implied in the eMLR (5, 10, 20 years). The same equations were used to calculate the regression variances for the reference factor (these would be $s_{ref,i}^2$ and $s_{ref,j}^2$ and their combination $s_{ref,ij}^2$).

We could assume that the datasets used to obtain the reference and comparison factors have a similar variability (i.e., the regression variances are the same) and perform a simple t-test, but instead we use a statistical test to objectively assess whether the regression variances belong to the same population or not (i.e., if we should perform a t-test or a Welch t-test). Therefore as a second step we compared the regression variance of the reference factor ($s_{ref,ij}^2$) to that of the comparison factor (s_{ij}^2) with an F-test statistic in the form of:

$$F = \frac{s_{ij}^2}{s_{ref,ij}^2} \tag{4.11}$$

The H_0 for this test is that $s_{ref,ij}^2$=s_{ij}^2, while the H_a is that these regression variances are different. If the H_0 is rejected then a Welch t-test should be used in place of a t-test. The majority of our comparisons showed that $s_{ref,ij}^2$ and s_{ij}^2 belonged to different populations, therefore we rejected the null-hypothesis and used a Welch t-test for all our comparisons using the following equation (modified from Equation 8 in *Andrade and Estévez-Pérez*

(2014)):

$$t^w = \frac{\beta_{ref,ij} - \beta_{ij}}{\sqrt{\frac{SSE_{ref,i}}{\Delta t^2 (n_{ref,i} - p) SSR_{ref,i}} + \frac{SSE_{ref,j}}{\Delta t^2 (n_{ref,j} - p) SSR_{ref,j}} + \frac{SSE_i}{\Delta t^2 (n_i - p) SSR_i} + \frac{SSE_j}{\Delta t^2 (n_j - p) SSR_j}}} \tag{4.12}$$

where $\beta_{ref,ij}$ and β_{ij} represent the slope of the reference and comparison factors, respectively. The terms $n_{ref,i}$ and $n_{ref,j}$ represent the number of θ, S and DO observations that were used in both of the original regressions to perform the eMLRs for the reference factor while n_i and n_j are the numbers of observations for the comparison factors. Finally SSR represent the sum of square of regressions and can be expressed as:

$$SSR = SST - SSE = \sum_k (y_k - \bar{y})^2 - \sum_k (\epsilon_k^2) \tag{4.13}$$

where SST is the squared deviations of DIC observations and SSE is the squared errors of regression. The test statistic, t^w, has a t-distribution with degrees of freedom, ν, calculated as:

$$\nu = \frac{A_{ref,i} + A_{ref,j} + A_i + A_j}{\frac{A_{ref,i}^2}{n_{ref,i} - p} + \frac{A_{ref,j}^2}{n_{ref,j} - p} + \frac{A_i^2}{n_i - p} + \frac{A_j^2}{n_j - p}} \tag{4.14}$$

where $A = \frac{SSE}{\Delta t^2 (n-p) SSR}$ and p represents the number of parameters estimated in the initial regressions (i.e., p = 4). The corresponding p-value was calculated and assessed at a significance level of α^* rather than α. In fact when multiple comparisons are performed on the same set of data, it is more likely to incur Type I errors (false positives, i.e., we think the slopes are different when in reality they aren't), therefore a correction of the α is necessary. We here applied a Bonferroni correction as follows:

$$\alpha^* = \frac{\alpha}{M} \tag{4.15}$$

where α = 0.05 and M represents the number of comparisons performed. Note that this correction ensures that we lower the occurance of Type I errors but also increases the chances of having Type II errors (false negatives, i.e., we think the slopes are the same when in fact they are different).

4.3.3 Comparison of ΔDIC Estimates Based on TTD, eMLR and Observed DIC

The analysis of regression with interaction terms was also used to compare results of ΔDIC based on the two C_{ant} estimation methods (TTD and eMLR) to those obtained from the overall increase of DIC based on direct observation (DIC_{obs}). For this analysis we used the cumulative ΔDIC_{eMLR} assessed with the year-to-year time interval. Unlike the TTD, the eMLR method provides estimates of the change in DIC due to anthropogenic carbon rather than its absolute concentration. Therefore, in order to compare results from these two methods to the overall increase in DIC from observations, we calculated year-to-year changes in C_{ant} column inventories (mol m^{-2}) based on the TTD method as well as the year-to-year change of the observed DIC. These values of ΔDIC based on the TTD method and DIC observations are identified as ΔDIC_{TTD} and ΔDIC_{obs}, respectively and, like the ΔDIC_{eMLR} column inventories, are reported as cumulative sums (see Equation 4.16 and 4.17). All values were calculated by first removing the top 300 m of the water column in order to avoid seasonal effects.

The TTD method was applied using CFC-12 as a tracer, and because of lack of observations or low quality of the data during some years, the time series of C_{ant} column inventories has some gaps compared to the DIC, temperature, salinity and oxygen time series used to assess ΔDIC_{obs} and ΔDIC_{eMLR}. To solve the lack of CFC-12 data, for each missing year we substituted an average value of C_{ant} column inventory based on the inventories of the two previous and two following years. Once the time series was completed as described, the change in DIC assessed with the TTD estimates (hereafter referred to as cumulative column inventory; ΔDIC_{TTD}) was calculated as a cumulative sum that can be simplified in the form of:

$$\Delta DIC_{(TTD)_n} = C_{ant(TTD)_n} - C_{ant(TTD)_{1993}} \tag{4.16}$$

where $C_{ant(TTD)n}$ represents the annual anthropogenic carbon column inventory (in mol m^{-2}) as estimated with the TTD at a given year in the time series (from 1994 to 2016). Similarly the cumulative column inventory of DIC_{obs} (ΔDIC_{obs}) was calculated as:

$$\Delta DIC_{(obs)_n} = DIC_{(obs)_n} - DIC_{(obs)_{1993}} \tag{4.17}$$

where $DIC_{(obs)n}$ represents the annual column inventory of DIC (in mol m^{-2}) assessed directly from the DIC observations at a given year in the time series. For the interaction term analysis on these three time series we have selected the ΔDIC_{obs} as our reference factor.

4.4 Results

In order to show the effects of the choice of time interval on the eMLR analysis, we present results separately: first the comparisons of different time intervals within each time period, followed by the comparison of same time intervals with different starting years.

4.4.1 Effect of Different Time-Intervals

In Table 4.1 we report the slopes of linear regressions for the cumulative ΔDIC_{eMLR} obtained for different time periods. Each time period is defined by a starting year (rows) and an ending year (columns). The different coloured sub-columns represent the slopes obtained using different time intervals to run the eMLR (year-to-year, 5-year, 10-year and 20-year). The white numbers represent the slopes of reference factors.

We were able to use all three time periods (5, 10 and 20 years) only for our comparisons of time intervals with starting years between 1993 and 1996. For all other starting years we could only assess two or one of the time periods (5 and 10 years).

When slopes obtained from different time intervals within the same time period were compared (i.e., comparison among the sub-columns of each main column of Table 4.1), we found that most time intervals produce slopes that are within $\pm$ 0.6 mol m^{-2} y^{-1} from the reference slope. Even though a few time intervals displayed larger differences from the reference slope (with a maximum difference of 1.2 mol m^{-2} y^{-1} for the 2011-2016 time period), the interaction term analysis revealed that none of the slopes of the comparison factors are significantly different from the reference factor.

4.4.2 Effect of Different Starting Years

Table 4.1 also allows comparison of results obtained with the same time interval but different starting years. Slopes obtained with 5-year time interval can be found along the second sub-column, while results for the 10-year and 20-year time intervals are reported along the fifth and ninth sub-columns, respectively.

Table 4.1: Slopes of linear regressions of cumulative ΔDIC_{eMLR} using eMLRs with different time intervals. Reference factors are represented with white font. Note that the units of the slopes are in mol m^{-2} y^{-1}.

Starting Year \ Ending Year	1998	2003	2013
1993	0.40 0.46	1.53 1.40 1.47	2.10 2.18 1.94 1.85
1994	1999: 1.37 1.29	2004: 1.69 1.72 1.55	2014: 2.15 2.25 2.14 1.85
1995	2000: 2.94 2.52	2005: 2.26 2.38 2.42	2015: 2.21 2.14 2.21 2.04
1996	2001: 2.89 2.71	2006: 2.67 3.12 3.07	2016: 2.25 2.49 2.63 2.55
1997	2002: 1.69 1.60	2007: 2.57 2.59 2.48	
1998	2003: 1.47 2.33	2008: 2.73 2.95 2.87	
1999	2004: 1.06 2.16	2009: 2.51 2.37 2.44	
2000	2005: 2.45 2.24	2010: 2.58 1.94 2.13	
2001	2006: 4.07 3.54	2011: 2.55 2.01 1.98	
2002	2007: 3.89 3.58	2012: 2.32 2.34 2.60	
2003	2008: 3.68 3.57	2013: 1.99 2.57 2.42	
2004	2009: 2.45 2.58	2014: 1.77 2.72 2.73	
2005	2010: 1.36 1.63	2015: 1.51 1.99 2.01	
2006	2011: 0.77 0.48	2016: 1.64 2.10 2.19	
2007	2012: 1.09 1.10		
2008	2013: 1.15 1.57		
2009	2014: 2.03 2.85		
2010	2015: 2.05 2.35		
2011	2016: 2.57 3.73		

Time Intervals: 1yr 5yr 10yr 20yr

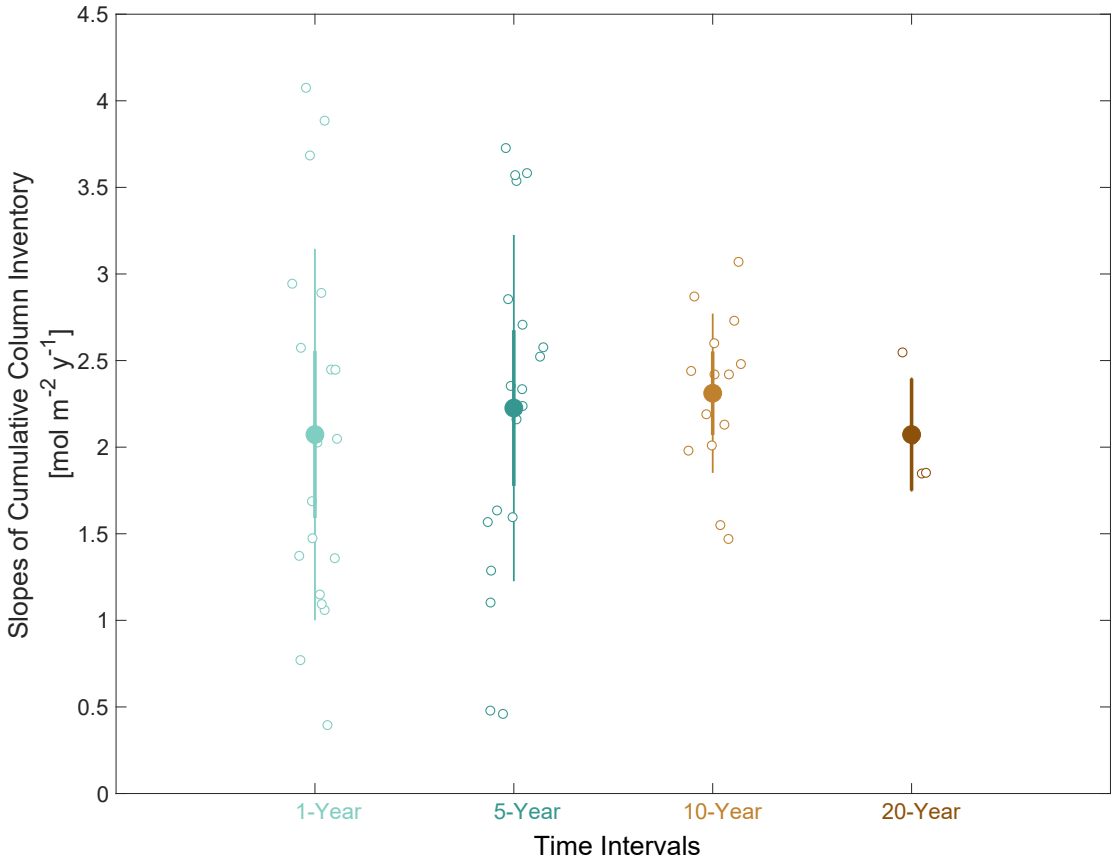

Figure 4.4: Slopes of cumulative column inventory of ΔDIC_{eMLR} obtained with different time intervals. We report the mean slopes (solid dots), standard errors of the mean (thick lines) and standard deviations (thin lines) for each time interval. The empty dots represent the slope obtained for each regression (values reported in Table 4.1).

While the values of the slopes are quite similar for the 20-year time interval regardless of the starting years (slopes ranging between 1.85 and 2.55 mol m^{-2} y^{-1}), this is not the case with the 5- and 10-year time intervals. In particular, whereas the 10-year time interval displayed a range of annual average increase of ΔDIC_{eMLR} between 1.47 and 3.07 mol m^{-2} y^{-1}, the 5-year time interval gave the widest range of values with slopes ranging between 0.46 and 3.58 mol m^{-2} y^{-1}. The differences between the time intervals are illustrated in Figure 4.4, where it is noticeable that the scatter of the values of slope for the year-to-year and 5-year estimates (standard deviation of $\sim \pm 1$) is much larger than the 20-year ones (standard deviation of $\sim \pm 0.3$).

The Welch t-tests revealed that, regardless of the choice of reference factor, significantly different slopes are obtained when the same time interval is applied with different starting

years although there were a few exceptions (result of this analysis can be found in Appendix C). For instance there is no significant difference between two of the four slopes obtained with the 20-year time interval (1993-2013 and 1994-2014; see Table C2), and no differences were found between slopes obtained with the 10-year time intervals starting in 1993 and 1994 (Table C3). A few additional exceptions were found for the 5-year time interval (see Table C1) but overall the majority of comparisons showed that, regardless of the time interval considered, significantly different slopes and therefore C_{ant} accumulation rates are obtained when the eMLR is performed with different starting years.

4.4.3 ΔDIC assessed with TTD, eMLR and DIC Observations

The cumulative ΔDIC column inventories assessed with the TTD and eMLR methods are represented in Figure 4.5 together with the changes from direct DIC observations (see Section 4.3.3). For reference, in Figure C.1 of Appendix C, we also report the year-to-year increase (not cumulative) of ΔDIC column inventories obtained from the three methods.

We found that, over the entire time series, the cumulative column inventories of ΔDIC increased by 50, 44 and 42 mol m^{-2} when assessed with ΔDIC_{obs}, ΔDIC_{eMLR} and ΔDIC_{TTD}, respectively. Whereas the rate of increase of ΔDIC_{eMLR} is comparable to that of ΔDIC_{obs} (accumulation rates of 2.3 and 2.1 mol m^{-2} y^{-1} for ΔDIC_{obs} and ΔDIC_{eMLR}, respectively), the slope of the regression obtained for the ΔDIC_{TTD} time series (1.4 mol m^{-2} y^{-1}) is statistically different than the reference factor.

Note that starting in early 2000's and throughout the period of C_{ant} accumulation slowdown identified in Chapter 3 (ending in 2012), the ΔDIC_{TTD} time series differs significantly from the other two methods and shows values of column inventories increasing at a slower rate compared to ΔDIC_{eMLR} and ΔDIC_{obs} (7-15 and 8-20 mol m^{-2} lower than ΔDIC_{eMLR} and ΔDIC_{obs}, respectively). Between 2013 and 2016 the differences between the ΔDIC_{TTD} and the other two estimates of ΔDIC start decreasing and the three time series converge again by 2016.

4.5 Discussion

4.5.1 Effects of Different ΔDIC Estimation Methods with all possible Starting Years and Time Intervals

To further illustrate the implications of using different starting years as well as of applying different C_{ant} estimation methods, we have calculated slopes of linear regressions

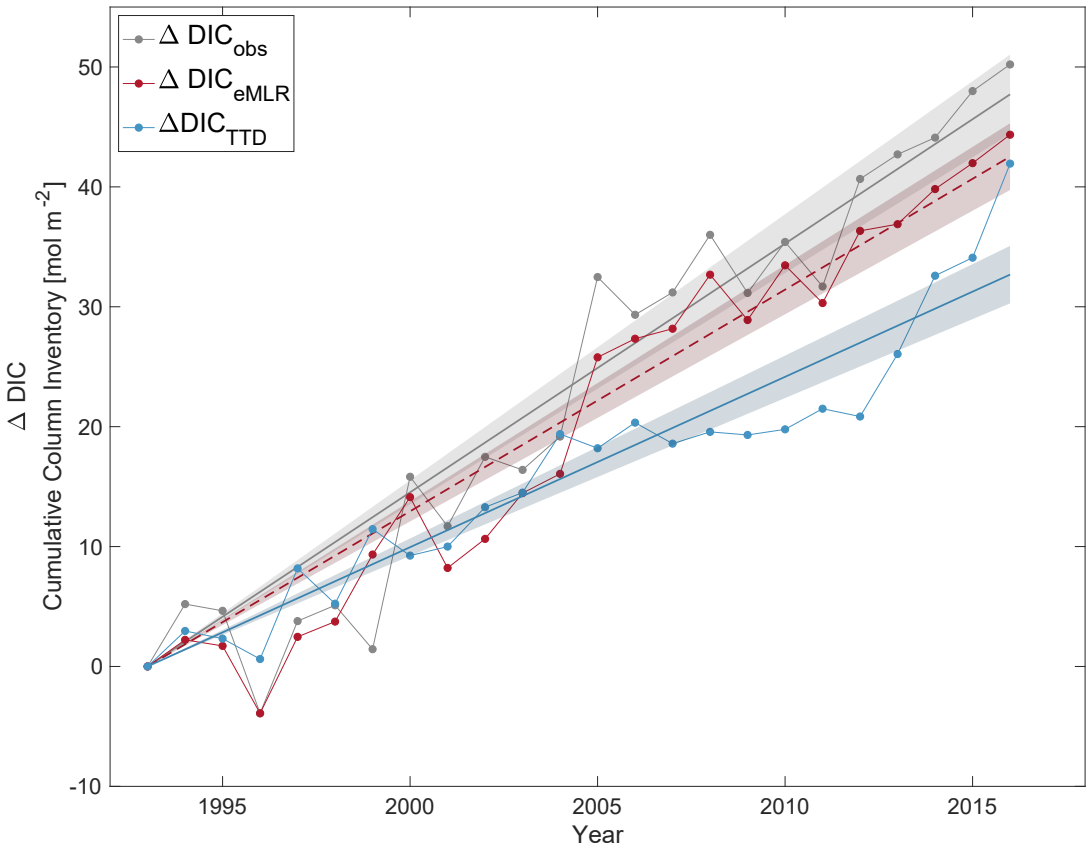

Figure 4.5: Cumulative column inventories of ΔDIC_{obs} (grey dots), ΔDIC_{eMLR} (red dots) and ΔDIC_{TTD} (blue dots). The lines and the shaded areas represent the linear regression models for each time series and their 95% confidence intervals, respectively. Notice that the regression lines for ΔDIC_{obs} and ΔDIC_{TTD} are solid because they are the reference factor and the comparison factor with statistically different slope, respectively. The ΔDIC_{eMLR} line is dashed because no statistical difference in slope is found compared to ΔDIC_{obs}.

between all starting and ending years (between 1993 and 2015) with the eMLR, TTD methods as well as with the observed DIC. These estimated rates of increase, which are presented in Figure 4.6, are calculated using only the column inventories of the starting and ending years and with data >300 m depth (for a better comparison with the eMLR approach).

Overall it is noticeable that depending on the starting year and time interval selected, different estimates of ΔDIC rate of increase are obtained, regardless of the method used. These differences in estimated accumulation rates can translate into contradictory conclusions on the role of the Labrador Sea depending on the years of observations considered.

Whereas the accumulation rates assessed with the TTD method are generally lower compared to those obtained with the eMLR and observed DIC (i.e., there is more blue than red in the TTD matrix), we still found some similarities among the three estimates of ΔDIC. For instance, all three methods display lower rates of increase of DIC in the early period of the time series (between 1990's and early 2000's) and for the late 2000's and early 2010's, nevertheless this latter period of slow increase in DIC assessed with the TTD method is more prolonged in time compared to other methods. A further similarity is that all three methods identified intermediate to fast rates of increase (slopes ranging between 2 to 6 mol m^{-2} y^{-1}) toward the very end of the time series.

There were also some clear discrepancies between the TTD method and the DIC_{obs}- and DIC_{eMLR}-based estimates. For instance, whereas fast rates of increase in DIC were obtained for periods starting in early 2000's and ending in late 2000's when using DIC_{obs} and eMLR method (slopes between 3-6 mol m^{-2} y^{-1}), the TTD method only produced fast rates for a few time periods but in general displayed intermediate to low rates of increase at this time (slopes between 1-2 mol m^{-2} y^{-1}). Further all the slopes obtained with starting years between 1993 and 2006 and ending years between 2010 and 2016 have overall slower rates of increase with the TTD method compared to the other DIC-based methods.

All three methods used to estimate ΔDIC showed that the rate of increase of C_{ant} is not constant over time. Instead there are alternating periods of fast and slow rate of increase of C_{ant} column inventories, which confirmed that the Labrador Sea is characterized by a non-steady accumulation of C_{ant}. Nevertheless the application of one method over the other could lead to different interpretation on the time of arise and/or duration of periods of fast and slow rates of increase.

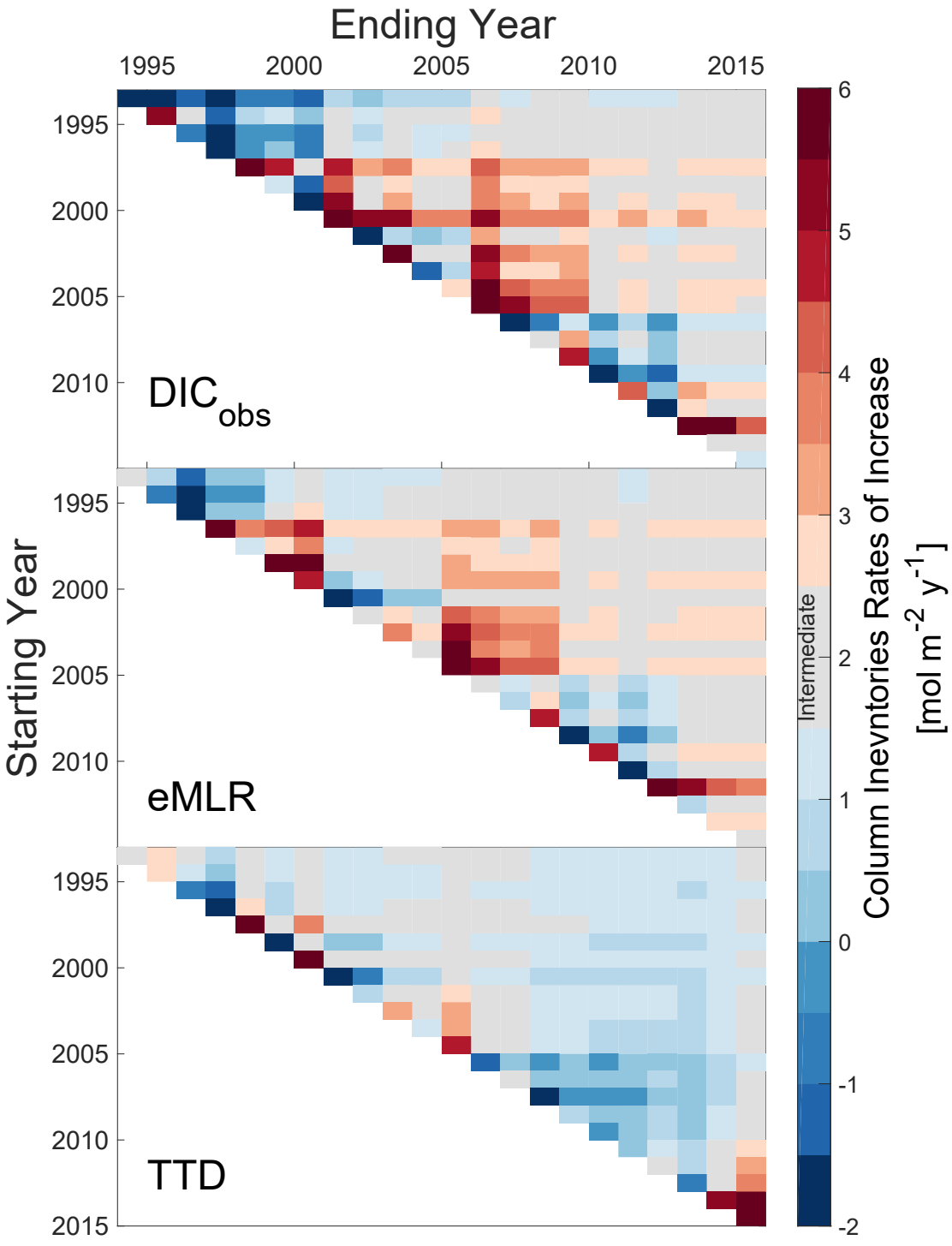

Figure 4.6: Matrices of column inventories' rates of increase (slopes between the starting and ending years) obtained from the DIC observations (top panel, DIC_{obs}), the eMLR method (middle panel) and the TTD method (bottom panel). Values of slopes are reported in mol m^{-2} y^{-1}, with grey, red and blue colours representing intermediate (value of 2 $\pm$ 0.5 mol m^{-2} y^{-1}), high and low rates of increase, respectively.

Gruber et al. (2019b) inferred the C_{ant} rate of increase between 1994 and 2007 based on observations as well as estimating the expected change since 1994 in storage assuming "transient steady state". The latter concept implies that after a long period of time the concentration of C_{ant} at any depth in the water column increases at a rate that is proportional to the increase in the surface layer. Comparison of predicted (based on transient steady state) and observed C_{ant} rates of increase showed that whereas these agree on a global scale, significant differences can be found on a regional basis. In particular *Gruber et al.* (2019b) showed that, between 1994 and 2007, the North West Atlantic displayed a change in inventory 20% lower than predicted assuming transient steady state. The anomalously low inventory change was attributed to changes in ocean circulation, although only temporary. We here show that despite the slowdown in C_{ant} accumulation rate during the 2000's (shown by all three methods used in this work) the Labrador Sea displayed a fast rate of increase in the 2010's as a result of renewed deep formation of LSW (see Chapter 3). These findings further support that ocean circulation plays a crucial role in the sequestration of C_{ant}, meaning that future changes in LSW formation will most likely affect the role of the Labrador Sea in storing C_{ant}.

4.5.2 Estimating Natural DIC

As reported in *Clement and Gruber* (2018), and as shown in Equation 4.2, overall changes in observed DIC between reoccupations of hydrographic transects (ΔC_{obs} or ΔDIC_{obs}) represent changes in both natural (ΔC_{nat} or ΔDIC_{nat}) and anthropogenic carbon (ΔC_{ant}). Natural changes in DIC occur due to climate and ocean variability that affect temperature, biology and circulation. On the other hand, anthropogenic changes are a consequence of the increase in atmospheric pCO_2.

In a steady state scenario (i.e., in absence of changes to the natural DIC over a given period of time) during a period with increasing atmospheric pCO_2, changes in observed DIC would be solely due to the oceanic uptake of C_{ant} (i.e., $\Delta DIC_{obs} = \Delta C_{ant}$). In this scenario, the C_{ant} behaves like a passive tracer (like CFCs) and its uptake is the result of air-sea disequilibrium and mixing. Nevertheless, in the real ocean the CO_2 system (as well as physical properties) is not necessarily in steady state and it is therefore possible to separate C_{ant} into both a steady state (SS) and a non-steady state (NSS) components.

$$\Delta C_{ant} = \Delta C_{ant(SS)} + \Delta C_{ant(NSS)} \tag{4.18}$$

where $\Delta C_{ant(SS)}$ represents the change in anthropogenic carbon due to rising atmospheric CO_2 and in absence of circulation and biological changes, and $\Delta C_{ant(NSS)}$ is the C_{ant} component that is modified by changes in circulation and biology due to climate change (e.g., temperature effects on CO_2 solubility and increasing stratification).

The temporal signal of the observed DIC is further affected by changes in circulation due to natural variability (i.e., decadal) therefore we separate the natural carbon into a SS and a NSS component as well:

$$\Delta DIC_{nat} = \Delta DIC_{nat(SS)} + \Delta DIC_{nat(NSS)} \tag{4.19}$$

By definition, in a steady state scenario there are no changes to the natural DIC dynamics (i.e., $\Delta DIC_{nat(SS)} = 0$), meaning that the ΔDIC_{nat} is exclusively driven by NSS changes that occur as a result of events such as El-Niño-Southern Oscillation. [2]

The availability of both the observed DIC and the two estimates of C_{ant} obtained in this thesis can allow us to identify whether changes in the pool of non-steady state natural DIC occurred during the years of observations in the Central Labrador Sea. We here identify ΔDIC_{nat} simply as the difference between the observed change in DIC (ΔDIC_{obs}) and the estimated change in C_{ant} based on both the TTD and eMLR methods (ΔDIC_{TTD} and ΔDIC_{eMLR}).

In Figure 4.7, where we report the ΔDIC_{nat}, it is noticeable that whereas the estimated changes in natural DIC assessed with both methods agree until early 2000's, different estimates were obtained starting in 2005 and until the end of the time series, when both C_{ant} estimation methods again produced similar results of ΔDIC_{nat}. The use of the eMLR-based C_{ant} column inventories resulted in ΔDIC_{nat} of 2.7 ± 3.0 mol m^{-2} on average. Whereas, use of TTD-based estimates of C_{ant} resulted in ΔDIC_{nat} of 6.7 ± 7.9 mol m^{-2} on average. In other words, whereas the use of the eMLR implies no trend in the ΔDIC_{nat}, the TTD-based estimates suggest a significant increase in ΔDIC_{nat} over time at a pace of ~ 0.9 mol m^{-2} y^{-1} ($R^2 = 0.6$).

[2] It is worth noting that when a correction is applied in back-calculation methods to remove the signal of natural DIC, both of these non-steady state signals ($\Delta DIC_{nat(NSS)}$ and $\Delta C_{ant(NSS)}$) are not accounted for, therefore only the steady state C_{ant} inventories are estimated by these methods.

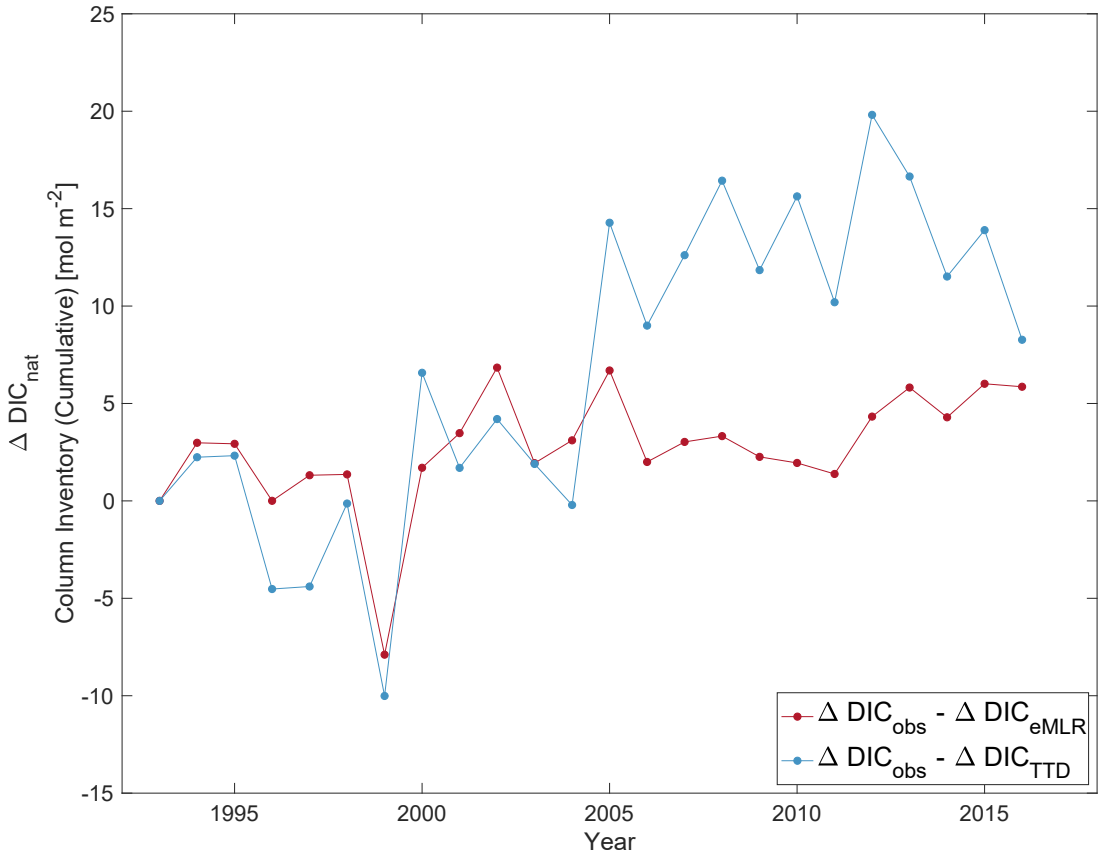

Figure 4.7: Changes in the natural component of DIC (ΔDIC$_{\text{nat}}$) estimated as the difference between the observed ΔDIC$_{\text{obs}}$ and the ΔC$_{\text{ant}}$ estimates based on the TTD and eMLR methods.

4.5.3 Possible Reconciliation of the Anthropogenic Carbon Estimates from Different Methods

In Figure 4.5 we showed there are significant differences between the time-histories of the column inventories of ΔDIC_{TTD} and those of ΔDIC obtained with the DIC observations and the eMLR method. These differences resulted in different conclusions on the role of ΔDIC_{nat} in the overall increase of DIC_{obs} (Figure 4.7). To explore possible causes of this divergence of estimates, we looked at the temporal variability of ΔDIC_{obs}, ΔDIC_{eMLR} and ΔDIC_{TTD} in the Labrador Sea's four major water masses: LSW, DIW, NEADW and DSOW. These water masses were defined as described in section 3.6.1 and B.2.2, and in Figure 4.8 we report their cumulative year-to-year change in ΔDIC average concentrations obtained with the three methods (ΔDIC_{obs} panel a, ΔDIC_{eMLR} panel b and ΔDIC_{TTD} in panel c).

It is noticeable that, although there is less noise in the eMLR-based estimates compared to the DIC_{obs}, both show similar concentrations changes among the four water masses (with all water masses concentrations ranging between -5 and 14 μmol kg^{-1}) as well as similar rates of increase (all water masses showed rates of increase of $\sim$ 0.65 and 0.60 μmol kg^{-1} y^{-1} for DIC_{obs} and DIC_{eMLR}, respectively). On the other hand the TTD method resulted in more obvious distinction between the water masses with wider concentration ranges (e.g., 0-19 μmol kg^{-1} for LSW compared to 0-11 μmol kg^{-1} for DSOW) as well as wider range of rates of increase (e.g., 0.78 μmol kg^{-1} y^{-2} for LSW compared to 0.34 for DSOW). At the time when the column inventories of ΔDIC_{TTD} diverge from the ΔDIC_{eMLR} and ΔDIC_{obs}, concentrations of ΔDIC assessed through the TTD method were increasing in LSW and DIW, but remained constant in the DSOW and NEADW.

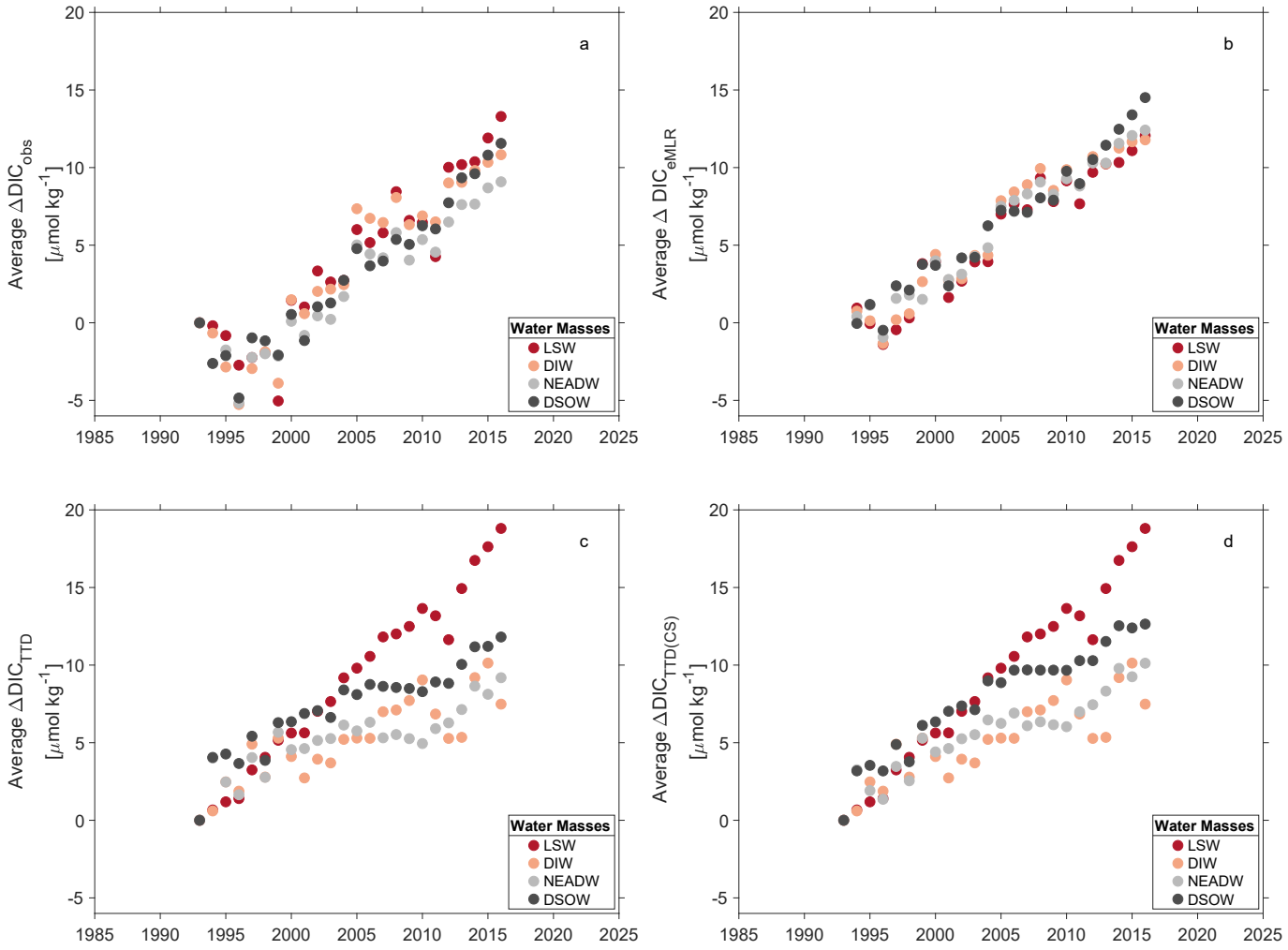

Figure 4.8: Cumulative annual average increase of ΔDIC_{obs} (panel a), ΔDIC_{eMLR} (panel b) and ΔDIC_{TTD} (panel c) concentrations in four major water masses of Labrador Sea. In panel d we report results of ΔDIC_{TTD} obtained using time-varying saturation for LSW and DIW but constant 100% for DSOW and NEADW. Note that in each panel the first datapoint of the time series of each water mass is a value of zero for 1993 as we are looking at the change in concentration from that year onward.

The reasons for the divergence of the "proxy" estimates based on CFCs tracers from the DIC-based approaches after 2004 are not clear. As noted, the different approaches converge on similar values for C_{ant} column inventories by the end of the time-series, however the trajectories vary with implications for estimates of natural carbon variability (see Figure 4.7). One possibility for the divergence could lie with the initial saturation assumption required with the TTD approach.

As explained in Chapter 3 we reconstructed the tracers' saturations in Labrador Sea using the portion of water that better represents the wintertime surface water in Labrador Sea, hence the CFC-12 and SF_6 saturations used in our refined TTD method are characteristic for water masses that have been ventilated in the Labrador Sea. While this reconstructed saturation should properly represent the tracers' saturations in LSW and DIW, the divergence of C_{ant} estimates in NEADW and DSOW raises the question as to whether this is also the case for DSOW and NEADW. These water masses are ventilated in other regions (in the Nordic Seas) and at a different time than the LSW. Further, the NEADW and DSOW are subject to modification of their original characteristics as they move toward the Labrador Sea further complicating the reconstruction of a realistic history of the tracers' initial saturation.

We hypothesize that the differences in C_{ant} column inventories between the TTD and eMLR methods are related to the reconstruction of the CFC-12 saturation in our refined TTD method and that a different saturation history could lead to higher concentrations of C_{ant} in DSOW and NEADW, when using a refined TTD method.

To roughly estimate to what extent the saturation assumption can affect the contribution of DSOW and NEADW to the total column inventory we here consider two approximate scenarios: (1) A mixed saturation that includes time-varying saturation for LSW and DIW, and constant 100% saturation for DSOW and NEADW; (2) Time-varying saturation for all four water masses but with a time-lag for DSOW and NEADW. Note that it may be possible to reconstruct an observations-based surface history of the effective mole fraction of CFC-12 (X_{CFC-12}) that better represents the saturation conditions when DSOW and NEADW were last in contact with the atmosphere (tracers data are available for the Greenland Sea since 1982 *Bullister and Weiss*, 1983; *Bullister*, 1984; *Karstensen et al.*, 2005; *Jeansson et al.*, 2010).

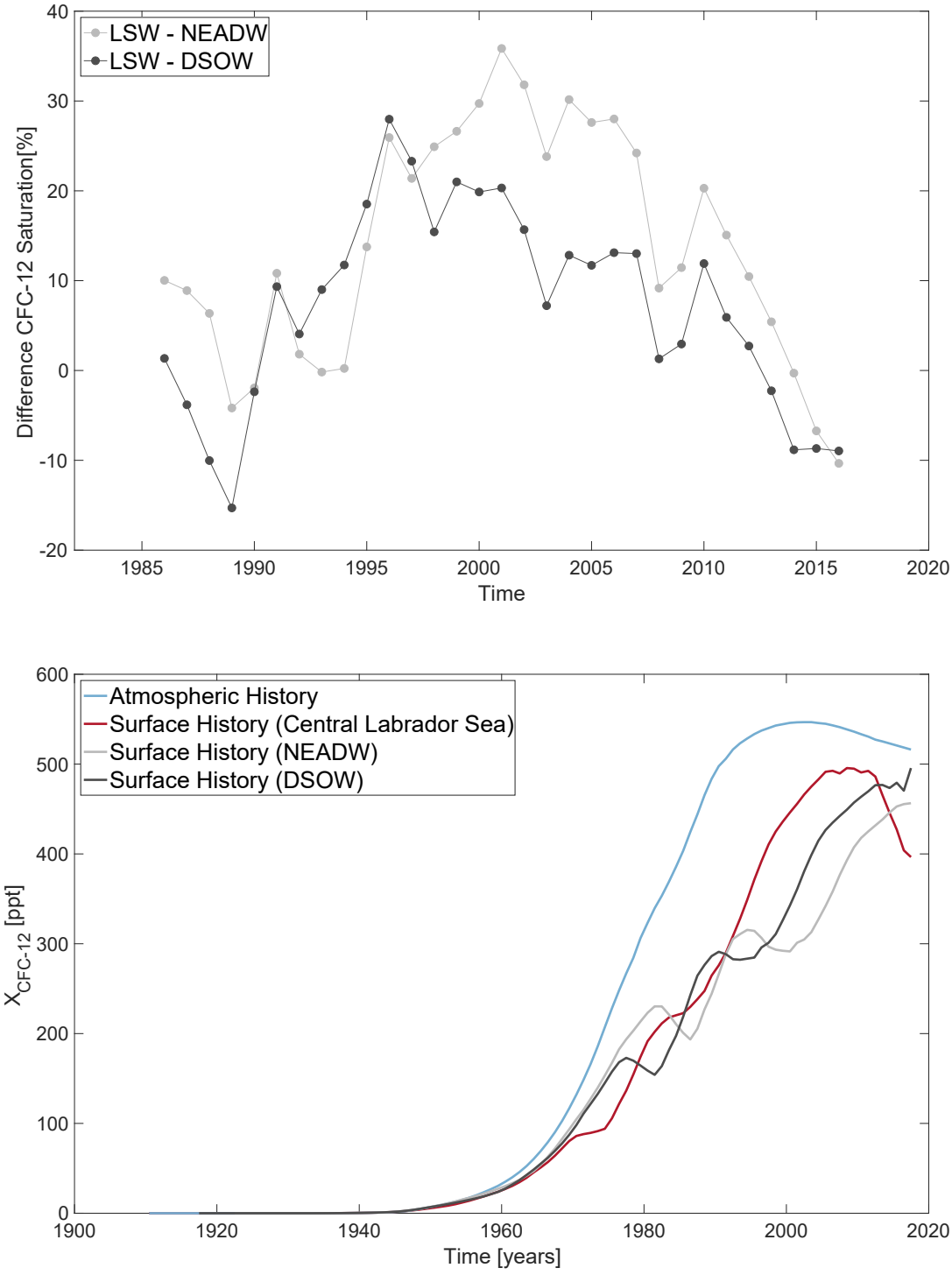

Figure 4.9: Caption in the next page.

Figure 4.9: (Previous page.) Top panel represents the difference in CFC-12 percent saturation between LSW and NEADW (light grey dots) and DSOW (dark grey dots). The NEADW and DSOW CFC-12 saturations reconstruction was performed by shifting the LSW reconstruction by 12 and 7 years, respectively. Bottom panel represents the comparison between the atmospheric history (blue line) the LSW (red line), NEADW (light grey line) and DSOW (dark grey line) winter-time surface history of the X_{CFC-12}. All the lines represents the smoothed function (moving average filter) of the surface history.

4.5.3.1 Mixed Saturation Scenario

In Figure 4.8 panel d we report results of ΔDIC_{TTD} obtained using a constant 100% saturation for DSOW and NEADW. Although the use of 100% constant saturation in these two water masses gave larger average values of the year-to-year increase of ΔDIC_{TTD}, the distinct differences between the four water masses was maintained. Note that if the absolute values of C_{ant} were considered (rather than the year-to-year change), the 100% saturation assumption leads to lower average concentrations of C_{ant} in DSOW and NEADW compared to using the time-varying saturation (see Figure C.2). The use of 100% constant saturation for DSOW and NEADW resulted in column inventories on average 4.8 ± 2.3 mol m^{-2} lower compared to using time-varying saturation for all water masses. Nevertheless we estimated that this mixed saturation scenario can determine larger year-to-year increases, leading to cumulative column inventory changes that are on average 2.5 ± 2.3 mol m^{-2} higher than the estimates obtained with the time-varying saturation for all water masses. Estimates from this scenario are still considerably lower compared to those from the eMLR method, therefore we consider a second possible scenario.

4.5.3.2 Time-Lagged Saturation Scenario

Previous studies in the Labrador Sea have reported ventilation ages (time elapsed since the water was last in contact with the atmosphere not considering mixing) for DSOW and NEADW. In particular *Azetsu-Scott et al.* (2005) reported ventilation ages of 5-8 and 11-13 years for DSOW and NEADW, while *Tait et al.* (2000) reported ventilation ages of 6-8 and 10-15 years. Therefore, if we assume that the reconstruction of the CFC-12 percent saturation we performed for the Labrador Sea (presented in Figure 3.2) is representative of the conditions in the Nordic Seas but with a time-lag, then we can roughly estimate the bias in percent saturation we have introduced by applying the Labrador Sea winter-time conditions to the DSOW and NEADW.

In the top panel of Figure 4.9, we report the estimated difference in CFC-12 percent saturation between LSW and the two water masses ventilated outside the Labrador Sea. These differences were obtained by applying a time-lag to the LSW saturation history of 7 and 12 years for DSOW and NEADW, respectively. These estimated CFC-12 percent saturation histories were then employed to reconstruct the winter-time surface histories of X_{CFC-12} for DSOW and NEADW. The latter are reported as smoothed functions in the bottom panel of Figure 4.9 together with the LSW surface history of X_{CFC-12} as well as the CFC-12 atmospheric input function. From these plots it is noticeable that the bias introduced by using the LSW surface history for water ventilated in the Nordic Seas is not constant over time, and while for certain periods we might have underestimated C_{ant} concentrations in these two water masses there are also few years where we might have overestimated C_{ant} here. In particular we find differences in percent saturation compared to the LSW ranging between -15 to +28% for DSOW and -10 to +36% for NEADW, with the highest differences in NEADW observed during the years when the column inventories of ΔDIC_{TTD} diverge from the other two estimates of ΔDIC (see top panel of Figure 4.9). On the other hand, in the first years of the time series and between 2011-2016 the difference in saturation of DSOW and NEADW with respect to LSW are characterized by negative values, with the lowest values observed in 2016 (notice that in Figure 4.9 we also reported saturation differences between 1986 and 1992 which were not considered for the column inventories comparisons).

If for instance the waters identified as DSOW and NEADW in 2005 were ventilated 7 to 12 years before (when the atmospheric rate of increase of CFC-12 was at its highest, therefore suggesting strong undersaturation of CFC-12), we would be using a much higher percent saturation of CFC-12 to calculate the mean age of these water masses. This leads to mean ages that are biased old resulting in lower C_{ant} concentrations. On the other hand, in the latest years of our time series we might have used a saturation percentage of CFC-12 that is too low for the DSOW and NEADW, therefore leading to overestimation of C_{ant} concentrations.

For illustration purposes we selected only two years within the period of divergence of the TTD method (2006 and 2010) and few values of CFC-12 percent saturation (65, 85 and 95%). We found that whereas a difference in saturation of 10% (between 95 and 85%) could increase the combined contribution of DSOW and NEADW by ~ 4 mol m^{-2},

a difference of 30% (between 95 and 65%) could lead to a combined contribution of $\sim$ 13 mol m^{-2} to the total column inventory of C_{ant}. Overall we found that the larger the difference between the saturation at time of ventilation of DSOW and NEADW and the one used based on the Labrador Sea CFC-12 time series, the larger the bias in C_{ant} column inventories. Despite the overall higher concentrations of C_{ant} in DSOW, the larger contribution to the bias in column inventory due to erroneous CFC-12 saturations, is primarily associated to the NEADW due to its larger volume compared to the underlying DSOW.

Overall these results imply that larger bias in DSOW and NEADW combined contribution to the total column inventory are to be expected for years between early 2000's and roughly 2011 compared to early 1990's and between 2013-2016. If a correction of $\sim$ +13 mol m^{-2} and $\sim$ -4 mol m^{-2} would be applied for years where the CFC-12 saturation was over- and underestimated for DSOW and NEADW, it would reconcile the column inventories from the three methods, further consolidating the conclusion that the increase of the inorganic carbon pool in this region is solely due to anthropogenic carbon invasion and no natural variability of inorganic carbon is identified.

4.5.4 Implications of Using Different Starting Years and Different Methods to Estimate Anthropogenic Carbon

The results presented in Figures 4.5 and 4.6 highlight several implications of the TTD method application in this region. The comparison of C_{ant} estimated with the TTD to results of eMLR and DIC_{obs} further showed that the assumptions implied in the TTD method are crucial in determining its performance. In particular, assumption of constant transient tracers' saturations is an over-simplification and can affect to a great extent the results obtained from this method. Even using an observation-based time-varying saturation can introduce a bias when not all ventilation and saturation histories of the different water masses are taken into account. Due to the time-varying nature of the tracers' saturation, using a constant saturation throughout the water column and over time introduces a bias that is not constant either in space or in time, which further complicates the interpretation of the Labrador Sea's role in the C_{ant} storage.

4.6 Conclusions

In this Chapter we presented estimates of C_{ant} based on the eMLR method. We performed regressions based on potential temperature, salinity and dissolved oxygen for each year and we calculated the eMLR with different time intervals. With this exercise we have shown that performing the eMLR with different time intervals within a selected time period does not affect results of average annual slope. Meaning that obtaining an appropriate average rate of increase (accumulation rate) of C_{ant} over one to two decades does not require finer temporal resolution of the data. On the other hand the choice of starting and ending year can greatly affect the results of average annual slope regardless of the time interval selected. In fact almost all starting years produced significantly different average annual slopes regardless of the time interval used, therefore leading to potentially erroneous conclusions on the carbon dynamics in this region. We have shown that although it is not necessary to have a higher temporal resolution to obtain a realistic average rate of accumulation of C_{ant} with the eMLR method, finer temporal resolution allows us to identify patterns of non-steady accumulation of C_{ant} in the Central Labrador Sea with the TTD method (presented in Chapter 3) as well as with the DIC-based methods. This result further proves the importance of long-term monitoring program in highly dynamic regions like the Labrador Sea.

Thanks to the yearly observations of DIC, we were able to assess changes in inorganic carbon pool based on the eMLR method but also to estimate the year-to-year increase of the total signal of DIC. In order to decipher whether changes observed in the DIC pool in the Central Labrador Sea are solely due to the increase of anthropogenic carbon concentrations, or whether there is some natural variability captured in this signal, we compared the ΔDIC_{obs} column inventories to those obtained with the TTD and eMLR methods and found contradictory results. In fact we observed significant differences in the average annual increase of ΔDIC between the three methods. Whereas the slope obtained for the eMLR time series, and the resulting estimates of ΔDIC_{nat} from this method, suggested that the increase in DIC signal in the Central Labrador Sea is solely due to anthropogenic carbon invasion, the TTD results suggested that the observed increase in inorganic carbon concentrations could partially be associated to natural variability of DIC in the region. We found that these contrasting results between TTD and eMLR were primarily due to divergence of the TTD-based column inventories in the 2000's with

respect to the ΔDIC_{obs} and ΔDIC_{eMLR} time series. These discrepancies between the TTD method compared to the carbon-based estimates suggested potential bias in the former method associated to the use of transient tracers rather than carbon.

Although the reasons for the TTD-based estimates divergence remain unclear, a possible explanation could lie with the assumptions regarding the transient tracers' saturation implied in the TTD method. Despite accounting for a time-varying saturation (tailored to Labrador Sea conditions), there is a potential that the CFC-12 saturations used in our refined TTD method may not be appropriate for water masses such as DSOW and NEADW which have been ventilated at a different time than LSW and outside the Labrador Sea (Nordic Sea).

To evaluate to what extent the saturation could affect the TTD-based estimates of ΔC_{ant}, we considered two scenarios: (1) a mixed saturation scenario (time-varying saturation for LSW and DIW and 100% constant saturation for DSOW and NEADW), and (2) a time-lagged scenario (with time-varying saturation for all water masses but accounting for time-lag in DSOW and NEADW). We found that whereas the first scenario would only increase the ΔDIC_{TTD} by 2.5 mol m^{-2} on average, not accounting for a time-lag in the CFC-12 saturation histories for DSOW and NEADW can lead to bias in percent saturation in these water masses ranging between $\sim$ -15-28 and -10-36% for DSOW and NEADW, respectively. These under- and overestimations of the CFC-12 saturations throughout the time series can translate into over-and underestimation of the TTD-based C_{ant} concentrations and resulting into biased column inventories (by up to 13 mol m^{-2}). The second scenario considered here, despite not representing a perfect resolution, suggests that an appropriate time-varying saturation for water masses ventilated outside the Labrador Sea could improve our refined TTD-based estimates.

The comparison of the eMLR method to the TTD as well as to the overall DIC signal, showed the importance of assumptions implied in the TTD method and revealed the, otherwise overlooked or underestimated, bias that one can introduce in the C_{ant} estimates when over-simplified assumptions are implied in this method. Overall these results further support what mentioned in Chapter 3 in that the transient tracers are imperfect analogues of CO_2 and great care needs to be taken with the assumptions of this more indirect method to estimate C_{ant}. Finally the many assumptions required to apply the TTD method suggest that direct, carbon-based methods (in particularly the eMLR) are more reliable than the

tracer-based ones in estimating C_{ant} in Labrador Sea.

CHAPTER 5

CONCLUSIONS AND OUTLOOK

5.1 Summary and Main Findings

This PhD thesis aimed to elucidate the temporal variability of the anthropogenic carbon storage in the Central Labrador Sea, a crucial region of the world's ocean for carbon sequestration.

The strength of this work relied on the unusually long time series along the AR7W transect. The Atlantic Zone Off-Shore Monitoring Program (AZOMP), which involves annual occupations of the AR7W line with measurements of both hydrographic and biogeochemical parameters, provided the opportunity to compare estimates of C_{ant} obtained with different approaches as well as to verify whether the assumption of steady state accumulation of C_{ant} is realistic for this region. The multi-decadal estimates of C_{ant} in the Central Labrador Sea between 1993 to 2016 were obtained with both the Transit Time Distribution method (which was further extended to 1986) and the extended Multiple Linear Regression. These estimates were used to test two hypotheses: (1) the C_{ant} concentrations and trends are the same regardless of the method used, (2) the increase observed in DIC is solely due to increase of the C_{ant} concentrations and no natural variability is associated to the observed DIC signal.

Overall, the AZOMP monitoring program allowed better understanding of the carbonate system in this region through full characterization of its parameters. In Chapter 2 we assessed the internal consistency of the marine carbonate system in Labrador Sea between 2013 and 2015 (when over determination of the carbonate system was available) with conversion to *in situ* conditions of temperature and pressure rather than the usually reported laboratory conditions. This study allowed us to identify the couples of input parameters

that lead to the best agreement between calculated and measured parameters. Using a Monte Carlo simulation, we assessed the propagated random uncertainty of calculated parameters which was useful for those years where over determination was not available. In fact between 1992 and 2012 only samples for TA and DIC determination were collected, requiring a better understanding of the propagated random uncertainty of calculated pH and pCO_2.

Based on the analysis provided in Chapter 2 we formulated several recommendations for future studies involving carbonate system parameters. We identified that the choice of the carbonate system parameters to be measured strongly affects both the accuracy and the uncertainty of calculated parameters. In particular we found that the combination of a T,P-dependent parameter to one that is T,P-independent is to be preferred and that the combination of pH and pCO_2 should be avoided due to the low accuracy and high combined uncertainty of the calculated parameters from this couple. We found that the best agreement between measured and calculated parameters is more likely to be achieved when the equilibrium constants of *Mehrbach et al.* (1973) as refit by *Dickson and Millero* (1987) and *Lueker et al.* (2000) are employed for calculations. Further this study of internal consistency revealed a bias in total alkalinity data in 2014 showing that this type of analysis is a useful quality control tool in the context of long-term monitoring programs. Finally the conversion of pH and pCO_2 measurements from laboratory to *in situ* conditions of temperature and pressure highlighted the uncertainty concerning the pressure effects on the equilibrium constants and how this challenges the comparison of *in situ* measurements performed by autonomous sensors, and can potentially compromise the sensor calibration.

In Chapter 3 we presented the first multi-decadal time series of column inventory and storage rates of C_{ant} in the Central Labrador Sea using a refined TTD method based on CFC-12 data between 1986 and 2016. We tested the validity of two assumptions that this method relies on: (1) constant saturation of transient tracers (often assumed to be 100%), and (2) constant air-sea CO_2 disequilibrium. The first assumption was addressed by reconstructing the histories of CFC-12 and SF_6 surface water saturations in winter by using observation between 1986 and 2016 for the former tracer and between 2012 and 2016 for the latter. This reconstruction revealed that both CFC-12 and SF_6 are significantly undersaturated throughout the three decades of the time series and that saturation varies over time, therefore requiring a refinement of the TTD method. The

constant air-sea CO_2 disequilibrium assumption was tested by using measurements of total alkalinity and dissolved inorganic carbon between 1992 and 2016 to calculate the wintertime pCO_2. When compared to the atmospheric values, these pCO_2 estimates revealed that in wintertime surface water's partial pressure of CO_2 tracks the atmospheric pCO_2 suggesting that a constant air-sea CO_2 disequilibrium is an appropriate assumption during the time our dataset was collected.

Compared to the typical application of the TTD method with constant saturation of transient tracers, the use of our refined TTD approach (which implied variable saturation) resulted in higher C_{ant} column inventories and better agreement between inventories obtained with TTDs based on CFC-12 and SF_6. This is a promising result considering that SF_6 is a more reliable tracer than CFC-12 to estimate the mean age of a water parcel in recent years. Further in Chapter 3, we explored the temporal variability of C_{ant} storage and related its changes to decadal variability of Labrador Sea Water (LSW) formation, highlighting the importance of this water mass in the transport and storage of C_{ant} in the region. In particular we found that a non-steady accumulation of C_{ant} occurred in the Central Labrador Sea between 1986 and 2016. We identified a period of slow-down in the rate of increase of the C_{ant} column inventories between 2003 and 2013 which was associated to changes in the relative thickness of LSW and Deep Intermediate Water (DIW) and to differences in the average C_{ant} concentrations in these two water masses. Our results were compared to previous work carried in the region (particularly to *Steinfeldt et al.*, 2009 and *Rhein et al.*,2017) as well as to global C_{ant} estimates (*Gruber et al.*, 2019b) highlighting some discrepancies in storage rate estimates. These differences are attributed to the use of our refined TTD method instead of the classical TTD method and to using almost annual estimates compared to a decadal average. Finally, the C_{ant} accumulation in the Central Labrador Sea identified with the application of the TTD method, highlighted the importance of sampling frequency especially in highly variable regions like the Labrador Sea.

Effects of sampling frequency were further explored in Chapter 4 where we estimated changes in DIC due to C_{ant} invasion using the eMLR method. We focused on the most basic eMLR which uses potential temperature, salinity and oxygen as independent variables and we performed and compared several iterations of this eMLR using different time intervals (year-to-year, every 5, 10 and 20 years). The objective of this exercise was to

understand the sampling frequency necessary to obtain a realistic estimate of the annual average increase of C_{ant} column inventory within a defined time period. Using linear regressions with interaction terms, we found that the choice of different time-intervals within a specific time period does not affect the results of C_{ant} accumulation, meaning that a finer temporal resolution of the data is not necessary in order to obtain a realistic average annual increase of C_{ant}. Nevertheless, when we compared same time intervals but with different starting years we found that significant differences in annual average increase are obtained depending on the starting year selected. Due to the non-steady behaviour of the Labrador Sea in accumulating C_{ant}, these differences in slopes can translate into contradictory conclusions regarding the role of the Labrador Sea in accumulating C_{ant} depending on the time period used for the eMLR.

Further, in this Chapter, we addressed the comparison of different methods used to indirectly estimate C_{ant} (TTD and eMLR) to the overall increase of the observed DIC (DIC_{obs}). All three methods to estimate changes in DIC showed that the increase in C_{ant} concentrations and the resulting accumulation rate is non-steady over time, and periods of fast and slow rate of increase alternate in the Central Labrador Sea throughout our time series. Nevertheless, different time of arise and duration of these periods could be identified, depending on the method selected.

The comparison between different method also allowed us to understand whether the observed changes in DIC concentrations are solely driven by the increase of anthropogenic carbon or they represent a combined signal of anthropogenic and natural carbon in the region. Whereas the eMLR suggests the increase in DIC is solely associated to the increase in C_{ant} concentrations, the application of the TTD method leaves some room for potential natural variability of inorganic carbon in this region. A further analysis of the C_{ant} distribution in major water masses (assessed from the three methods), suggested that potential bias in column inventories obtained with the TTD method are to be considered, possibly due to uncertainty on the saturation histories of Denmark Strait Overflow Water (DSOW) and North East Atlantic Deep Water (NEADW) which have been ventilated outside the Labrador Sea and at different times than the LSW. A rough estimate of the potential bias in column inventory introduced by the different saturation histories of these water masses suggested that results of the TTD would align with those obtained with the eMRL method, and would rule out any potential natural variability of DIC in the

region. Nevertheless it is important to highlight that the time-lagged saturation presented in Chapter 4 does not represent a perfect resolution of the discrepancies between the TTD and eMLR methods.

5.2 Significance, Outlook and Future Work

By exploring the temporal variability of C_{ant} in the Central Labrador Sea, this PhD Thesis highlighted a few key points.

The first key point concerns autonomous platforms to measure carbonate systems parameters at depth. As technology develops to obtain *in situ* measurements of pH and pCO_2 in the deep ocean, more efforts should be focused on accurate determination of the pressure effects on the equilibrium constants of the carbonate system. A better characterization of the pressure effects will be fundamental to improve *in situ* measurements. This will be particularly important in the Labrador Sea where signals of anthropogenic impacts can be detected at depth and where we heavily rely on measurements from autonomous platforms to characterize wintertime conditions.

A second key point is that long-term monitoring programs are crucial in our understanding of the ocean. In fact repeated observations allowed us to test several assumptions which were either shared by different methods to estimate C_{ant} (e.g., steady state assumption or constant air-sea CO_2 disequilibrium) or specific to one method (e.g., tracers' constant saturation assumption). The opportunity to test critical assumptions is not constrained to the carbon cycle alone and could be extended to other assumptions often implied in biogeochemical research (e.g., constant Redfield ratio). Therefore monitoring programs, like the AZOMP, should be maintained in order to answer critical questions that will enhance our understanding of the ocean but should also evolve by implementing new technology (expanding the use of autonomous sensors) as well as including new measurements (e.g., new tracers to replace the decreasing CFC-12).

Further with this work we identified decadal trends in the accumulation of anthropogenic carbon, and provided estimates of C_{ant} that could allow biogeochemical model validation in this region. Whereas we observe increasing CO_2 in the atmosphere still today, other gases like CFCs have currently decreasing atmospheric concentrations and, recent findings have demonstrated that the ocean could become a source rather than a sink for these gases in the future (*Wang et al.*, 2021). As more restrictions on CO_2 emissions are established,

the role of the ocean in storing carbon could similarly change in the future. Therefore time series, like the one presented here, represent a building block for our understanding of the ocean's current state (through model validation) as well as for predicting future scenarios.

This thesis has emphasized that assumptions implied in the C_{ant} estimation methods do matter (particularly for the TTD method) and, depending on them, different conclusions can be attained. In particular the constant tracer's saturation assumption of the TTD method can lead to significant bias in the C_{ant} estimates if this is not addressed with great care. This implies that carbon-based method, particularly the eMLR method, may be more reliable in estimating C_{ant} compared to tracer-based methods.

Finally, this thesis showed that the Labrador Sea has a non-steady behaviour in accumulating C_{ant}. Periods of fast and slow rates of increase alternate in this region and are tightly connected to changes in LSW formation. Recent model projections suggested potential changes in the formation of this water mass (*Böning et al.*, 2016), therefore based on our results we conclude that if these changes were to happen they will strongly impact the ability of the Labrador Sea to store C_{ant} in the future.

APPENDIX A

A.1 Internal Consistency: Residuals

Table A1: Average ($\overline{\mu}$), standard deviation (σ), minimum (min) and maximum (max) values of DIC residuals obtained by subtracting calculated values from measured ones for each pair of input parameters and set of constants. The residuals of DIC in 2014 calculated using TA as input parameter are those obtained from original TA data. For DIC residuals in 2014 calculated using corrected TA see Table A5.

	ΔDIC 2013	**R**	**GP**	**H**	**M73**	**HM**	**L**	**MPM**	**M06**
(TA,pH)	$\overline{\mu}$	10.2	7.3	3.2	0.7	2.6	0.5	2.1	-1.5
	σ	5.9	5.9	5.9	5.9	5.9	5.9	5.9	5.9
	min	-10.0	-13.0	-17.1	-19.6	-17.7	-19.8	-18.2	-21.8
	max	30.6	27.7	23.6	21.1	23.0	20.8	22.5	18.9
(TA,pCO_2)	$\overline{\mu}$	12.0	11.4	8.2	1.1	7.2	0.9	3.0	1.0
	σ	4.3	4.3	4.3	4.2	4.3	4.2	4.3	4.2
	min	3.4	2.7	-0.5	-7.6	-1.5	-7.9	-5.8	-7.8
	max	26.9	26.3	23.0	15.8	22.0	15.5	17.7	15.7
(pH,pCO_2)	$\overline{\mu}$	32.2	59.1	67.9	4.6	62.0	3.8	11.9	30.1
	σ	29.3	28.9	28.8	29.8	29.0	29.8	29.7	29.4
	min	-9.5	17.9	27.0	-37.7	20.8	-38.5	-30.3	-11.6
	max	125.4	151.1	159.6	99.2	154.2	98.4	106.5	123.7

	ΔDIC 2014	**R**	**GP**	**H**	**M73**	**HM**	**L**	**MPM**	**M06**
(TA,pH)	$\overline{\mu}$	3.3	0.4	-3.8	-6.4	-4.4	-6.6	-5.0	-8.5
	σ	7.8	7.9	7.9	7.9	7.9	7.9	7.9	7.9
	min	-14.6	-17.5	-21.5	-23.9	-22.1	-24.1	-22.6	-26.0
	max	23.6	20.9	17.1	15.0	16.6	14.9	16.1	13.2
(TA,pCO_2)	$\overline{\mu}$	-2.2	-2.8	-6.1	-13.3	-7.1	-13.5	-11.4	-13.4
	σ	6.3	6.3	6.3	6.4	6.4	6.4	6.3	6.4
	min	-11.3	-11.9	-15.2	-22.3	-16.2	-22.6	-20.5	-22.5
	max	17.8	17.4	14.4	7.0	13.7	6.7	9.0	6.9

(pH,pCO_2)	$\overline{\mu}$	1.0	28.5	37.5	-26.0	32.0	-26.9	-18.3	-0.2
	σ	33.6	33.1	33.0	33.9	33.1	33.9	33.7	33.5
	min	-56.6	-28.4	-19.1	-84.3	-24.9	-85.2	-76.5	-57.7
	max	105.6	131.5	140.0	78.7	134.3	78.0	85.9	103.4

	$\triangle$DIC 2015	**R**	**GP**	**H**	**M73**	**HM**	**L**	**MPM**	**M06**
(TA,pH)	$\overline{\mu}$	12.4	9.4	5.2	2.6	4.6	2.4	4.1	0.4
	σ	5.3	5.3	5.3	5.2	5.3	5.2	5.2	5.2
	min	-3.9	-6.8	-10.7	-13.0	-11.3	-13.3	-11.7	-15.2
	max	32.4	29.1	24.2	20.9	23.4	20.7	22.5	18.4
(TA,pCO_2)	$\overline{\mu}$	17.2	16.4	12.7	5.4	11.3	5.1	6.8	4.9
	σ	5.4	5.4	5.3	5.1	5.2	5.1	5.1	5.1
	min	9.4	8.7	5.1	-2.3	3.8	-2.5	-0.8	-2.7
	max	34.5	33.7	29.4	21.2	27.9	20.9	22.8	20.7
(pH,pCO_2)	$\overline{\mu}$	30.5	56.3	60.8	0.9	51.6	0.5	2.4	22.7
	σ	56.4	55.8	55.7	58.0	56.4	57.9	58.1	57.2
	min	-60.0	-32.8	-27.8	-89.6	-36.9	-90.0	-87.9	-66.7
	max	203.5	227.2	231.9	177.7	223.9	177.3	179.2	197.9

Table A2: Same as Table A1 for TA. The residuals of TA in 2014 are those obtained from original TA data. For TA residuals in 2014 calculated using corrected TA see Table A5

	ΔTA 2013	**R**	**GP**	**H**	**M73**	**HM**	**L**	**MPM**	**M06**
(DIC,pH)	$\overline{\mu}$	-10.7	-7.6	-3.3	-0.7	-2.7	-0.5	-2.2	1.5
	σ	6.1	6.1	6.1	6.1	6.1	6.1	6.1	6.1
	min	-32.0	-28.9	-24.6	-21.9	-23.9	-21.7	-23.4	-19.6
	max	10.5	13.5	17.8	20.4	18.4	20.6	18.9	22.6
(DIC,pCO_2)	$\overline{\mu}$	-13.6	-12.9	-9.2	-1.3	-8.1	-1.0	-3.3	-1.1
	σ	4.9	4.9	4.9	4.8	4.9	4.8	4.8	4.8
	min	-30.6	-29.8	-26.1	-17.8	-24.9	-17.5	-19.9	-17.6
	max	-3.8	-3.1	0.5	8.6	1.7	8.8	6.5	8.7
(pH,pCO_2)	$\overline{\mu}$	22.9	53.9	67.3	3.9	61.7	3.3	10.0	32.7
	σ	30.0	29.6	29.4	30.4	29.6	30.4	30.4	30.0
	min	-24.9	6.8	20.5	-44.2	14.7	-44.8	-38.1	-14.8
	max	111.6	141.3	154.2	93.8	149.1	93.1	99.9	121.3

	ΔTA 2014	**R**	**GP**	**H**	**M73**	**HM**	**L**	**MPM**	**M06**
(DIC,pH)	$\overline{\mu}$	-3.5	-0.4	4.0	6.6	4.6	6.9	5.2	8.9
	σ	8.2	8.2	8.2	8.2	8.2	8.2	8.2	8.3
	min	-24.4	-21.7	-17.7	-15.5	-17.2	-15.4	-16.6	-13.6
	max	15.2	18.2	22.4	24.8	22.9	25.0	23.5	26.9
(DIC,pCO_2)	$\overline{\mu}$	2.5	3.2	6.9	14.9	8.0	15.2	12.8	15.1
	σ	7.1	7.2	7.1	7.2	7.2	7.1	7.1	7.2
	min	-19.8	-19.3	-15.9	-8.0	-15.2	-7.7	-10.4	-7.9
	max	12.8	13.5	17.1	25.1	18.2	25.4	23.0	25.2
(pH,pCO_2)	$\overline{\mu}$	3.2	35.0	48.7	-14.8	43.6	-15.5	-8.2	14.3
	σ	39.0	38.4	38.2	38.8	38.1	38.9	38.6	38.5

	min	-73.4	-40.7	-28.8	-89.7	-31.8	-91.3	-80.9	-62.9
	max	125.0	154.9	167.8	106.4	162.4	105.9	112.5	134.3

	$\triangle$TA 2015	**R**	**GP**	**H**	**M73**	**HM**	**L**	**MPM**	**M06**
(DIC,pH)	$\overline{\mu}$	-13.0	-9.9	-5.4	-2.7	-4.8	-2.5	-4.2	-0.5
	σ	5.6	5.6	5.5	5.5	5.5	5.5	5.5	5.4
	min	-34.3	-30.8	-25.6	-22.1	-24.7	-21.8	-23.7	-19.5
	max	4.1	7.0	11.1	13.5	11.7	13.8	12.1	15.7
(DIC,pCO_2)	$\overline{\mu}$	-19.7	-18.8	-14.4	-6.1	-12.8	-5.8	-7.8	-5.6
	σ	6.3	6.3	6.1	5.8	6.0	5.8	5.9	5.8
	min	-40.4	-39.4	-34.3	-24.6	-32.5	-24.2	-26.5	-24.0
	max	-10.6	-9.8	-5.8	2.6	-4.3	2.8	0.9	3.1
(pH,pCO_2)	$\overline{\mu}$	11.9	42.2	51.5	-8.8	42.3	-8.9	-8.8	16.4
	σ	56.2	55.6	55.7	57.5	56.1	57.5	57.5	57.1
	min	-82.2	-50.1	-39.9	-101.5	-48.7	-101.8	-101.3	-75.0
	max	210.2	238.2	247.5	193.4	239.8	193.3	193.6	216.9

Table A3: Same as Table A1 for pCO_2. The residuals of pCO_2 in 2014 calculated using TA as input parameter are those obtained from original TA data. For pCO_2 residuals in 2014 calculated using corrected TA see Table A5.

	ΔpCO_2 2013	**R**	**GP**	**H**	**M73**	**HM**	**L**	**MPM**	**M06**
(TA,DIC)	$\overline{\mu}$	-9.7	-9.8	-28.1	-3.1	-13.8	-4.5	-13.2	-10.4
	σ	12.1	12.1	12.0	11.4	12.0	11.3	11.6	11.4
	min	-51.8	-51.8	-70.4	-43.5	-55.7	-44.8	-54.5	-51.1
	max	13.0	13.0	-4.5	18.8	9.1	17.4	9.4	11.9
(TA,pH)	$\overline{\mu}$	16.6	9.5	-19.0	-0.8	-6.4	-2.8	-7.1	-13.8
	σ	5.8	5.9	5.8	5.6	5.9	5.6	5.7	5.7
	min	-1.1	-8.4	-36.8	-17.9	-24.5	-19.8	-24.7	-31.2
	max	25.2	18.3	-9.7	7.7	2.8	5.7	1.7	-5.0
(DIC,pH)	$\overline{\mu}$	15.0	8.3	-19.6	-0.9	-6.9	-2.9	-7.5	-13.6
	σ	6.0	6.0	5.9	5.8	6.1	5.7	5.9	5.8
	min	-4.3	-11.1	-39.0	-19.6	-26.5	-21.5	-26.6	-32.5
	max	23.0	16.5	-10.9	6.9	1.7	4.9	0.7	-5.4

	ΔpCO_2 2014	**R**	**GP**	**H**	**M73**	**HM**	**L**	**MPM**	**M06**
(TA,DIC)	$\overline{\mu}$	26.7	26.7	8.4	31.3	22.0	29.9	22.2	24.6
	σ	12.4	12.5	14.8	14.6	14.0	14.8	14.3	14.8
	min	-15.2	-15.3	-36.3	-14.2	-23.8	-15.4	-23.0	-20.5
	max	46.6	46.7	30.0	53.0	43.0	51.7	43.6	46.4
(TA,pH)	$\overline{\mu}$	21.0	14.1	-15.0	2.8	-2.1	0.7	-3.4	-9.9
	σ	8.1	8.1	7.0	6.8	7.2	6.8	6.9	6.9
	min	-1.4	-8.7	-37.3	-19.1	-24.7	-21.1	-25.4	-32.2
	max	49.3	42.6	-3.6	15.5	15.3	12.6	10.7	2.4
(DIC,pH)	$\overline{\mu}$	20.7	14.3	-13.4	4.7	-0.5	2.7	-1.6	-7.5

	σ	6.7	6.7	6.3	6.3	6.5	6.3	6.3	6.3
	min	0.8	-5.9	-33.5	-15.1	-21.0	-17.0	-21.5	-27.7
	max	36.4	30.1	-2.9	15.6	12.8	13.7	8.8	3.2

	ΔpCO_2 2015	**R**	**GP**	**H**	**M73**	**HM**	**L**	**MPM**	**M06**
(TA,DIC)	$\overline{\mu}$	-18.0	-18.0	-35.8	-12.3	-22.0	-13.7	-21.7	-19.2
	σ	11.6	11.6	11.8	11.1	11.6	11.1	11.4	11.2
	min	-41.6	-41.6	-57.6	-36.6	-45.2	-37.9	-45.0	-42.8
	max	1.0	0.9	-17.6	4.8	-3.9	3.6	-4.3	-1.6
(TA,pH)	$\overline{\mu}$	18.4	11.8	-15.1	1.7	-3.2	-0.2	-4.3	-10.4
	σ	9.7	9.5	8.8	9.1	9.2	9.0	9.0	8.9
	min	-14.6	-20.7	-45.4	-29.6	-34.9	-31.3	-35.5	-41.0
	max	32.6	25.7	-0.3	16.3	10.8	14.5	9.8	4.2
(DIC,pH)	$\overline{\mu}$	15.6	9.5	-17.2	0.0	-4.9	-1.9	-6.1	-11.7
	σ	9.8	9.6	9.7	9.8	9.5	9.8	9.6	9.7
	min	-15.2	-20.9	-44.9	-28.7	-34.2	-30.3	-34.8	-39.6
	max	29.5	23.1	-1.9	14.8	9.4	12.9	8.3	3.4

Table A4: Same as Table A1 for pH. The residuals of pH in 2014 calculated using TA as input parameter are those obtained from original TA data. For pH residuals in 2014 calculated using corrected TA see Table A5.

	$\triangle$pH 2013	**R**	**GP**	**H**	**M73**	**HM**	**L**	**MPM**	**M06**
(TA,DIC)	$\overline{\mu}$	0.009	0.004	0.020	0.002	0.010	0.002	0.014	0.005
	σ	0.016	0.016	0.015	0.016	0.016	0.016	0.016	0.016
	min	-0.044	-0.048	-0.032	-0.051	-0.042	-0.050	-0.038	-0.047
	max	0.064	0.060	0.077	0.058	0.066	0.059	0.071	0.062
(TA,pCO_2)	$\overline{\mu}$	-0.022	-0.025	-0.001	-0.001	-0.009	0.000	0.007	0.003
	σ	0.006	0.006	0.006	0.006	0.006	0.006	0.006	0.006
	min	-0.038	-0.042	-0.019	-0.018	-0.026	-0.017	-0.010	-0.015
	max	-0.014	-0.017	0.008	0.008	0.000	0.009	0.016	0.012
(DIC,pCO_2)	$\overline{\mu}$	-0.025	-0.028	-0.003	-0.001	-0.010	0.000	0.006	0.003
	σ	0.006	0.006	0.006	0.006	0.006	0.006	0.006	0.006
	min	-0.044	-0.047	-0.023	-0.021	-0.030	-0.020	-0.014	-0.018
	max	-0.017	-0.019	0.006	0.008	-0.002	0.009	0.015	0.012

	$\triangle$pH 2014	**R**	**GP**	**H**	**M73**	**HM**	**L**	**MPM**	**M06**
(TA,DIC)	$\overline{\mu}$	-0.009	-0.014	0.003	-0.016	-0.008	-0.016	-0.004	-0.013
	σ	0.020	0.021	0.021	0.021	0.021	0.021	0.020	0.021
	min	-0.056	-0.061	-0.043	-0.063	-0.054	-0.062	-0.050	-0.059
	max	0.051	0.047	0.071	0.046	0.055	0.047	0.058	0.051
(TA,pCO_2)	$\overline{\mu}$	-0.019	-0.022	0.004	0.003	-0.005	0.003	0.010	0.006
	σ	0.007	0.007	0.009	0.007	0.007	0.007	0.007	0.007
	min	-0.042	-0.045	-0.021	-0.020	-0.028	-0.020	-0.013	-0.017
	max	-0.005	-0.008	0.033	0.017	0.011	0.020	0.025	0.023
(DIC,pCO_2)	$\overline{\mu}$	-0.019	-0.022	0.005	0.005	-0.004	0.006	0.013	0.009

σ	0.007	0.007	0.009	0.007	0.007	0.007	0.007	0.007
min	-0.041	-0.044	-0.019	-0.017	-0.026	-0.016	-0.010	-0.013
max	-0.006	-0.009	0.035	0.017	0.008	0.018	0.024	0.022

	ΔpH 2015	**R**	**GP**	**H**	**M73**	**HM**	**L**	**MPM**	**M06**
(TA,DIC)	$\overline{\mu}$	0.014	0.009	0.026	0.007	0.015	0.007	0.020	0.011
	σ	0.014	0.014	0.014	0.014	0.014	0.014	0.014	0.014
	min	-0.030	-0.034	-0.014	-0.035	-0.027	-0.035	-0.023	-0.031
	max	0.067	0.062	0.078	0.060	0.068	0.060	0.073	0.063
(TA,pCO_2)	$\overline{\mu}$	-0.021	-0.023	0.003	0.002	-0.005	0.002	0.011	0.006
	σ	0.010	0.010	0.011	0.011	0.010	0.011	0.010	0.011
	min	-0.057	-0.061	-0.035	-0.036	-0.042	-0.036	-0.027	-0.032
	max	-0.004	-0.007	0.020	0.018	0.012	0.019	0.027	0.023
(DIC,pCO_2)	$\overline{\mu}$	-0.025	-0.028	0.000	0.000	-0.008	0.000	0.008	0.004
	σ	0.012	0.012	0.012	0.012	0.012	0.012	0.012	0.012
	min	-0.062	-0.065	-0.039	-0.038	-0.045	-0.037	-0.029	-0.034
	max	-0.006	-0.009	0.018	0.018	0.011	0.019	0.027	0.023

Table A5: Average ($\overline{\mu}$), standard deviation (σ), minimum (min) and maximum (max) values for all carbonate parameters calculated using 2014 TA as input corrected for the 12.2 μmol kg^{-1} offset. The residuals were obtained by subtracting calculated values from measured ones for each of pair of input parameters and set of constants.

	ΔDIC	**R**	**GP**	**H**	**M73**	**HM**	**L**	**MPM**	**M06**
(TA,pH)	$\overline{\mu}$	15.0	12.1	7.9	5.3	7.3	5.1	6.7	3.2
	σ	7.8	7.9	7.9	7.9	7.9	7.9	7.9	8.0
	min	-2.9	-5.8	-9.8	-12.2	-10.4	-12.4	-10.9	-14.2
	max	35.3	32.7	28.9	26.8	28.4	26.7	27.9	25.0
(TA,pCO_2)	$\overline{\mu}$	8.6	8.0	4.7	-2.4	3.7	-2.7	-0.6	-2.6
	σ	6.3	6.3	6.3	6.3	6.3	6.3	6.3	6.4
	min	-0.5	-1.1	-4.4	-11.5	-5.4	-11.8	-9.6	-11.6
	max	28.8	28.3	25.3	17.7	24.4	17.4	19.7	17.5
	ΔTA	**R**	**GP**	**H**	**M73**	**HM**	**L**	**MPM**	**M06**
(DIC,pH)	$\overline{\mu}$	-15.7	-12.6	-8.2	-5.5	-7.6	-5.3	-7.0	-3.3
	σ	8.2	8.2	8.2	8.2	8.2	8.2	8.2	8.3
	min	-36.6	-33.8	-29.9	-27.7	-29.3	-27.5	-28.8	-25.8
	max	3.1	6.0	10.2	12.6	10.8	12.8	11.3	14.8
(DIC,pCO_2)	$\overline{\mu}$	-9.7	-9.0	-5.3	2.7	-4.2	3.0	0.6	2.9
	σ	7.1	7.2	7.1	7.2	7.2	7.1	7.1	7.2
	min	-32.0	-31.5	-28.1	-20.2	-27.3	-19.9	-22.5	-20.0
	max	0.6	1.3	4.9	12.9	6.1	13.2	10.8	13.1
(pH,pCO_2)	$\overline{\mu}$	-9.0	22.8	36.6	-27.0	31.4	-27.7	-20.4	2.2
	σ	39.0	38.4	38.2	38.8	38.1	38.9	38.6	38.5
	min	-85.6	-52.9	-41.0	-101.9	-44.0	-103.5	-93.1	-75.1
	max	112.8	142.7	155.6	94.3	150.2	93.7	100.3	122.1

	ΔpCO_2	R	GP	H	M73	HM	L	MPM	M06
(TA,DIC)	$\overline{\mu}$	0.4	0.4	-18.1	6.1	-3.8	4.6	-3.5	-1.1
	σ	14.4	14.4	15.8	15.5	14.8	15.6	15.2	15.7
	min	-44.1	-44.1	-67.4	-40.2	-47.8	-43.1	-48.0	-49.2
	max	22.0	22.1	4.5	28.8	18.2	27.4	18.9	21.8
(TA,pH)	$\overline{\mu}$	22.8	15.9	-13.0	4.7	-0.2	2.6	-1.4	-8.0
	σ	8.1	8.1	6.9	6.8	7.2	6.8	6.9	6.9
	min	0.4	-6.8	-35.2	-17.1	-22.7	-19.1	-23.3	-30.2
	max	51.1	44.4	-1.6	17.4	17.3	14.5	12.6	4.4

	ΔpH	R	GP	H	M73	HM	L	MPM	M06
(TA,DIC)	$\overline{\mu}$	0.022	0.017	0.033	0.015	0.023	0.015	0.027	0.018
	σ	0.022	0.022	0.022	0.022	0.022	0.022	0.022	0.022
	min	-0.026	-0.031	-0.014	-0.033	-0.024	-0.032	-0.020	-0.029
	max	0.089	0.085	0.105	0.083	0.092	0.084	0.095	0.086
(TA,pCO_2)	$\overline{\mu}$	-0.017	-0.020	0.006	0.005	-0.003	0.006	0.013	0.009
	σ	0.007	0.007	0.009	0.007	0.007	0.007	0.007	0.007
	min	-0.040	-0.043	-0.019	-0.018	-0.026	-0.017	-0.011	-0.014
	max	-0.002	-0.005	0.035	0.020	0.014	0.022	0.028	0.026

Table A6: Statistics of residuals in Aragonite Saturation State (Ω_{Ar}), obtained by calculating differences between values from specific pairs of carbonate parameters. Values of mean ($\overline{\mu}$), standard deviation (σ), minimum (min) and maximum (max) values are reported. The labels represent $\Delta\Omega_{Ar1}$ = Ω_{Ar}(TA,DIC)-Ω_{Ar}(DIC,pH); $\Delta\Omega_{Ar2}$ = Ω_{Ar}(TA,DIC)-Ω_{Ar}(DIC,pCO$_2$); $\Delta\Omega_{Ar3}$ = Ω_{Ar}(DIC,pCO$_2$)-Ω_{Ar}(DIC,pH); $\Delta\Omega_{Ar4}$ = Ω_{Ar}(pH,pCO$_2$)-Ω_{Ar}(DIC,pH); $\Delta\Omega_{Ar5}$ = Ω_{Ar}(pH,pCO$_2$)-Ω_{Ar}(DIC,pCO$_2$).

Ω_{Ar} Residuals	$\overline{\mu}$	σ	min	max
$\Delta\Omega_{Ar1}$	-0.006	0.044	-0.126	0.122
$\Delta\Omega_{Ar2}$	-0.011	0.036	-0.147	0.044
$\Delta\Omega_{Ar3}$	0.004	0.018	-0.015	0.070
$\Delta\Omega_{Ar4}$	-0.004	0.019	-0.069	0.016
$\Delta\Omega_{Ar5}$	-0.007	0.037	-0.138	0.032

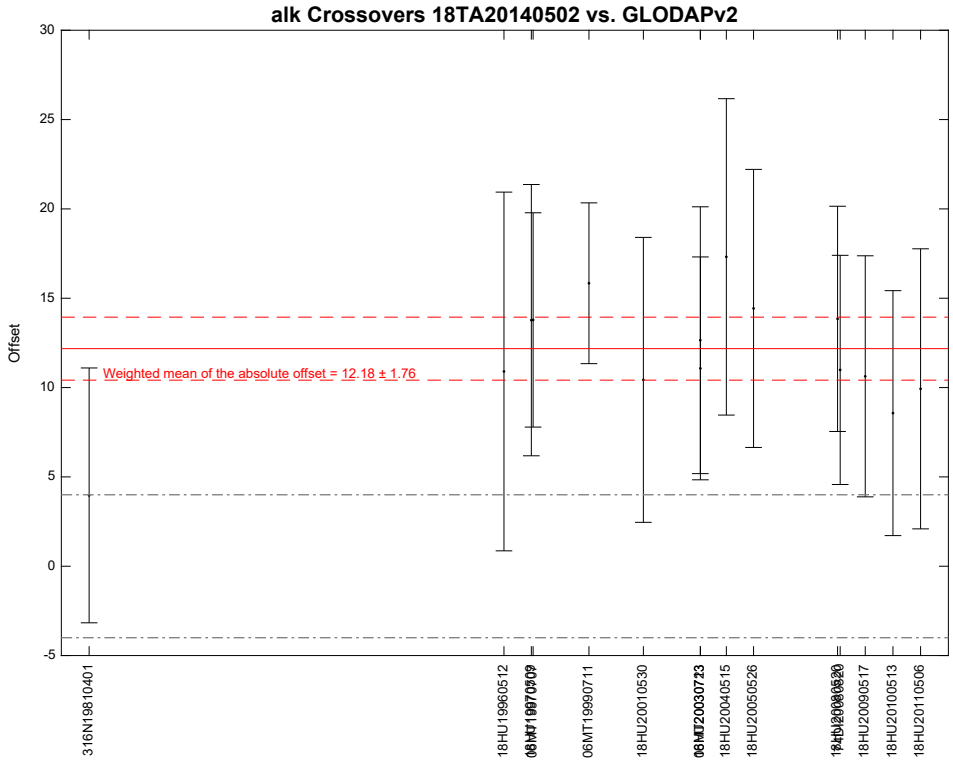

Figure A.1: Evaluation of the TA crossover offset for the 2014 cruise (*Olsen et al.*, 2016). The plot shows crossovers between TA from the 2014 cruise and all other cruises in the Labrador Sea available in the GLODAPv2 data product. An offset of 12.2 μmol kg^{-1} was identified.

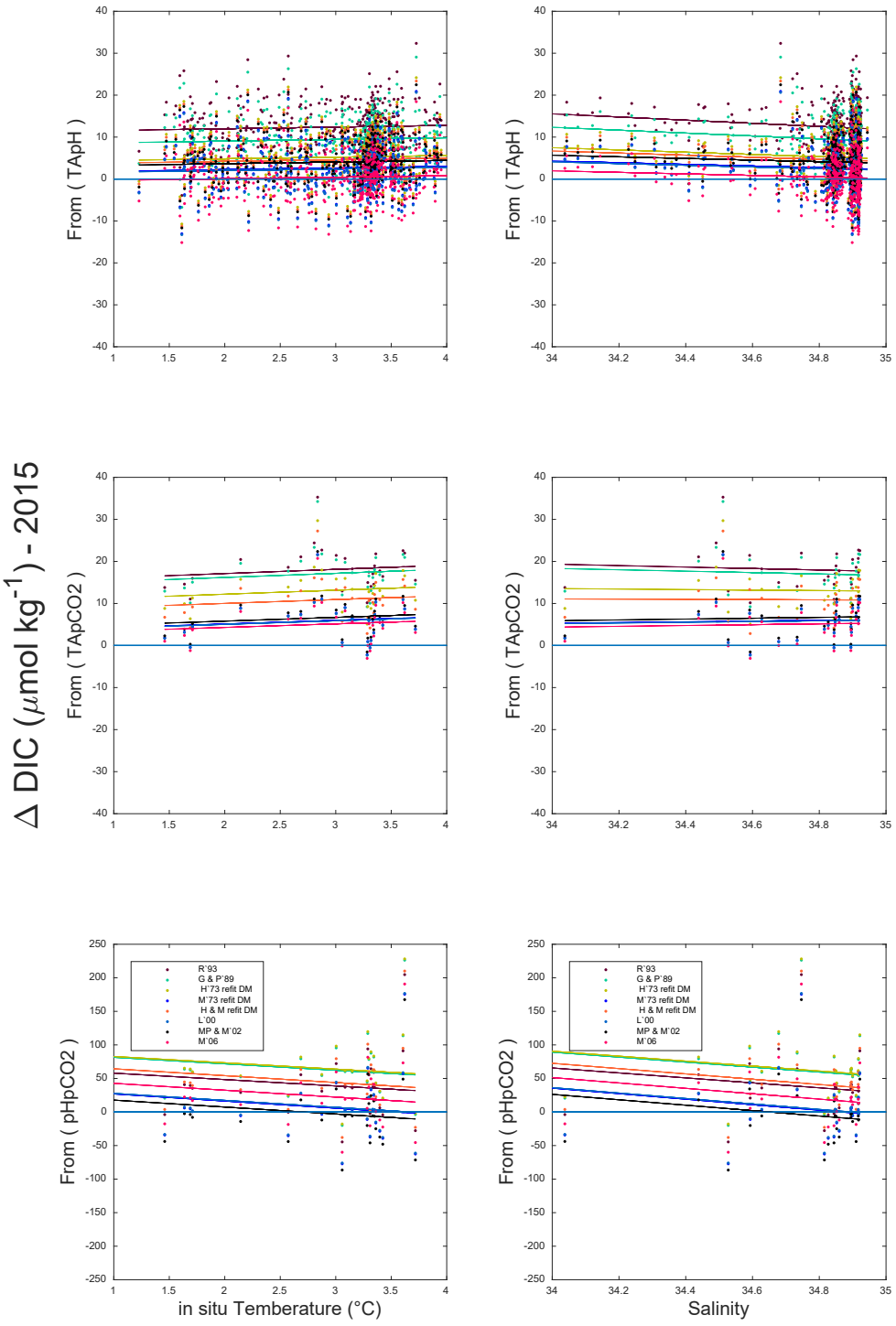

Figure A.2: ΔDIC from (TA,pH), (TA,pCO_2) and (pH,pCO_2) from eight different sets of constants as a function of Temperature (left panels) and Salinity (right panels).

A.2 Estimating Combined Uncertainty on Computed Carbonate System parameters by Monte Carlo simulation[1]

A.2.1 Introduction

This appendix outlines the method employed in the paper to estimate combined uncertainty on computed carbonate system parameters using Monte Carlo simulation. The method involves randomly sampling from the uncertainty distributions of various input parameters and internal variables of CO2SYS as a means of capturing the uncertainty associated with each. The combined uncertainties so derived incorporate each of these individual uncertainty contributions.

Two types of methodological design flaws have been made in the past when estimating combined uncertainties by Monte Carlo simulation. One has been to neglect uncertainties in the equilibrium constants of the carbonate system (K_0, K_1, K_2 etc.). The other has been to use insufficient random samples in the simulations. This latter type of flaw is illustrated in Figure A.3 where we can see that using too small a sample size (e.g., 1000) results in different uncertainty estimates each time the Monte Carlo simulation is run. In these cases, the uncertainty estimates do not converge. On the other hand, using very large sample sizes comes at computational cost. This study adopts a random sample size of 100,000 as a reasonable compromise.

A.2.2 Method

Here, uncertainties on the measured input parameters (TA, DIC, $p\mathrm{CO}_2$, pH, T, S, $\mathrm{P_T}$, $\mathrm{Si_T}$) and in the formulations of the key equilibrium constants (K_0, K_1, K_2, K_B, K_W, K_{Ar}) are both accounted for, including uncertainty in the pressure corrections applied to K_1, K_2, K_B and K_{Ar} ($K_{1_{fac}}$, $K_{2_{fac}}$, $K_{B_{fac}}$ and $K_{Ar_{(p=0)}}$, respectively). Uncertainty in the computation of Ca^{2+} from salinity is also incorporated. Figure A.4 shows the uncertainties that are accounted for and how these propagate through CO2SYS via relations between the various parameters/variables. Note that for internal variables computed from measured temperature and/or salinity, both analytical uncertainty in the T,S measurements and uncertainty in the formulations themselves are accounted for. For combinations of input parameters involving $p\mathrm{CO}_2$ or pH (for which measurements had to first be converted to $25°C$ and

[1]Matthews, J. B. R. and Raimondi, L.

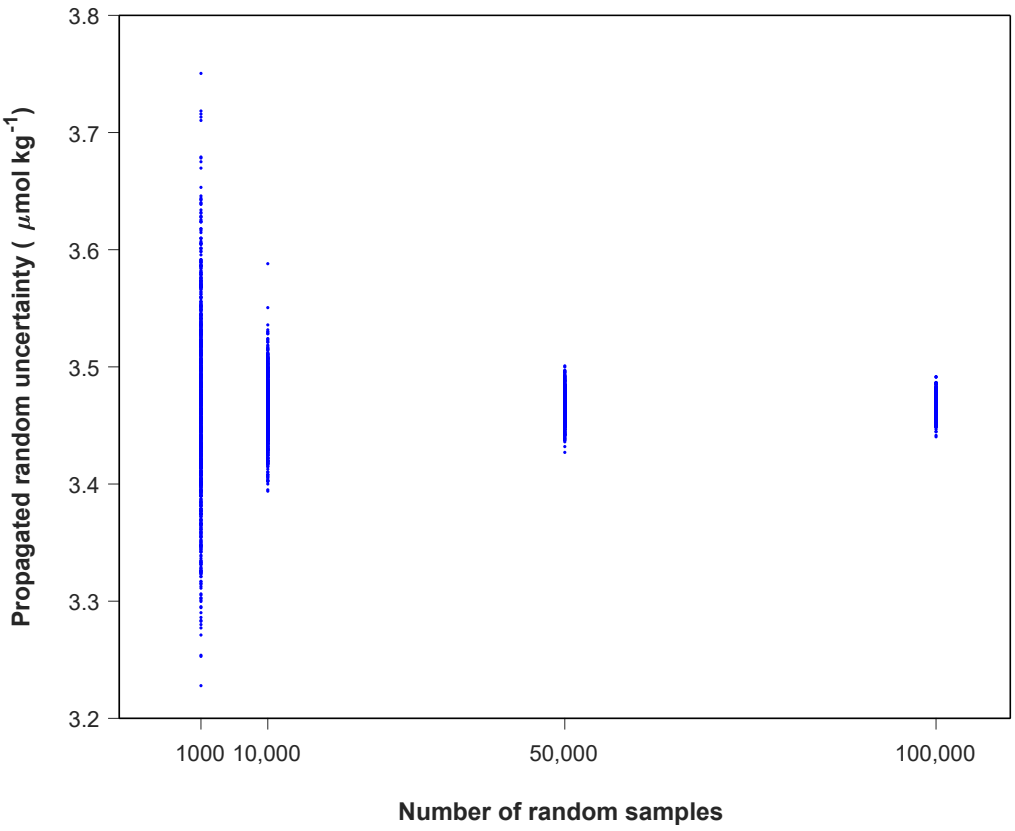

Figure A.3: Repeat estimates of combined uncertainty for computed DIC (from TA, pH) when using different random sample sizes. One thousand estimates are plotted at each sample size, each corresponding to a single run of the Monte Carlo simulation using different random samples each time. The following input values were used together with M73 for K_1, K_2: TA = 2303.6 μmol kg^{-1}, pH at 25°C = 7.713 (total scale), T = 1.636°C, S = 34.8964 psu, P = 3601.1 db, P_T = 0.959 μmol kg^{-1}, Si_T = 9.9 μmol kg^{-1}

then to *in situ* temperature as described in section 2.2.1), Monte Carlo simulation was undertaken at each conversion step. Uncertainties were thus propagated from one step to the next step, capturing uncertainty across all conversion computations. Note, however, that since pseudo-potential pCO_2 was computed, uncertainty in the pressure dependencies of K_0 and the fugacity factor was not accounted for.

The various uncertainty estimates used to conduct the Monte Carlo simulations are provided in Table A7. The uncertainty distributions of each input parameter and internal variable were taken to be normal, with mean equal to the measured value for input parameters or computed value for internal variables, and with the standard deviation

equal to the analytical precision (from Table 2.2) or reported precision (from Table A7), respectively. For K_1 and K_2, different values were used to represent the uncertainty depending on the formulation employed. The Monte Carlo uncertainties presented in the paper are the standard deviations of the combined uncertainty distributions ultimately output from CO2SYS.

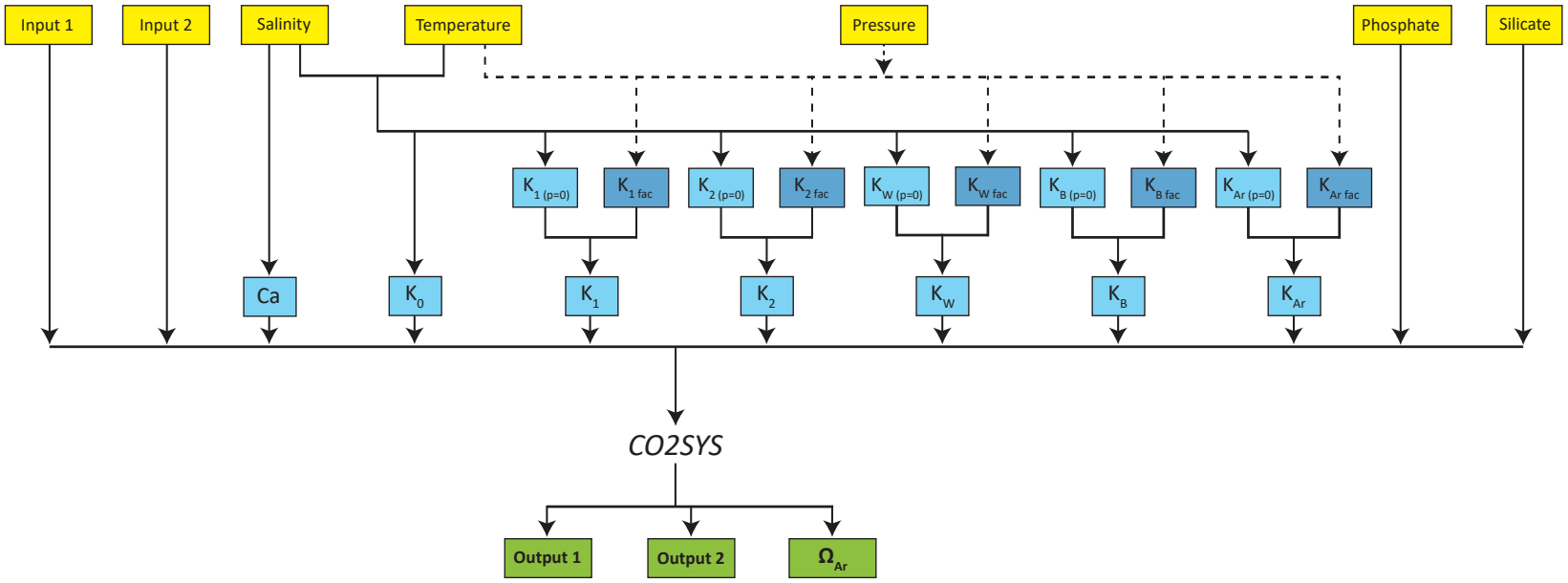

Figure A.4: Schematic illustrating the various contributions to combined uncertainty for computed carbonate system parameters (green boxes), as estimated by Monte Carlo simulation using COSYS. Uncertainties were assigned to each input parameter (yellow boxes) and internal variable (light and dark blue boxes), except for measured pressure, which was assumed to have negligible uncertainty. The dashed lines lead to temperature and pressure -dependent parameters (dark blue boxes). The unspecified input and output parameter couples can be any complete combination of DIC, TA, pCO_2 and TA. Note that K_{Ar} is only used for the computation of Ω_{Ar}.

Table A7: Uncertainty estimates used in the Monte Carlo analysis. Numbers in bold are those stated in the source publications.

Parameter	Formulation	Abbreviation	Uncertainty		Reference for Uncertainty
			$\pm 1\sigma$	$\pm 2\sigma$	
K_0	*Weiss* (1974)		**0.25%**	0.5%	*Dickson and Riley* (1978), p.2
pK_1	*Roy et al.* (1993)	*R*	**0.004**	0.008	Matlab CO2SYSv1.1 (*Van Heuven et al.*, 2011)
	Goyet and Poisson (1989)	*GP*	0.0055	**0.011**	*Goyet and Poisson* (1989), p.1652
	Hansson (1973) as refit by *Dickson and Millero* (1987)	*H*	0.0065	**0.013**	*Dickson and Millero* (1987), p. 1739
	Mehrbach et al. (1973) as refit by *Dickson and Millero* (1987)	*M73*	0.0055	**0.011**	*Dickson and Millero* (1987), p. 1739
	Hansson (1973) and *Mehrbach et al.* (1973) as refit by *Dickson and Millero* (1987)	*HM*	0.0085	**0.017**	*Dickson and Millero* (1987), p. 1740

Continued on next page

Table A7 – *Continued from previous page*

Parameter	Formulation	Abbreviation	Uncertainty		Reference for Uncertainty
			$\pm 1\sigma$	$\pm 2\sigma$	
	Lueker et al. (2000)	*L*	**0.0055**	0.011	*Lueker et al.* (2000), p. 110
	Mojica Prieto and Millero (2002)	*MPM*	**0.0056**	0.0112	*Mojica Prieto and Millero* (2002), p. 2536
	Millero et al. (2006)	*M06*	**0.0054**	0.0108	*Millero et al.* (2006), p.81
$K_{1_{fac}}$	*Millero* (1979)		1%	**2%**	*Culberson and Pytkowicz* (1968), p. 410
pK_2	*Roy et al.* (1993)	*R*	**0.003**	0.006	Matlab CO2SYSv1.1 (*Van Heuven et al.*, 2011)
	Goyet and Poisson (1989)	*GP*	0.01	**0.02**	*Goyet and Poisson* (1989), p.1652
	Hansson (1973) as refit by *Dickson and Millero* (1987)	*H*	0.0085	**0.017**	*Dickson and Millero* (1987), p. 1739
	Mehrbach et al. (1973) as refit by *Dickson and Millero* (1987)	*M73*	0.01	**0.02**	*Dickson and Millero* (1987), p. 1739

Continued on next page

Table A7 – *Continued from previous page*

Parameter	Formulation	Abbreviation	Uncertainty		Reference for Uncertainty
			$\pm 1\sigma$	$\pm 2\sigma$	
	Hansson (1973) and *Mehrbach et al.* (1973) as refit by *Dickson and Millero* (1987)	*HM*	0.013	**0.026**	*Dickson and Millero* (1987), p. 1740
	Lueker et al. (2000)	*L*	**0.01**	0.02	*Lueker et al.* (2000), p. 110
	Mojica Prieto and Millero (2002)	*MPM*	**0.01**	0.02	*Mojica Prieto and Millero* (2002), p. 2536
	Millero et al. (2006)	*M06*	**0.011**	0.022	*Millero et al.* (2006), p.81
$K_{2_{fac}}$	*Millero* (1979)		1%	**2%**	*Culberson and Pytkowicz* (1968), p. 410
lnK_B	*Dickson* (1990)		**0.0042**	0.0084	Matlab CO2SYS v1.1 (*Van Heuven et al.*, 2011)
$K_{B_{fac}}$	*Millero* (1979)		1%	**2%**	*Culberson and Pytkowicz* (1968), p. 410
lnK_W	*Millero* (1995)		**0.01**	0.02	*Dickson* (1990), p. 763

Continued on next page

Table A7 – *Continued from previous page*

Parameter	Formulation	Abbreviation	Uncertainty		Reference for Uncertainty
			$\pm 1\sigma$	$\pm 2\sigma$	
$K_{Ar_{(p=0)}}$	*Mucci* (1983)		2.5%	**5%**	*Mucci* (1983), p. 797
$K_{Ar_{(p)}}$	*Millero* (1979)		1.2%/km	**2.4% / km**	*Millero* (1979), p.1660
Ca^{2+}	*Riley and Tongudai* (1967)		0.05%	**0.1%**	*Jiang et al.* (2015), p.3

APPENDIX B

B.1 Δ/Γ Selection

In Figure B.1 we show the approach to select the proper Δ/Γ using mean ages from CFC-12 and SF_6 (as described in section 3.4.3 of the main text). In Table B1 we provide average differences between each Δ/Γ and reference ratio (Δ/Γ = 1.8) when applying our refined TTD method.

B.2 Mixed Layer Depth and Water Masses Definitions

B.2.1 Mixed Layer Depth

The MLD values used in this study were obtained from an empirical model based on a correlation between convection depths and winter-time weight-averaged cumulative heat losses. In order to account for the effect of ocean preconditioning, the annual heat loss was quantified as a weighted average value obtained from the 5 preceding years. A decreasing weight was attributed from the 1^{st} to the 5^{th} year prior the year of observation (*Yashayaev and Loder*, 2017).

In the figure B.2 we show results of MLD from four simulations where the weight attributed to the preceding years was varied. For our CFC-12 saturation calculations, we used the MLD-4 which was the modelled MLD that best matched the observed MLD.

B.2.2 Water Masses Definitions

The principal water masses of the central Labrador Sea were here defined both based on σ_2 (LSW and NEADW) and on depth ranges (Surface Water and DSOW). These definitions were introduced in previous studies in the region (e.g., *Yashayaev*, 2007; *Yashayaev and Loder*, 2016). In Table B2 we report the limits of each water mass. Because the Labrador

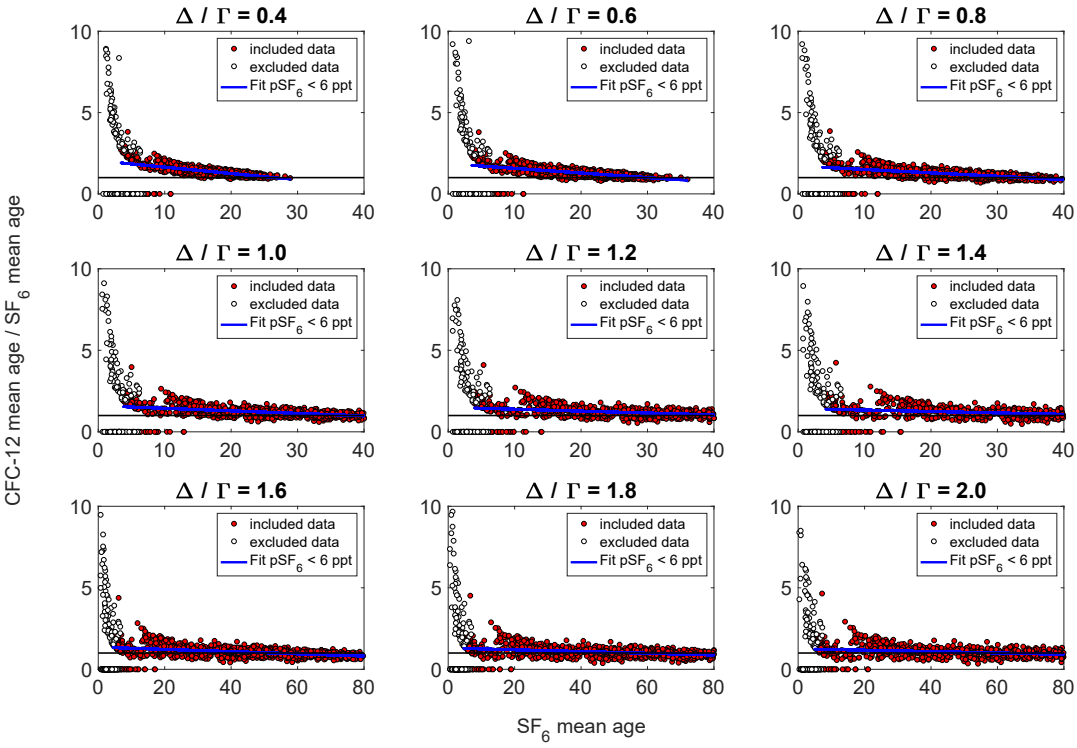

Figure B.1: Representation of quantitative selection of the Δ/Γ ratio that better represents physical conditions of the studied area. To objectively select the Δ/Γ, the ratio of mean ages from CFC-12 to mean ages from SF_6 is plotted against mean ages from SF_6, the data points were the SF_6 concentration is $<$6 ppt were included to obtain a fit of which the slope should be close to 0, the intercept close to 1 and the distance of each data point to the fit should be close to 0.

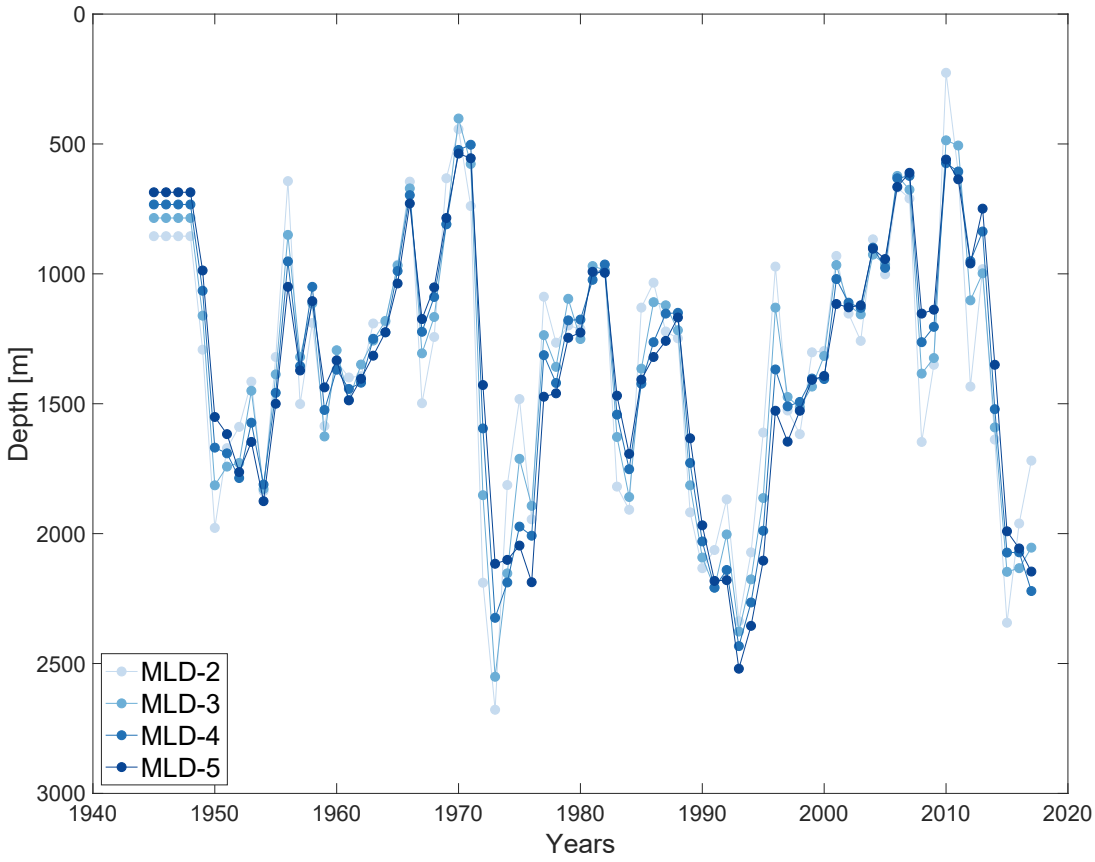

Figure B.2: Modelled mixed layer depth from an empirical model. The colours represent the different realizations obtained from the empirical model.

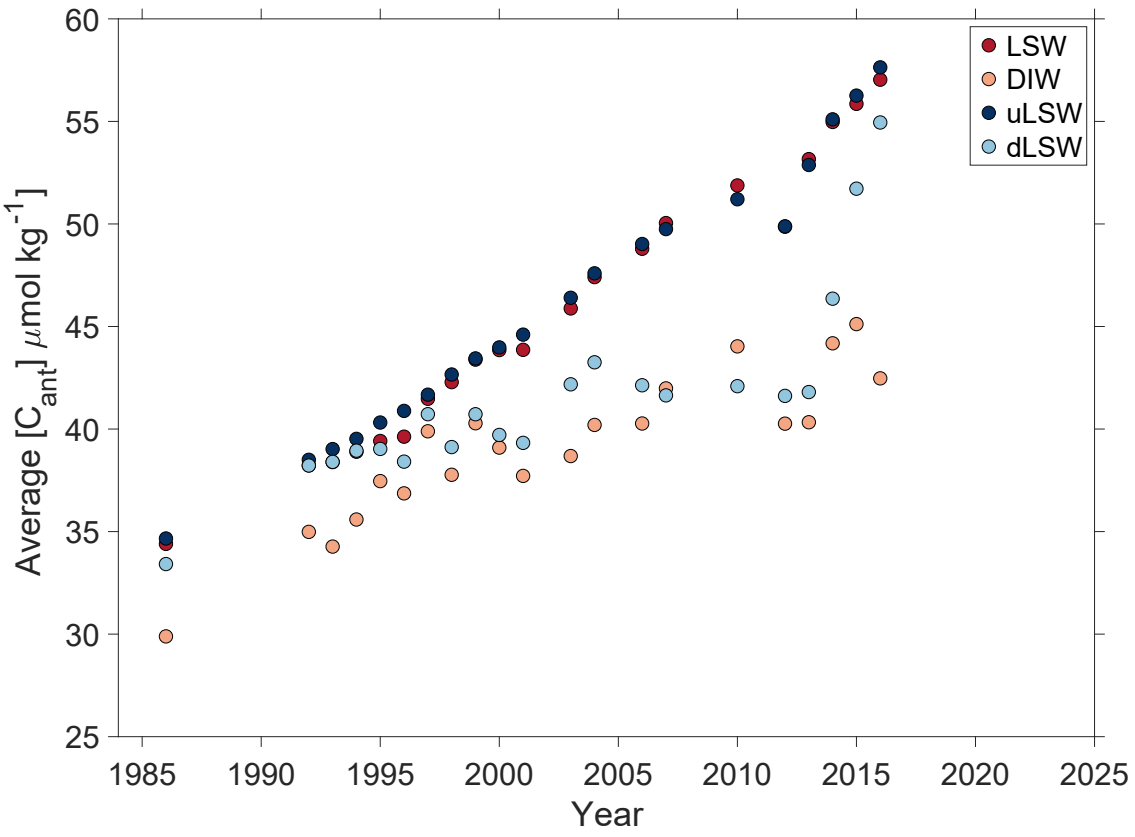

Figure B.3: Average C_{ant} concentrations in LSW and DIW as defined in this paper and in uLSW and dLSW as defined in the paper by *Rhein et al.* (2017).

Sea Water definition changes over time we also report the σ_2 limit identified for each year for this water mass in table B3.

For comparison purposes we also calculated average C_{ant} concentrations and inventories for the *upper* LSW (uLSW) and *deep* LSW (dLSW) as defined by *Stramma et al.* (2004) and used in *Rhein et al.* (2017). These results are reported in Figure B.3 and B.4. Although there are some differences between the two water mass definitions, both display a change in the relative contribution of the two layers ventilated in the Labrador Sea to the C_{ant} column inventory at the time when the storage rate was at its lowest (see top and middle panel of Figure B.4).

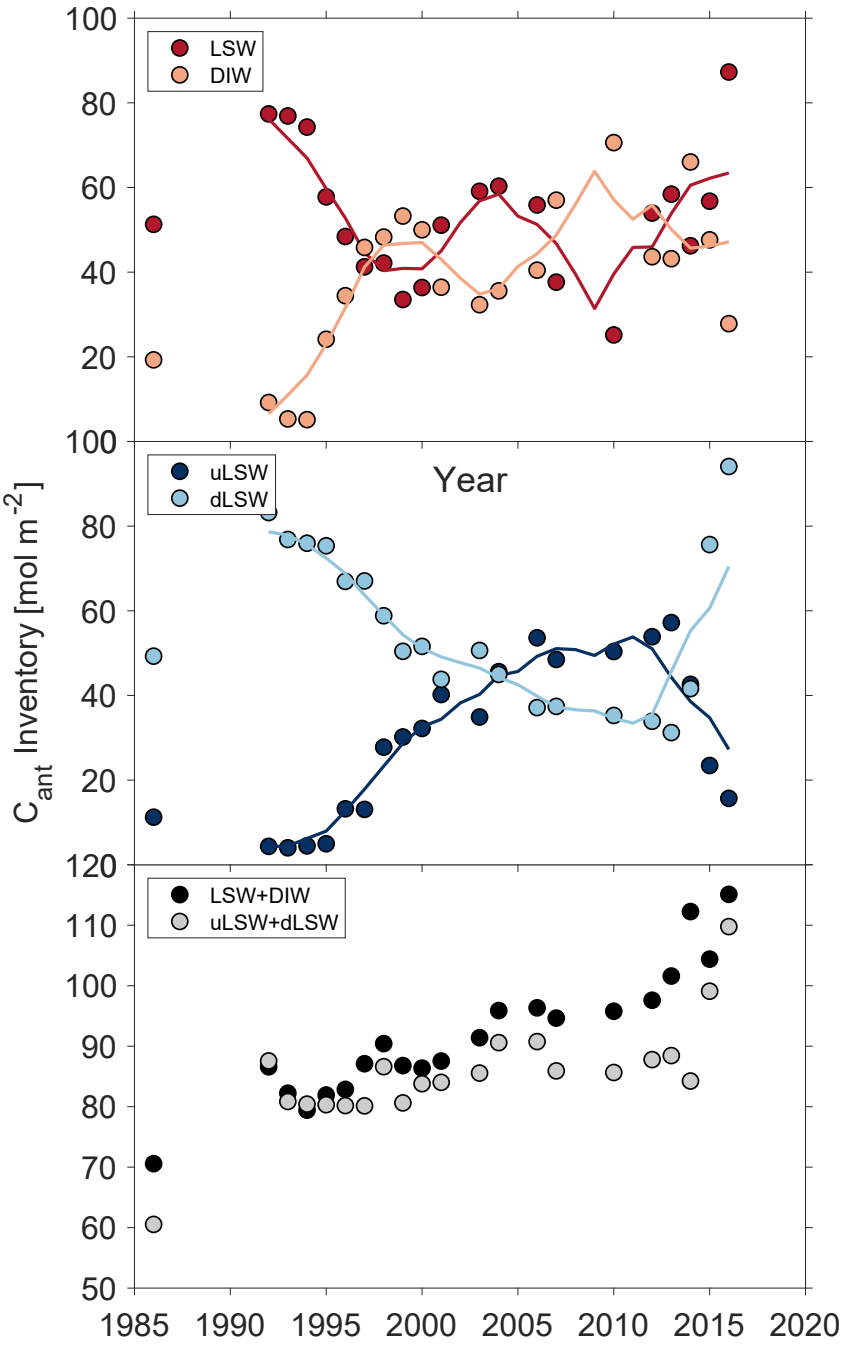

Figure B.4: C_{ant} inventories in mol m^{-2} in LSW and DIW defined in this paper (top panel) and in uLSW and dLSW as defined by *Stramma et al.* (2004) (middle panel). The bottom panel shows the inventory of the sum of the two layers with both definitions (LSW+DIW) and (uLSW+dLSW). Solid lines represent 5 years running means.

B.3 C_{ant} Results Using SF_6 as Tracer to Constrain Mean Ages

B.3.1 C_{ant} Estimates Based on Two SF_6 Saturation Reconstructions

As previously mentioned in the main text in section 3.5, we estimated anthropogenic carbon using both CFC-12 and SF_6. We included different scenarios to calculate C_{ant}: constant 100% saturation for both tracers, time varying saturation based on MLR using tracers' saturation observations. For SF_6 we also modelled the time varying saturation applying the regression coefficients obtained from the MLR with CFC-12 data to the atmospheric history of SF_6. We here report results of C_{ant} calculated from these different scenarios.

Compared to assuming a constant 100% saturation, the C_{ant} concentrations obtained using variable saturation of SF_6 modelled with the CFC-12 regression coefficients were on average $\sim 3 \pm 1$ μmol kg^{-1} higher. This difference was found to be even higher when the SF_6 variable saturation was obtained using regression coefficients based on the SF_6 observations (5 ± 1 μmol kg^{-1} higher).

Inventories calculated with 100% saturation of SF_6, were between 10.5 and 15.9 mol m^{-2} lower when compared to results with SF_6 saturation percentage constrained using the CFC-12 regression coefficients. This difference was between 17.2 and 20.1 mol m^{-2} when the constant saturation was compared to results with SF_6 saturations constrained through the SF_6 regression coefficients instead.

We obtained a rate of increase (C_{ant} storage rate) of 5.8 and 5.2 mol m^{-2} y^{-1} for values calculated using a variable saturation modelled from CFC-12 and SF_6 regression coefficients, respectively. While with the constant 100% saturation assumption the rate of increase was 4.4 mol m^{-2} y^{-1}. The storage rates reported for SF_6 only cover the period between 2012-2016 therefore in Table B4 we also report results of storage rate obtained with CFC-12. The table B4 and Figure B.5 show how the use of a refined TTD leads to better agreement of C_{ant} column inventories obtained with CFC-12 and SF_6.

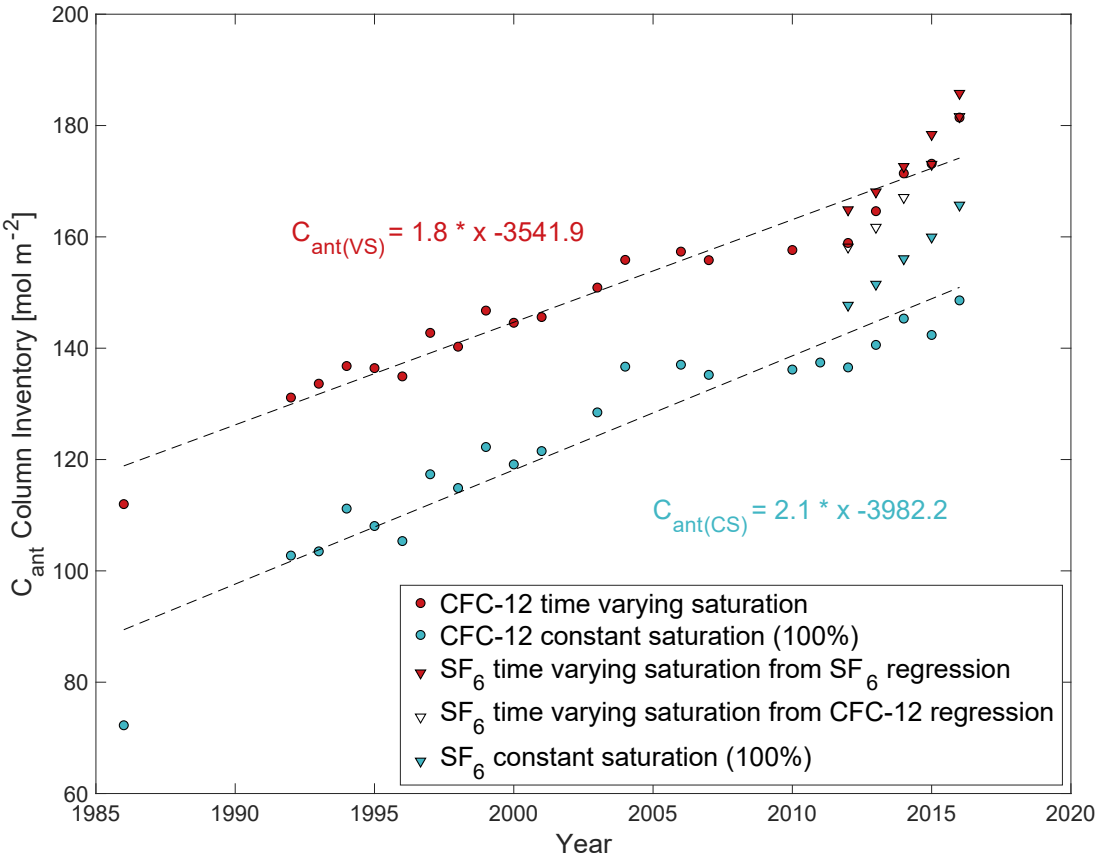

Figure B.5: Column inventories of C_{ant} in central Labrador Sea obtained from mean ages calculated using a constant 100% saturation assumption (teal markers) of CFC-12 (dots) and SF_6 (triangles) and the column inventory obtained from our refined TTD methods (red markers). For the SF_6 we also included results obtained with the CFC-12-based regression coefficients applied to the atmospheric history of SF_6 (clear triangles). All calculations of mean ages where performed with Δ/Γ = 1.8 for all these C_{ant} estimates.

B.3.2 C_{ant} Results from Different Δ/Γ

In Figure B.6 we report C_{ant} column inventories for central Labrador Sea from 2012 to 2016 as an average for all the Δ/Γ ratios listed in section 3.4.3 of the main text (dots) together with their standard deviations (shaded area). We found that using SF_6, the average increase in column inventory was between 163.2 and 185.1 mol m^{-2} over the period 2012 and 2016 using saturations based on the CFC-12 regression coefficients, and between 169.3 and 189.0 mol m^{-2} when saturation was based on SF_6.

Comparing the C_{ant} concentrations based on time variable saturations of SF_6 obtained with the two methods described earlier, we found that the percent difference between C_{ant} concentrations calculated with a Δ/Γ = 1.8 and all other ratios ranged from a minimum

of -7.9 to a maximum of -0.9% when CFC-12-based regression coefficients were applied to model the SF_6 saturation (see Table B5). This range was found to be between -11 and -3.3% when the SF_6-based regression coefficients were used to model the SF_6 saturation instead (see Table B6). The different concentrations obtained from the Δ/Γ ratios presented here translated into a maximum difference $\sim$ 2.5% in column inventory.

Caption Movie S1 (uploaded as separate document): Time evolution of C_{ant} obtained from the refined TTD method. The animation shows the C_{ant} section plots along the AR7W line between 1986 and 2016.

Caption Movie S2 (uploaded as separate document): Time evolution of C_{ant} spatial anomaly. The animation shows the C_{ant} spatial anomaly section plots along the AR7W line between 1986 and 2016. The anomaly was calculated as difference between C_{ant} concentrations at every location minus the average C_{ant} concentration of two end-members: the LSW and the NEADW ($\Delta C_{ant(i,t)} = C_{ant(i,t)} - C_{ant(LSW-NEADW,t)}$, where i is the location and t is year and $C_{ant(LSW-NEADW,t)}$ is the annual average C_{ant} concentrations obtained from LSW and NEADW).

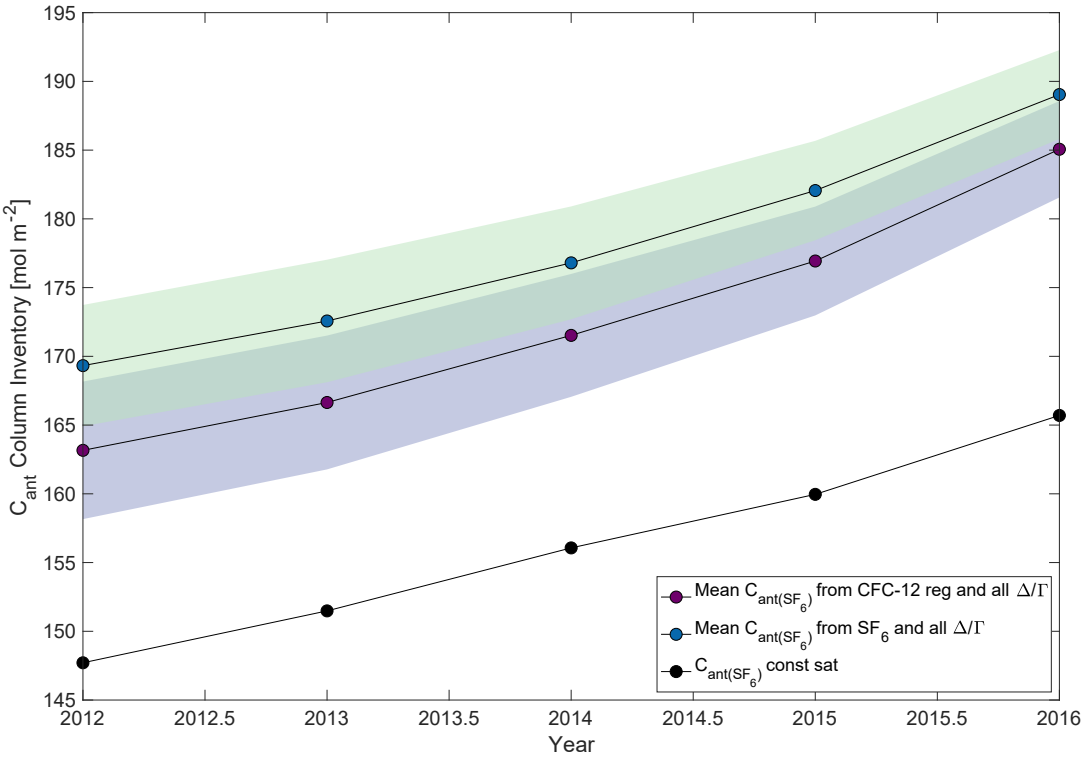

Figure B.6: Average column inventories of C_{ant} in central Labrador Sea from 2012 and 2016 using SF_6 data. The data shown were calculated using different Δ/Γ and time variable saturation. For SF_6 we present results using both a time variable saturation modelled with CFC-12-based regression coefficients (purple dots) and with SF_6-based regression coefficients (blue dots). The shaded areas represent the standard deviation obtained from all Δ/Γ. For reference we also report results obtained with constant saturation (black dots).

Table B1: Average percent difference in C_{ant} concentrations between each Δ/Γ ratio and a Δ/Γ = 1.8 (chosen as our reference based on our ratio selection procedure) obtained with CFC-12. Note that these numbers reflect conditions in Labrador Sea therefore these would be different for regions that are characterized by different ventilation pattern.

	Difference with respect to Δ/Γ = 1.8							
	Δ/Γ	Δ/Γ	Δ/Γ	Δ/Γ	Δ/Γ	Δ/Γ	Δ/Γ	Δ/Γ
Year	0.4	0.6	0.8	1.0	1.2	1.4	1.6	2.0
1986	-3.6	-3.0	-2.3	-1.8	-1.2	-0.7	-0.3	0.3
1992	-3.0	-2.8	-2.3	-1.8	-1.3	-0.8	-0.4	0.3
1993	-2.2	-2.0	-1.7	-1.3	-1.0	-0.6	-0.3	0.3
1994	-2.4	-2.1	-1.7	-1.3	-0.9	-0.6	-0.3	0.3
1995	-2.5	-2.2	-1.8	-1.4	-1.0	-0.6	-0.3	0.3
1996	-3.5	-3.0	-2.4	-1.8	-1.3	-0.8	-0.4	0.4
1997	-3.0	-2.6	-2.1	-1.6	-1.1	-0.7	-0.4	0.3
1998	-3.6	-3.0	-2.3	-1.8	-1.2	-0.8	-0.4	0.3
1999	-2.8	-2.3	-1.8	-1.3	-0.9	-0.6	-0.3	0.2
2000	-4.5	-3.6	-2.8	-2.0	-1.4	-0.9	-0.4	0.3
2001	-3.8	-3.0	-2.4	-1.8	-1.2	-0.8	-0.4	0.2
2002								
2003	-4.0	-3.2	-2.5	-1.9	-1.3	-0.8	-0.4	0.3
2004	-3.0	-2.4	-1.9	-1.4	-1.0	-0.6	-0.3	0.2
2005								
2006	-2.6	-2.2	-1.7	-1.3	-0.9	-0.5	-0.3	0.1
2007	-4.2	-3.5	-2.7	-2.0	-1.3	-0.8	-0.4	0.3
2008								
2009								
2010	-3.0	-2.5	-2.0	-1.4	-1.0	-0.6	-0.3	0.2
2011								
2012	-1.0	-1.0	-0.8	-0.6	-0.4	-0.2	-0.1	0.1
2013	-1.8	-1.7	-1.4	-1.0	-0.7	-0.4	-0.2	0.1
2014	-1.2	-1.2	-1.0	-0.7	-0.5	-0.3	-0.1	0.1
2015	-1.5	-1.3	-1.1	-0.8	-0.5	-0.3	-0.1	0.1

2016	-0.7	-0.7	-0.5	-0.4	-0.3	-0.1	-0.1	0.0

Table B2: Water Masses Definitions based on σ_2 and depth. LSW stands for Labrador Sea Water, DIW stand for Deep-Intermidiate Water, NEADW for North East Atlantic Deep Water and DSOW for Denmark Strait Overflow Water. The LSW_{σ_2} is the σ_2 that defines the extent of LSW. These are reported in Table B3.

Water Mass	Depth/σ_2 Range
SURFACE	0-200m
LSW	$>$200m - LSW_{σ_2}
DIW	$LSW_{\sigma_2}>\sigma_2<36.96$
NEADW	$36.96>\sigma_2<37.1$
DSOW	bottom 200m

Table B3: Inter-annual variability of the LSW σ_2 limit.

Year	LSW_{σ_2}
1986	36.910
1992	36.943
1993	36.952
1994	36.953
1995	36.942
1996	36.931
1997	36.913
1998	36.893
1999	36.870
2000	36.875
2001	36.887
2002	36.885
2003	36.887
2004	36.881
2005	36.868
2006	36.864
2007	36.842
2008	36.874
2009	36.860
2010	36.817
2011	36.823
2012	36.852
2013	36.850
2014	36.860
2015	36.879
2016	36.896

Table B4: Column inventories ($I_{C_{ant}}$; in mol m^{-2}) and storage rates (SR; in mol m^{-2} y^{-1}) of C_{ant} from different scenarios of tracer's saturation: constant 100% saturation of CFC-12 (CFC-$12_{(CS)}$ (100%)), time varying saturation of CFC-12 (CFC-$12_{(VS)}$), constant 100% saturation of SF_6 ($SF_{6(CS)}$ (100%)), time-varying saturation of SF_6 modelled with CFC-12-based regression coefficients ($SF_{6(VS)}$ (CFC-12 Reg)) and with SF_6-based regression coefficients ($SF_{6(VS)}$ (SF_6 Reg)).

	CFC-$12_{(CS)}$ (100%)	CFC-$12_{(VS)}$	$SF_{6(CS)}$ (100%)	$SF_{6(VS)}$ (CFC-12 Reg)	$SF_{6(VS)}$ (SF_6 Reg)
$I_{C_{ant}}$ (1986-2016)	72.3 - 148.6	112.0-181.4	-	-	-
$I_{C_{ant}}$ (2012-2016)	136.5-148.6	158.9-181.4	147.7-165.7	158.2-181.6	164.9-185.8
SR (1986-2016)	2.1	1.8	-	-	-
SR (2012-2016)	2.6	5.3	4.4	5.8	5.2

Table B5: Average percent difference in C_{ant} concentrations between each Δ/Γ ratio and a Δ/Γ = 1.8 (chosen as our reference based on our ratio selection procedure) using SF_6 time varying saturation obtained from CFC12-based regression coefficients.

	Difference with respect to Δ/Γ = 1.8							
	Δ/Γ	Δ/Γ	Δ/Γ	Δ/Γ	Δ/Γ	Δ/Γ	Δ/Γ	Δ/Γ
Year	0.4	0.6	0.8	1.0	1.2	1.4	1.6	2.0
2012	-6.6	-5.5	-4.2	-3.1	-2.1	-1.2	-0.6	0.5
2013	-7.9	-6.5	-5.0	-3.6	-2.4	-1.4	-0.6	0.4
2014	-7.1	-5.7	-4.3	-3.1	-2.1	-1.2	-0.5	0.4
2015	-6.1	-4.9	-3.7	-2.6	-1.7	-1.0	-0.4	0.3
2016	-5.3	-4.2	-3.2	-2.3	-1.5	-0.9	-0.4	0.3

Table B6: Average percent difference in C_{ant} concentrations between each Δ/Γ ratio and a Δ/Γ = 1.8 (chosen as our reference based on our ratio selection procedure) using SF_6 time varying saturation obtained from SF_6-based regression coefficients.

	Difference with respect to Δ/Γ = 1.8							
	Δ/Γ	Δ/Γ	Δ/Γ	Δ/Γ	Δ/Γ	Δ/Γ	Δ/Γ	Δ/Γ
Year	0.4	0.6	0.8	1.0	1.2	1.4	1.6	2.0
2012	-9.6	-8.6	-7.5	-6.5	-5.6	-4.9	-4.3	-3.4
2013	-11.0	-9.8	-8.5	-7.3	-6.2	-5.3	-4.6	-3.5
2014	-9.6	-8.5	-7.3	-6.2	-5.3	-4.5	-3.8	-2.9
2015	-8.5	-7.6	-6.5	-5.6	-4.8	-4.1	-3.6	-2.8
2016	-7.2	-6.4	-5.5	-4.6	-3.9	-3.3	-2.8	-2.1

APPENDIX C

Table C1: Comparisons of slopes between reference and comparison factors for 5-year time-interval. Slopes that are significantly different than the reference factor (or reference time interval) are reported in red.

Starting Year	Ending Year	Reference Time Interval	Slope (mol m^{-2} y^{-1})
1993	1998	2011-2016	0.46
1994	1999	(max slope)	1.29
1995	2000		2.52
1996	2001		2.71
1997	2002		1.60
1998	2003		2.33
1999	2004		2.16
2000	2005		2.24
2001	2006		3.54
2002	2007		3.58
2003	2008		3.57
2004	2009		2.58
2005	2010		1.63
2006	2011		0.48
2007	2012		1.10
2008	2013		1.57
2009	2014		2.85

Continued on next page

Table C1 – *Continued from previous page*

Starting Year	Ending Year	Reference Time Interval	Slope (mol m^{-2} y^{-1})
2010	2015		2.35
1993	1998	1994-1999	0.46
1995	2000	(median slope)	2.52
1996	2001		2.71
1997	2002		1.60
1998	2003		2.33
1999	2004		2.16
2000	2005		2.24
2001	2006		3.54
2002	2007		3.58
2003	2008		3.57
2004	2009		2.58
2005	2010		1.63
2006	2011		0.48
2007	2012		1.10
2008	2013		1.57
2009	2014		2.85
2010	2015		2.35
2011	2016		3.73
1994	1999	1993-1998	1.2
1995	2000	(min slope)	2.52
1996	2001		2.71
1997	2002		1.60
1998	2003		2.33
1999	2004		2.16
2000	2005		2.24
2001	2006		3.54
2002	2007		3.58

Continued on next page

Table C1 – *Continued from previous page*

Starting Year	Ending Year	Reference Time Interval	Slope (mol m^{-2} y^{-1})
2003	2008		3.57
2004	2009		2.58
2005	2010		1.63
2006	2011		0.48
2007	2012		1.10
2008	2013		1.57
2009	2014		2.85
2010	2015		2.35
2011	2016		3.73

Table C2: Comparisons of slopes between reference and comparison factors for 10-year time-interval.

Starting Year	Ending Year	Reference Time Interval	Slope (mol m^{-2} y^{-1})
1993	2003	1996-2006	1.47
1994	2004	(max slope)	1.55
1995	2005		2.42
1997	2007		2.48
1998	2008		2.87
1999	2009		2.44
2000	2010		2.13
2001	2011		1.98
2002	2012		2.60
2003	2013		2.42
2004	2014		2.73
2005	2015		2.01
2006	2016		2.19

Continued on next page

Table C2 – *Continued from previous page*

Starting Year	Ending Year	Reference Time Interval	Slope (mol m^{-2} y^{-1})
1993	2003	1995-2005	1.47
1994	2004	(median slope)	1.55
1996	2006		3.07
1997	2007		2.48
1998	2008		2.87
1999	2009		2.44
2000	2010		2.13
2001	2011		1.98
2002	2012		2.60
2003	2013		2.42
2004	2014		2.73
2005	2015		2.01
2006	2016		2.19
1994	2004	1993-2003	1.55
1995	2005	(min slope)	2.42
1996	2006		3.07
1997	2007		2.48
1998	2008		2.87
1999	2009		2.44
2000	2010		2.13
2001	2011		1.98
2002	2012		2.60
2003	2013		2.42
2004	2014		2.73
2005	2015		2.01
2006	2016		2.19

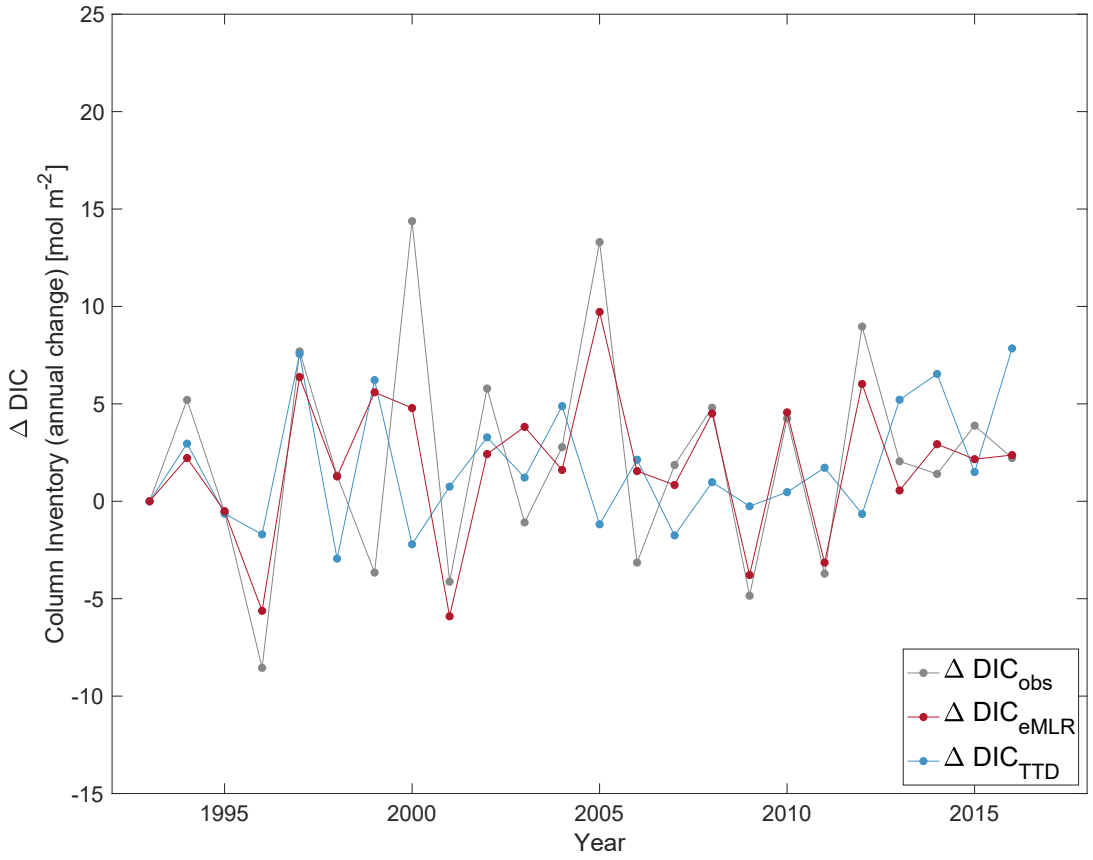

Figure C.1: Year-to-year change in column inventories of ΔDIC_{obs} (grey dots), ΔDIC_{eMLR} (red dots) and ΔDIC_{TTD} (blue dots).

Table C3: Comparisons of slopes between reference and comparison factors for 20-year time-interval.

Starting Year	Ending Year	Reference Time Interval	Slope (mol m^{-2} y^{-1})
1993	2013	1996-2016	1.85
1994	2014	(max slope)	1.85
1995	2015		2.04
1994	2014	1993-2013	1.85
1995	2015	(min slope)	2.04
1996	2016		2.55

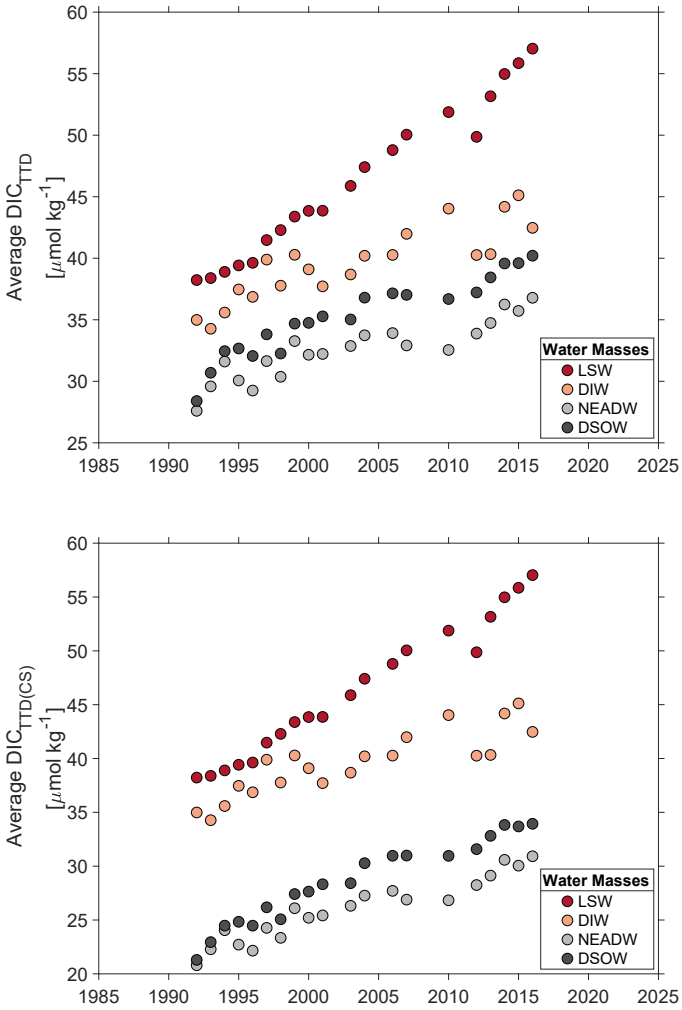

Figure C.2: Absolute values of C_{ant} average concentrations obtained with the TTD method in four major water masses of the Labrador Sea. Panel a shows values obtained using a time-varying saturation for all four water masses. Panel b shows average concentrations obtained using time-varying saturation for LSW and DIW and 100% constant saturation for DSOW and NEADW.

APPENDIX D

Dear Lorenza Raimondi,

We hereby grant you permission to reprint the material below at no charge in your thesis subject to the following conditions:

1. If any part of the material to be used (for example, figures) has appeared in our publication with credit or acknowledgement to another source, permission must also be sought from that source. If such permission is not obtained then that material may not be included in your publication/copies.

2. Suitable acknowledgment to the source must be made, either as a footnote or in a reference list at the end of your publication, as follows:

"This article was published in Publication title, Vol number, Author(s), Title of article, Page Nos, Copyright Elsevier (or appropriate Society name) (Year)."

3. Your thesis may be submitted to your institution in either print or electronic form.

4. Reproduction of this material is confined to the purpose for which permission is hereby given.

5. This permission is granted for non-exclusive world English rights only. For other languages please reapply separately for each one required. Permission excludes use in an electronic form other than submission. Should you have a specific electronic project in mind please reapply for permission.

6. As long as the article is embedded in your thesis, you can post/share your thesis in the University repository.

7. Should your thesis be published commercially, please reapply for permission.

8. Posting of the full article/ chapter online is not permitted. You may post an abstract with a link to the Elsevier website www.elsevier.com, or to the article on ScienceDirect if it is available on that platform.

Kind regards,

Roopa Lingayath Senior Copyrights Coordinator

BIBLIOGRAPHY

Andrade, J., and M. Estévez-Pérez, Statistical comparison of the slopes of two regression lines: A tutorial, *Analytica chimica acta*, *838*, 1–12, 2014.

Atamanchuk, D., J. Koelling, U. Send, and D. Wallace, Rapid transfer of oxygen to the deep ocean mediated by bubbles, *Nature Geoscience*, *13*, 232–237, 2020.

Azetsu-Scott, K., E. P. Jones, I. Yashayaev, and R. M. Gershey, Time series study of cfc concentrations in the labrador sea during deep and shallow convection regimes (1991–2000), *Journal of Geophysical Research: Oceans*, *108*, 2003.

Azetsu-Scott, K., E. P. Jones, and R. M. Gershey, Distribution and ventilation of water masses in the labrador sea inferred from cfcs and carbon tetrachloride, *Marine chemistry*, *94*, 55–66, 2005.

Azetsu-Scott, K., A. Clarke, K. Falkner, J. Hamilton, E. P. Jones, C. Lee, B. Petrie, S. Prinsenberg, M. Starr, and P. Yeats, Calcium carbonate saturation states in the waters of the Canadian Arctic Archipelago and the Labrador Sea, *Journal of Geophysical Research: Oceans*, *115*, 1–18, 2010.

Bernardello, R., I. Marinov, J. B. Palter, E. D. Galbraith, and J. L. Sarmiento, Impact of weddell sea deep convection on natural and anthropogenic carbon in a climate model, *Geophysical Research Letters*, *41*, 7262–7269, 2014.

Bockmon, E. E., and A. G. Dickson, An inter-laboratory comparison assessing the quality of seawater carbon dioxide measurements, *Marine Chemistry*, *171*, 36–43, 2015.

Böning, C., E. Behrens, A. Biastoch, K. Getzlaff, and J. Bamber, Emerging impact of greenland meltwater on deepwater formation in the north atlantic ocean, *Nature Geoscience*, *9*, 523–527, 2016.

Bullister, J., and R. Weiss, Anthropogenic chlorofluoromethanes in the greenland and norwegian seas, *Science*, *221*, 265–268, 1983.

Bullister, J. L., Atmospheric chlorofluoromethanes as tracers of ocean circulation and mixing: measurement and calibration techniques and studies in the greenland and norwegian seas, Ph.D. thesis, University of California, San Diego, 1984.

Bullister, J. L., Atmospheric histories (1765-2015) for cfc-11, cfc-12, cfc-113, ccl4, sf6 and n2o, *Carbon Dioxide Information Analysis Center, Oak Ridge National Laboratory, US Department of Energy, Oak Ridge, Tennessee*, 2017.

Carter, B., R. Feely, S. Mecking, J. Cross, A. Macdonald, S. Siedlecki, L. Talley, C. Sabine, F. J. Millero, J. Swift, et al., Two decades of pacific anthropogenic carbon storage and ocean acidification along global ocean ship-based hydrographic investigations program sections p16 and p02, *Global Biogeochemical Cycles*, *31*, 306–327, 2017.

Chen, B., W.-J. Cai, and L. Chen, The marine carbonate system of the Arctic Ocean: Assessment of internal consistency and sampling considerations, summer 2010, *Marine Chemistry*, *176*, 174–188, 2015.

Chierici, M., and A. Fransson, Calcium carbonate saturation in the surface water of the Arctic Ocean: undersaturation in freshwater influenced shelves, *Biogeosciences Discussions*, *6*, 4963–4991, 2009.

Chierici, M., A. Fransson, D. Turner, E. Pakhomov, and P. W. Froneman, Variability in pH, fCO_2, oxygen and flux of CO_2 in the surface water along a transect in the atlantic sector of the southern ocean, *Deep Sea Research Part II: Topical Studies in Oceanography*, *51*, 2773–2787, 2004.

Clayton, T., and R. Byrne, Spectrophotometric seawater pH measurements: Total hydrogen ion concentration scale calibration of m-cresol purple and at-sea results, *Deep Sea Research Part I: Oceanographic Research Papers*, *40*, 2115–2129, 1993.

Clayton, T., R. Byrne, J. Breland, R. Feely, F. Millero, D. Campbell, P. Murphy, and M. Lamb, The role of pH measurements in modern oceanic CO_2-system characterizations: precision and thermodynamic consistency, *Deep Sea Research Part II: Topical Studies in Oceanography*, *42*, 411–429, 1995.

Clement, D., and N. Gruber, The emlr (c*) method to determine decadal changes in the global ocean storage of anthropogenic co2, *Global Biogeochemical Cycles*, *32*, 654–679, 2018.

Culberson, C., and R. Pytkowicz, Effect of pressure on carbonic acid, boric acid, and the pH in seawater, *Limnology and Oceanography*, *13*, 403–417, 1968.

De Lavergne, C., J. B. Palter, E. D. Galbraith, R. Bernardello, and I. Marinov, Cessation of deep convection in the open southern ocean under anthropogenic climate change, *Nature Climate Change*, *4*, 278–282, 2014.

DeGrandpre, M., A. Körtzinger, U. Send, D. Wallace, and R. J. Bellerby, Uptake and sequestration of atmospheric CO_2 in the Labrador Sea deep convection region, *Geophysical Research Letters*, *33*, 1–5, 2006.

DeVries, T., The oceanic anthropogenic CO_2 sink: Storage, air-sea fluxes, and transports over the industrial era, *Global Biogeochemical Cycles*, *28*, 631–647, 2014.

Dickson, A., An exact definition of total alkalinity and a procedure for the estimation of alkalinity and total inorganic carbon from titration data, *Deep Sea Research Part A. Oceanographic Research Papers*, *28*, 609–623, 1981.

Dickson, A., and F. Millero, A comparison of the equilibrium constants for the dissociation of carbonic acid in seawater media, *Deep Sea Research Part A. Oceanographic Research Papers*, *34*, 1733–1743, 1987.

Dickson, A., and J. Riley, The effect of analytical error on the evaluation of the components of the aquatic carbon-dioxide system, *Marine Chemistry*, *6*, 77–85, 1978.

Dickson, A., D. Wesolowski, D. Palmer, and R. Mesmer, Dissociation constant of bisulfate ion in aqueous sodium chloride solutions to 250°C, *Journal of Physical Chemistry*, *94*, 7978–7985, 1990.

Dickson, A., C. Sabine, and J. Christian, Guide to best practices for ocean CO_2 measurements., *PICES Special Publication*, *3*, p191, 2007.

Dickson, A. G., Thermodynamics of the dissociation of boric acid in synthetic seawater from 273.15 to 318.15 k, *Deep Sea Research Part A. Oceanographic Research Papers*, *37*, 755–766, 1990.

Dlugokencky, E., J. Mund, A. Crotwell, M. Crotwell, and K. Thoning, Atmospheric carbon dioxide dry air mole fractions from the noaa esrl carbon cycle cooperative global air sampling network, 1968-2018, version: 2019-07, 2019.

Environment & Climate Change Canada, National inventory report 1990–2018: Greenhouse gas sources and sinks in canada, 2020.

Friis, K., A. Körtzinger, J. Pätsch, and D. Wallace, On the temporal increase of anthropogenic CO_2 in the subpolar North Atlantic, *Deep Sea Research Part I: Oceanographic Research Papers*, *52*, 681–698, 2005.

Gerber, M., F. Joos, M. Vázquez-Rodríguez, F. Touratier, and C. Goyet, Regional air-sea fluxes of anthropogenic carbon inferred with an Ensemble Kalman Filter, *Global Biogeochemical Cycles*, *23*, 2009.

Goodkin, N. F., N. M. Levine, S. C. Doney, and R. Wanninkhof, Impacts of temporal co2 and climate trends on the detection of ocean anthropogenic co2 accumulation, *Global Biogeochemical Cycles*, *25*, 2011.

Goyet, C., and A. Poisson, New determination of carbonic acid dissociation constants in seawater as a function of temperature and salinity, *Deep Sea Research Part A. Oceanographic Research Papers*, *36*, 1635–1654, 1989.

Gruber, N., J. L. Sarmiento, and T. F. Stocker, An improved method for detecting anthropogenic CO_2 in the oceans, *Global Biogeochemical Cycles*, *10*, 809–837, 1996.

Gruber, N., P. Landschützer, and N. S. Lovenduski, The variable southern ocean carbon sink, *Annual review of marine science*, *11*, 159–186, 2019a.

Gruber, N., M. Gloor, S. Mikaloff Fletcher, S. Doney, S. Dutkiewicz, M. Follows, M. Gerber, A. Jacobson, F. Joos, K. Lindsay, et al., Oceanic sources, sinks, and transport of atmospheric CO_2, *Global Biogeochemical Cycles*, *23*, 2009.

Gruber, N., D. Clement, B. R. Carter, R. A. Feely, S. Van Heuven, M. Hoppema, M. Ishii, R. M. Key, A. Kozyr, S. K. Lauvset, et al., The oceanic sink for anthropogenic co2 from 1994 to 2007, *Science*, *363*, 1193–1199, 2019b.

Haine, T. W., and K. J. Richards, The influence of the seasonal mixed layer on oceanic uptake of cfcs, *Journal of Geophysical Research: Oceans*, *100*, 10727–10744, 1995.

Hall, T., T. Haine, and D. Waugh, Inferring the concentration of anthropogenic carbon in the ocean from tracers, *Global Biogeochemical Cycles*, *16*, 2002.

Hall, T. M., D. W. Waugh, T. W. Haine, P. E. Robbins, and S. Khatiwala, Estimates of anthropogenic carbon in the indian ocean with allowance for mixing and time-varying air-sea co2 disequilibrium, *Global Biogeochemical Cycles*, *18*, 2004.

Hansson, I., A new set of acidity constants for carbonic acid and boric acid in sea water, *Deep Sea Research*, *20*, 461–478, 1973.

Holfort, J., K. Johnson, B. Schneider, G. Siedler, and D. W. Wallace, Meridional transport of dissolved inorganic carbon in the south atlantic ocean, *Global Biogeochemical Cycles*, *12*, 479–499, 1998.

Holzer, M., and T. M. Hall, Transit-time and tracer-age distributions in geophysical flows, *Journal of the atmospheric sciences*, *57*, 3539–3558, 2000.

Hsieh, P.-Y., Deconvolution of the labrador sea transit-time distribution from combined measurements of cfc-11 and cfc-12, Ph.D. thesis, UC Irvine, 2016.

Jayne, S. R., D. Roemmich, N. Zilberman, S. C. Riser, K. S. Johnson, G. C. Johnson, and S. R. Piotrowicz, The argo program: present and future, *Oceanography*, *30*, 18–28, 2017.

Jeansson, E., K. Olsson, T. Tanhua, and J. Bullister, Nordic seas and arctic ocean cfc data in carina, *Earth System Science Data*, *2*, 79–97, 2010.

Jiang, L.-Q., R. A. Feely, B. R. Carter, D. J. Greeley, D. K. Gledhill, and K. M. Arzayus, Climatological distribution of aragonite saturation state in the global oceans, *Global Biogeochemical Cycles*, *29*, 1656–1673, 2015.

Johnson, K., A. King, and J. Sieburth, Coulometric TCO_2 analyses for marine studies; an introduction, *Marine Chemistry*, *16*, 61–82, 1985.

Johnson, K., A. Körtzinger, L. Mintrop, J. Duinker, and D. Wallace, Coulometric total carbon dioxide analysis for marine studies: measurement and internal consistency of underway TCO_2 concentrations, *Marine Chemistry*, 1999.

Johnson, K., H. Jannasch, L. Coletti, V. Elrod, T. Martz, Y. Takeshita, R. Carlson, and J. Connery, Deep-sea durafet: A pressure tolerant pH sensor designed for global sensor networks, *Analytical Chemistry*, *88*, 3249–3256, 2016.

Johnson, K., W. Berelson, E. Boss, Z. Chase, H. Claustre, S. Emerson, N. Gruber, A. Körtzinger, M. Perry, and S. Riser, Observing biogeochemical cycles at global scales with profiling floats and gliders: prospects for a global array, *Oceanography*, *22*, 216–224, 2009.

Juranek, L. W., R. A. Feely, D. Gilbert, H. Freeland, and L. A. Miller, Real-time estimation of pH and aragonite saturation state from Argo profiling floats: Prospects for an autonomous carbon observing strategy, *Geophysical Research Letters*, *38*, 1–7, 2011.

Jutterström, S., and L. G. Anderson, The saturation of calcite and aragonite in the Arctic Ocean, *Marine Chemistry*, *94*, 101–110, 2005.

Karstensen, J., P. Schlosser, D. W. Wallace, J. L. Bullister, and J. Blindheim, Water mass transformation in the greenland sea during the 1990s, *Journal of Geophysical Research: Oceans*, *110*, 2005.

Keeling, C., S. Piper, R. Bacastow, M. Wahlen, T. Whorf, M. Heimann, and H. Meijer, Atmospheric CO_2 and $^{13}CO_2$exchange with the terrestrial biosphere and oceans from 1978 to 2000: observations and carbon cycle implications, in *A history of atmospheric CO_2 and its effects on plants, animals, and ecosystems*, pp. 83–113, Springer, 2005.

Keeling, C. D., The suess effect: 13carbon-14carbon interrelations, *Environment International*, *2*, 229–300, 1979.

Khatiwala, S., F. Primeau, and T. Hall, Reconstruction of the history of anthropogenic co 2 concentrations in the ocean, *Nature*, *462*, 346–349, 2009.

Khatiwala, S., T. Tanhua, S. Mikaloff Fletcher, M. Gerber, S. Doney, H. Graven, N. Gruber, G. McKinley, A. Murata, A. Ríos, et al., Global ocean storage of anthropogenic carbon, *Biogeosciences*, *10*, 2169–2191, 2013.

Kieke, D., and I. Yashayaev, Studies of Labrador Sea Water formation and variability in the subpolar North Atlantic in the light of international partnership and collaboration, *Progress in Oceanography*, *132*, 220–232, 2015.

Kim, H.-C., and K. Lee, Significant contribution of dissolved organic matter to seawater alkalinity, *Geophysical Research Letters*, *36*, 2009.

Koelling, J., D. W. Wallace, U. Send, and J. Karstensen, Intense oceanic uptake of oxygen during 2014–2015 winter convection in the labrador sea, *Geophysical Research Letters*, *44*, 7855–7864, 2017.

Körtzinger, A., J. Schimanski, U. Send, and D. Wallace, The ocean takes a deep breath., *Science*, *306*, 1337, 2004.

Körtzinger, A., U. Send, D. W. R. Wallace, J. Karstensen, and M. DeGrandpre, Seasonal cycle of O_2 and pCO_2 in the central Labrador Sea: Atmospheric, biological, and physical implications, *Global Biogeochemical Cycles*, *22*, 2008.

Lauvset, S. K., and T. Tanhua, A toolbox for secondary quality control on ocean chemistry and hydrographic data, *Limnology and Oceanography: Methods*, *13*, 601–608, 2015.

Le Quéré, C., R. Andrew, P. Friedlingstein, S. Sitch, J. Pongratz, A. Manning, J. Korsbakken, G. Peters, J. Canadell, R. Jackson, et al., Global carbon budget 2017, *Earth System Science Data*, *10*, 405, 2018.

Lee, K., F. Millero, and R. Wanninkhof, The carbon dioxide system in the Atlantic Ocean, *Journal of Geophysical Research*, *102*, 15,693 – 15,707, 1997.

Lee, K., F. J. Millero, R. H. Byrne, R. A. Feely, and R. Wanninkhof, The recommended dissociation constants for carbonic acid in seawater, *Geophysical Research Letters*, *27*, 229, 2000.

Lee, K., T.-W. Kim, R. Byrne, F. Millero, R. Feely, and Y.-M. Liu, The universal ratio of boron to chlorinity for the North Pacific and North Atlantic oceans, *Geochimica et Cosmochimica Acta*, *74*, 1801–1811, 2010.

Legge, O., D. Bakker, M. Johnson, M. Meredith, H. Venables, P. Brown, and G. Lee, The seasonal cycle of ocean-atmosphere CO_2 flux in Ryder Bay, west Antarctic Peninsula, *Geophysical Research Letters*, *42*, 2934–2942, 2015.

Levine, N. M., S. C. Doney, R. Wanninkhof, K. Lindsay, and I. Y. Fung, Impact of ocean carbon system variability on the detection of temporal increases in anthropogenic co2, *Journal of Geophysical Research: Oceans*, *113*, 2008.

Lewis, E., D. Wallace, and L. Allison, *Program developed for CO_2 system calculations*, Carbon Dioxide Information Analysis Center, managed by Lockheed Martin Energy Research Corporation for the US Department of Energy Tennessee, 1998.

Liu, X., M. Patsavas, and R. Byrne, Purification and characterization of meta-cresol purple for spectrophotometric seawater pH measurements, *Environmental Science & Technology*, *45*, 4862–4868, 2011.

Lozier, M., F. Li, S. Bacon, F. Bahr, A. Bower, S. Cunningham, M. De Jong, L. De Steur, B. Deyoung, J. Fischer, et al., A sea change in our view of overturning in the subpolar north atlantic, *Science*, *363*, 516–521, 2019.

Lueker, T., A. Dickson, and C. Keeling, Ocean pCO_2 calculated from dissolved inorganic carbon, alkalinity, and equations for K_{FL_1} and K_{FL_2}: validation based on laboratory measurements of CO_2 in gas and seawater at equilibrium, *Marine Chemistry*, *70*, 105–119, 2000.

Marion, G., F. Millero, M. Camões, P. Spitzer, R. Feistel, and C.-T. Chen, pH of seawater, *Marine Chemistry*, *126*, 89–96, 2011.

Martz, T., M. DeGrandpre, P. Strutton, W. McGillis, and W. Drennan, Sea surface pCO_2 and carbon export during the Labrador Sea spring-summer bloom: An in situ mass balance approach, *Journal of Geophysical Research: Oceans*, *114*, 2009.

Matsumoto, K., and N. Gruber, How accurate is the estimation of anthropogenic carbon in the ocean? an evaluation of the δc* method, *Global Biogeochemical Cycles*, *19*, 2005.

McKinley, G. A., A. R. Fay, N. S. Lovenduski, and D. J. Pilcher, Natural variability and anthropogenic trends in the ocean carbon sink, *Annual review of marine science*, *9*, 125–150, 2017.

Mehrbach, C., C. H. Culberson, J. E. Hawley, and R. M. Pytkowicz, Measurement of the apparent dissociation constants of carbonic acid in seawater at atmospheric pressure, *Limnology and Oceanography*, *18*, 897–907, 1973.

Mikaloff Fletcher, S., N. Gruber, A. Jacobson, S. Doney, S. Dutkiewicz, M. Gerber, M. Follows, F. Joos, K. Lindsay, D. Menemenlis, et al., Inverse estimates of anthropogenic CO_2 uptake, transport, and storage by the ocean, *Global Biogeochemical Cycles*, *20*, 2006.

Millero, F., Effects of pressure and temperature on activity coefficients, *Activity coefficients in electrolyte solutions*, *2*, 63–151, 1979.

Millero, F., The marine inorganic carbon cycle., *Chemical Review*, *107*, 308–341, 2007.

Millero, F., D. Pierrot, K. Lee, R. Wanninkhof, R. Feely, C. Sabine, R. Key, and T. Takahashi, Dissociation constants for carbonic acid determined from eld measurements, *Deep-Sea Research*, *49*, 1705–1723, 2002.

Millero, F. J., Thermodynamics of the carbon dioxide system in the oceans, *Geochimica et Cosmochimica Acta*, *59*, 661–677, 1995.

Millero, F. J., Carbonate constants for estuarine waters, *Marine and Freshwater Research*, *61*, 139–142, 2010.

Millero, F. J., T. B. Graham, F. Huang, H. Bustos-Serrano, and D. Pierrot, Dissociation constants of carbonic acid in seawater as a function of salinity and temperature, *Marine Chemistry*, *100*, 80–94, 2006.

Mojica Prieto, F., and F. Millero, The values of $pK_1 + pK_2$ for the dissociation of carbonic acid in seawater, *Geochimica et Cosmochimica Acta*, *66*, 2529–2540, 2002.

Mucci, A., The solubility of calcite and aragonite in seawater at various salinities, temperatures, and one atmosphere total pressure, *American Journal of Science*, *283*, 780–799, 1983.

Neill, C., K. M. Johnson, E. Lewis, and D. W. Wallace, Accurate headspace analysis of fCO_2 in discrete water samples using batch equilibration, *Limnology and Oceanography*, *42*, 1774–1783, 1997.

Olsen, A., R. Key, S. van Heuven, S. Lauvset, A. Velo, X. Lin, C. Schirnick, A. Kozyr, T. Tanhua, M. Hoppema, et al., The Global Ocean Data Analysis Project version 2 (GLODAPv2) – an internally consistent data product for the world ocean, *Earth System Science Data*, *8*, 297, 2016.

Orr, J., and J.-M. Epitalon, Improved routines to model the ocean carbonate system: mocsy 2.0, *Geoscientific Model Development*, *8*, 485–499, 2015.

Orr, J. C., J. M. Epitalon, and J. P. Gattuso, Comparison of ten packages that compute ocean carbonate chemistry, *Biogeosciences*, *12*, 1483–1510, 2015.

Orr, J. C., J.-M. Epitalon, A. G. Dickson, and J.-P. Gattuso, Routine uncertainty propagation for the marine carbon dioxide system, *Marine Chemistry*, *207*, 84–107, 2018.

Patsavas, M., R. Byrne, R. Wanninkhof, R. Feely, and W.-J. Cai, Internal consistency of marine carbonate system measurements and assessments of aragonite saturation state: Insights from two U.S. coastal cruises, *Marine Chemistry*, *176*, 9–20, 2015.

Perez, F. F., M. Vazquez-Rodriguez, E. Louarn, X. Padín, H. Mercier, and A. F. Ríos, Temporal variability of the anthropogenic co2 storage in the irminger sea, *Biogeosciences*, *5*, 1669–1679, 2008.

Pérez, F. F., H. Mercier, M. Vázquez-Rodríguez, P. Lherminier, A. Velo, P. C. Pardo, G. Rosón, and A. F. Ríos, Atlantic ocean co 2 uptake reduced by weakening of the meridional overturning circulation, *Nature Geoscience*, *6*, 146–152, 2013.

Plancherel, Y., K. Rodgers, R. Key, A. Jacobson, and J. Sarmiento, Role of regression model selection and station distribution on the estimation of oceanic anthropogenic carbon change by emlr, *Biogeosciences*, *10*, 4801, 2013.

Prinn, R., R. Weiss, P. Fraser, P. Simmonds, D. Cunnold, F. Alyea, S. O'doherty, P. Salameh, B. Miller, J. Huang, et al., A history of chemically and radiatively important gases in air deduced from ale/gage/agage, *Journal of Geophysical Research: Atmospheres*, *105*, 17751–17792, 2000.

Punshon, S., D. Childs, and K. Azetsu-Scott, A purge-and-trap gas chromatographic method for shipboard determination of the transient tracers sulphur hexafluoride and dichlorodifluoromethane in seawater and in air, *Canadian Technical Report of Hydrography and Ocean Sciences 309*, p. 21 pp., 2016.

Raimondi, L., J. B. R. Matthews, D. Atamanchuk, K. Azetsu-Scott, and D. W. Wallace, The internal consistency of the marine carbon dioxide system for high latitude shipboard and in situ monitoring, *Marine Chemistry*, *213*, 49–70, 2019.

Rhein, M., R. Steinfeldt, D. Kieke, I. Stendardo, and I. Yashayaev, Ventilation variability of labrador sea water and its impact on oxygen and anthropogenic carbon: a review, *Philosophical Transactions of the Royal Society A: Mathematical, Physical and Engineering Sciences*, *375*, 20160321, 2017.

Ribas-Ribas, M., V. Rerolle, D. Bakker, V. Kitidis, G. Lee, I. Brown, E. Achterberg, N. Hardman-Mountford, and T. Tyrrell, Intercomparison of carbonate chemistry measurements on a cruise in northwestern European shelf seas, *Biogeosciences*, *11*, 4339–4355, 2014.

Ridge, S., and G. McKinley, Advective controls on the north atlantic anthropogenic carbon sink, *Global Biogeochemical Cycles*, *34*, e2019GB006457, 2020.

Riley, J., and M. Tongudai, The major cation/chlorinity ratios in sea water, *Chemical Geology*, *2*, 263–269, 1967.

Riser, S., H. Freeland, D. Roemmich, S. Wijffels, A. Troisi, M. Belbéoch, D. Gilbert, J. Xu, S. Pouliquen, A. Thresher, et al., Fifteen years of ocean observations with the global Argo array, *Nature Climate Change*, *6*, 145–153, 2016.

Roemmich, D., Optimal estimation of hydrographic station data and derived fields, *Journal of Physical Oceanography*, *13*, 1544–1549, 1983.

Roy, R., L. Roy, K. Vogel, C. Porter-Moore, T. Pearson, C. Good, F. Millero, and D. Campbell, The dissociation constants of carbonic acid in seawater at salinities 5 to 45 and temperatures 0 to 45$^{\circ}C$, *Marine Chemistry*, *44*, 249–267, 1993.

Sabine, C., and T. Tanhua, Estimation of anthropogenic CO_2 inventories in the ocean., *Annual Review of Marine Science*, *2*, 175–198, 2010.

Sabine, C. L., R. A. Feely, N. Gruber, R. M. Key, K. Lee, J. L. Bullister, R. Wanninkhof, C. S. Wong, D. W. R. Wallace, B. Tilbrook, F. J. Millero, T.-H. Peng, A. Kozyr, T. Ono, and A. F. Rios, The Oceanic Sink for Anthropogenic CO_2, *Science*, *305*, 367–371, 2004.

Salt, L., H. Thomas, Y. Bozec, A. Borges, and H. De Baar, The internal consistency of the North Sea carbonate system, *Journal of Marine Systems*, *157*, 52–64, 2016.

Schneider, A., T. Tanhua, A. Körtzinger, and D. W. Wallace, High anthropogenic carbon content in the eastern mediterranean, *Journal of Geophysical Research: Oceans*, *115*, 2010.

Sloyan, B. M., R. Wanninkhof, M. Kramp, G. C. Johnson, L. Talley, T. Tanhua, E. McDonagh, C. Cusack, E. A. O'Rourke, E. McGovern, et al., The global ocean ship-base hydrographic investigations program (go-ship): a platform for integrated multidisciplinary ocean science, *Frontiers in Marine Science*, *6*, 445, 2019.

Smethie Jr, W. M., and R. A. Fine, Rates of north atlantic deep water formation calculated from chlorofluorocarbon inventories, *Deep Sea Research Part I: Oceanographic Research Papers*, *48*, 189–215, 2001.

Smith, J. N., W. M. Smethie, I. Yashayev, R. Curry, and K. Azetsu-Scott, Time series measurements of transient tracers and tracer-derived transport in the deep western boundary current between the labrador sea and the subtropical atlantic ocean at line w, *Journal of Geophysical Research: Oceans*, *121*, 8115–8138, 2016.

Steinfeldt, R., M. Rhein, J. L. Bullister, and T. Tanhua, Inventory changes in anthropogenic carbon from 1997–2003 in the atlantic ocean between 20 s and 65 n, *Global Biogeochemical Cycles*, *23*, 2009.

Stramma, L., D. Kieke, M. Rhein, F. Schott, I. Yashayaev, and K. P. Koltermann, Deep water changes at the western boundary of the subpolar north atlantic during 1996 to 2001, *Deep Sea Research Part I: Oceanographic Research Papers*, *51*, 1033–1056, 2004.

Tait, V., R. Gershey, and E. Jones, Inorganic carbon in the labrador sea: Estimation of the anthropogenic component, *Deep Sea Research Part I: Oceanographic Research Papers*, *47*, 295–308, 2000.

Takahashi, T., R. A. Feely, R. F. Weiss, R. H. Wanninkhof, D. W. Chipman, S. C. Sutherland, and T. T. Takahashi, Global air-sea flux of co2: An estimate based on measurements of sea–air pco2 difference, *Proceedings of the National Academy of Sciences*, *94*, 8292–8299, 1997.

Tanhua, T., and R. Keeling, Changes in column inventories of carbon and oxygen in the atlantic ocean, *Biogeosciences (BG)*, *9*, 4819–4833, 2012.

Tanhua, T., A. Körtzinger, K. Friis, D. W. Waugh, and D. W. Wallace, An estimate of anthropogenic co2 inventory from decadal changes in oceanic carbon content, *Proceedings of the National Academy of Sciences*, *104*, 3037–3042, 2007.

Tanhua, T., D. W. Waugh, and D. W. Wallace, Use of sf6 to estimate anthropogenic co2 in the upper ocean, *Journal of Geophysical Research: Oceans*, *113*, 2008.

Terenzi, F., T. Hall, S. Khatiwala, C. Rodehacke, and D. LeBel, Uptake of natural and anthropogenic carbon by the labrador sea, *Geophysical research letters*, *34*, 2007.

Thacker, W. C., Regression-based estimates of the rate of accumulation of anthropogenic co2 in the ocean: A fresh look, *Marine Chemistry*, *132*, 44–55, 2012.

Uppström, L., The boron/chlorinity ratio of deep-sea water from the Pacific Ocean, *Deep Sea Research and Oceanographic Abstracts*, *21*, 161–162, 1974.

Våge, K., R. S. Pickart, V. Thierry, G. Reverdin, C. M. Lee, B. Petrie, T. A. Agnew, A. Wong, and M. H. Ribergaard, Surprising return of deep convection to the subpolar north atlantic ocean in winter 2007–2008, *Nature Geoscience*, *2*, 67–72, 2009.

Van Heuven, S., D. Pierrot, J. Rae, E. Lewis, and D. Wallace, MATLAB Program Developed for CO_2 System Calculations. ORNL/CDIAC-105b. Carbon Dioxide Information Analysis Center, Oak Ridge National Laboratory, US Department of Energy, Oak Ridge, Tennessee, *cdiac. ornl. gov/ftp/co2sys/CO2SYS_calc_MATLAB_v1*, *1*, l, 2011.

van Heuven, S. M., M. Hoppema, O. Huhn, H. A. Slagter, and H. J. de Baar, Direct observation of increasing co2 in the weddell gyre along the prime meridian during 1973–2008, *Deep Sea Research Part II: Topical Studies in Oceanography*, *58*, 2613–2635, 2011.

Vázquez-Rodríguez, M., F. Touratier, D. Waugh, X. Padin, R. Bellerby, C. Goyet, N. Metzl, A. Ríos, F. Pérez, et al., Anthropogenic carbon distributions in the atlantic ocean: data-based estimates from the arctic to the antarctic., *Biogeosciences*, *6*, 439–451, 2009.

Walker, S. J., R. F. Weiss, and P. K. Salameh, Reconstructed histories of the annual mean atmospheric mole fractions for the halocarbons cfc-11 cfc-12, cfc-113, and carbon tetrachloride, *Journal of Geophysical Research: Oceans*, *105*, 14285–14296, 2000.

Wallace, D., Monitoring global ocean inventories, OOSDP Background Rep. 5, Ocean Observ, *Syst. Dev. Panel, Texas A&M Univ*, 1995.

Wallace, D., Introduction to special section: Ocean measurements and models of carbon sources and sinks, *Global Biogeochemical Cycles*, *15*, 3–10, 2001.

Wallace, D. W., and J. R. Lazier, Anthropogenic chlorofluoromethanes in newly formed labrador sea water, *Nature*, *332*, 61–63, 1988.

Wang, P., J. R. Scott, S. Solomon, J. Marshall, A. R. Babbin, M. Lickley, D. W. Thompson, T. DeVries, Q. Liang, and R. G. Prinn, On the effects of the ocean on atmospheric cfc-11 lifetimes and emissions, *Proceedings of the National Academy of Sciences*, *118*, 2021.

Wanninkhof, R., and K. Thoning, Measurement of fugacity of CO_2 in surface water using continuous and discrete sampling methods, *Marine Chemistry*, *44*, 189–204, 1993.

Wanninkhof, R., E. Lewis, R. Feely, and F. Millero, The optimal carbonate dissociation constants for determining surface water pCO_2 from alkalinity and total inorganic carbon, *Marine Chemistry*, *65*, 291–301, 1999.

Waters, J., F. Millero, and R. Woosley, Corrigendum to"the free proton concentration scale for seawater ph",[marche: 149 (2013) 8-22], *Marine Chemistry*, *165*, 66–67, 2014.

Waugh, D., T. Hall, B. McNeil, R. Key, and R. Matear, Anthropogenic CO_2 in the oceans estimated using transit time distributions, *Tellus B*, *58*, 376–389, 2006.

Weiss, R., Carbon dioxide in water and seawater: the solubility of a non-ideal gas, *Marine chemistry*, *2*, 203–215, 1974.

Williams, N., L. Juranek, R. Feely, K. Johnson, J. Sarmiento, L. Talley, A. Dickson, A. Gray, R. Wanninkhof, J. Russell, et al., Calculating surface ocean pCO_2 from biogeochemical Argo floats equipped with pH: An uncertainty analysis, *Global Biogeochemical Cycles*, *31*, 591–604, 2017.

Woosley, R., F. Millero, and T. Takahashi, Internal consistency of the inorganic carbon system in the Arctic Ocean, *Limnology and Oceanography: Methods*, 2017.

Yashayaev, I., Hydrographic changes in the Labrador Sea, 1960-2005, *Progress in Oceanography*, *73*, 242–276, 2007.

Yashayaev, I., and B. Dickson, Transformation and fate of overflows in the northern north atlantic, in *Arctic–Subarctic ocean fluxes*, pp. 505–526, Springer, 2008.

Yashayaev, I., and J. Loder, Recurrent replenishment of Labrador Sea Water and associated decadal-scale variability, *Journal of Geophysical Research: Oceans*, *121*, 8095–8114, 2016.

Yashayaev, I., and J. W. Loder, Further intensification of deep convection in the labrador sea in 2016, *Geophysical Research Letters*, *44*, 1429–1438, 2017.